JPL Publication 87-30

Proceedings of the Third Airborne Imaging Spectrometer Data Analysis Workshop

June 2–4, 1987

Gregg Vane

Editor

August 15, 1987

NASA
National Aeronautics and Space Administration

Jet Propulsion Laboratory
California Institute of Technology
Pasadena, California

JPL Publication 87-30

Proceedings of the Third Airborne Imaging Spectrometer Data Analysis Workshop

June 2–4, 1987

Gregg Vane

Editor

August 15, 1987

NASA

National Aeronautics and
Space Administration

Jet Propulsion Laboratory
California Institute of Technology
Pasadena, California

This publication was prepared by the Jet Propulsion Laboratory, California Institute of Technology, under a contract with the National Aeronautics and Space Administration.

ABSTRACT

The third and final Airborne Imaging Spectrometer (AIS) Data Analysis Workshop was held at the Jet Propulsion Laboratory on June 2, 3, and 4, 1987. It was attended by 106 people from 9 countries. Papers were presented by 20 investigators; summaries of 17 of these papers are published in these Workshop Proceedings. After a morning devoted to a status overview of the JPL imaging spectrometer program the first day of the Workshop, the remaining time was spent discussing AIS calibration, performance, information extraction techniques, and the application of high spectral resolution imagery to problems in geology and botany. Partly as a result of improvements to the sensor and additional time spent in analyzing data since the last Workshop, this Workshop produced the most convincing evidence of the power of imaging spectroscopy presented to date. Nevertheless, much work yet remains to be done to pave the way for routine application of this new tool to the full suite of earth science problems addressable with high spectral resolution remote sensing. Considerable enthusiasm was expressed for the new sensors now becoming available to replace AIS, the Airborne Visible/Infrared Imaging Spectrometer (AVIRIS) and the Portable Instant Display and Analysis Spectrometer (PIDAS).

FOREWORD

In the text and figure captions of some of the papers in the Proceedings, reference is made to color slides in a pocket at the end of the Proceedings. These 35 millimeter slides are sometimes color versions of the referenced black and white figures within the Proceedings. A limited number of copies were printed with the color slides included.

Contents

Omit 70
P.f

INTRODUCTION TO THE PROCEEDINGS OF THE THIRD AIRBORNE IMAGING SPECTROMETER (AIS) DATA ANALYSIS WORKSHOP

GREGG VANE, Jet Propulsion Laboratory, California Institute of Technology, Pasadena, California

The third and final Airborne Imaging Spectrometer (AIS) Data Analysis Workshop was held at the Jet Propulsion Laboratory in Pasadena, California, June 2, 3, and 4, 1987. The Workshop was attended by 106 people from 9 countries and was the capstone of an intensive effort begun in 1983 that has resulted in the successful establishment of a fundamentally new and powerful approach to earth remote sensing called imaging spectroscopy. In 1983, the first known sensor to image the earth in many narrow contiguous spectral bands in the short-wavelength infrared began operations aboard the NASA Ames C-130 research aircraft. AIS was built originally as an engineering test bed for two-dimensional infrared detector arrays operating in the 0.8 to 2.5 micrometer (μm) region. Early test flights over natural vegetation along the Santa Clara River in southern California and over the hydrothermally altered Cuprite Mining District in Nevada confirmed that the capability to acquire a complete reflectance spectrum for each pixel in the image provides the earth scientist with a powerful new class of data for identifying and assessing the characteristics of surface materials. Acquisition of data was immediately expanded to encompass a much wider range of surface cover types and earth science disciplines. Throughout the succeeding years since the first image was acquired with AIS, some 7000 flight line miles of data have been acquired throughout the US, Australia and Europe for over 50 scientists. Three sets of Workshop proceedings have been published, well over a dozen papers have appeared in the peer-reviewed literature, and a special issue of *Remote Sensing of Envirnoment* dedicated to research conducted with AIS data will be published in February, 1988. Considerable improvements were made in the sensor over this period as well, with a major upgrade to the original instrument in the winter of 1985/86 to incorporate a larger area detector array. Most of the papers in this set of proceedings summarize research conducted with data from the improved AIS-2.

The Airborne Imaging Spectrometer was retired in 1987 as an instrument for earth remote sensing, although it is still being used for engineering studies related to detector and sensor design and performance. AIS has been replaced by a much more capable sensor called the Airborne Visible/Infrared Imaging Spectrometer (AVIRIS) that covers the entire spectrum from 0.4 to 2.45 μm at high spectral and spatial resolution over an 11 kilometer swath. In addition, a new field instrument has been built called the

Portable Instant Display and Analysis Spectrometer (PIDAS), to provide high spectral resolution ground truth for use in conjunction with AVIRIS imagery. Finally, the pioneering scientific work done with AIS has led NASA to direct JPL to build an observatory-class imaging spectrometer for the polar-orbiting Earth Observing System (Eos) to be launched in the mid-1990s.

The 17 papers published in these proceedings attest to the power of the new tool of imaging spectroscopy. That so much has been accomplished in so short a time is a tribute to those who have worked so bravely and diligently with such a fundamentally new class of data which up to the date of the Third AIS Workshop was available only from an instrument that was designed to be an engineering test bed. A brief summary of each of the papers in these proceedings follows on the remaining pages of this introduction. For a more complete overview of the accomplishments of the AIS Program, see Vane and Goetz (1985, 1986, 1987), Goetz et al. (1985), and Vane (1986).

SENSORS, SENSOR PERFORMANCE, CALIBRATION AND INFORMATION EXTRACTION

The papers presented at the Third AIS Workshop fall generally into three broad categories: (1) Those related to the sensor, its calibration and performance, and techniques for extracting information; (2) those related to botanical research conducted with AIS; and (3) those reporting on geological research with AIS. During the first morning of the Workshop, an overview of the imaging spectrometer program at JPL was presented, including status summaries on the Eos instrument HIRIS (High Resolution Imaging Spectrometer) and AVIRIS, and Alex Goetz presented a talk on the new Portable Instant Display and Analysis Spectrometer (PIDAS), a summary of which is included in these proceedings. PIDAS is a field instrument weighing 67 pounds which in 2 seconds acquires an 872-point spectrum from 0.4 to 2.5 μm. The entire instrument is attached to a backpack and has been carried to many remote locations where it is operated on internal batteries. Through the use of bubble memory cards, over 700 spectra can be acquired before downloading to a Toshiba T1100 Plus personal computer is required for further data acquisition. A hand-held display unit allows the user to display the current spectrum or any others in memory, including a library of 128 permanently stored library spectra for comparison and interpretation in the field. PIDAS was built at JPL for Caltech under funding from the W. M. Keck Foundation and Caltech. JPL has proposed to NASA for funds to acquire PIDAS from Caltech and build a second instrument, both to be operated under the AVIRIS Project in support of NASA-sponsored research in the earth sciences.

Conel et al. reported on the use of AIS-2 and PIDAS for the recovery of ground reflectance at the Rogers Dry Lake in California. An experiment was conducted in October, 1986, to examine AIS radiometry in flight compared to in the lab. Results of the study indicate that the in-flight radiance measurement of the Rogers Dry Lake is about 30 percent higher than that obtained

using the laboratory calibration, the spectral sampling interval is 20 to 30 nm in flight, and the instrument-atmosphere-surface signal-to-noise ratio lies between 40 and 110, depending on how scene averages are taken. This is 30 percent lower than in the laboratory and is due probably to atmospheric and surface variations. In the study, various methods were explored for reducing the data to ground reflectance. It was found that the so-called log-residual method was least effective, due probably to the great homogeneity of the surface, while the empirical line method returned surface reflectance values that were within a few percent of the actual observed values.

Feldman discussed the use of principal component analysis for extracting geologically useful information from AIS-1 data from the hydrothermally altered Hot Creek Range in Nevada. Using a technique involving three separate PC analyses, she was able to achieve a good mineralogical separation in the Hot Creek Range. The first analysis used the first 16 of 32 AIS bands in the 2048 to 2337 μm range as input, the second used 7 intermediate bands, and the third used the last 16 bands from the 32 flat-field-corrected bands over this spectral region. While this approach is computationally intensive, it employs algorithms existing on most image processing systems.

Heric et al. have attempted to use AIS-1 imagery in conjunction with NS001 and Large Format Camera (LFC) color IR and black and white imagery to perform improved land cover and land use classification of Cairns, Queensland, Australia. Challenges in integrating the images from all three sensors limited the full utility of the data sets in performing an integrated study, but the classification of the LFC images was enhanced by taking advantage of the spectral content of the AIS imagery. The overall classification accuracy was determined to be 89 percent.

In another report on AIS calibration, Smith et al. discussed a method for calibrating images to reflectance in a way which transforms the image into a measure that is independent of the solar radiant flux. The transformation also makes the image spectra directly comparable to spectra from the laboratory and from field spectrometers. Applying the approach developed to AIS-2 imagery over the Tucson Mountains, Arizona, the authors show that first, the response of AIS-2 is nearly linear, second, the spectral variance in the data is caused primarily by sub-pixel mixtures of spectrally distinct materials and shade, and third, the sub-pixel mixtures can be treated as linear mixtures of pure spectral end members which are relatively few in number. The approach employed thus makes it possible to separate surface effects from those of the instrument, the atmosphere and the solar spectrum.

Clark and King discussed causes of spurious features in spectral reflectance data that can lead the unsuspecting investigator to draw incorrect conclusions from the data. Wavelength instability from one scan line to the next is one obvious cause of such spurious features, but several of the techniques being employed in the analysis of imaging spectrometer data can also introduce artifacts. Continuum removal by ratioing

an averaged spectrum from the scene to each pixel in the scene can produce band shifts and/or changes in band width or shape. Band positions can also be shifted if continuum removal is done by subtraction rather than division. In a companion paper, Clark et al. describe an algorithm for automated analysis of the continuum and features in spectra. The continuum algorithm is based on a "segmented upper hull" method in which an upper hull is performed on segments of the spectrum defined by local maxima and minima. The segments making a complete spectrum are then combined. This approach allows the continuum to be both convex and concave, adapting to the shape of the spectrum under study. The algorithm adapts to the widths of absorption features so that all features are found, including doublets, triplets, etc. Clark et al. report that the algorithm is reasonably fast on a minicomputer, making it applicable to the analysis of data from imaging spectrometers.

APPLICATION OF AIS IMAGERY TO BOTANICAL RESEARCH

Five of the 8 papers on botanical research presented at the Third AIS Workshop are summarized here in these proceedings. The first, by Swanberg and Matson, deals with the use of AIS-2 data to study induced variations in coniferous canopy chemistry. Wet chemistry analysis was used to confirm that treatments applied to an even-aged forest of Douglas fir trees near Mt. Taylor, New Mexico, were effective in providing a range of foliar nitrogen concentrations. At the time of the Workshop, work was just getting under way in performing a correlation study of the AIS and wet chemistry data. Preparation of the AIS data for the analysis included the removal of image lines dropped during the original decommutation of the AIS data, application of a notch filter to the Fourier transform of the image to remove vertical striping, and resampling to correct the aspect ratio of the imagery. Work yet to be done includes the examination of first and second difference AIS spectra from study plots at spectral channels known to contain information about a given foliar constituent, and exploration of multiple stepwise linear regression techniques for determining spectral bands correlated to foliar chemical composition.

The next paper in the proceedings is a progress report by Banninger on the AIS-2 experiment conducted in Austria in 1986. Data were collected over 8 sites in conjunction with studies in forest damage assessment, geobotany, alpine vegetation mapping, and land-use classification. In the geobotanical study, preliminary spectral reflectance curves showed an increase in reflectance for metal-stressed spruce trees compared with non-stressed trees.

Gross et al. reported on their research with AIS-2 data from the wetlands of San Francisco and Suisun Bays, California. Using broad-band differences in brightness, it was possible to accurately delineate the major cover types which included stands of green *Salicornia virginica*, green *Sesuvium verrocosum*, senescing *Distichlis spicata*, a mixture of senescing *Scirpus acutus* and *Scirpus californicus*, senescing *Scirpus paludosus*, senescent *Scirpus paludosus*, mowed senescent *Scirpus paludosus*, and soil. No

differences among narrow-band spectral reflectance of the cover types was apparent in the region between 0.8 and 1.6 μm. In performing the analysis of the distribution of the cover types using broad-band differences in reflectance, a procedure was used that assumed an additive linear mixture of surface spectra.

Price and Westman have used AIS-2 data from coastal scrub vegetation in the Santa Monica Mountains, California, to determine whether narrow spectral features might be used to assess concentrations of certain canopy chemical constituents. They applied a Fourier notch filter to the data, which were then ratioed against a flat field spectrum constructed from the reflectance of the nearby Interstate 5 freeway north of Griffith Park. Portions of the resulting spectra resemble spectra for plant cellulose and starch in that both show reduced reflectance at 2100 and 2270 nm; these are regions of absorption of energy by organic bonds found in starch and cellulose. Further study over larger fields of vegetation will be required to determine whether the observed relationship will be sufficient to recover concentrations of these chemicals remotely from AIS or AVIRIS spectra.

Riggs and Running reported on an AIS-2 experiment designed to look for spectral differences over water stressed conifer stands. The experiment was conducted in Germany where two paired stands, one of Norway spruce near Munich, the other of white pine near Frankfurt, were stressed by girdling the trunks of half the trees 13 days before the AIS-2 overflight in mid-July, 1986, and leaving the others alone. Water stress was evaluated during the overflight using shoot water potential and relative water content measurements. Preliminary analysis of the AIS data using SPAM yielded small, inconsistent differences in spectral reflectance between the stressed and natural canopies in the spectral region between 0.97 and 1.3 μm. The reflectance of the stressed white pines was slightly lower than that of the natural trees, while the reflectance of the stressed Norway spruce was greater than that of the control canopy in the morning, but lower in the afternoon. A lower reflectance relative to the unstressed trees is not consistent with the currently accepted hypothesis that near infrared reflectance increases with leaf water stress. Further work is under way with NS001 and Thermal Infrared Mapping Spectrometer (TIMS) data acquired at the same time as the AIS data.

GEOLOGICAL RESEARCH WITH AIS IMAGERY

The final 5 papers of the Third AIS Workshop Proceedings deal with geological research conducted with AIS-1 and -2. The first, by Mustard and Pieters, is a summary of a workshop paper and papers in press in the *Journal of Geophysical Research* and *Remote Sensing of Environment* related to a study of the Moses Rock diatreme in Utah. Using AIS-1 data collected over Moses Rock in 1984 and 1985, Mustard and Pieters have successfully mapped the distribution and abundance of the serpentinized ultramafic microbreccia contained in the Moses Rock diatreme, and have used this information to unravel the details of the eruption which formed the dike. The approach to

their research began with a careful calibration of the AIS data done by dividing the raw AIS imagery by a spectrum from an internal standard area, then multiplying the resulting relative reflectance data by the absolute bidirectional reflectance of a carefully selected sample from the standard area which was measured in the laboratory. From the calibrated data, it was possible to identify the minerals serpentine, gypsum, and illite, as well as desert varnish, various sandstones, and the lithologies of the serpentinized ultramafic microbreccia. Six end members were chosen to represent the dominant lithologies on the surface at the Moses Rock dike. Spectra of these end members were then used in an intimate mixture model to deconvolve the AIS data into surface abundance for each component. Field observations confirmed these results. Finally, the distribution and abundance of the serpentinized ultramafic microbreccia in the matrix of the diatreme were studied to reveal the styles of dispersion that were responsible for its occurrence throughout the Moses Rock dike.

The paper by Lyon describes his on-going work in the Singatse Range of Nevada with AIS-2. Several steps in data pre-processing are described to bring the data to an interpretable level. These included application of a 3 by 3 filter to remove dark pixels resulting from tape recorder problems during data decommutation, removal of vertical striping by a column-by-column histogram matching procedure, and finally, calculation of a log-residual spectrum showing departure of a 2 by 2 pixel area from the spatially- and spectrally-averaged scene. Field spectra were gathered with a Collins visible/infrared intelligent spectrometer (VIRIS) for comparison with the AIS spectra. Lyon found the VIRIS and AIS spectra matched as long as the pixel imaged with AIS was sufficiently well exposed. He was also able to locate a large open pit area of gypsum, an area with known serecite, and occasionally, areas with outcropping dolomitic limestone from the AIS imagery. A further validation of the specific log-residual approach employed in the study was the noted absence of any O-H absorption features over an area known to be free of O-H bearing minerals.

Mackin et al. have been using AIS-1 data to study an area of epithermal alteration in the Seventy Mile Range in northern Queensland, Australia. The area contains undifferentiated sequences of acidic to intermediate volcanics and intrusives, meta-sediments, and a series of partially lateritized sedimentary rocks. Using both the log residual and the internal average relative reflectance techniques to enhance the spectral features related to the known mineralogy did not yield significant results because of the vegetation cover in the area. However, the application of a hybrid approach based on the relative reflectance differences between vegetated and non-vegetated surfaces at 1.2 and 2.1 μm did enhance the features believed to be associated with clays and epidote. By using SPAM software interactively, it was possible to identify the clay kaolinite despite the presence of spectral effects caused by vegetation and second order overlap.

Brickey et al. reported on their work with AIS-1 data over the Ruby Mountains, Montana, using absorption-band-depth images to

study an area of amphibolite-grade metamorphic rocks that have a moderate rangeland vegetation cover. Rock exposures are few at the site, but exposed soil accounts for about 20 to 30 percent of the surface. A spectral-channel-averaging, low-pass spatial filtering process was applied to the AIS data to produce band-depth images for diagnostic soil/rock absorption bands. Sets of three such images were combined to produce color-composite band-depth images. The resulting images from this relatively simple approach, which does not require extensive calibration, were effective for revealing a number of spectrally distinctive rocks and soils, including soils having high talc concentrations. The authors note that such results indicate considerable promise for mapping mineral variations in soil, even with moderate vegetation cover.

Kruse has completed a study of seven AIS flight lines acquired in 1984, 1985, and 1986 over the Northern Grapevine Mountains between California and Nevada, in an area of hydrothermal alteration. He reduced the AIS images to reflectance relative to an average spectrum, then used an automated procedure to produce a color coded image showing absorption band information. Analysis of this image was supplemented by extracting spectra from the AIS images to determine the detailed mineralogy of the Grapevine Mountains. Two alteration types were mapped based on the mineralogy identified using the AIS data. The primary alteration type is quartz-serecite-pyrite alteration occurring in northwest trending zones in quartz monzonite porphyry. The second alteration type occurs as a zone of argillic alteration associated with a granitic intrusion. The mineralogy associated with each of these alteration types is discussed and examples of AIS-derived spectra are shown. The AIS alteration map produced by the study was field checked and shows good correspondence with the field mapping.

REFERENCES

Goetz, A.F.H., G. Vane, J.E. Solomon, and B.N. Rock, Imaging spectrometry for earth remote sensing, *Science*, v. 228, pp. 1147-1153, 1985.

Vane, G., Hyperspectral resolution remote sensing of the earth, *Sensors*, v. 2, no. 12, pp. 11-19, 1986.

Vane, G. and A.F.H. Goetz, eds., Proceedings of the Airborne Imaging Spectrometer Data Analysis Workshop, *JPL Publication 85-41*, 173 p., Jet Propulsion Laboratory, Pasadena, California, 1985.

_____, Proceedings of the Second Airborne Imaging Spectrometer Data Analysis Workshop, *JPL Publication 86-35*, 212 p., Jet Propulsion Laboratory, Pasadena, California, 1986.

Vane, G. and A.F.H. Goetz, Terrestrial imaging spectroscopy, *Remote Sensing of Environment*, v. 24, no. 1 (in press).

THE PORTABLE INSTANT DISPLAY AND ANALYSIS SPECTROMETER (PIDAS)

ALEXANDER F. H. GOETZ
Center for the Study of Earth from Space (CSES)
Cooperative Institute for Research in Environmental Sciences (CIRES)
University of Colorado, Boulder, Colorado 80309

ABSTRACT

A field spectrometer covering the range 0.4-2.5 μm has been developed that acquires spectra in 2 seconds at 872 points within the spectrum. The Portable Instant Display and Analysis Spectrometer (PIDAS) can acquire spectra every 8 seconds and stores up to 288 spectra in bubble memory. A hand-held display unit allows for display of the current spectrum acquired and superimposed, one of 128 permanently stored library spectra. PIDAS represents a major advance in the technology of field spectral data acquisition and for the first time makes possible the acquisition of enough spectra to characterize the mean and intraclass variance within a Landsat MSS or TM pixel.

INTRODUCTION

The need and the idea for the Portable Instant Display and Analysis Spectrometer (PIDAS) developed beginning at the time of completion of the first Portable Field Reflectance Spectrometer (PFRS) (Goetz *et al.*, 1975). One of the major goals in *in situ* spectrometric measurements that has eluded us until now is the ability to define the average spectral reflectance characteristics within one Landsat MSS or TM pixel and to define the intraclass variance within a pixel. Another major goal is to be able to make *in situ* spectral measurements with a resolution comparable to or higher than the new class of imaging spectrometers such as the Airborne Imaging Spectrometer (AIS) and the Airborne Visible and Infrared Imaging Spectrometer (AVIRIS). Most laboratory instruments do not have adequate spectral resolution beyond 2.0 μm (Inouye *et al.*, 1987). A field spectrometer with sufficient resolution is available commercially (GER Corporation) but the 3- to 4-minute scan time required for a single spectrum is not ideal. PIDAS achieves these long awaited goals with the addition of near-real-time display of spectral reflectance.

Support for the construction of PIDAS was obtained from the W. M. Keck Foundation with grants in 1983 and 1984. The instrument was field tested in July 1986.

REQUIREMENTS

The main requirement arising from previous experience with field instruments was for a lightweight, rugged spectrometer covering the 0.4-2.5 μm region at high resolution, able to acquire and store complete spectra in several seconds, and display the results for immediate viewing. In addition, there was a need to display a set of stored spectra for comparison with the field-acquired spectra. The display and the ability to call up stored spectra comprise the "analysis" aspect of the instrument. The display capability is a major advance in field measurements because many of the spectral characteristics of surface materials are found in the spectral region beyond the sensitivity of the human eye. Proper sample location and identification is made possible by a near real-time display.

DESIGN

In order to meet the requirements discussed above, it was necessary to develop a spectrometer with features not available in existing instruments. In particular, the implementation required the use of very fast, lightweight rugged spectrometers and an optical head connected to the spectrometers with optical fibers. Table 1 lists the new features required for the design.

Table 1. Design features

Hand-held liquid crystal display
Silica and "exotic" fluoride fibers
Fast (f/1.2) solid silica spectrometers
Stored library of spectra
Spectral resolution greater than most laboratory instruments
2-second data acquisition time

Figure 1 shows the PIDAS in operation; Figure 2 shows the major features of the instrument. The requirement for high spectral resolution could only be met by using grating spectrometers. A great saving in weight and volume could have been achieved by using circular variable filters, as used in the PFRS, but these filters have a limitation in spectral performance, particularly in the visible portion of the spectrum. The $\Delta\lambda/\lambda$ values in the visible are approximately 0.04 and 0.015 in the short wavelength infrared (SWIR). At 2.2 μm this translates into a resolution of

Fig. 1. PIDAS during field trials in Cuprite, Nevada.

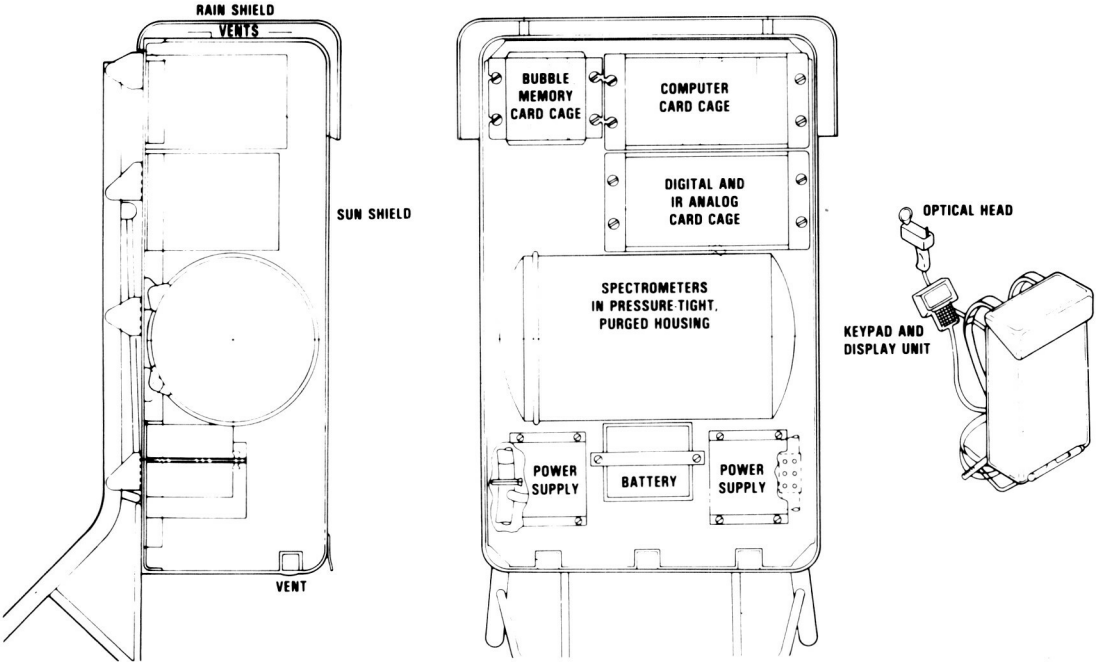

Fig. 2. PIDAS configuration.

approximately 33 nm or a resolution 60% poorer than that available from AVIRIS. The spectral resolution of PIDAS in the SWIR is defined by the 4.8 nm sampling interval and is approximately 10 nm. The sampling interval in the visible portion of the spectrum is 0.88 nm.

A major design goal was to make the optical head as lightweight as possible which meant that the spectrometers had to be separated from the fore-optics. Therefore, the optical head consists solely of the fore-optics, a shutter and a chopper, and the incoming energy is transmitted to the spectrometers by means of optical fibers. Figure 3 shows a block diagram of the spectrometer system. The optical components consisting of three spectrometers with detectors, the amplifiers, and grating drives are contained in a pressure vessel shown in Figure 4. The spectrometer covering the VNIR portion of the spectrum consists of a camera lens, a fixed grating and a 512-element silicon detector array. This spectrometer covers the region 0.425-0.922 μm. The VNIR spectrometer assembly is shown in Figure 5.

The spectrometers for the SWIR portion of the spectrum ranging from 0.86 to 2.5 μm posed a more difficult problem. Lead sulfide detectors provided the best compromise between sensitivity and ease of cooling. A disadvantage of lead sulfide detectors is that it is not possible to obtain multiplexed arrays of detectors. This means that each detector requires its own preamplifier and analog circuitry. Unlike the visible spectrometer which contained no moving parts, it was necessary to step the grating in each of the SWIR spectrometers through four positions in 2 seconds. Using 45-element detector arrays in each spectrometer, 360 channels spaced approximately 4.7 nm apart were obtained in the 0.86-2.5 μm region. A very compact spectrometer design was developed employing a solid block of water-free silica incorporating all the optical surfaces in one unit. By this means, the only alignment required was to focus and align the detectors and the optical fibers. This solid-Schmidt design made possible a fast, f/1.2 spectrometer in order to acquire the maximum signal-to-noise ratio. The fast spectrometer design in turn placed a requirement for a high numerical aperture (0.5) for the optical fibers. A further complication arose from the fact that silica optical fibers are not completely water-free and, therefore, exhibited absorption features at 1.4, 1.9 and 2.2 μm. Fluoride optical fibers are used to couple the fore-optics to the SWIR spectrometers. The solid-Schmidt spectrometer optics are shown in Figure 6, and the grating drive assembly in Figure 7. Figure 8 shows the spectrometer enclosure viewed from the side of the SWIR detectors and the 90-channel analog PC boards.

The electronics and data handling are designed around a CMOS 8-bit processor with storage in bubble memory. The

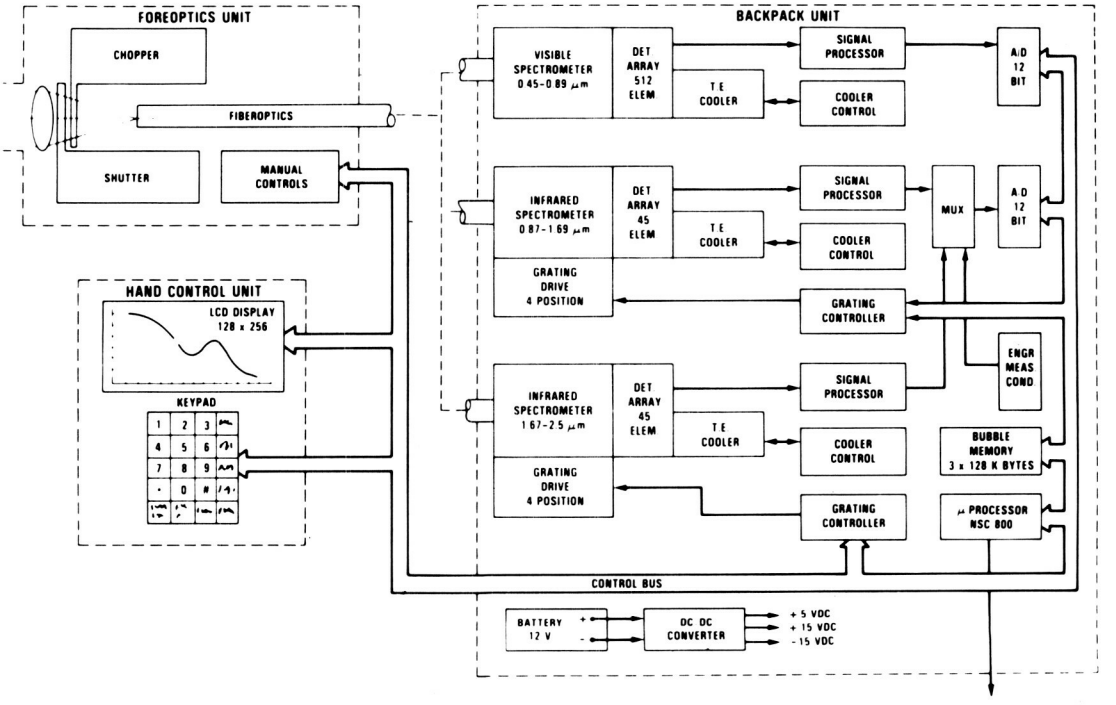

Fig. 3. PIDAS block diagram.

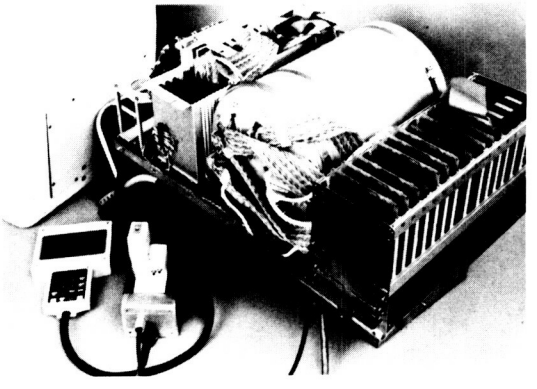

Fig. 4. PIDAS with cover removed showing the pressurized container housing the spectrometers, the hand-held display unit and the fore-optics head.

Fig. 5. VNIR spectrometer assembly.

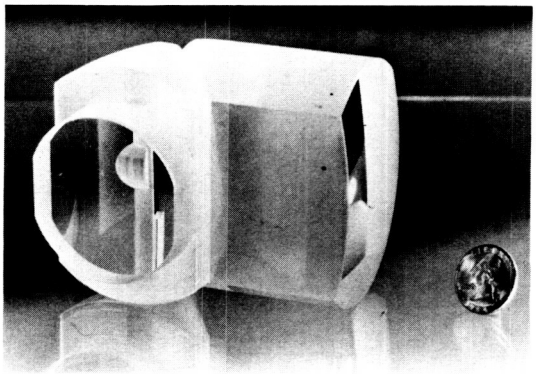

Fig. 6. Solid Schmidt SWIR spectrometer optics.

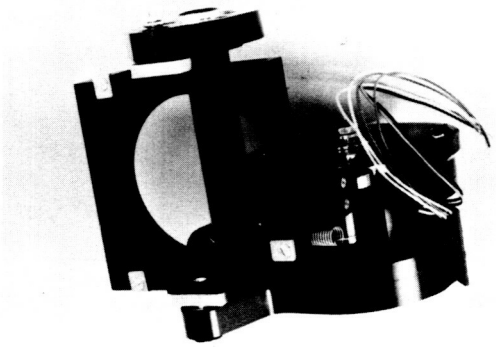

Fig. 7. SWIR grating drive assembly.

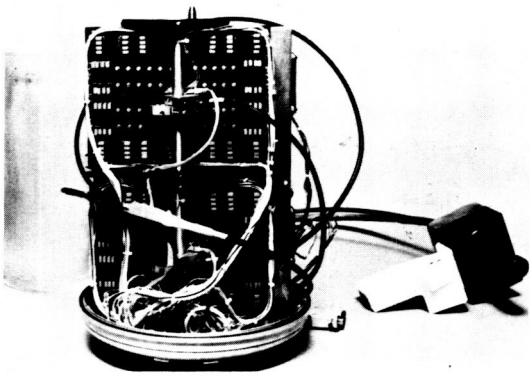

Fig. 8. Pressure vessel with the housing removed showing the detector preamplifier boards.

processor handles all the input/output functions and provides the data acquisition sequence, display and memory access. The hand-held terminal consists of a key pad and a 128- x 256-element liquid crystal display. Software stored on a prom allows the display of engineering data and individual spectra at various magnifications. Data from a 128-spectra bubble memory library can be superimposed upon the current data acquired or stored in the 288 spectra data bubble memory. The software features include the ability to expand the scale by use of gain and offset functions so that the full 8-bit resolution can be displayed.

PIDAS is a single channel instrument, and, therefore, spectra of standards and samples are collected separately. In normal operation, a spectrum of a standard is collected and encoded to 12 bits. The most significant 8 bits are stored as a reference for all subsequent sample spectra until a new standard spectrum is acquired. When the sample spectrum is acquired, the instrument automatically creates a

ratio of sample to standard before storing the spectrum in bubble memory. The advantage of this method is that no gain changes are required and storage is optimized. The disadvantage is that, particularly for dark samples, digitization error becomes a major factor and limits the ability to increase the signal-to-noise ratio by averaging sample spectra. A summary of the major instrument characteristics is given in Table 2.

Table 2. PIDAS characteristics

Portable, backpack, self-contained, approx. 67 pounds
Spectral range - 0.45 to 2.5 μm
Sampling interval
Visible - 0.88 nm (512 channels) 0.425-0.922 μm
Infrared - 4.7 nm (360 channels) 0.856-2.490 μm
Fore-optics - f/1.2, 6 degree circular FOV
Spectrometers
VIS - Nikon optics, f/2.8, 512 Si.
IR-2 - solid Schmidt, f/1.2, 45 PbS.
Processor-low power Z80 type, 16K RAM, 8K ROM
Data Memory - bubble, 288 spectra, 128 spectra sample library
Hand-held terminal-display 128 x 256 element LCD keypad-custom numeric and command entry
Data acquisition time: 2 sec., repeat interval: 8 sec.

Data stored in the bubble memories are downloaded onto a floppy disc across an RS 232 interface to a PC. Battery power consists of ten NiCd D cells. One charge will run the instrument for approximately two and a half hours, sufficient time to collect a full memory load of 288 spectra. The bubble memories as well as the batteries are exchangeable in the field.

The initial target instrument weight was 42 pounds. The present weight is 67 pounds; however, it is anticipated that in subsequent versions of the instrument the weight will be reduced significantly.

TEST RESULTS

In the last year, PIDAS has acquired thousands of spectra for applications in mineralogy, botanical stress, AVIRIS calibration, BRDF measurements of snow and ice and non-destructive testing of artifacts in the National Museum of Guatemala. Transportation and field use have not brought about any major instrument failures, and it can be assumed that it will continue to be reliable in the field.

The signal-to-noise characteristics of the instrument are shown in Figure 9. These data were acquired at Rogers

Dry Lake during an AVIRIS calibration test. The low signal-to-noise ratio at 1.4 and 1.9 μm is associated with the atmospheric water absorption features. The effects of other minor water and CO_2 bands are also visible. The rapid variation in the signal-to-noise values is caused by the variation in detector characteristics within the 45-element arrays.

PIDAS measurements in the field have been compared with laboratory spectra reflectance curves of the same samples. Figure 10 shows such a comparison for alunite. The combination-overtone absorption feature in alunite at 2.22 μm has a true absorption band in the PIDAS data (upper curve) but shows only as a shoulder in the laboratory data. The Beckman 5240 spectral resolution in this region is approximately 25 nm (Inouye *et al*, 1987). The PIDAS resolution of approximately 10 nm is sufficient to reproduce essentially all the spectral features of solids in the 0.4-2.5 μm region and has about twice the resolution of the current and proposed imaging spectrometer systems.

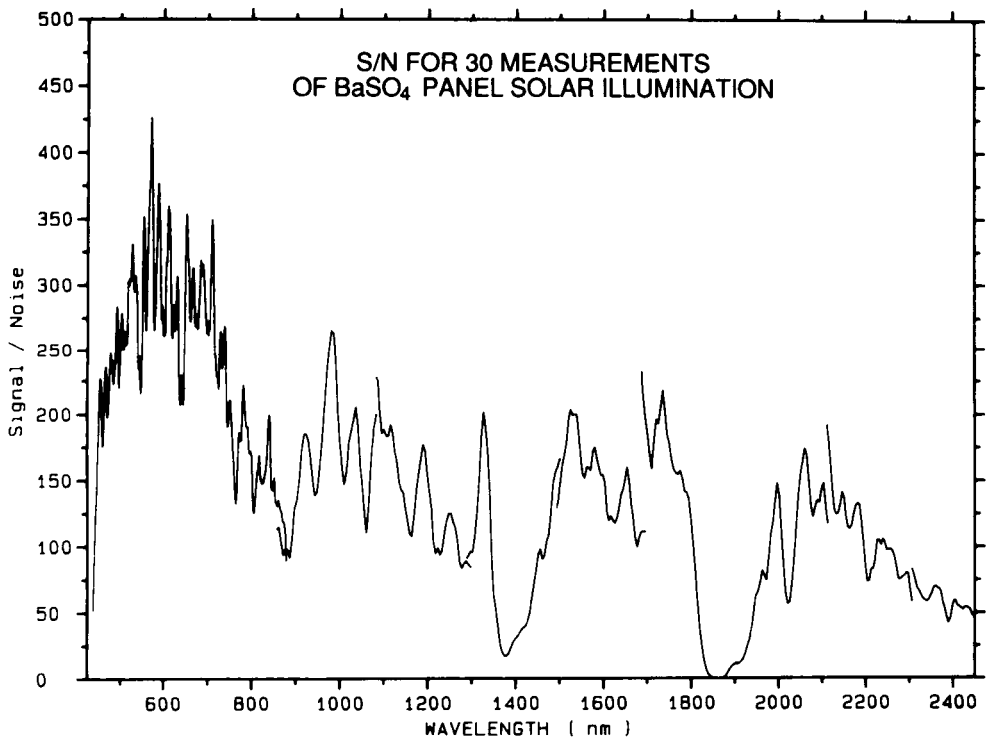

Fig. 9. Signal-to-noise as a function of wavelength obtained from 30 sequential measurements of Rogers Dry Lake. S/N is defined as the mean/std. deviation for each wavelength.

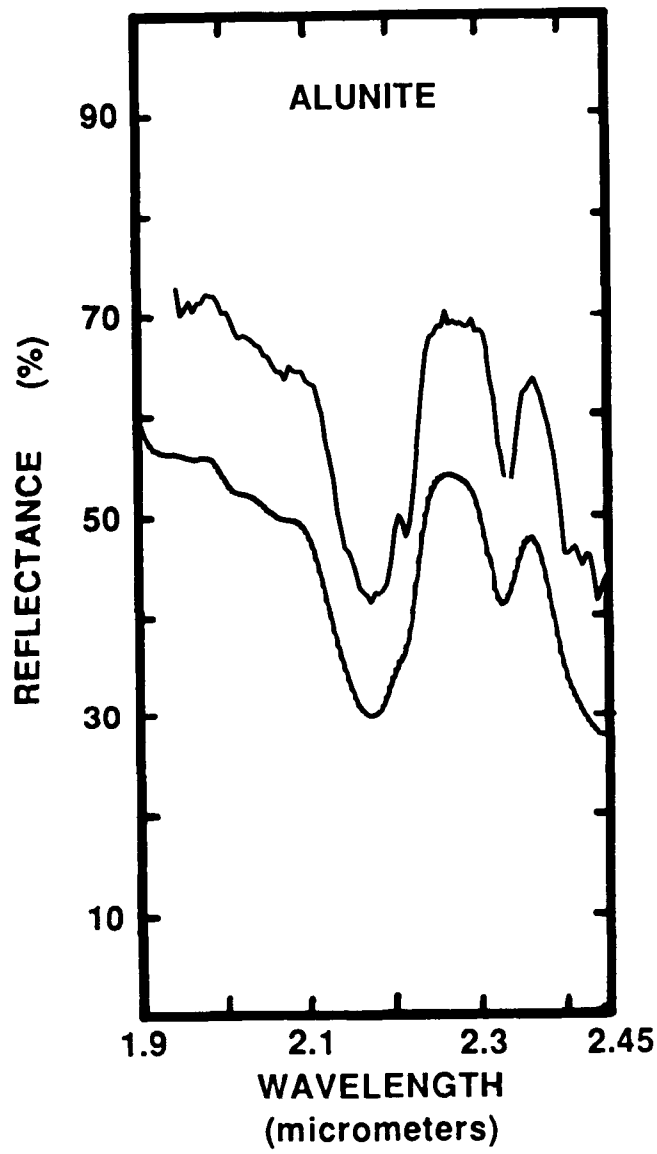

Fig. 10. Reflectance spectra of alunite taken by PIDAS (upper) and the Beckman 5240 (lower). The superior resolution of PIDAS is shown for the absorptive feature at 2.22 μm.

ACKNOWLEDGEMENTS

The development of PIDAS could not have taken place without the support of many individuals at JPL, among those Harry Enmark, Project Manager, Bob Irigoyen, Project Engineer, and Norm Page, Optics Designer. Arden Albee was the Caltech Principal Investigator, Brian Curtiss of Caltech provided invaluable support in the latter phases of instrument development and developed all the data analysis software. PIDAS is covered by U. S. Patent #4,560,275 issued to the California Institute of Technology. This research was

supported in large part by a grant from the W. M. Keck Foundation.

REFERENCES

Goetz, A. F. H. 1975. Portable Field Reflectance Spectrometer, Appendix E in Application of ERTS Images and Image Processing to Regional Geologic Problems and Geologic Mapping in Northern Arizona, JPL Technical Report 32-1597.

Inouye, C., A. F. H. Goetz and S. Schultz. 1987. Reflectance Spectra of 156 minerals, 0.4-2.5 μm. JPL Technical Report, in press.

AIS-2 RADIOMETRY AND A COMPARISON OF METHODS FOR THE RECOVERY OF GROUND REFLECTANCE

James E. Conel, Robert O. Green, Gregg Vane, Carol J. Bruegge, and Ronald E. Alley, Jet Propulsion Laboratory, California Institute of Technology, USA; Brian J. Curtiss, University of Colorado, Boulder, USA.

ABSTRACT

A field experiment and its results involving AIS-2 data for Rogers Lake, CA are described. The radiometry and spectral calibration of the instrument are critically examined in light of laboratory and field measurements. Three methods of compensating for the atmosphere in the search for ground reflectance are compared. We find, preliminarily, that the laboratory-determined responsivities are 30 to 50% less than expected for conditions of the flight for both short- and long-wavelength observations. The spectral sampling interval is 20 to 30 nm. The combined system-atmosphere-surface signal-to-noise ratio, as indexed by the mean response divided by the standard deviation for selected areas, lies between 40 and 110, depending upon how scene averages are taken, and is 30% less for flight conditions than for the laboratory. Atmospheric and surface variations may contribute to this difference. It is not possible to isolate instrument performance from the present data. As for methods of data reduction, the so-called scene average or log-residual method fails to recover any feature present in the surface reflectance, probably because of the extreme homogeneity of the scene. The empirical line method returns predicted surface reflectances that are systematically high but within a few percent of actual observed values using either calibrated or uncalibrated data. LOWTRAN-6, acting as an approximate theoretical model of the atmosphere for these exercises, predicts reflectance values 30 to 50% below the measured ones, based on the lower than expected radiances under solar illumination given by the instrument. This emphasizes the importance of accurate radiometric calibration in the study of surface or atmospheric properties.

INTRODUCTION

On October 14, 1986 the second version of the Airborne Imaging Spectrometer (AIS-2) with a 64- x 64-element HgCdTe array detector was flown over Rogers Lake, CA (Edwards Air Force Base) to (1) develop in-flight radiometric and spectral calibrations for the instrument and (2) compare the following three methods of compensation for the atmosphere in the recovery of ground reflectance: a scene-averaging (log-residual) technique, an empirical calibration line method, and a radiative transfer model. To support the radiative transfer modeling (the results of which are presented elsewhere [Conel, et al., 1987a]), ground measurements were made of atmospheric optical depth, the ratio of diffuse to direct incident light at the surface, and total precipitable water (cm^{-2}). Bidirectional spectral reflectance measurements of a bright lake bed and dark asphalt runway were made with a Portable Instant Display and Analysis Spectrometer (PIDAS) to

define empirical calibration lines of surface reflectance versus AIS response for the scenes generated during the overflight. Field spectral reflectance measurements of a concrete tarmac at North Base were taken as an unknown target against which results for the various methods of atmospheric compensation could be compared.

The primary focus of this paper is to describe the reduction of the AIS data to spectral radiance utilizing the detector responsivity equations developed by a laboratory calibration of the instrument with a $BaSO_4$-coated integrating sphere. From these data and from the spectral response to the standard ground targets, we develop estimates of the signal-to-noise ratio for laboratory and flight conditions. The effective in-flight instrumental spectral sampling interval is estimated by using atmospheric CO_2 absorption lines generated from LOWTRAN simulations. Some preliminary analyses of the atmospheric compensation problem are also described.

The AIS-2 instrument is described by Vane (1986). Discussed in this paper are observations made over two separate spectral intervals, 809-2143 nm and 1184-2523 nm, colloquially referred to as "tree" and "rock" mode observations, respectively.

FIELD MEASUREMENTS

Site Description and Flight Data

Rogers Lake (Lat. 34°55'N; Long. 117°50'W) is a dry playa located in Kern County, CA at an approximate elevation of 2270 feet (692 m) and contained within the Air Force Flight Test Center of Edwards Air Force Base. The flat, largely uniformly bright playa surface (Figure 1) is crossed by dark asphalt runways and is surrounded by terrain of low relief consisting of isolated rocky knobs and alluvial fans. The adjacent alluvial surfaces are covered with sparse desert scrub vegetation.

During the fall 1986 experiment, we acquired two lines of imaging spectral data, one in the rock mode (1184-2523 nm) and the other in the tree mode (809-2142 nm) at a flight altitude of 24,000 feet along roughly north to south tracks over the playa with vegetated terrain to the north.

Reflectance of Standard and Unknown Targets

Simultaneous with the overflight of AIS-2, spectral reflectance field observations were taken of three target areas within the AIS-2 field of view (Figure 1) using PIDAS. PIDAS has a spectral sampling interval of approximately 1 nm from 400 to 800 nm and 4 nm from 800 to 2500 nm (Goetz, 1987). The field spectra given in Figure 2 are averages from 30 to 60 sites. The field reflectance standard is $BaSO_4$. The targets are a uniformly high-reflectance playa surface and the low- and intermediate-reflectance runways. The runways of intermediate reflectance are used as an unknown in some of the atmospheric compensation studies described below. The standard deviation of all observations is everywhere less than a few percent and is greatest at longer wavelengths of observation, beyond about 2100 nm. Field observations were possible across the 1400-nm water

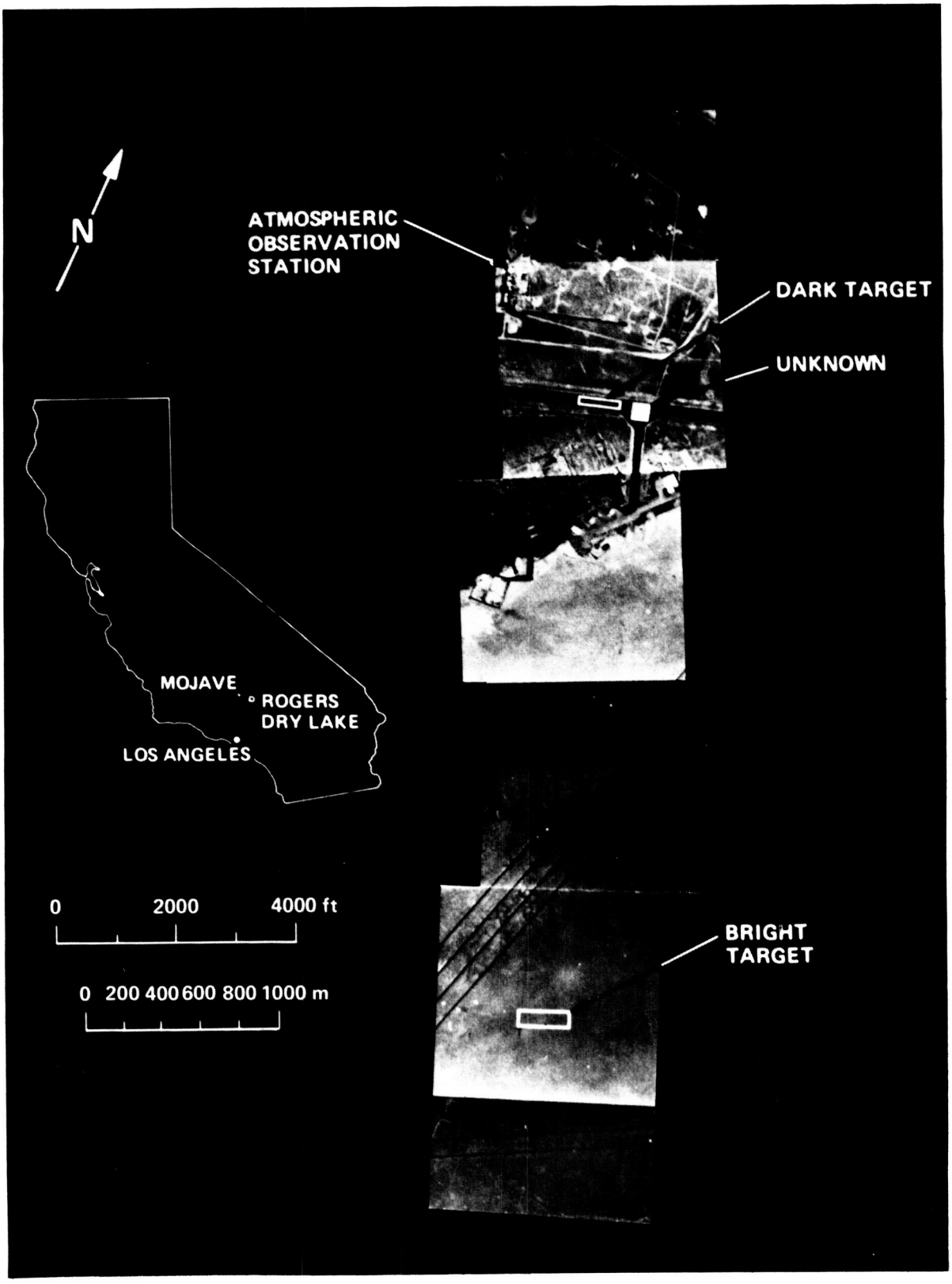

Figure 1. Locations of the October 14, 1986 AIS-2 calibration experiment at Rogers Lake, California

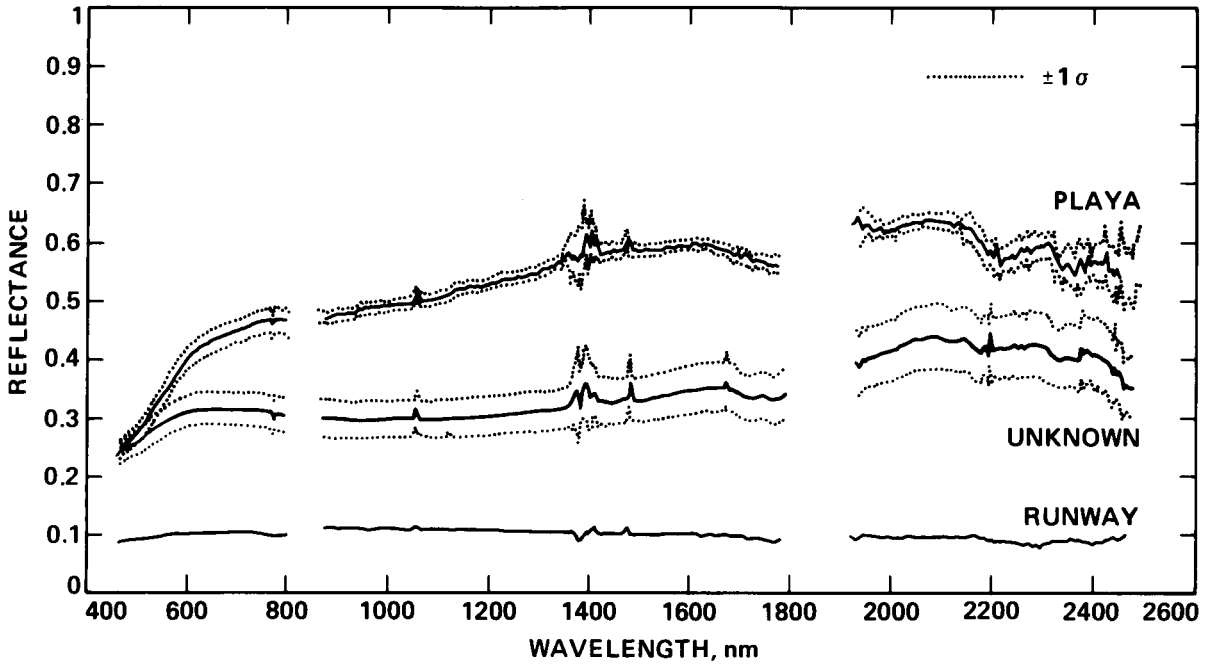

Figure 2. Spectral bidirectional reflectance of the standard and unknown targets as determined with PIDAS with respect to $BaSO_4$. Curves are averages ($\pm$ 1σ where shown) of 60 spectra for the playa and runway and of 30 spectra for the unknown target.

absorption feature, but the reflectance data have been deleted between 1800 and 1900 nm because of strong atmospheric interference. In addition, simple linear interpolations have been used to fill in gaps in these curves between 800 and 900 nm arising at the transition between spectrometers.

Measurements of Optical Depth

Measurements of incident solar illumination in the Thematic Mapper (TM) bandpasses were made with a standard Eppley Laboratories normal incidence pyrheliometer (NIPS) between 7:00 A.M. and 12:40 P.M. solar time on October 14. The data were cast in the form of conventional Langley plots of relative incident solar radiance versus air mass (1/cos [zenith angle]) and the optical depths for all filter bandpasses were determined from least square determinations of the slope. The results of these determinations are given in Table 1.

RADIOMETRIC CHARACTERISTICS FROM LABORATORY CALIBRATION

The purpose of the laboratory radiometric calibration of AIS-2 has been to establish the instrument's responsivity for each detector in each spectral sampling interval over a range of input radiances appropriate to the observation of natural targets. For the full 64 x 64 array, these calibrations lead to the compilation of 8192 curves for both grating positions in each sampling mode.

Table 1. Optical Depths Determined in the TM Bandpasses for the October 14 Experiment at Rogers Lake

Wavelength, nm	Optical Depth
485	0.195 ± 0.001
560	0.144 ± 0.001
660	0.080 ± 0.002
830	0.038 ± 0.001
1650	0.019 ± 0.002
2200	0.042 ± 0.003

The AIS-2 radiometric calibration employs a 40-inch integrating sphere coated with $BaSO_4$ whose spectral radiance is determined using an Optronics Laboratory Spectroradiometer. The spectroradiometer itself is calibrated against a standard illumination source that is National Bureau of Standards (NBS) traceable. The integrating sphere and spectroradiometer calibration procedures have recently been described by Tucker (1987). Aperture wheels placed between the externally mounted tungsten lamp sources and entrance ports of the integrating sphere control the radiance entering the sphere. The spectral radiance distribution of the integrating sphere measured as a function of channel and aperture wheel setting ([1], [2], ...) is shown in Figure 3 for the 1200- to 2500-nm spectral interval. The prominent absorption bands near channels 24 and 72 represent water present in the sphere coating. Some absorption from atmospheric path water may also be present. The major bands lie at somewhat shorter wavelengths, principally near channels 20 and 64, a difference that will serve to distinguish them from bands arising in the adsorbed or chemically bound component.

The response of AIS-2 to the assumed flat-field illumination, presented by the exit aperture of the integrating sphere and averaged over 500 lines of observations, is shown in Figure 4(a) for the greatest source illumination used in the calibration. The data are presented sequentially in terms of wavelength in blocks of 64, each block representing the spatial variation across a row. The beginning and ending detectors of each row (i.e., where each row represents 64 detector elements in one wavelength channel) show lower response than neighboring detectors. This is due to vignetting in the fore-optics. In addition to these strong edge effects, which may extend in a reduced amount further into the array, other periodicities as well as an overall gradient in response are apparent across each row. The origin of these various effects is, at this writing, unknown. The variation in mean detector response over all 128 bands is shown at a compact scale in Figure 4(b). The prominent water absorption features contributed by the integrating sphere appear near detector locations 1536 (channel 24) and 4600 (channel 72). A small discontinuity between grating positions is found at location 4096. The standard deviation of the set of 500 repetitive observations is not uniform with column number or channel. This variation is shown in Figure 4(c).

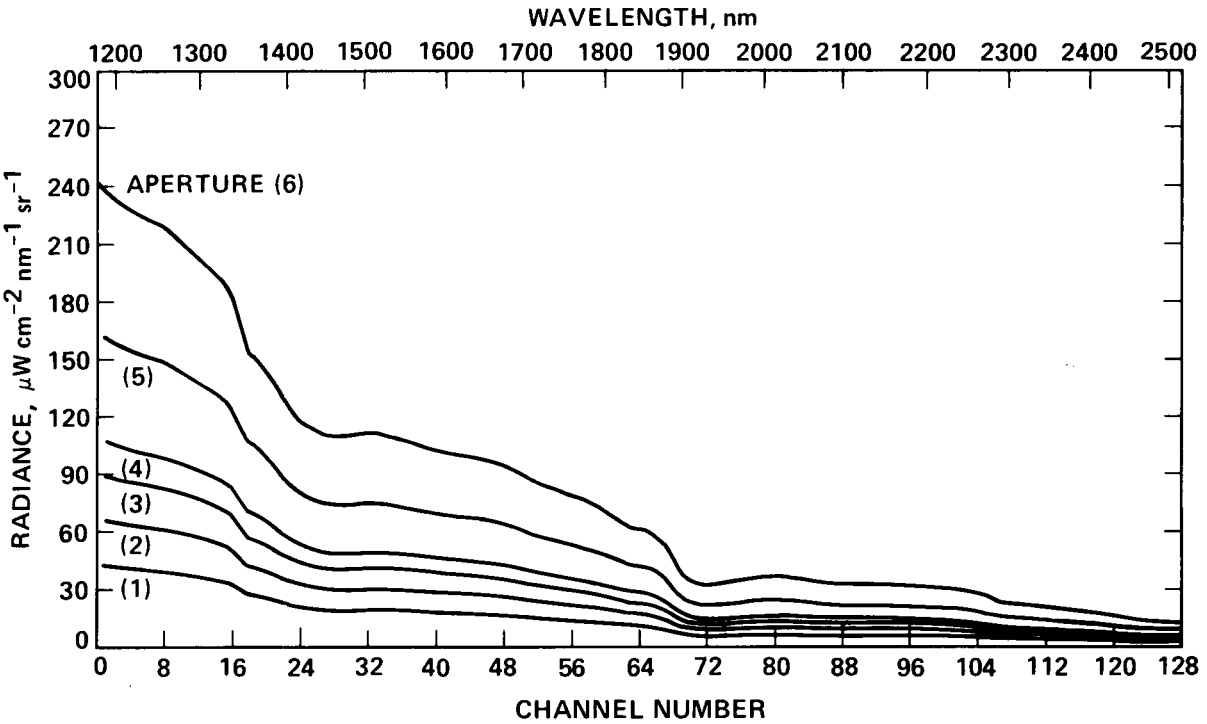

Figure 3. Spectral radiance of the integrating sphere (May, 1987) for the spectral interval 1185-2500 nm ("rock" spectral mode). Prominent absorption features near channels 24 and 72 are due to adsorbed or chemically bound water.

From the data of Figure 4(b), the response of any column of the detector array to illumination by the integrating sphere may be worked out. An example is shown in Figure 5 for column 3 (channel 3), with the spectrum corresponding to channel numbers 3, 67, 131, and so forth, of Figures 4(a) and (b). The major minima at channel numbers 24 and 72 again reflect water absorptions originating in the coating of the integrating sphere. An abrupt sawtooth variation occurs between grating positions. The finer jagged variations shown in Figure 5 are random variations in detector response, examples of which are depicted in Figures 4(a) and (b).

The responsivity equations represent relationships between the response of the imaging spectrometer and the input radiance. These relationships emerge by combining the plots of Figures 3 and 5 into a single diagram and by including the presence of an ND 0.9 filter in the optical train of AIS during its calibration. Examples are shown in Figure 6.

WAVELENGTH ASSIGNMENTS OF CHANNELS

To establish a correspondence between the channel number of the imaging spectrometer and the wavelength, we used the positions of atmospheric CO_2 and water vapor absorption lines of a model LOWTRAN-6 spectrum to fix in wavelength all identical, resolvable absorption bands in the AIS data. The wavelengths of 8 to 10 additional atmospheric bands from the LOWTRAN spectra

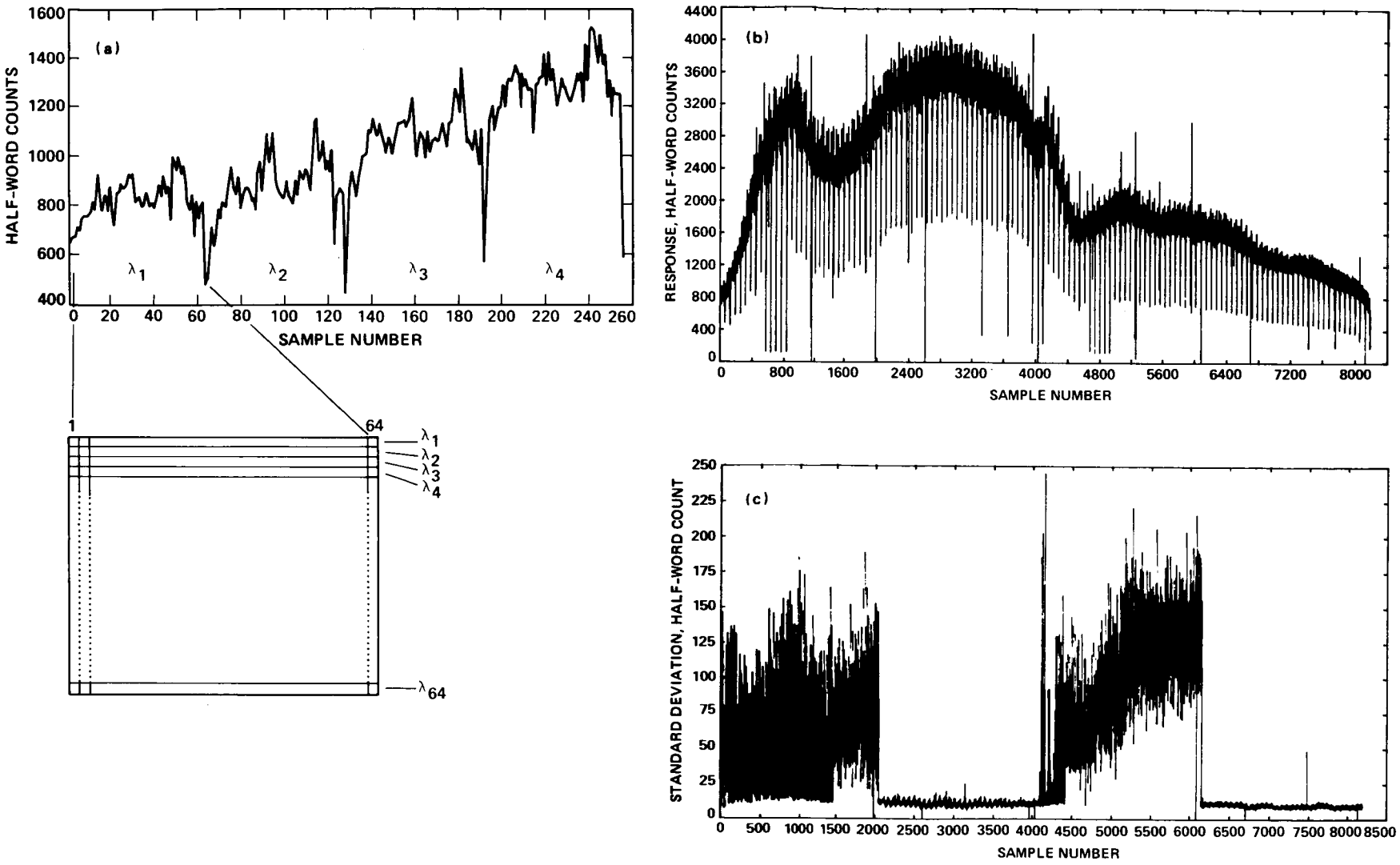

Figure 4. Mean spectral response of the AIS detector (64 x 64 HgCdTe) under flat-field illumination of the integrating sphere for an average of 500 lines: (a) Detailed variations for the first four wavelengths across rows of the array; (b) a compressed version of the spectra shown in 4(a) but covering channels 1-128 (1185-2522 nm); and (c) standard deviation of the 500 samples.

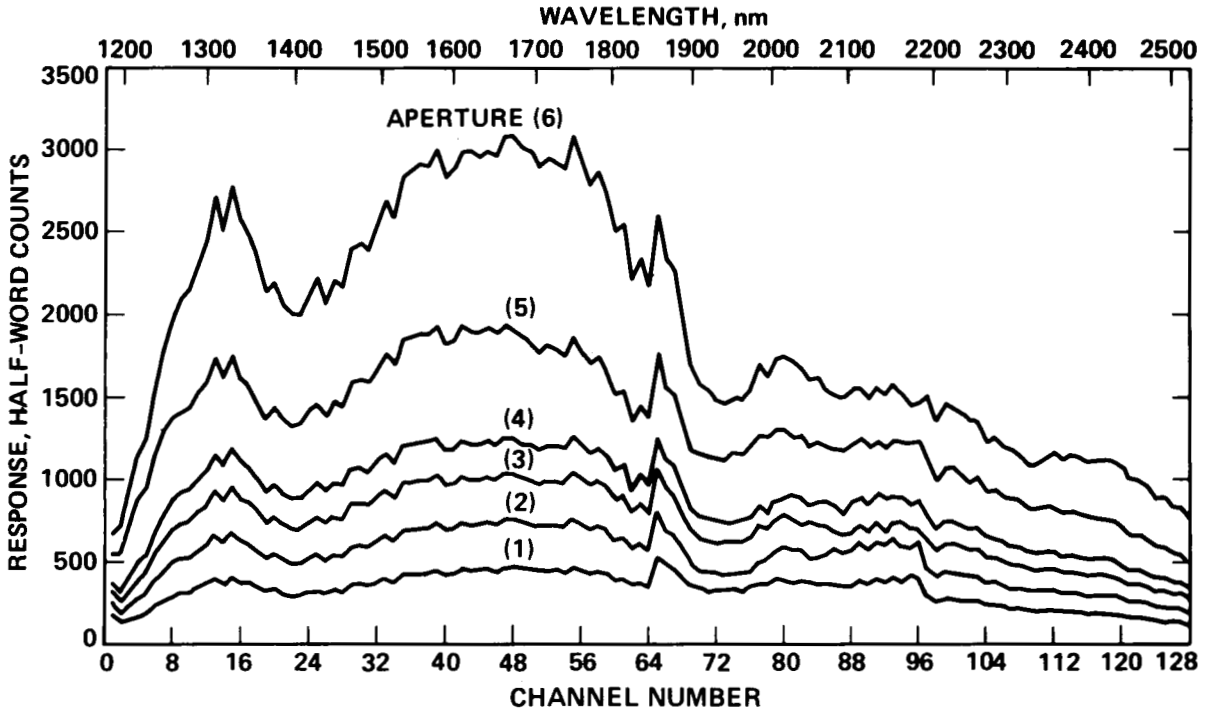

Figure 5. An example of detector response for the column 3 array, determined from the data of Figure 4. Note the discontinuity in responses between channels 64 and 65.

not detected in the observations were identified by channel numbers, and the complete sets of wavelengths and channel numbers were regressed against one another. The resulting equations relating wavelength to channel number N are

$$\lambda(\text{nm}) = 799 + 10.54\ N$$

for $809 \leq \lambda \leq 2143$ nm with $r^2 = 1.0000$ and

$$\lambda(\text{nm}) = 1174 + 10.54\ N$$

for $1184 \leq \lambda \leq 2523$ nm with $r^2 = 0.9999$. For both equations, $1 \leq N \leq 128$. The wavelengths provided from these equations for the beginning and ending of each measurement interval are in accord with positions measured with a standard monochromator in the laboratory to within 6 nm or better except for the long wavelength limit provided by the first equation above. The predicted wavelength is 2143 nm, and the measured is 2132 nm. Since this is very close to one channel, it seems probable that the single equation provided does not represent precisely the channel assignments for both grating positions, assuming the same slope requires an adjustment of the constant in the first equation to 788 nm for $65 \leq N \leq 128$. However, this adjustment has been ignored in practice (see below).

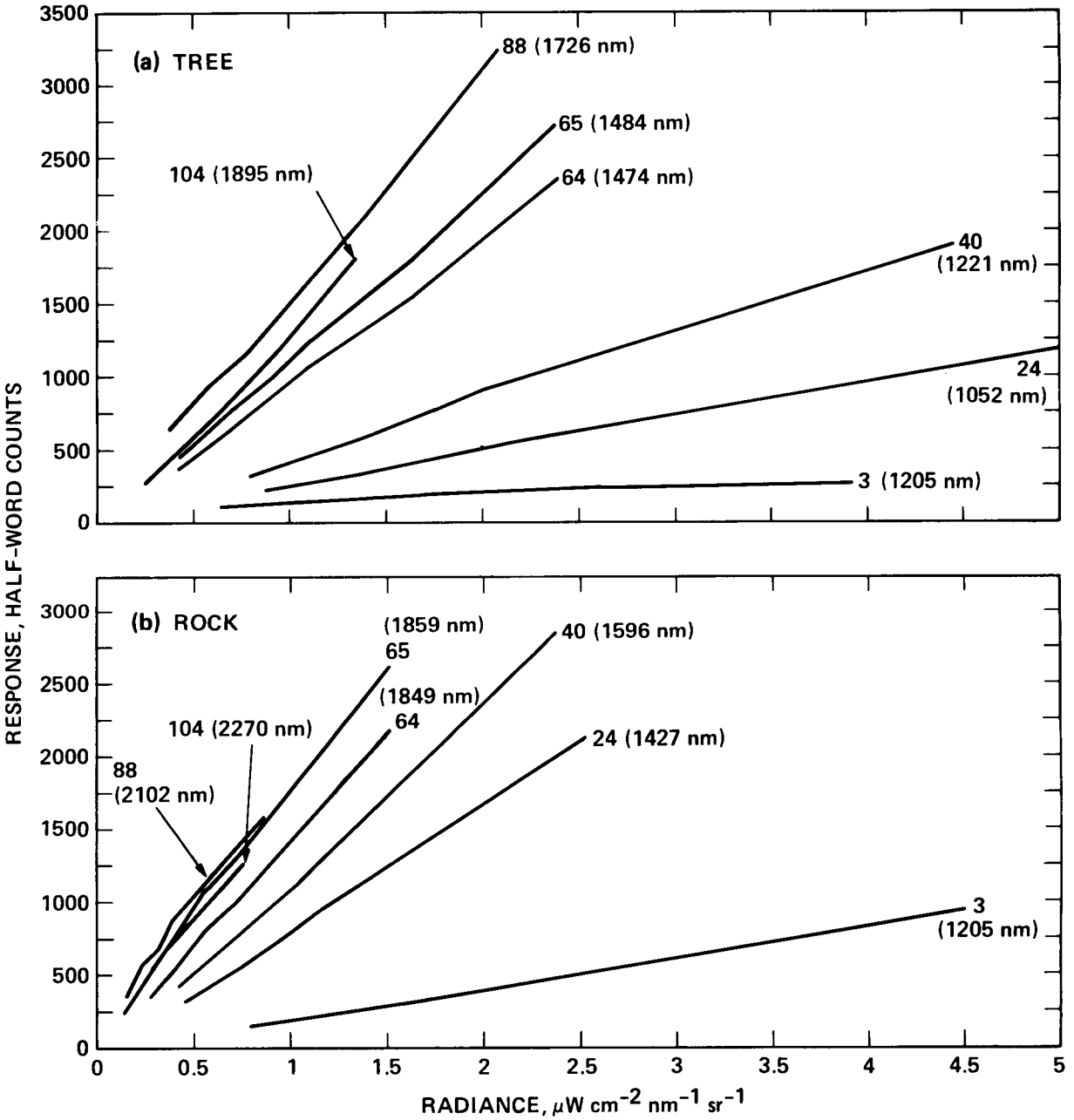

Figure 6. Response curves for detectors of column 3 in the array

ESTIMATION OF AN EFFECTIVE IN-FLIGHT SPECTRAL SAMPLING INTERVAL

Based on the wavelength calibration equations given in the previous section, the limiting spectral sampling interval is very close to 10.5 nm for both tree and rock mode observation intervals. To provide a measure of the in-flight effective sampling interval, we compared raw AIS spectra of the bright playa surface stated in terms of half-word DN with irradiance at the instrument as provided by LOWTRAN-6, and calculated at a spectral resolution of 10 cm^{-1} or about 2 nm. Apart from major absorptions related

to atmospheric water near 1400 and 1900 nm, the only additional bands of atmospheric origin resolved or unresolved in the AIS spectra arise from CO_2. We compare in Figure 7 the observed AIS playa spectrum with five LOWTRAN simulations, one at full resolution, and the others degraded using square filters of spectral width 20, 30, 40, and 100 nm. The prominent CO_2 absorptions near channel 40 (specifically 1572 and 1603 nm) are resolved at 20 but not at 30 nm, and thus the spectral sampling interval is probably between 20 and 30 nm. At a filter width of 40 nm the pair of CO_2 features near 2000 nm are just resolved, and any vestige of these is entirely removed at 100 nm. (These simple considerations may explain the highly variable but generally reduced or missing CO_2 absorptions and the smaller than anticipated and distorted water band absorption features in AIS-1 data, as reported by Conel et al. [1987b] and as resulting from a significantly degraded spectral sampling interval in those data, on the order of 50 nm or perhaps greater.)

On the expectation that the apparent signal-to-noise ratio could be improved by averaging large numbers of pixels, thereby suppressing the noise component of any spectral degradation present, we produced AIS spectra composed of averages of 1, 25, and 100 pixels over the playa. No improvement in the effective separation of either the 1600-nm or the 2000-nm set of CO_2 bands was achieved by these averaging procedures.

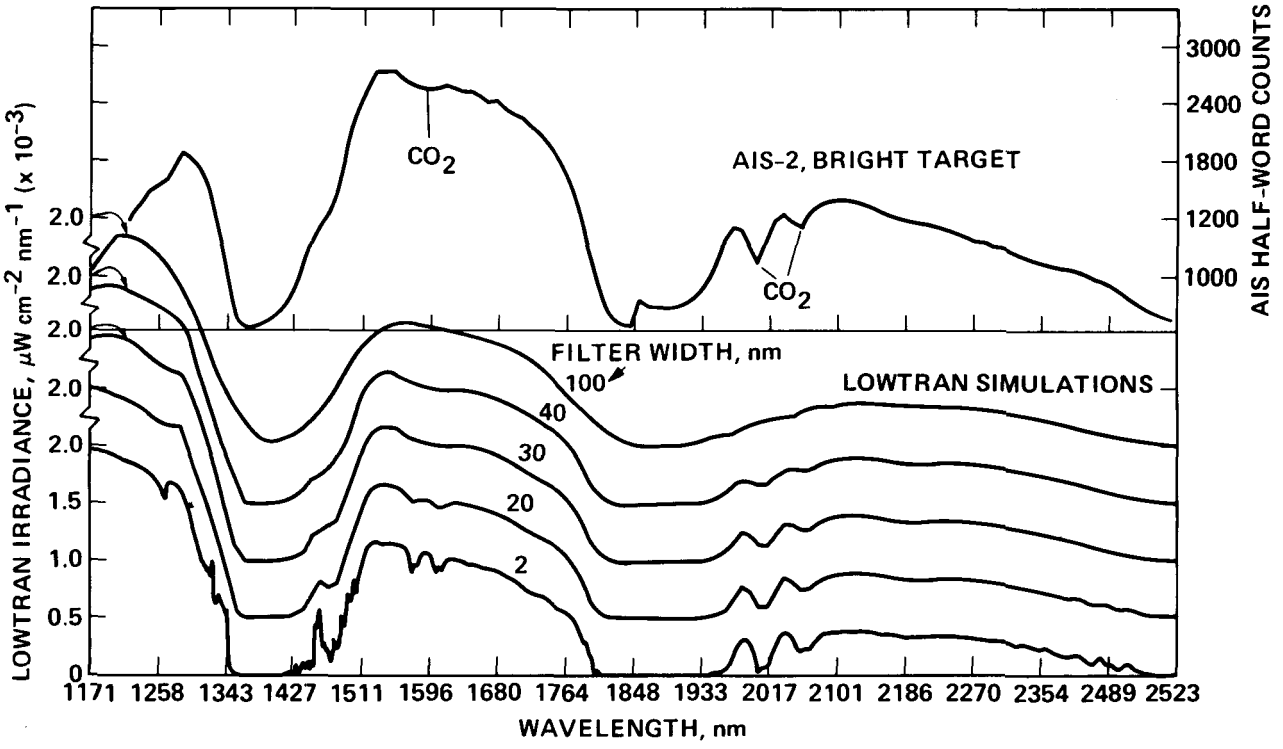

Figure 7. Examples of degradation of LOWTRAN spectra with square filters and comparison with observed AIS-2 spectrum for a target simulating a bright playa surface. AIS-2 has an equivalent spectral sampling interval between 20 and 30 nm.

REDUCTION OF FLIGHT DATA TO RADIANCE AND COMPARISONS WITH EXPECTED SOLAR RADIANCE AT THE INSTRUMENT

An important test of the validity of the laboratory determined responsivities (e.g., the curves of Figure 6) for flight conditions, and in addition the data reduction procedures, is the calculation of radiance at the instrument for a ground target of known reflectance. These results can be compared with radiances expected for a detailed atmospheric model. A simple method is to calculate the radiance expected at the instrument in a region of high atmospheric transparency (e.g., near 1200 or 1700 nm) and compare it to the radiance predicted from the responsivities at these wavelengths. The radiance $L(\lambda)$ is approximately equal to $\mu_o F_o(\lambda) R(\lambda)$ where $\pi F_o(\lambda)$ is the seasonally adjusted solar irradiance at λ, μ_o is the cosine of the solar zenith angle, and $R(\lambda)$ is the surface spectral reflectance. This procedure was followed by Conel et al. (1987a, 1987b) for the AIS-1 radiometric calibration study. The more elaborate calculation, taking into account atmospheric attenuation and scattering, involves computing the expected radiance at the aircraft from a realistic atmospheric model throughout the entire spectrum. This is the procedure adopted here, where for the sake of expediency we employ the standard midlatitude winter model of LOWTRAN-6 in the comparisons. However, the LOWTRAN model is only approximate, in particular accounting for only a single order of scattering at shorter wavelengths. The comparisons are therefore approximate although we scale results for the standard model at longer wavelengths (> 830 nm) using our field-determined optical depths.

In Figure 8 we present the spectral radiance from the standard bright playa target expected according to (1) the LOWTRAN-6 simulation utilizing the field measured reflectance in Figure 2 and (2) AIS-2 utilizing the laboratory determined responsivities, examples of which have been given in Figure 6. Data from both instrument configurations (rock and tree modes) are shown. According to these determinations, the predicted AIS responses are lower than the LOWTRAN simulations by 30 to 50% for the longer wavelength data (rock mode) and by 30 to 40% for the short wavelength data (tree mode). To assess the appropriateness of the midlatitude winter model LOWTRAN simulation for this comparison, we give the optical depths measured on October 14 and the optical depths derived from the LOWTRAN atmospheric transmittances averaged over the TM bands in Figure 9. The LOWTRAN optical depths are larger at all wavelengths, but of particular significance are the differences at 1650 nm and 2215 nm because aerosol and Rayleigh scattering are negligible at these wavelengths and would not contribute significantly to the LOWTRAN-derived numbers no matter how scattering is accounted for in the LOWTRAN model. We estimate the adjustments required in the LOWTRAN-derived radiance curves from the relationship

$$L(\text{AIS conditions}) = L(\text{LOWTRAN conditions}) \times [T_{dn}\ (\text{AIS}) T_{up}\ (\text{AIS}) / T_{dn}(\text{LOWTRAN})\ T_{up}(\text{LOWTRAN})]$$

where L(AIS conditions) is the radiance for the optical depth appropriate to the AIS observing date, L(LOWTRAN conditions) is the radiance from the

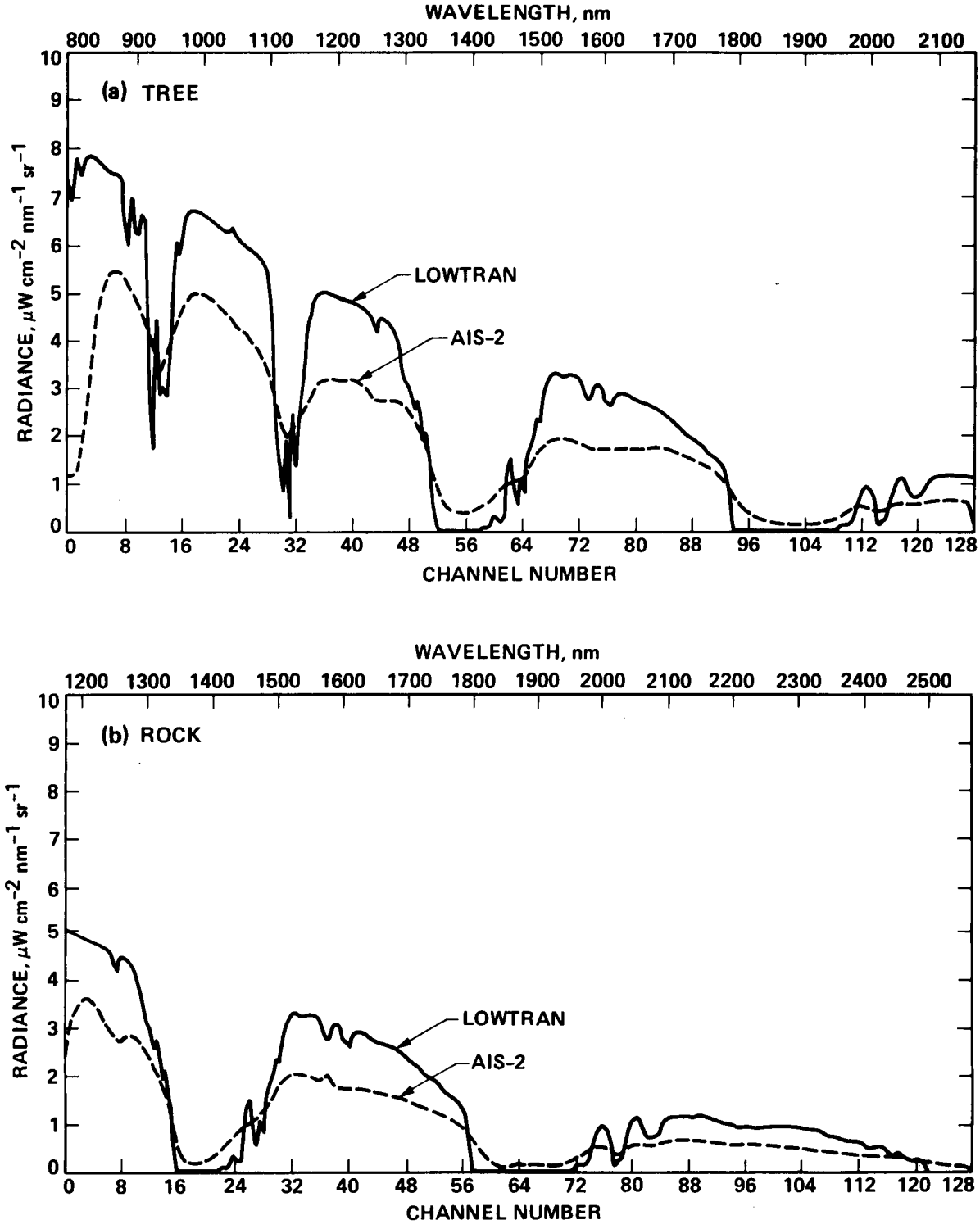

Figure 8. Examples of the reduction of raw AIS-2 half-word spectra to radiance compared to LOWTRAN simulations of the radiance expected at the instrument for the measured surface reflectance. The standard mid-latitude model for October 14, 1986 is used.

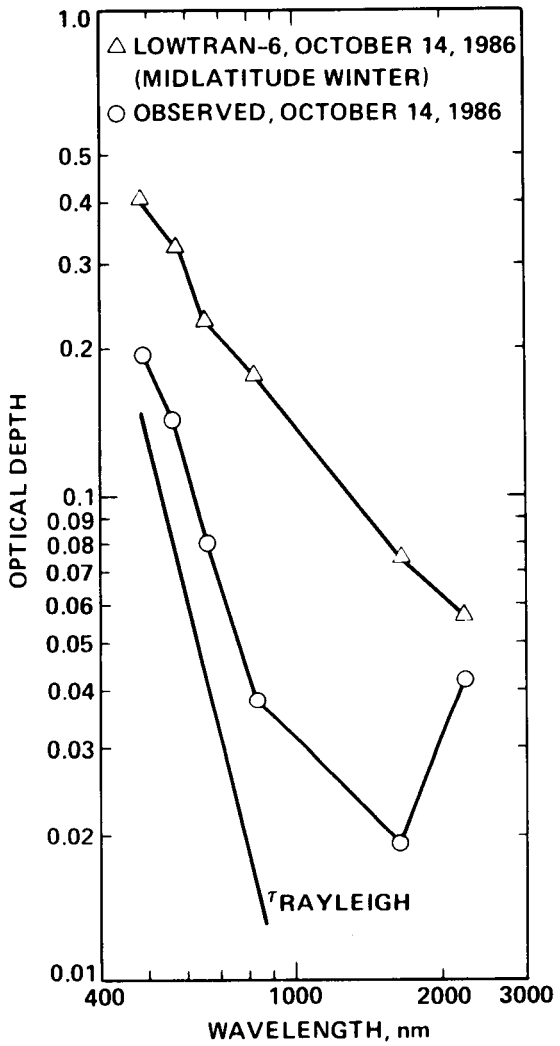

Figure 9. Comparison of optical depth measured for the site on October 14, 1986 with LOWTRAN optical depths at the same wavelengths. The optical depth for Rayleigh scattering, $\tau_{RAYLEIGH}$, is from a formula by Hansen and Travis (1974).

standard LOWTRAN model, and T_{dn} and T_{up} are the atmospheric transmittance for the downward and upward paths, respectively. Specifically,

$$T_j = \exp[-\tau_j/\mu_j]$$

where j = either up or down, and μ_{dn} = cos (42.6 deg) for the downward leg and μ_{up} = unity for the upward portion. For the two long-wavelength TM bands the ratio L(AIS)/L(LOWTRAN) is given in Table 2. Note that T_{up} (AIS) is calculated assuming the same proportional reduction in optical depth between up and down paths as LOWTRAN. As expected, radiances calculated from LOWTRAN relevant to the time of AIS observations need to be increased; the discrepancies between the model and observations accordingly widen somewhat.

SECOND ORDER MIXING AND STRAY LIGHT CONTAMINATION

The problem of spectral contamination from overlapping orders of diffraction from the grating in AIS-1 data was discussed in detail by Conel

Table 2. The Ratio L(AIS conditions)/L(LOWTRAN conditions) for TM Bands 5 (1650 nm) and 7 (2215 nm)

Band	T_{dn}		T_{up}		L(AIS)/
	AIS	LOWTRAN	AIS	LOWTRAN	L(LOWTRAN)
1650	0.974	0.903	0.996	0.986	1.091
2215	0.944	0.926	0.990	0.987	1.024

et al. (1986, 1987b), and by Cocks et al. (1986). This problem has been eliminated in AIS-2 by the use of appropriate order sorting filters (see Airborne Imaging Spectrometer Supplement, 1986) except at wavelengths longer than 1600 nm in tree mode observations and beyond 2400 nm in rock mode. The nature of this problem is illustrated in Figure 10, where both the long- and short-wavelength radiometrically calibrated data for the standard bright playa target are displayed together.

A residual radiance is also present within the 1400- and 1900-nm water absorption bands for both rock and tree mode spectra and is somewhat greater in the latter (Figure 8). Such residuals in bands thought to be saturated are a concern from the standpoint of the possible presence of stray light. During the time of overflight we also measured precipitable water with a spectral hygrometer. This instrument handily indexes the water present by looking at the sun and measuring the ratio of water band depth to continuum height with two narrow filters (880 and 935 nm). These ratios are calibrated against numerous radiosonde observations where the distribution

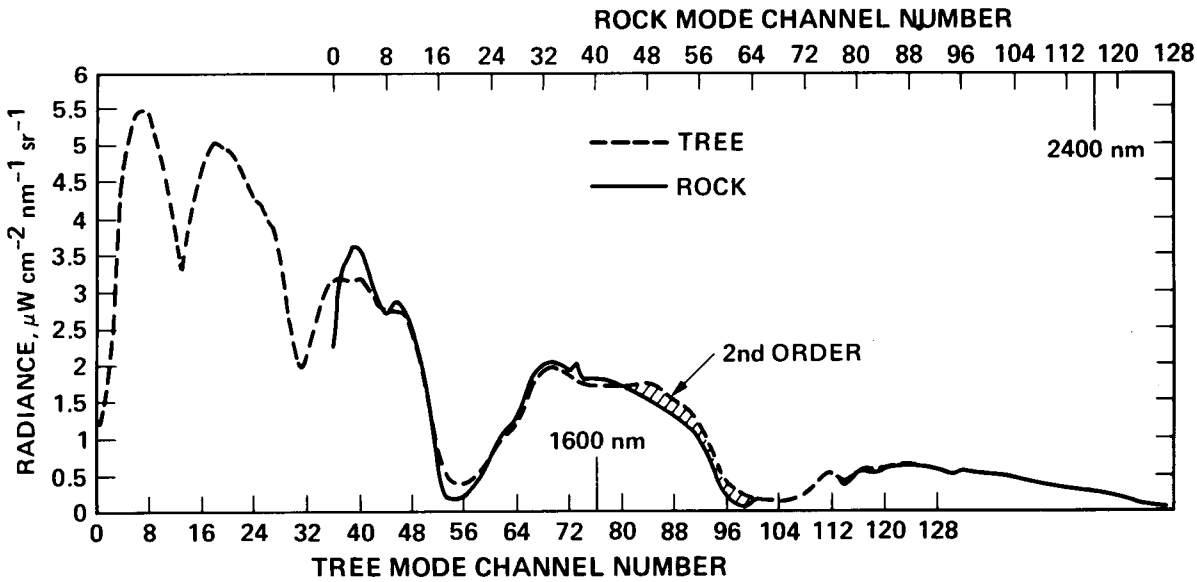

Figure 10. Comparison of rock and tree mode spectra to show the possible presence of a second order component

of water with height is measured (B. Gary, JPL, personal communication, 1986). Near 11:30 A.M. solar time, the vertical column abundance was determined to be 0.47 gm/cm^{-2}, which for a solar zenith angle of 42 deg gives about 1.1 gm/cm^{-2} for the total water present in the path. This value is slightly less than that assumed in the standard LOWTRAN-6 model (about 0.6 gm/cm^{-2} total in the vertical column or 1.41 gm/cm^{-2} over the path). The expected atmospheric transmittance was estimated for the measured water abundance using the formula and absorption coefficients given by LaRocca (1978, Eq. 5.53 and Table 5-4). At 1400 nm the transmittance was calculated to be 3%, whereas the measured value is close to 12%; at 1900 nm the transmittance is 2%, and the measured value roughly 15%. These approximate determinations suggest the possible presence of stray light in the instrument.

REMOVAL OF UNEQUAL DETECTOR RESPONSE IN IMAGERY

Once the laboratory-determined responsivities (or instrumental light transfer curves) are available, it is not difficult to reduce the raw image data to radiance, thereby eliminating the effects of variable detector response. The effect of this transformation on the image data is illustrated in Figure 11 for channels 48 through 64, where a considerable reduction in vertical striping with calibration and a consequent enhancement in surface detail can be seen.

ESTIMATION OF SIGNAL-TO-NOISE RATIO

The playa surface presents a large, uniform target with a spectrum that varies more or less slowly with wavelength. We attempted to take advantage of these features to make estimates of the system signal-to-noise ratio using the radiometrically corrected imaging spectrometer data. The radiometrically adjusted data can be expected to yield somewhat better values than the raw spectra because the random variations in detector responsivity, examples of which are shown in Figure 4(a), have been reduced. This is evident by comparing the radiometrically calibrated and uncalibrated images in Figure 11. We take as estimates of the signal the mean value of the radiance averaged over row, column, or area, all for a single wavelength. The noise estimate is provided by the standard deviation of the observations. The mean (μ), standard deviation (σ), and the ratio (μ/σ) are plotted in Figure 12 for various cases involving row, column, and areal averages, all beginning in column 17 of the detector array and for Channel 40 (1592 nm). Figure 12(a) gives the laboratory result derived from flat-field illumination with the integrating sphere and isolates the variation in the quantities plotted for a single detector. For this artificial illumination the value of μ/σ is about 180. A similar average for flight conditions is shown in Figure 12(b). The estimated signal-to-noise ratio is seen to be reduced about 30% for flight conditions, but the significance of this apparent reduction needs discussion.

In addition to a possible reduction in performance of the system under flight conditions, there are sources of variation inherent in the standard target over the area sampled and variations in the atmospheric conditions

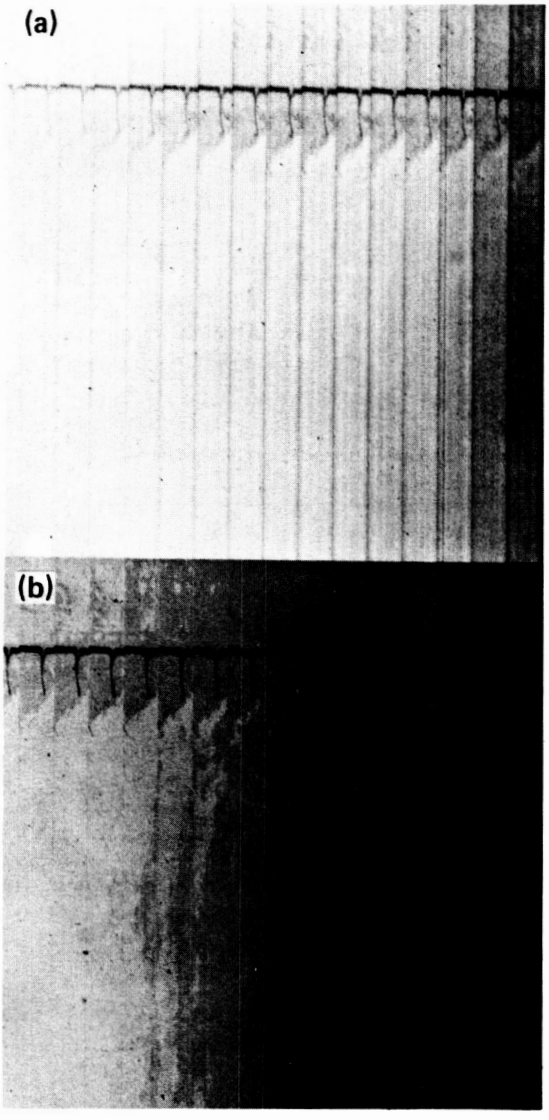

Figure 11. Removal of vertical striping with accompanying radiometric calibration of AIS-2 data: (a) before calibration and (b) after calibration.

over paths from the instrument to these samples. Let us consider the propagation of uncertainties from such sources. (We assume a nonscattering atmospheric model of two-way transmittance T and a linear instrument responsivity with gain factor G connecting the output [in DN] and radiance at the instrument [L]. The model will be described in more detail below.) A straightforward calculation leads to the formula for the fractional standard deviation (squared) of the DN

$$(\sigma_{DN}/DN)^2 = (\sigma_R/R)^2 + (\sigma_T/T)^2 + (\sigma_G/G)^2$$

Here, σ_{DN}^2, σ_R^2, σ_T^2 and σ_G^2 are the variances of, respectively, the DN, surface reflectance, atmospheric transmittance, and instrumental gain factor. We have assumed that instrumental noise sources can be represented as random variations in the gain factor alone. This equation gives an estimate of σ_G/G under flight conditions when the other terms are

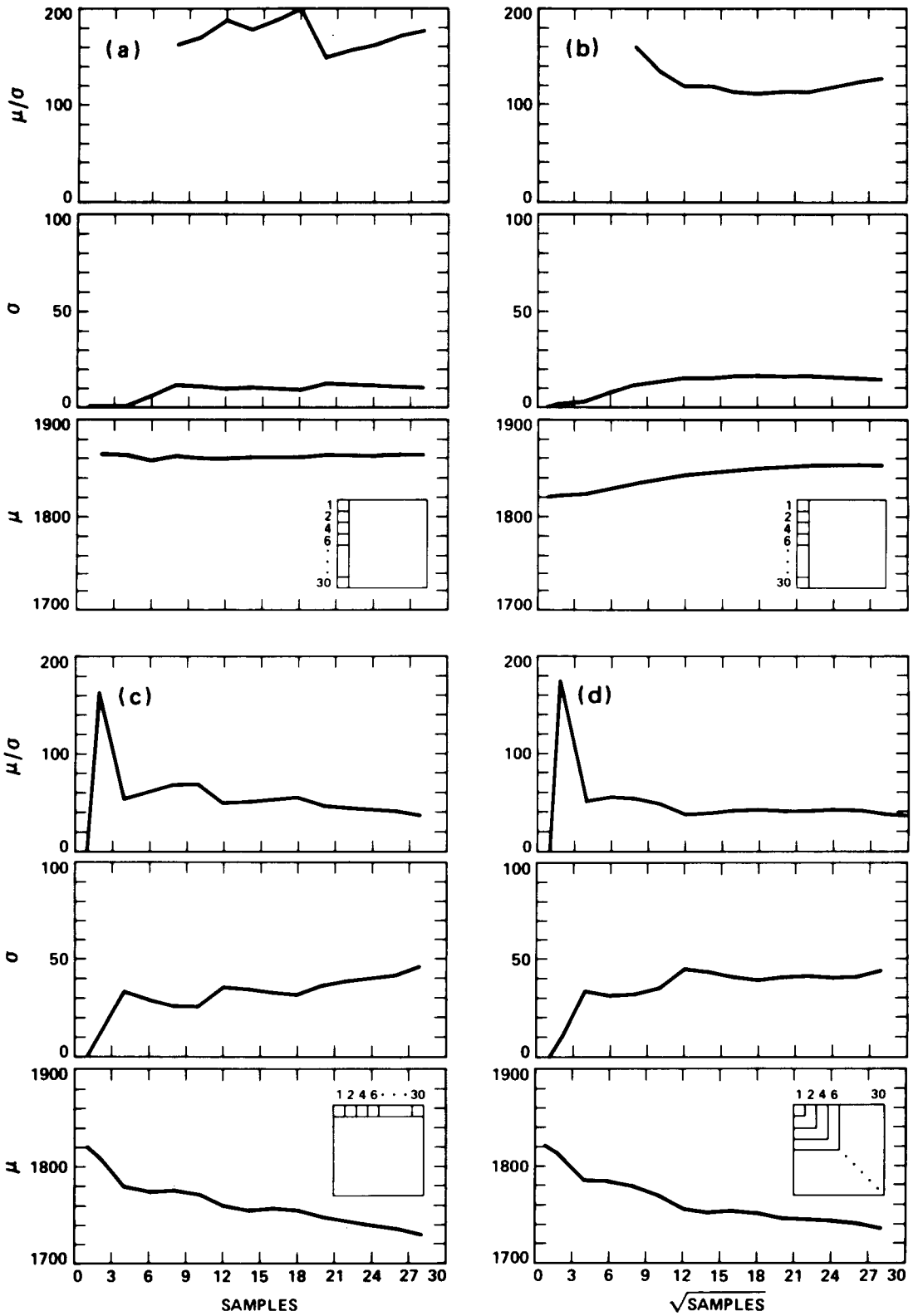

Figure 12. Variation of mean (μ), standard deviation (σ), and ratio for pixel samples of various sizes and configurations on the playa.

determined. A numerical value for the left-hand side is obtained from the flight data for the standard target, given in Figure 12(b). This value is about $(1/110)^2$. From Figure 2, at 1592 nm, the first term on the right-hand side measuring the fractional variance of R is about $(1/60)^2$. Adopting this number assumes the PIDAS measurements themselves are error-free. This is certainly questionable considering that the determination of the ground reflectance itself depends upon two observations (target and reference) that individually are functions of all the factors described in the model above plus possible operator variability stemming from the fact that the instrument is hand-held. (One of us [R.O.G.] has made a preliminary study of the repeatability of PIDAS measurements. For 20 consecutive observations of a target and reference spanning a period of a few minutes, the scatter in the calculated reflectance is about one part in thirty.) With respect to fluctuations in T, no direct measurements are available of atmospheric variability over the paths and on a time scale commensurate with the frequency of data acquisition (16 lines/sec). We used our measurements of diffuse and direct incident total radiation acquired during the experiment to establish approximately the magnitude of the variability over periods on the order of a few minutes. From the analog records, the ratio of peak to peak variability of the diffuse light to the total of diffuse and direct components is 1/1700. No variation in the direct component itself can be detected from the record. These observations suggest that for the present calculations, the sky variation is negligible.

Comparing the magnitudes of the various terms just given shows the fractional variance of the surface reflectance to be by far the largest term, which is inconsistent with the measured total value. Two possible causes of this problem may be (1) unrepresentative sampling of the surface at a pixel scale with PIDAS or (2) poor repeatability of the PIDAS observations themselves. Both of these questions will be the focus of future studies.

An alternative viewpoint is to adopt the laboratory determined fractional variance of G (i.e., σ_G/G is given by $1/(\mu/\sigma)$ in Figure 12(a), which is about $(1/180)^2$ and to ascribe the degeneration of the total fractional variance to the sum of uncertainties from atmospheric and surface sources. The combination of these two terms has a value of $(1/110)^2 - (1/180)^2$ or approximately $(1/140)^2$. It is certainly plausible that the differences observed between laboratory and flight values could be contributed by these sources that are totally dominated by variations in the target reflectance. Isolating instrument performance has remained elusive.

The variations observed in averages across columns, Figure 12(c) and, with area, Figure 12(d), are larger than those found in the row averages, and in general lead to the lower values of μ/σ of about 40. The across-column averages are thought to contain additional sources of banding in addition to that arising from variations in detector response already compensated for. This contributes to the larger scatter, and consequently lower signal-to-noise ratio, estimate.

REDUCTION OF THE RADIANCE DATA TO GROUND REFLECTANCE

In this section we compare the results of three largely independent methods that may be used to compensate for atmospheric effects in imaging spectrometer data: (1) scene average or residual, (2) empirical line, and (3) radiative transfer modeling. Similar studies comparing methods (1) and (2) were carried out by Roberts, et al. (1986). In principle, method (1) can be employed independent of any ground measurement wherever the atmosphere is uniform and the path radiance is zero. Methods (2) and (3) possess the same theoretical basis. In both, the scanner response (or radiance) can be arranged as an essentially linear function of ground reflectance. The fundamental difference in these two approaches from our point of view is that in the empirical method (2), the slope and intercept of the response curves at each wavelength are fixed by two-point ground observations of the reflectance, whereas in the modeling approach (3), these constants are calculated from theory after measurements of the optical depth and single scattering albedo have been used. In what follows, the parameter of interest is assumed to be surface spectral reflectance, although in other applications the atmospheric properties themselves might be of equal concern.

The strategy employed made predictions of the surface reflectance (by the methods mentioned) which were then compared with field-measured values. For this purpose, the unknown target of reflectance, whose spectrum is given in Figure 2, was used. Actually, for methods (1) and (3) this target as well as the two standard targets could have been used, while for method (2) only one target was available because two standards are used to construct the prediction relationships.

Residual or Scene-Averaged Method

An intriguing method of atmospheric compensation that is based entirely upon manipulation of the image data themselves without intervention of ground measurements is the residual (log-residual if logarithmic variables are employed) or scene average method (Green and Craig, 1985; Solomon, 1984). The radiance observed by an aircraft-mounted scanner system can be expressed as

$$L(x,y,\tau - \tau') = P(x,y,\tau - \tau') + T(x,y, \tau - \tau')\, R(x,y) \qquad (1)$$

where the coordinates of a particular point in the image are (x,y) and where τ and τ' refer to the total optical depth of the atmosphere and the optical depth of observation measured from the top downward. This notation suppresses the dependence of the quantities L, P, T, and R on wavelength, and directions of solar incidence and observation. The first term in Eq. (1) is path radiance and represents sunlight that is directly and diffusely transmitted by the upper part of the atmosphere (above the depth of observation) and that is reflected upward by the lower part of the atmosphere (below the depth of observation). The second term is directly and diffusely transmitted upwelling surface radiation. The surface reflectance, R(x,y), is assumed to be Lambertian. It is further assumed that the scanner response has been converted to absolute radiance units for

all detector elements. The required steps are discussed elsewhere in this paper. For the long wavelength (rock) mode of observation (1180-2523 nm) the path radiance P is often negligible, so that Eq. (1) simplifies to

$$L(x,y,\tau - \tau') = T(x,y,\tau - \tau')\, R(x,y) \tag{2}$$

For a homogeneous atmosphere, constant elevation of the terrain above sea level, and constant observation elevation and attitude of the aircraft, it would also be justified to assume $T(x,y,\tau - \tau') = \langle T(\tau - \tau')\rangle$, a constant independent of position. A simple method for estimating $\langle T(\tau - \tau')\rangle$ is to form averages of the radiance L (x,y) over the image area to get

$$\langle L\rangle = \langle T\rangle\, \langle R\rangle \tag{3}$$

where $\langle L\rangle = (1/\text{Area}) \iint L(x,y)\, dxdy$, etc. Applying this to Eq. (2) particularized for constant transmittance $\langle T\rangle$ yields

$$L(x,y) = (\langle L\rangle/\langle R\rangle)R(x,y)$$

which expresses the scaled reflectances $R(x,y)/\langle R\rangle$ in terms of the image-derived quantities. If the atmosphere is inhomogeneous or the terrain uneven, or if the aircraft altitude above sea level and attitude are not constant, then averages of the image-derived radiances over the scene yield

$$\begin{aligned} \langle L(\tau - \tau')\rangle &= (1/\text{Area}) \iint T(x,y,\tau - \tau')\, R(x,y)\, dxdy \\ &= T(u,v,\tau - \tau')\, \langle R\rangle \end{aligned} \tag{4}$$

where $T(u,v,\tau - \tau')$, by the mean value theorem, is some value contained in the set of $T(x,y,\tau - \tau')$ but is otherwise unconstrained. In this case, applying Eq. (4) to Eq. (2) yields

$$L(x,y)/\langle L\rangle = [T(x,y)/T(u,v)]\, [R(x,y)/\langle R\rangle] \tag{5}$$

A key assumption required for the application of these methods is that the $\langle R\rangle$ produced by averaging is independent of wavelength. As emphasized by Solomon (1987, personal communication), this is never true for homogeneous scenes. For homogeneous terrain, $R(x,y)/\langle R\rangle \sim$ unity, and

$$L(x,y)/\langle L\rangle = T(x,y)/T(u,v) \tag{6}$$

Thus the technique yields a function that is proportional to the transmittance properties of the atmosphere and that tends to be independent of the surface for the case of homogeneous ground reflectance.

In the following preliminary treatment we have used the raw half-word AIS data with the spectral analysis manager SPAM (SPAM Handbook, 1987). Using the uncalibrated numbers introduces additional factors related to detector responsivity into the analysis as follows. Assuming that dark current responses have been eliminated from the data, the relationship between radiance and instrumental response measured in DN is

$$L(x,y,\lambda) = DN(x,y,\lambda)/G(x,\lambda) \tag{7}$$

where $G(x,\lambda)$ is a gain factor that depends on column position in the detector array (x) and row position (λ) only. Assuming the atmospheric part to be homogeneous so that $T(x,y,\tau - \tau')$ is equal to a constant ($\langle T \rangle$, say), then approximately

$$\langle DN(\lambda) \rangle = \langle T \rangle G(u,\lambda) \langle R \rangle \tag{8}$$

where $G(u,\lambda)$ is some value of G found within the set $G(x,\lambda)$ but is otherwise not constrained. Thus,

$$DN(x,y,\lambda)/\langle DN(\lambda) \rangle = [G(x,\lambda)/G(u,\lambda)]\ [R(x,y,\lambda)/\langle R(\lambda) \rangle] \tag{9}$$

We studied the scaled surface reflectance function based on this formula for the unknown (runway tarmac) and bright (playa) targets for the rock mode observations. In Figure 13 these functions are compared to a LOWTRAN transmittance spectrum derived from the midlatitude winter model and to the surface bidirectional spectral reflectance for the site as measured at 2-nm spectral resolution with PIDAS. (Note: The assumption of zero path radiance, implicit in formulating equation [2], is probably not valid for the shorter wavelength portion of the tree mode observations, which extend in wavelength from 809 to 2143 nm.) For the most part, these spectra are dominated by the presence of atmospheric absorption bands, and it is difficult to isolate with confidence any feature of the surface spectrum in the log residual spectrum without the actual surface spectrum as a guide. These results may be explained by resorting to equation (6) and the discussion following that equation. The proposed similarity between $\langle R \rangle$ and $R(x,y)$ that may have generated this result will eventually be examined by a calculation of $\langle R \rangle$ from the empirical line method of recovering surface spectral reflectance, and will be compared with locally computed values via the same set of calibration relationships.

Empirical Line Method

The empirical calibration line method is very simple to apply in principle. Field observations are made of surface reflectance for

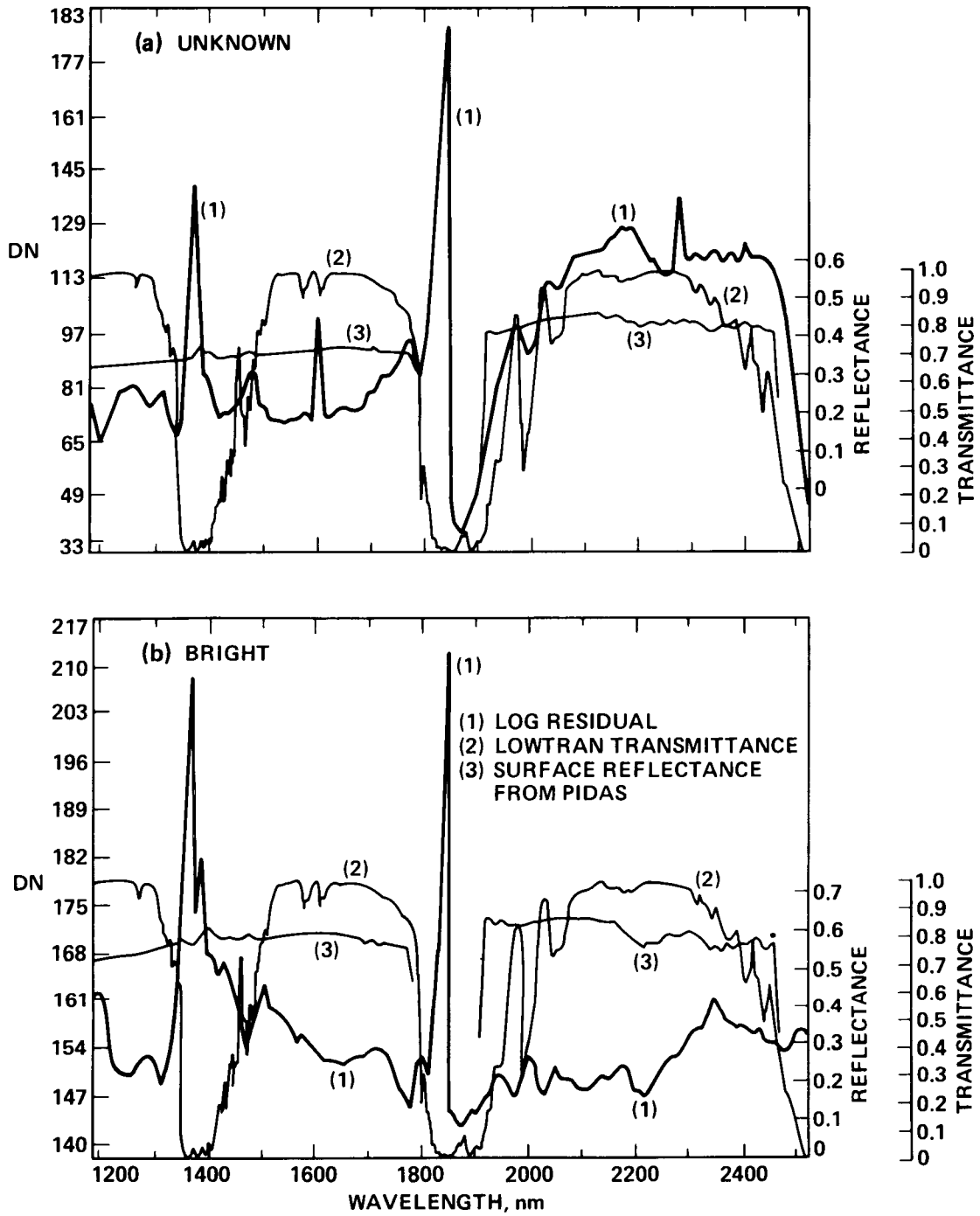

Figure 13. Comparison of spectra for two targets produced by the log-residual (scene average) method, a LOWTRAN transmission spectrum of the atmosphere, and the measured surface reflectance obtained from PIDAS.

homogeneous targets recognizable in the AIS imagery, and the scanner response for these areas is obtained. Plots of response (DN) (or radiance if the data are calibrated) vs surface reflectance are prepared as the basis

for compensation of the atmosphere elsewhere. Examples of two of the calibration lines obtained using the bright and dark targets are shown in Figure 14. The slope and intercept values L_o and dL/dR in the relationship

$$L(k) = L_o(k) + [dL(k)/dR(k)]\ R(k), \qquad k = 1,2, \ldots, 128$$

are shown in Figure 15. The spectral variation of dL/dR is proportional to the two-way atmospheric transmittance as multiplied by the solar spectral radiance, which it functionally resembles, while L_o, which declines with wavelength, is the path radiance.

The empirical method is applied to the target with unknown reflectance, and the result compared to the field-observed spectrum in Figure 16. Both calibrated (radiance) and uncalibrated (half-word DN) data have been included in the transformations. The results of these two different reductions are comparable. On the whole the fit is good, but the predicted spectra are systematically greater in reflectance by a few percent than the observed spectra, except between about 2018 and 2280 nm where the departures reach about 5%. A small minimum in the predicted reflectances near 2017 nm straddles major atmospheric absorptions from CO_2, and may represent poor compensation for this species in the reductions.

The differences between observations and predictions by the present method must originate in the calibration lines themselves. Two potential sources of concern are (1) how well the field-measured reflectances represent the standard targets and (2) whether spatial resolution of the target of unknown reflectance in the imagery is good. With respect to (1),

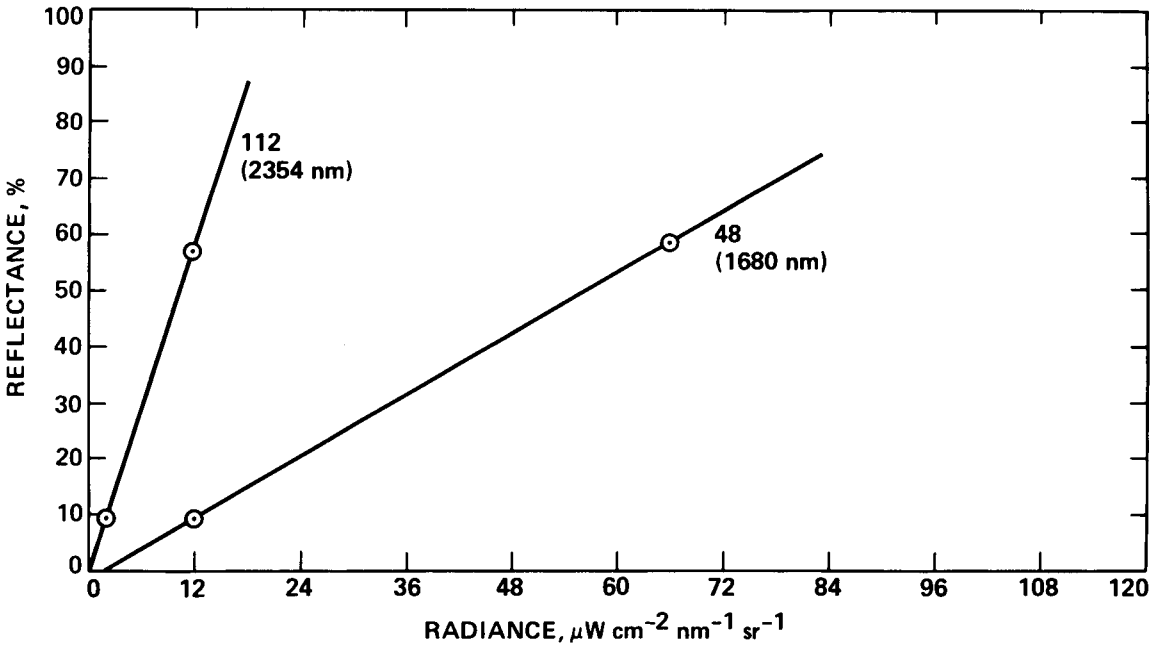

Figure 14. Examples of empirical calibration lines produced from bright playa and dark runway reflectance observations

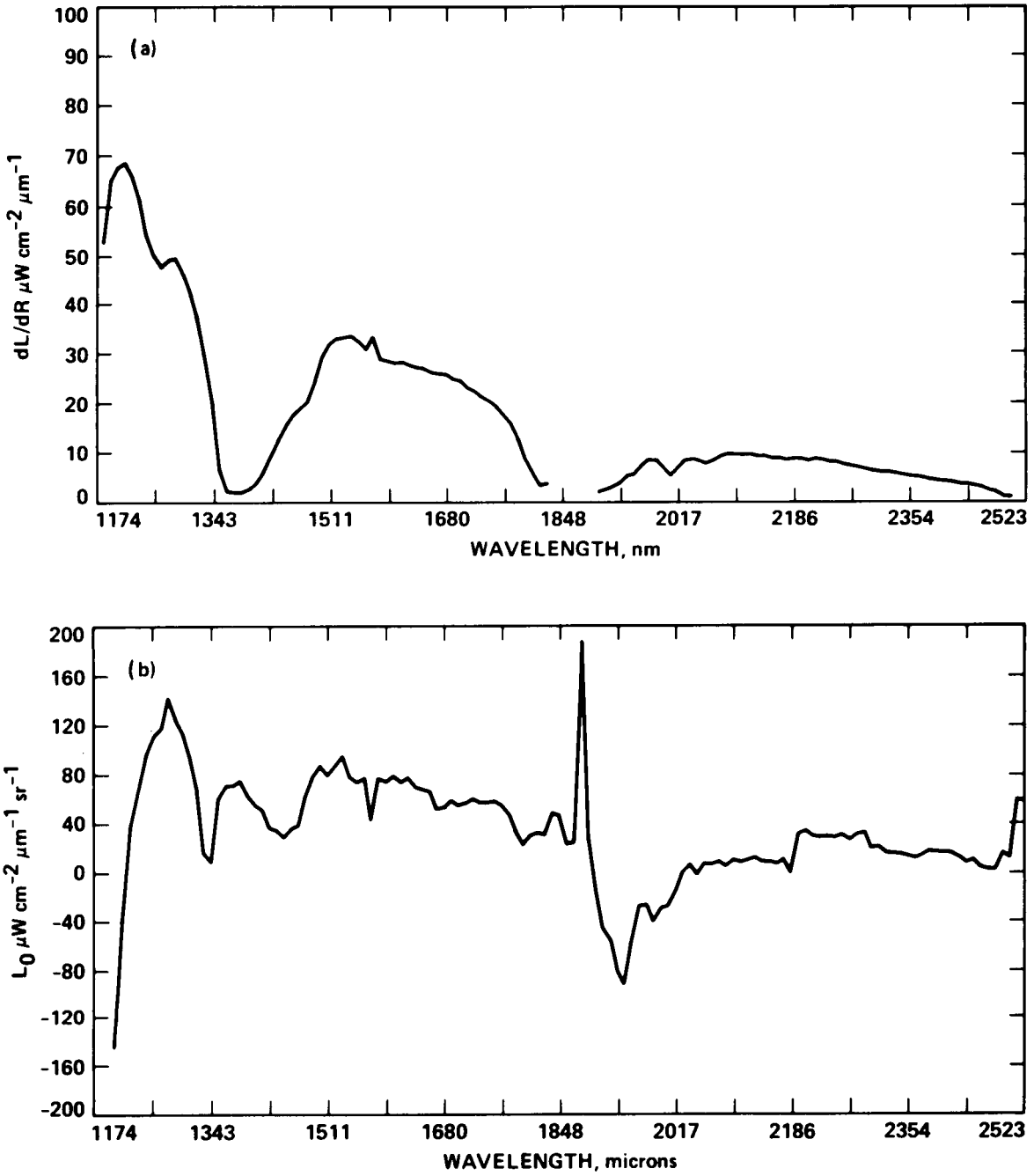

Figure 15. Values for the empirical calibration lines

field sampling of the dark target included both asphalt surface and bright lines painted on it, but no precise accounting of this mixture could be achieved because the runway is poorly resolved and the lines are not at all visible. If, for example, in the field-measured average spectrum the abundance of painted surface were overestimated, the slope of the resulting calibration line would be too steep. Accordingly, reflectances predicted for targets elsewhere would be too great. With respect to (2), the unknown, relatively bright target is surrounded on three sides by dark runways. If

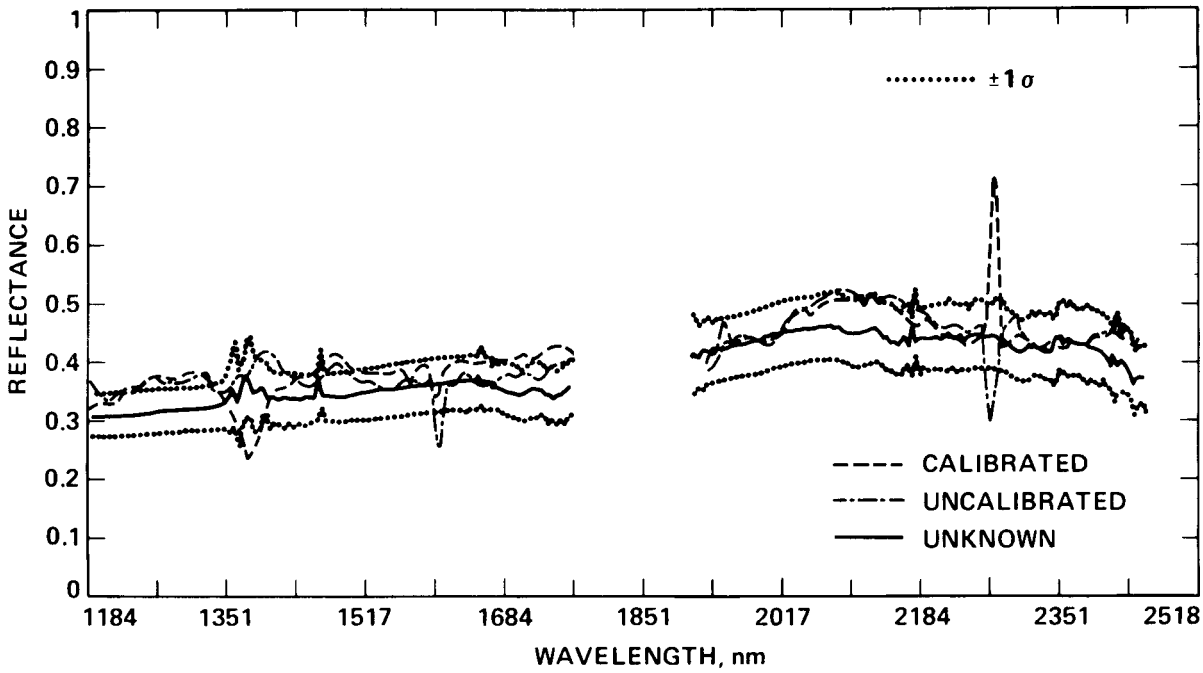

Figure 16. Comparison of spectra predicted for the unknown target from the empirical line method for both radiometrically reduced (calibrated) and unreduced (uncalibrated) data

this target is poorly resolved against the dark background, the apparent AIS response would be too low and would again lead to discrepancies of the sign observed.

Radiative Transfer Model

The radiative transfer modeling method of reduction to ground reflectance can be applied in a forward iterative fashion starting with the observed radiances and incrementally adjusting the surface reflectance value until the observed and predicted radiances equal each other. In order to apply this method, the following need to be supplied or estimated for the model: values of the optical depth for the atmosphere at each wavelength, the single scattering albedo, precipitable water abundance, concentration of CO_2, asymmetry factors for the aerosol scatterers, and variations of these quantities as height above the surface and horizontal position vary. As a first approximation, the LOWTRAN simulations and their comparisons with the observed radiances from AIS serve as a preliminary test of the ideas involved. LOWTRAN-6 supplies only a single scattering description of aerosol scattering (see Kneizys et al., 1983), so the use of it as a standard for comparison is less satisfactory at shorter wavelengths. For these problems the code developed by Diner and Martonchik (1984) will eventually be employed.

The principal source of concern here is the systematically lower value of the radiance returned from the laboratory calibration of AIS at each wavelength compared to the expected values from the LOWTRAN model. In a general way, if the laboratory calibration is taken as correct, then

directly adjusting the LOWTRAN model to match radiances leads to surface reflectances that are 30 to 50% too low compared to the field-determined numbers. The relationship is

$$R(AIS) = [L(AIS)/L(LOWTRAN)]\ R(PIDAS)$$

where R(AIS) is the surface reflectance implied by the AIS-observed radiance L(AIS), and R(PIDAS) is the surface reflectance as measured with PIDAS and used to produce a LOWTRAN model radiance L(LOWTRAN). Figure 8 shows L(AIS) and L(LOWTRAN), and Figure 17 is a plot of R(AIS) for the bright playa standard target. The appearance of uncompensated atmospheric bands in the predicted spectrum arises from dissimilarities between the assumed model and the observed spectrum in spectral resolution.

It does not seem worthwhile to go beyond this level of analysis, until the major extant discrepancies between the two data sets are removed.

SUMMARY

We have assembled a field experiment using AIS-2 over Rogers Lake, California to (1) provide an assessment of the engineering performance of the instrument with respect to in-flight radiometric calibration, spectral sampling interval, and signal-to-noise ratio and (2) compare various methods for the reduction of the data to ground reflectance, i.e., for atmospheric compensation. The Rogers Lake site presents a large, high-reflectance surface target (playa lake), dark targets (runways), and other surfaces (concrete runways) that can be used interchangeably as areas of known and unknown surface reflectance. Surface bidirectional spectral reflectance was determined with PIDAS. In addition, to support radiative transfer modeling and other exercises, we made observations of atmospheric optical depth, precipitable water abundance, and the ratio of direct to diffuse incident light.

With respect to the instrument-related questions we find (1) a spectral sampling interval between 20 and 30 as opposed to the ~10 nm expected from the instrument design, (2) a "signal-to-noise" ratio of 40 to 110, and (3) laboratory radiometric calibration radiances that are 30 to 50% lower than those expected.

In comparing the methods of data reduction we find the following: (1) The so-called scene average or log-residual method proves powerless to recover any feature of the surface reflectance, perhaps because of the homogeneity of the scene. (2) The empirical line method returns predicted surface reflectances that are within a few percent of the actual observed values using calibrated or uncalibrated data. The method encounters problems in detail in compensating for both water and CO_2 bands at various places in the spectrum. This suggests that both these gasses deserve detailed attention in the atmospheric modeling. (3) The radiative transfer question has been studied preliminarily using LOWTRAN-6. Apart from possible problems with the representation of scattering in this code, the

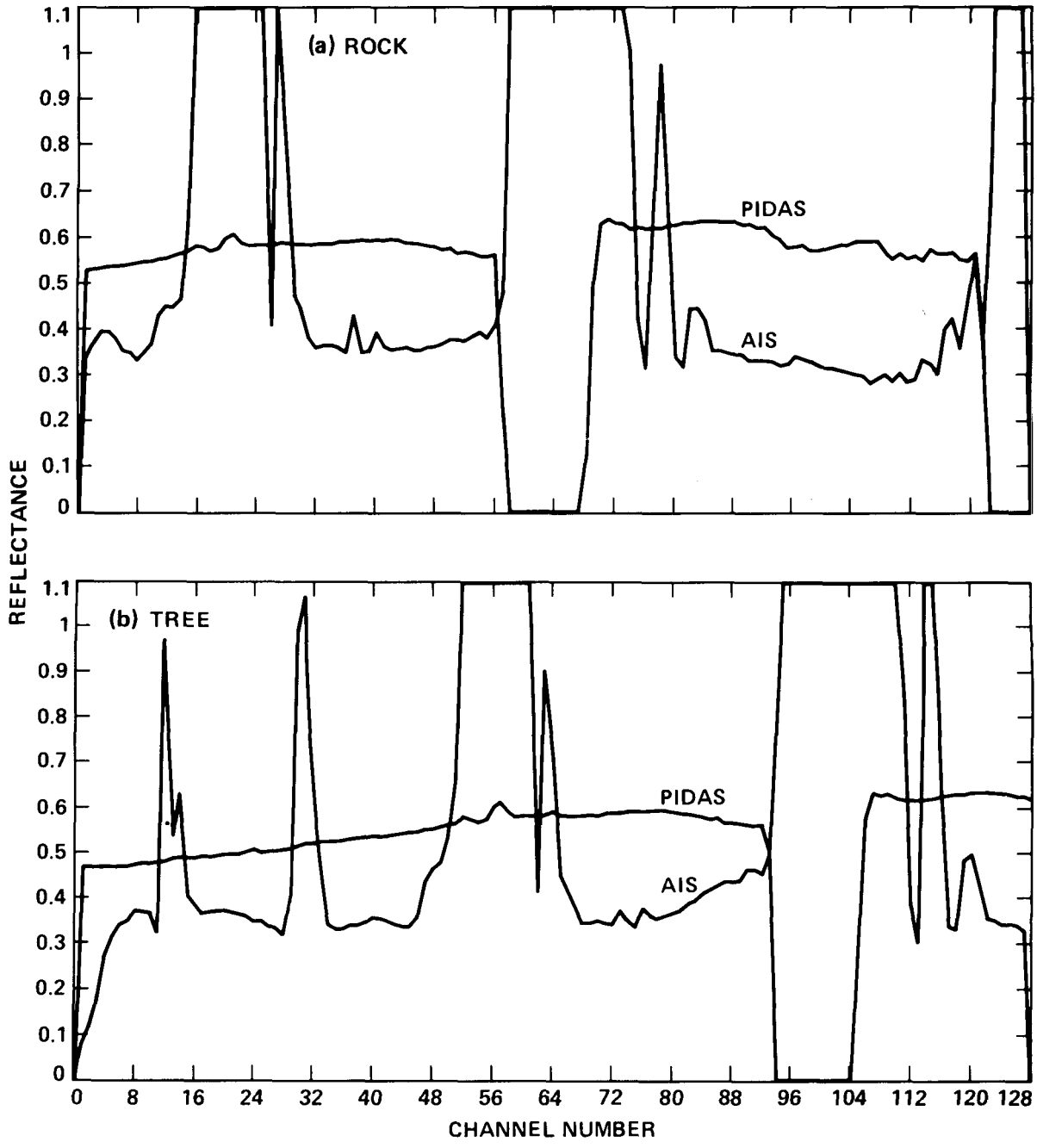

Figure 17. Surface reflectances derived from the AIS-2 data for the bright standard target using the LOWTRAN-6 atmospheric model: (a) rock mode and (b) tree mode

major concern for its application is the uncertain radiometry of AIS, since that code or any other relying on direct measurements of the radiance would return values of the surface reflectance lower than expected by 30 to 50% under solar illumination.

NOTE IN PROOF

An important factor in the radiometric analysis of AIS-2 presented earlier is the surface spectral reflectance returned by PIDAS, namely R(PIDAS). This quantity impacts directly the value of the expected radiance returned from LOWTRAN-6, as presented in Figure 8. P. Slater, R. Jackson and their associates (personal communication, 1987) have analysed surface reflectance measurements of the playa site taken with other radiometers in the field and have compared these data to measurements with a laboratory spectrometer. They find agreement between their laboratory and field-determined reflectances, which are 20 to 30% lower than the reflectance determined with PIDAS for the same site and time of observation. This difference, if true, reduces the radiance given by the LOWTRAN-6 simulation in Figure 8 by the same factor. The discrepancy between predicted and observed curves is accordingly narrowed and is roughly 30% of the AIS response itself rather than 60 or 70%. A similar reduction in the differences between the observed and calculated spectra of the test area shown in Figure 17 is also achieved if the reflectance determinations of Slater et al. are used.

ACKNOWLEDGEMENTS

Discussions with Jerry Solomon, Gordon Hoover, Dave Diner, Frank Palluconi, Harold Lang, and Anne Kahle are appreciated. Lisa Barge worked at displaying the AIS images on the AVIRIS VAX and helped us with SPAM. Jeff Dozier of the University of California at Santa Barbara, and Bob Wrigley, NASA Ames Research Center, offered useful comments.

Research described here was carried out at the Jet Propulsion Laboratory, California Institute of Technology, under contract with the National Aeronautics and Space Administration.

REFERENCES

Airborne Imaging Spectrometer Supplement. Supplement to the Science Investigators' Guide to AIS Data. May 1, 1986. JPL internal document, Jet Propulsion Laboratory, Pasadena, CA, 20 pp.

Cocks, T.D., and A.A. Green. 1986. Airborne spectroradiometry: The application of AIS data to detecting subtle mineral absorption features. Proceedings of the Second Airborne Imaging Spectrometer Data Analysis Workshop (G. Vane and A. F. H. Goetz, eds.). JPL Publication 86-35, Jet Propulsion Laboratory, Pasadena, CA, pp. 52-62.

Conel, J.E., S. Adams, R.E. Alley, G. Hoover, and S. Schultz. 1986. Analysis of AIS radiometry with emphasis on determination of atmospheric properties and surface reflectance. Proceedings of the Second Airborne Imaging Spectrometer Data Analysis Workshop (G. Vane and A. F. H. Goetz, eds.). JPL Publication 86-35, Jet Propulsion Laboratory, Pasadena, CA, pp. 31-51.

Conel, J.E., R.O. Green, G. Vane, C.J. Bruegge, R.E. Alley, and B.J. Curtiss. 1987a. Airborne Imaging Spectrometer-2: Radiometric and spectral characteristics and comparison of ways to compensate for the atmosphere. Paper presented at SPIE 1987 Symposium, San Diego, CA, August 1987.

Conel, J.E., S. Adams, R.E. Alley, G. Hoover and S. Schultz. 1987b. AIS radiometry and the problem of contamination from mixed spectral orders. Remote Sensing of Environ. Elsevier (in press).

Diner, D.J., and J.V. Martonchik. 1984. Atmospheric transfer of radiation above an inhomogeneous non-Lambertian reflective ground-I. Theory. J. Quant. Spectrosc. Radiat. Transfer. 31 (2): 97-125.

Goetz, Alexander F.H. 1987. The Portable Instant Display and Analysis Spectrometer (PIDAS). In Proceedings of the 3rd Airborne Imaging Spectrometer (AIS) Data Analysis Workshop (G. Vane, ed.). JPL Publication 87-30, Jet Propulsion Laboratory, Pasadena, CA.

Green, A.A., and M.D. Craig. 1985. Analysis of aircraft spectrometer data with logarithmic residuals. Proceedings of the Airborne Imaging Spectrometer Data Analysis Workshop, JPL Publication 85-41, Jet Propulsion Laboratory, Pasadena, CA, pp. 111-119.

Hansen, J.E., and L.D. Travis. 1974. Light scattering on planetary atmospheres. Space Science Reviews. 16: 527-610.

Kneizys, F.X., E.P. Shettle, W.O. Gallery, J.H. Chetwynd, Jr., L.W. Abrew, J.E.A. Selby, S.A. Clough, and R.W. Fenn. 1983. Atmospheric Transmittance/Radiance: Computer code LOWTRAN 6. AFGL-TR-83-0187, AFGL Hanscom AFB, MA. 200 pp.

LaRocca, A.J. 1978. Atmospheric absorption, Chap. 5, in The Infrared Handbook (W.L. Wolfe and G.J. Zissis, eds.). Environmental Research Institute of Michigan, Ann Arbor, MI, pp. 5-3 - 5-132.

Roberts, D.A., Y. Yamaguchi, and R.J.P. Lyon. 1986. Comparison of various techniques for calibration of AIS data. Proceedings of the Second Airborne Imaging Spectrometer Data Analysis Workshop (G. Vane and A.F.H. Goetz, eds.). JPL Publication 86-35, Jet Propulsion Laboratory, Pasadena, CA, pp. 21-30.

Solomon, J.E. 1984. Thoughts on atmospheric "corrections" for AIS imagery. JPL IOM IAS: 384-84-JES102ed. JPL internal document, Jet Propulsion Laboratory, Pasadena, CA.

SPAM Handbook. 1987. Spectral Analysis Manager, Software for imaging spectrometry data analysis, October 1, 1986. JPL internal document, Jet Propulsion Laboratory, Pasadena, CA.

Tucker, D. 1987. Integrating sphere calibration - bulb set #2. JPL internal document, Jet Propulsion Laboratory, Pasadena, CA.

Vane, G. 1986. Introduction to the Proceedings of the Second Airborne Imaging Spectrometer (AIS) Data Analysis Workshop. In Proceedings of the Second Airborne Imaging Spectrometer (AIS) Data Analysis Workshop (G. Vane, and A.F.H. Goetz, eds.). JPL Publication Number 86-35, Jet Propulsion Laboratory, Pasadena, CA, pp. 1-16.

EFFECTIVE USE OF PRINCIPAL COMPONENT ANALYSIS WITH HIGH RESOLUTION REMOTE SENSING DATA TO DELINEATE HYDROTHERMAL ALTERATION AND CARBONATE ROCKS

SANDRA C. FELDMAN, Mackay School of Mines, University of Nevada-Reno, Reno, NV 89557, USA

ABSTRACT

Methods of applying principal component (PC) analysis to high resolution remote sensing imagery were examined. Using Hot Creek Range, Nevada Airborne Imaging Spectrometer (AIS) data, principal component analysis was found to be useful for removing the effects of albedo and noise and for isolating the significant information on argillic alteration, zeolite, and carbonate minerals.

The most effective technique for using PC analysis for mineralogical discrimination was to perform three separate PC analyses using as input the first 16 AIS bands, 7 intermediate bands, and the last 16 bands from the 32 flat-field-corrected bands between 2048 and 2337 nm. Most of the significant mineralogical information resided in the second principal components. PC color composites and density sliced images provided a good mineralogical separation when applied to the Hot Creek AIS data set.

Although computer-intensive, the advantage of principal components analysis is that it employs algorithms which already exist on most image processing systems.

INTRODUCTION

Very effective software packages and algorithms have been developed specifically for use with high resolution remote sensing imagery (Goetz and others, 1985; Mazer and others, in press; Lyon and Lanz, 1985). Some of these packages, however, are not easily implemented with many users' existing image processing hardware configurations, and the software is often not compatible with other image processing software packages without a significant amount of reprogramming. The objective of this paper is to suggest methods for analyzing high resolution remote sensing data, specifically Airborne Imaging Spectrometer (AIS) imagery, that can take advantage of algorithms which already exist on most image processing systems. Principal component (PC) analysis is one such method.

Principal component analysis has been successfully used with Landsat Thematic Mapper (TM) imagery and TM simulator imagery to differentiate geologic units and to identify hydrothermally altered areas (Abrams and others, 1983; Conel and Alley, 1985). The effectiveness of this method with Airborne Imaging Spectrometer (AIS) data was tested during this investigation using 32 of the 128 bands from the Hot Creek Range, Nevada AIS-1 data set. These 32 bands contain the most important mineralogical absorption features in the 1200 to 2400 nm wavelength range. The data set has a 9.3 nm spectral sampling interval and a 12 m spatial resolution.

The Hot Creek AIS site is located in the Tybo mining district and contains hydrothermally altered and unaltered Paleozoic carbonate and clastic rocks, and Tertiary rhyolitic ash-flow tuffs. From field mapping, laboratory work, and measurements on samples collected along the flight line with an IRIS spectroradiometer, the ash-flow tuffs were found to be altered to clay, zeolite, and silica minerals (Feldman and Taranik, [a], in press). Kaolinite and calcite are widespread in the Music Canyon area, and kaolinite, montmorillonite, and clinoptilolite are common in the Red Rock Canyon area.

AIS METHODOLOGY

The 32 spectral bands between 2048 and 2337 nm in the Red Rock Canyon and Music Canyon areas, Hot Creek Range AIS-1 data set, were used to test the effectiveness of principal component analysis. Spectra of kaolinite, montmorillonite, clinoptilolite, and calcite from samples along the AIS flight line, recorded with a GER IRIS spectroradiometer, are shown in Figure 1.

Signal-to-noise ratios calculated for AIS-1 data sets vary between 40:1 and 10:1 (Vane, 1986; Tucker and Vane, 1986). In order to remove systematic noise, to correct for variations in detector response, and to remove atmospheric absorption features and the effects of the solar irradiance curve, a flat field correction was applied to the "raw" AIS data prior to performing principal component analyses. The correction was performed by choosing a spectrally flat area in the alluvium and dividing the brightness value of each pixel in each band along the flight line by the average value of the flat field in that band. The flat field correction does not remove albedo, but alters the albedo, leaving a relative albedo component in the data.

The application of principal component analysis to AIS data was considered successful if localities containing kaolinite, montmorillonite, clinoptilolite, and calcite, as determined from field mapping and laboratory analyses, were separable from each other in images constructed with principal components. Because of

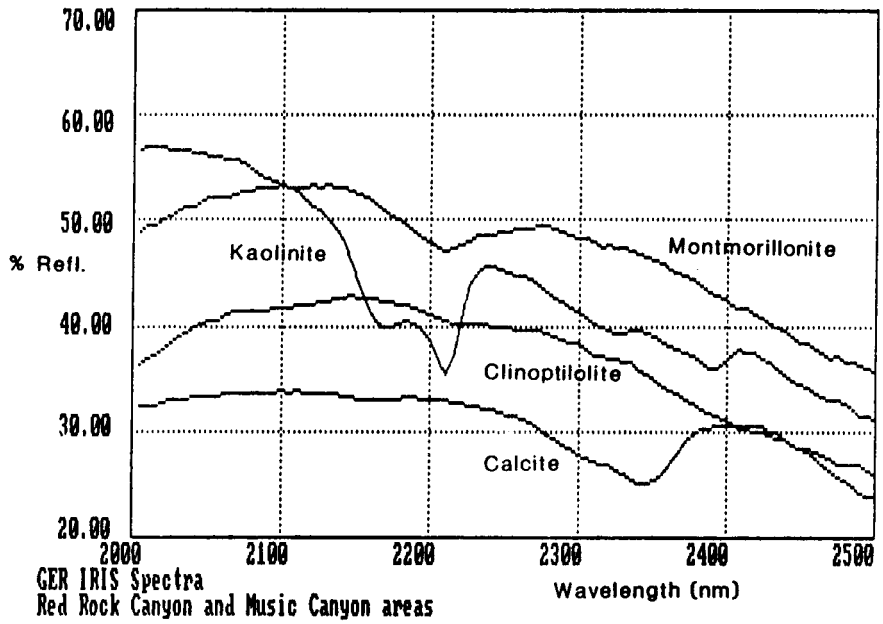

Fig. 1. IRIS spectroradiometer curves for samples collected along the AIS flight line, Hot Creek Range, Nevada.

the large volume of AIS data (128 bands by 32 pixels by the number of lines in the data set) and the low signal-to-noise ratio, desirable analysis methods are those which isolate the noise from the significant data, those which take a minimum of computer time, and those which are compatible with many users' system architecture, operating system, compiler, and peripherals.

PRINCIPAL COMPONENT ANALYSIS

Principal component analysis has been used for many years to enhance geologic features on Landsat Thematic Mapper (TM) or TM simulator imagery (Abrams and others, 1983; Conel and Alley, 1985). A principal component analysis decreases the dimensionality of the data without losing significant information. The correlation between variables is reduced to produce a more fundamental set of independent variables. The first component accounts for the greatest amount of total variance; components 2 and higher contain successively less variance. In areas of low vegetative cover, spectral variation in principal component images produced from TM-type imagery has often been correlated with changes in lithology.

Principal component analyses were executed on 512 lines of AIS data from the Music Canyon area and 512 lines from the Red Rock Canyon area. Three separate

principal component analyses were performed on the first 16 bands, 7 intermediate bands, and the last 16 bands from each of the two localities. The purpose of executing three analyses was to isolate significant mineralogical information from different parts of the spectrum and place it into the PCs with the greatest amounts of variance. The first PC analysis was performed using the first 16 bands (2048 to 2188 nm) as input, where kaolinite has an absorption feature. In the second, bands 12 through 18 (2151 to 2206 nm) were utilized to include longer wavelength clay absorption features. The last 16 bands (2197 to 2337 nm), where carbonate and clinoptilolite absorption features are present, were used in the third PC analysis.

From a series of experiments using different AIS bands as input to the principal component analysis, it was found that the number of bands used as input must be balanced against the amount of noise in the data set and the number of significant spectral features expected in that portion of the spectrum. The input of fewer bands into the principal component analysis results in a higher concentration of noise in PCs 2 and 3, making them less useful. Using a large number of bands as input into the PC analysis, from portions of the spectrum where many different absorption features are located (for instance clay minerals and calcite), causes the segregation of significant spectral information into higher number, noisy PCs.

The scaled and Gaussian stretched images of the 16 principal components (Figures 2a and 2b) of the Music Canyon area illustrate that PC 1 accounts for the greatest percent of the total variance (97 percent). PC 2 contains 2.5 percent of the total variance while PC 3, 4, and 5 each contain less than 0.5 percent. While there is significant information in PCs 3, 4, and 5, much of the information content is masked by noise. Horizontal striping accumulates in PC 3 and 4, while random noise collects in higher number PCs.

From an analysis of eigenvectors for both the Red Rock Canyon and Music Canyon images, it was found that each of the 16 input bands contributes equally to PC 1; PC 1 is a relative albedo image which also contains information on aspect and slope. PC 2 and, to a lesser extent, PC 3 contain the most significant information on mineralogy and surficial cover. The AIS bands which are highly correlated with PCs 2 and 3 (Table 1) are, most often, those bands located adjacent to spectral absorption features for kaolinite, montmorillonite, calcite, and clinoptilolite.

A color composite which effectively shows the distribution of kaolinite and calcite (limestone) in the Music Canyon area was produced using PC 2s and PC 3s from the three separate principal component analyses (Feldman and Taranik, [b], in press). Density slicing PC 2 images

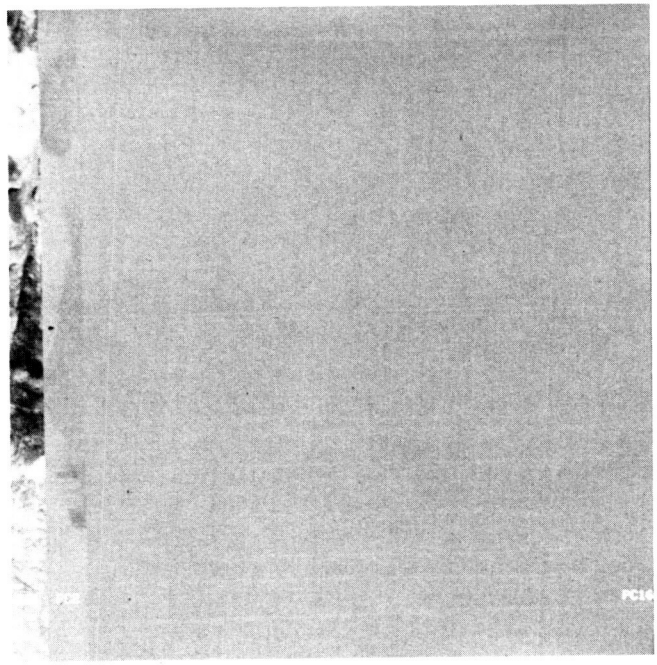

Fig. 2a. Principal components 1 through 16 (left to right) using the first 16 AIS bands in the fourth grating position as input. Real values scaled and converted to byte data for display.

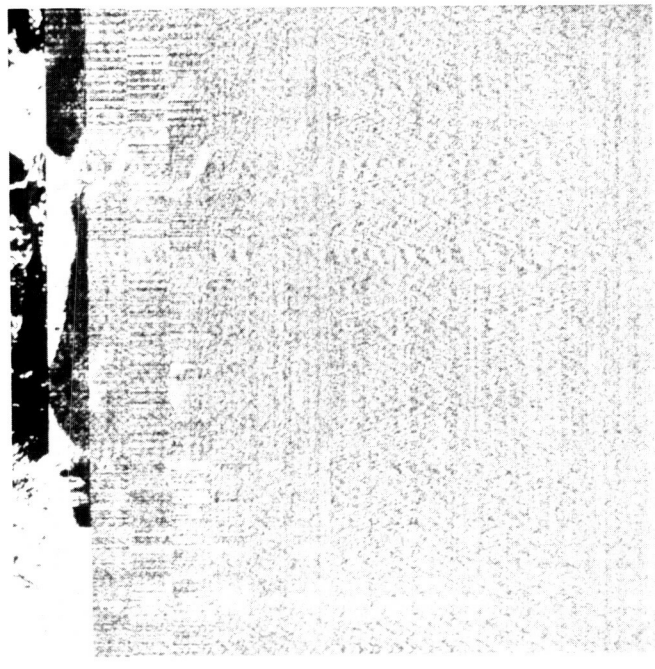

Fig. 2b. Principal components 1 through 16 (left to right) using the first 16 AIS bands in the fourth grating position as input. Gaussian stretch applied.

Table 1. AIS bands in the fourth grating position which are highly correlated with principal components 2 and 3

MUSIC CANYON SCENE

PC	AIS band Band no.	Wavelength midpoint (nm)
Principal component analysis on bands 1 to 16		
2	14, 15, 16	2169, 2178, 2188
3	10, 11	2132, 2141
Principal component analysis on bands 12 to 18		
2	17, 18	2197, 2206
3	18	2206
Principal component analysis on bands 17 to 32		
2	--	--
3	30, 31, 32	2318, 2328, 2337

RED ROCK CANYON SCENE

PC	AIS band Band no.	Wavelength midpoint (nm)
Principal component analysis on bands 1 to 16		
2	14, 15, 16	2169, 2178, 2188
3	3, 4	2067, 2076
Principal component analysis on bands 12 to 18		
2	17, 18	2197, 2206
3	18	2206
Principal component analysis on bands 17 to 32		
2	31, 32	2328, 2337
3	28, 29	2300, 2309

was also found to be very effective for mineralogical discrimination.

A similar method was used to produce a principal component image for the Red Rock Canyon area. The color composite image which most successfully separated kaolinite and montmorillonite-clinoptilolite alteration zones was formed using PC 2s from the three principal component analyses.

CONCLUSIONS

The most appropriate technique for applying principal component analysis to high spectral resolution data sets is dependent on the signal-to-noise ratio and on the width of significant spectral features of minerals which may be present. Input bands should be from portions of the spectrum where significant spectral features of minerals are located. This method cuts down on the amount of computer time needed to perform the principal component analyses.

For a signal-to-noise ratio of about 40:1, as in the Hot Creek AIS data set, in an area containing clay, zeolite, and carbonate minerals, it was found that three separate PC analyses, using the first 16 AIS bands, 7 intermediate bands, and the last 16 bands as input, was the most efficient technique. Most of the mineralogical information was found to be contained in PC 2s. PC color composites and density sliced images, composed primarily of PC 2s, yielded good mineralogical separation in the Red Rock and Music Canyon areas.

Principal component analysis is an effective way to separate argillic alteration, zeolite, and carbonate mineral localities using high resolution remote sensing imagery. PC analysis separates out relative albedo and aspect and slope effects, mineralogically significant information, and noise in the Hot Creek Range AIS data set. Although principal component analysis is computer-intensive, algorithms for PC analysis are already implemented on most image processing systems, and major reprogramming is not required. PC analysis methods are a viable option for many users of multidimensional spectral data.

ACKNOWLEDGEMENTS

The author would like to thank James V. Taranik for reviewing the manuscript and making helpful comments.

REFERENCES

Abrams, M. J., Brown, D., Lepley, L., and Sadowski, R., 1983, Remote sensing for porphyry copper deposits in Southern Arizona: Economic Geology, v. 78, p. 591-604.

Conel, J. E., and Alley, R. E., 1985, Lisbon Valley, Utah, uranium test site report, in The Joint NASA/Geosat Test Case Project, Final Report: Tulsa, Oklahoma, American Association of Petroleum Geologists.

Feldman, S. C., and Taranik, J. V., [a], in press, The use of high resolution remote sensing techniques to define hydrothermal alteration mineralogy: Tybo mining district, Nevada, in Proceedings of the Bulk Mineable Precious Metal Deposits Symposium: Reno, Nevada Geological Society of Nevada.

Feldman, S. C., and Taranik, J. V., [b], in press, Comparison of techniques for discriminating hydrothermal alteration minerals on Airborne Imaging Spectrometer data: Remote Sensing of Environment.

Goetz, A. F. H., Vane, G., Solomon, J. E., and Rock, B. N., 1985, Imaging spectrometry for earth remote sensing: Science, v. 228, p. 1147-1153.

Lyon, R. J. P., and Lanz, K., 1985, Field utilization and analysis of AIS 128-channel imagery using microcomputers: Application to Yerington, Nevada field area, in Proceedings of the Airborne Imaging Spectrometer Data Analysis Workshop, ed. G. Vane, and A. F. H., Goetz: Pasadena, California, Jet Propulsion Laboratory Publ. 85-41, p. 56-61.

Mazer, A. S., Martin, M., Lee, M., and Solomon, J. E., in press, Image processing software for imaging spectrometry data analysis: Remote Sensing of Environment.

Tucker, D., and Vane, G., 1986, Radiometric calibration of the Airborne Imaging Spectrometer, in Proceedings of the Second Airborne Imaging Spectrometer Data Analysis Workshop, ed. G. Vane and A. F. H. Goetz: Pasadena, California, Jet Propulsion Laboratory Publ. 86-35, p. 17-20.

Vane, G., 1986, Introduction to the Proceedings of the Second Airborne Imaging Spectrometer (AIS) Data Analysis Workshop, in Proceedings of the Second Airborne Imaging Spectrometer Data Analysis Workshop, ed. G. Vane and A. F. H. Goetz: Pasadena, California, Jet Propulsion Laboratory Publ. 86-35, p. 1-16.

LAND COVER/USE CLASSIFICATION OF CAIRNS, QUEENSLAND, AUSTRALIA: A REMOTE SENSING STUDY INVOLVING THE CONJUNCTIVE USE OF THE AIRBORNE IMAGING SPECTROMETER, THE LARGE FORMAT CAMERA AND THE THEMATIC MAPPER SIMULATOR

MATTHEW HERIC, WILLIAM COX AND DANIEL K. GORDON, Autometric, Incorporated, Falls Church, Virginia 22041, USA.

ABSTRACT

In an attempt to improve the land cover/use classification accuracy obtainable from remotely sensed multispectral imagery, AIS-I images have been analyzed in conjunction with TMS (NS001), LFC color infrared photography and black and white aerial photography. Specific portions of the combined data set were registered and used for classification. Following this procedure, the resulting derived data was tested using an overall accuracy assessment method.

This study is not based upon the use of precise photogrammetric 2D-3D-2D geometric modeling techniques. Instead, the discussion exposes resultant spectral findings from the image-to-image registrations. Problems associated with the AIS-I - TMS integration are considered, and useful applications of the imagery combination are presented.

More advanced methodologies for imagery integration are needed if multisystem data sets are to be utilized fully. Nevertheless, fundamental research, such as described herein, provides a formulation for future Earth Observation Station-related multisensor studies.

INTRODUCTION

Considerable technical research and development have been completed with regard to the design of remote sensing systems, and as more sophisticated imaging systems have been brought on-line, there has been greater interest directed towards the utilization of an ever increasing amount of data. In particular, as a method for realizing the full potential of remotely sensed imagery, some research has addressed the various aspects of combining complementary sensor data. In an effort to broaden the applicability of remotely sensed data, Airborne Imaging Spectrometer-I (AIS-I), Thematic Mapper Simulator (NS001 or TMS) and Large Format Camera (LFC) imagery have been analyzed conjunctively for purposes of land use/cover classification. Specifically, all data was examined to assist in the classification of Cairns, Queensland, Australia. The research objectives focused on the compatibility of an LFC, AIS-I and TMS-AIS-I imagery set.

The space-based photography was obtained by the NASA LFC during the Space Transportation System Mission 41-G, from aboard the Shuttle Challenger at an altitude of approximately 225.75 kilometers. The individual frames used for this study, 1696-1698, were taken on 11 October 1984 using Eastman Kodak SO-131 high definition aerochrome color infrared (positive) film. Without magnification, the approximate scale of the photography was 1:778,630 which, in turn, yielded an estimated spatial resolution of 20 meters (Lucas, Pearson, and Biache, 1986).

AIS-I imagery were collected aboard the NASA Ames C-130 aircraft on 22 October 1985. The altitude of the aircraft during the flight was nominally 7000 meters. Aerial black and white photography was also collected by the C-130 using a bore-sighted 35mm referencing camera along with imagery from the NS001 multispectral scanner. A second set of black and white photographs, taken on 13 August 1984 at 450 meters (provided by Northern Air Surveys under contract to the Queensland Department of Surveying and Mapping), was also included. Table 1 summarizes all data available for this land classification.

Table 1

Sensor/Camera	Spectral Range (micrometers)
Large Format Camera	
Kodak SO-131 film	0.50 - 0.90
Airborne Imaging Spectrometer-I	
128 spectral bands	
spectral sampling at 9.6 nm	1.20 - 2.40
Thematic Mapper Simulator (NS001)	
Band 1	0.448 - 0.519
Band 2	0.529 - 0.603
Band 3	0.633 - 0.697
Band 4	0.767 - 0.910
Band 5	1.00 - 1.30
Band 6	1.57 - 1.71
Band 7	2.10 - 2.38
Band 8	10.90 - 12.30
Aerial Photography (from 7 kilometers)	Black and White Aerochrome
Aerial Photography (from 450 meters)	Black and White Aerochrome

ANALYSIS TECHNIQUES

The basis for this study was the Anderson et al (1976) land use/cover classification system. This technique was deemed most suitable since the hierarchical design of the Anderson system is structured to be driven primarily by the interpretation of remote sensing data obtained at various scales and resolutions and not data collected in situ (Jensen, 1986).

The initial research goal was to incorporate the AIS-I imagery to the maximum extent possible in the respective phases of the classification.

Extreme amounts of distortion in the original AIS-I data, however, prohibited use of the entire flight-line. Efforts to remove this skewing problem were not employed. Hence, the first 35% and the last 12% of the imagery were not analyzed. This narrowed the choice of specific study sites considerably. Therefore, the specific study area began at Admiralty Island, continued through Smith's Creek, Trinity Inlet, various loading pier areas, and finally, ending in downtown Cairns.

Photographic analysis of the LFC hard-copy was performed using a Bausch & Lomb binocular zoom microscope. Stereo analysis was performed with a Zeiss Aerotopo stereoscope as well as with the Autometric-developed Analytical Photogrammetric Processing System (APPS-IV). AIS-I and TMS imagery were analyzed using the Earth Resources Data Analysis System (ERDAS) version 7.2, which was installed in a COMPAQ 386 micro computer. Finally, AIS-I data were also analyzed using the Spectral Analysis Manager (SPAM) and a Gould DeAnza FD5000 image processor with a VAX 11/750 computer as the host.

PHOTOGRAPHIC ANALYSIS RESULTS

From analysis of the LFC photography, a basic delineation of land use/cover was possible. For example, the vast abundance of healthy wetlands was particularly striking. The delineation of specific items, however, was difficult to ascertain with the LFC hard-copy. Most notably, definition of specific vegetation type was not attainable. Under magnification, some urban land use functions were apparent. In particular, loading piers and adjacent structural features were discriminated. One area of unknown cover type was an open field just north of the dock area. This field, larger than two Cairns city blocks, displayed an even-toned green signature over the southern half, which transitioned into a highly irregular gray-white tone in the northern half. The deep red signatures of the neighboring lush marshes and forested areas were missing from the open field. Reasons for this highly irregular site could not be defined using the LFC imagery.

In support of these initial findings, the medium and low altitude panchromatic aerial photography was analyzed in an attempt to obtain a stronger identification of the Cairns areas in question. By interpreting the photography, the industrial layout of these sites became somewhat more apparent. Indeed, the dominant structural features were devoted to the local sugar industry. In addition, the open field appeared to have some grasses, but reasons for the change in signature were still undeterminable. Generally, information regarding soil moisture and soil type is difficult to obtain using aerial photography. To address this problem and further substantiate the classification, the multispectral imagery was accessed.

AIRBORNE IMAGING SPECTROMETER-I ANALYSIS AND RESULTS

Using only the photography, preliminary classification was possible. Two major concerns however, were not met with the hard-copy: (1) the wetland vegetation could not be species determined (2) the vegetation in the aforementioned field near the loading dock could not be accurately identified. To solve these problems, a discriminate analysis of the AIS-I imagery with SPAM was employed.

The first step in this process involved creating a series of spectral library plots based on the Cairns data from areas of known composition. For example, based on the photography and topographic maps of the region, certain distinguishable areas, such as grass from urban parks, shallow water bodies and concrete/steel urban structures, were located on the AIS-I imagery. Based on these specific pixels, brightness value plots were created for the first 80 bands of the 128 band data set and saved using the SPAM SAVEPLOT command. The second step for this method involved plotting pixel brightness values from the previously charted areas in question. Thus, from within the field area, pixel brightness value plots were created and, using the LIBPLOT command, compared to the newly created library plots. Based on these and other LIBPLOT comparisons, the wetland vegetation in question was determined to be lush wetland scrub brush. With regard to the open field, the northern half was determined to be covered by an even expanse of grass with intermittent groups of herbaceous shrubs. The southern extent of the field appeared to share a similar signature. The difference in tone, however, was determined to be the presence of high soil moisture levels.

REGISTERED IMAGERY (AIS-I AND TMS) ANALYSIS AND RESULTS

The third approach to analyzing the Cairns area involved superimposing the AIS-I with the TMS imagery and performing a statistical analysis of the resultant data file. Specifically, band extraction, based on examples documented by Ustin, Rock and Woodward (1986), was employed to remove selected bands of interest from the near infrared region of the AIS-I imagery. When examined visually using SPAM, bands 9, 16 and 30 were determined to exhibit significant brightness variations and were therefore extracted. Following this, the 3-band AIS-I data set and the 7-band (band 8 was not included) TMS data were downloaded from the VAX 11/750 to the COMPAQ 386/ERDAS image processing system.

Before performing a statistical classification on the AIS-I and TMS imagery together, the two data sets had to be registered. This image registration process involved translating and rotating the imagery so that objects were positioned coincident with respect to one another and corresponding elements of the same ground appeared in the same place on the registered imagery (Jensen, 1986). In this case, the AIS-I imagery were geometrically shifted to overlay the TMS "base map" image. It should be noted, however, that this process was not based on traditional photogrammetric techniques for 2D-3D-2D geometric modeling. Instead, this procedure simply represents an image-to-image registration.

The image registration was accomplished using the ERDAS CURSES, COORD2 and RECTIFY programs. First, using CURSES, ground control points were taken from both sets of imagery. Second, the COORD2 program was used to calculate the image transformation matrix and list the resultant coefficients. Root mean square error for this routine was set at 1.5. Third, RECTIFY was accessed to perform the actual image registration. During this process, the AIS-I imagery were rectified to "fit" the TMS imagery. The brightness values of the shifted AIS-I pixels were determined via an internal nearest neighbor function. Thus,

following this series of routines, the newly created image file contained 10 bands: 7 from the TMS and 3 from the AIS-I.

The classification of the TMS-AIS-I imagery was accomplished using the ERDAS CLUSTER program. This unsupervised classification algorithm operated in a two-pass mode. The first pass through the data set built the clusters by collecting points in the image's spectral space. For each collection of points, the CLUSTER routine calculated the accompanying cluster mean vectors. The second pass through the data set separately assigned each pixel of the 11 band data set to one of the mean vectors created in pass 1.

20 clusters were created from the imagery. With regard to spectral space, axes skip factors (for the x and y directions) were set at 2. Minimum distance between clusters was also established at 2. Finally, minimum allowable cluster radius was 14 and the cluster elimination threshold percentage was 1.

Following the classification process, two-dimensional two-band plots of the mean vector values were created. These scatterplots represented the intersections of the individual mean vectors and the specific location of the 20 cluster groupings. For comparison, scatterplots from the AIS-I vs TMS as well as from the TMS vs TMS are provided in Figures 1 and 2. After plotting these mean vectors, the final process involved translating the clusters into information classes. The final land use/cover classification or "derived" map was created using ERDAS geographic information systems color assignment routines.

Accuracy for this classification process was estimated using an overall accuracy assessment method based on acceptance sampling which has been documented by Arnoff (1982). In addition, Ginevan (1979) provides a methodology for applying this procedure to classified maps. Using this technique, 92 separate pixels were plotted and labeled from the classified imagery. These were then charted on 1:100,000 Royal Australian Survey Corps topographic maps. Based on this procedure, overall accuracy was determined to be 89%. Thus, the classified imagery is above the lower limit of 85% set by Arnoff and, in turn, represents an acceptable "derived" map.

CONCLUSIONS

This three-tiered approach to land cover/use classification discusses some of the benefits from combining complementary data sets. Admittedly, this investigation was somewhat simplistic. Nevertheless, imagery from the TMS, LFC and AIS-I were used to obtain an acceptable level of derived map accuracy. By using both discriminate and statistical techniques, each data set provided unique spectral information valuable to the goal of this preliminary study. In particular, the accuracy obtained from the image-to-image registration provides incentive to develop photogrammetric models for purposes of correlating and analyzing multisensor data sets.

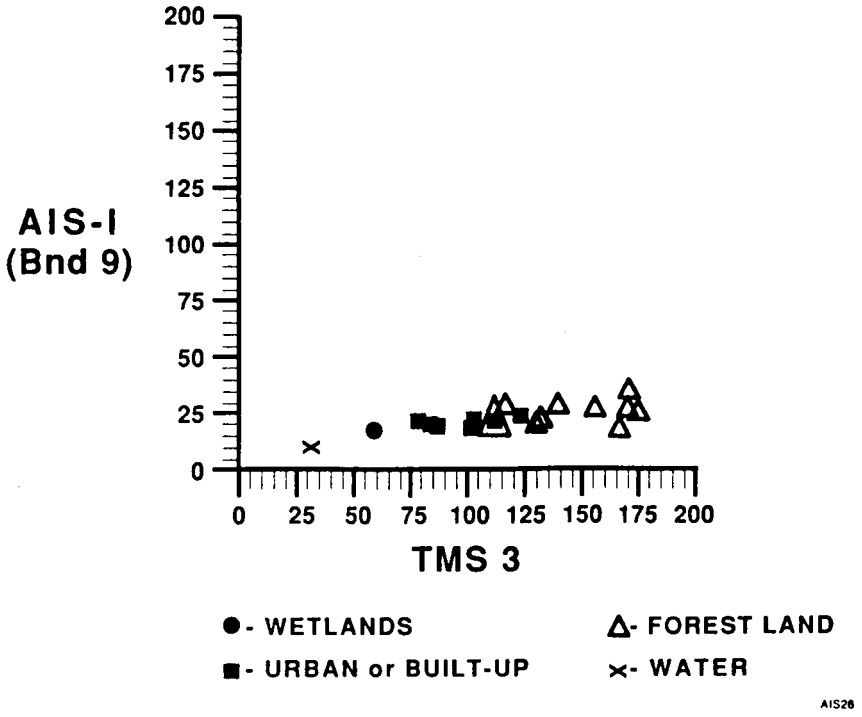

FIGURE 1. RESULTS FROM CLUSTERING ON THE REGISTERED AIRBORNE IMAGING SPECTROMETER-I - THEMATIC MAPPER SIMULATOR DIGITAL IMAGERY.

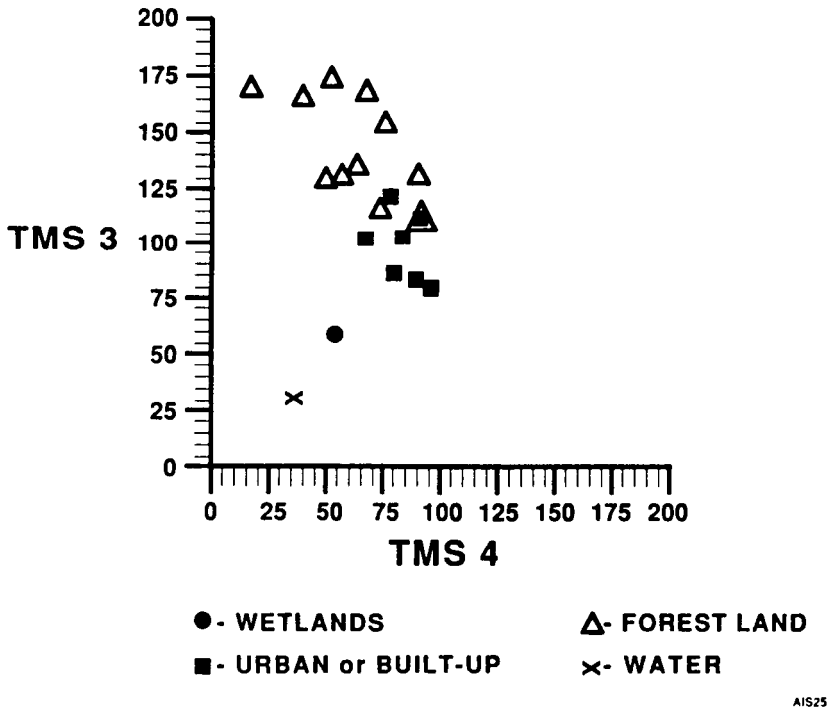

FIGURE 2. RESULTS FROM CLUSTERING ON THE REGISTERED AIRBORNE IMAGING SPECTROMETER-I - THEMATIC MAPPER SIMULATOR DIGITAL IMAGERY.

REFERENCES

Anderson, J. P., et al. 1976. A land Use and Land Cover Classification System for Use with Remote Sensor Data. Geological Survey Professional Paper 964.

Arnoff, S. 1982. "Classification Accuracy: A User Approach." Photogrammetric Engineering and Remote Sensing, Vol. 48, pp. 1299-1307.

Ginevan, M. E. 1979. "Testing Land Use Accuracy: Another Look." Photogrammetric Engineering and Remote Sensing, Vol. 45, pp. 1371-1377.

Jensen, J. R. 1986. Introductory Digital Image Processing. Englewood Cliffs, New Jersey: Prentice-Hall.

Lucas, C., J. Pearson, and A. Biache. 1986. "Potential Applications for the Large Format Camera Products." Technical Papers of the 1986 American Congress on Surveying and Mapping - American Society for Photogrammetry and Remote Sensing Annual Convention, 4th Volume, pp. 445-455.

Ustin, S. L., B. N. Rock, and R. A. Woodward. 1986. "Patterns of Vegetation in the Owens Valley, California." Proceedings of the Airborne Imaging Spectrometer (AIS) Data Analysis Workshop. JPL PUB 86-35, pp. 180-186.

Calibrating AIS Images Using the Surface as a Reference

M. O. Smith, D. A. Roberts, H. M. Shipman, J. B. Adams, S. C. Willis and A. R. Gillespie
University of Washington
Seattle, WA. 98195

ABSTRACT

We have tested a method of evaluating the initial assumptions and uncertainties of the physical connection between AIS image data and laboratory / field spectrometer data. To first order, the Tuscon AIS-2 image (flight #601) connects to laboratory reference spectra by an alignment to the image spectral endmembers through a system gain and offset for each band.

We have chosen to calibrate images to reflectance so as to transform the image into a measure that is independent of the solar radiant flux. This transformation also makes the image spectra directly comparable to data from laboratory and field spectrometers. Our objective in this paper is to test a method for calibrating AIS images using the surface as a reference. The surface heterogeneity is defined by laboratory / field spectral measurements.

We have developed an approach to calibration that maps the n-dimensional volume defined by image spectra into the n-dimensional volume defined by laboratory/ field reference spectra. The dimension of the volume is equivalent to the number of image bandpasses. We assume that to first order 1) the image spectra are linear mixtures of the laboratory or field reference spectra and 2) that there is a set of system gains and offsets for each band. However, it is not necessary that the image spectra be mixtures of the reference spectra; they could be pure endmembers themselves. The system gains and offsets include all contributions from the entire system (e.g., atmosphere, solar spectrum, instrument, lighting geometry, etc.) not solely those due to the instrument.

We tested these assumptions on an AIS-2 image (flight #601) obtained in September 1986 of the Tucson Mountains just west of Tucson, Arizonia. The instrument was flown in rock mode and included the wavelength range from 1200 nm to 2500 nm. We used only bandpasses where the signal to noise ratio was near 100 or better, which resulted in a reduction of the original 128 bands (rock mode) to 64 bands. Prior to analysis the image was destriped by adjusting gains for each column to equalize the column means.

Representative spectra of surface samples were measured on a Beckman DK-2A spectrometer. We term this set of spectra the reference endmembers, since they describe pure surface components (Figure 1). Other reference spectra could be modeled as linear mixtures of these spectra. In addition to these three spectra the reference endmembers also include the spectrum shade which has 0% reflectance. A precise definition of the endmember shade is given in Adams et al. 1986. These reference spectra are used to define the n-dimensional volume of all reference spectral measurements.

To complement the reference endmembers, we need to determine a set of image endmembers such that they define the n-dimensional volume of the image. The image volume is defined by single pixel image endmembers that, when linearly mixed,

adequately fit the image spectral variance and yield fractions between 0 and 1. The spectral image endmembers do not necessarily have any physical identity. For the 64 selected AIS-2 bands we found the linear mixtures of four image endmember spectra could model the fans south of the Desert Museum (Figure 2) to within 10 DN rms error. The rms error is computed as the difference between the measured image data and that predicted by a least square fit of mixtures of the four endmembers. Only random spatial patterns were present in the rms error image indicating the four image endmembers adaquately defined the image n-dimensional volume.

The connection between the image endmembers and laboratory reference endmembers is made using the following equation:

$$G_b \, DN_{iem,b} + O_b = \Sigma \, F_{em} \, R_{e,b} \qquad (1)$$

subject to the constraint : $\Sigma \, F_{em} = 1$

where $DN_{iem,b}$ is the digital number for each image endmember for each band, G_b the system gain to convert image digital numbers to total hemispherical reflectance for each band b, O_b the offset in reflectance for each band b, F_{em} the fractional contribution of each reference spectral endmember, and $R_{e,b}$ the total hemispherical reflectance for each reference spectral endmember for each band b. The summation in Equation 1 is over the number of relevant spectral endmembers. The equation is solved iteratively first for the gains and offsets and then for the fractions F_{em}.

Equation 1 formalizes our hypothesis that the primary connection between the imaged surface and laboratory reference spectra involves first an alignment of mixed pixels in the image to unmixed reference spectra, and secondly a calibration between image digital numbers and total hemispherical reflectance. The calibration model uses a simple linear equation consisting of a single gain and offset for each band. However, imbedded in the gains and offsets are more than the instrument calibration; in addition, there are effects caused by the solar spectrum, the atmosphere, and differences in lighting geometry between image and laboratory measurement systems. We are testing whether or not the entire system including the atmosphere, solar spectrum, and conversion of bidirectional to total hemispherical reflectance can, to first order, be approximated by a linear equation.

The solution consists of finding the fractions F_{em} that align the mixed pixel endmember spectra from the image to the unmixed reference endmembers. The results of the alignment (Table 1) are physically realizable, i.e., the image endmember set consists of fractions between 0 and 1 for each reference endmember spectrum, and each image endmember spectrum fits well to linear combinations of the reference spectra (rms errors are all < 0.3% reflectance). Table 1 now makes possible a physical identification of the image endmembers from the reference spectra. For example, em-1 is predominantly equivalent to an arkose spectrum (f=0.6 arkose), but unlike the reference spectrum of arkose, is mixed with vegetation, shade, and rhyolite. Similarly, each of the other image endmembers connect predominantly to an equivalent reference endmember spectrum.

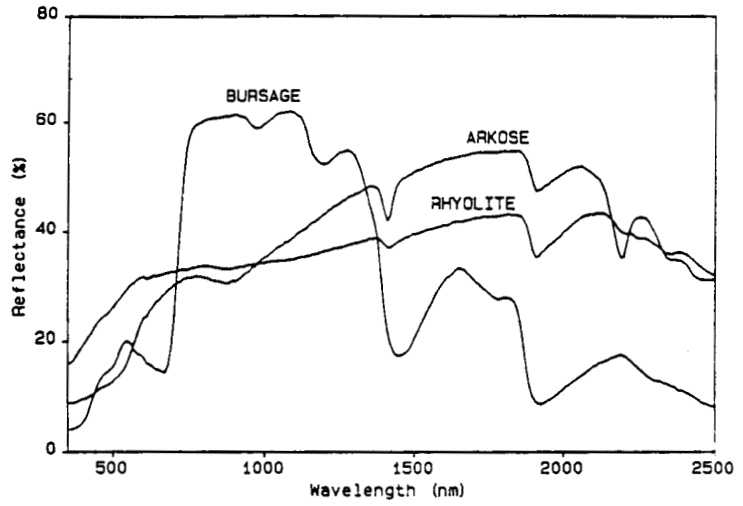

Figure 1. Total hemispherical reflectance of the field spectral endmembers. Measurements were made with a Beckman 2K-DA spectrometer.

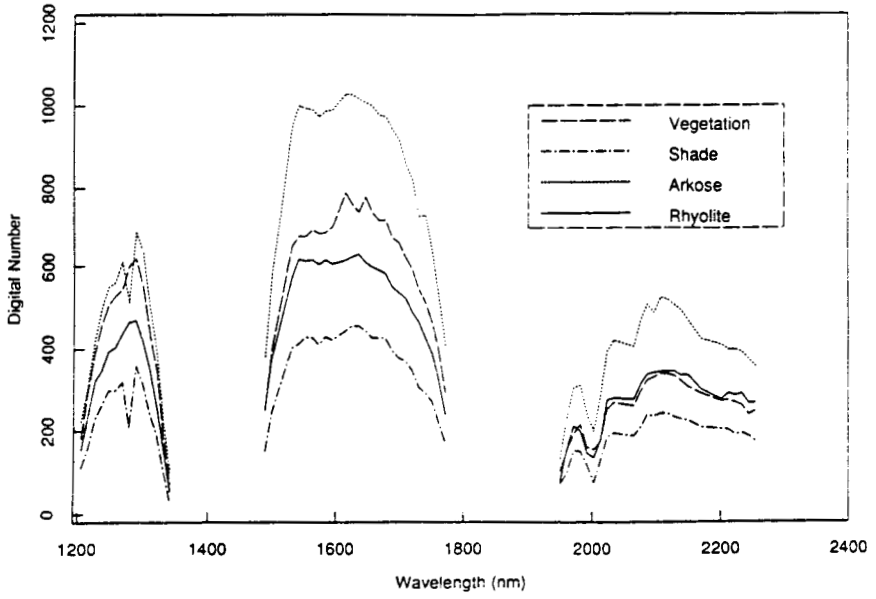

Figure 2. Raw digital numbers of the image spectral endmembers. Wavelengths shown were those with high signal to noise ratios used in our analysis. Note abscissas for Figures 1 and 2 are different.

Table I. Results of Image Endmember Alignment to Reference Spectra

	Fraction of Reference Endmember				
	arkose	rhyolite	bursage	shade	rms error
Image Endmember					
em-1	0.60	0.14	0.24	0.03	0.002
em-2	0.01	0.52	0.21	0.27	0.001
em-3	0.36	0.02	0.42	0.19	0.002
em-4	0.03	0.32	0.14	0.51	0.002

The gains and offsets from Equation 1 characterize the total system response to a linear calibration. The predominant pattern in the gain curves (Figure 3) is an inverted response to the water bands at 1400 and 1900 nm. In addition, the CO_2 absorption bands near 2000 nm are evident. These characteristics are resolved in the gains because they are constant for the entire image. Similarly, the offsets for most bands (Figure 4) typically were below 1% reflectance. However, many bands near 1200 nm have erratic scatter and high offsets. This type of pattern is indicative of faulty detector elements in the two-dimensional CCD array of the AIS-2 instrument.

To test the appropriateness of the reference endmembers with respect to the image endmembers, we determined the quality of fit (correlation) between each of the four image and reference endmembers for each band independently (Figure 5). The wavelengths between 1200 nm and 1300 nm exhibit some of the variability observed in the offsets (Figure 5) and gains (Figure 3). This does not fit the pattern of variation we observe in the reference endmembers (Figure 1). We interpret the almost random variation in corrlelations between 1200nm and 1300nm, and the significantly lower correlations at 1900 nm to be typical of that caused by the instrumentation.

In contrast, the systematic lack of fit near 2200 nm corresponds to the absorption feature of the arkose reference spectra (Figure 1). A plot of the image and reference endmembers for the 2200 nm wavelength (Figure 6) illustrates the deviation of the arkose from a linear calibration. We interpret this lack of fit at 2200 nm as a mismatch between the image and reference arkose endmember spectrum. What we have interpreted as an arkose for the image endmember has the general shape of the reference arkose spectrum, but lacks the 2200 nm absorption band. Even though the arkose reference spectrum does not fit the image data at 2200 nm we can use the other three reference endmembers to determine the gains and offsets in this wavelength region to maintain calibration integrity.

To determine if areas in the image contained the 2200 nm clay absorption band found in the arkose reference spectrum, we examined the difference images between that predicted by mixtures of the calibrated image endmembers and the raw image. Three of the difference images corresponding to the bands of the 2200 nm clay absorption contained distinct spatial patterns relating to the reference arkose spectrum. Distinct spatial patterns in the difference images provide a means of determining if subtle absorption features present in the surface mineralogy can be detected over that of the AIS-2 instrument noise. Further resolution of the 2200 nm

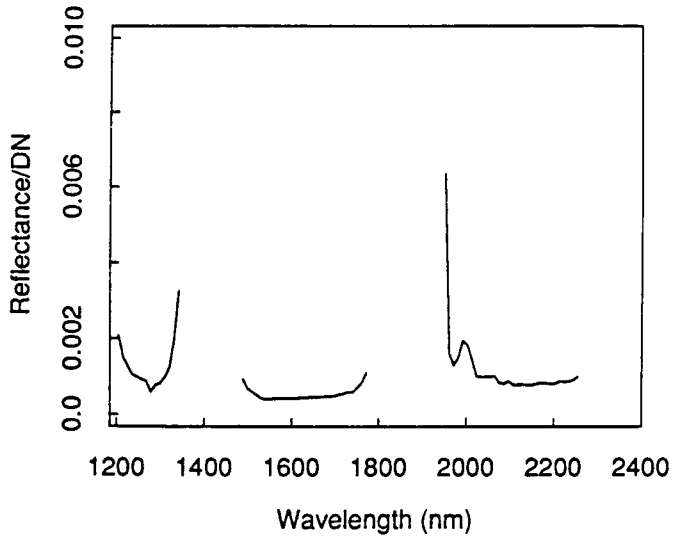

Figure 3. System gains (G_b) obtained by solving Equation 1.

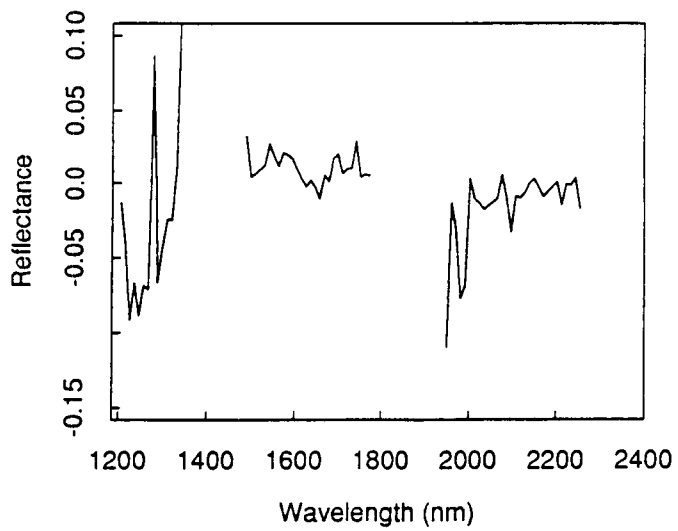

Figure 4. System offsets (O_b) obtained by solving Equation 1.

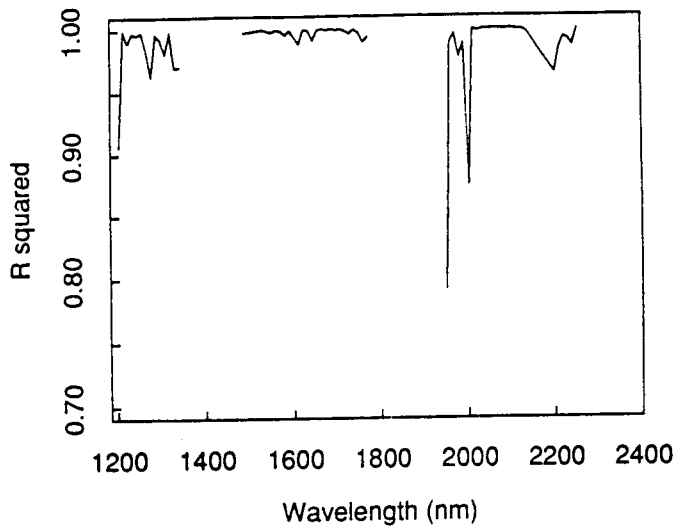

Figure 5. The fit (correlation) between each of the four image and reference endmembers for each band is computed independently.

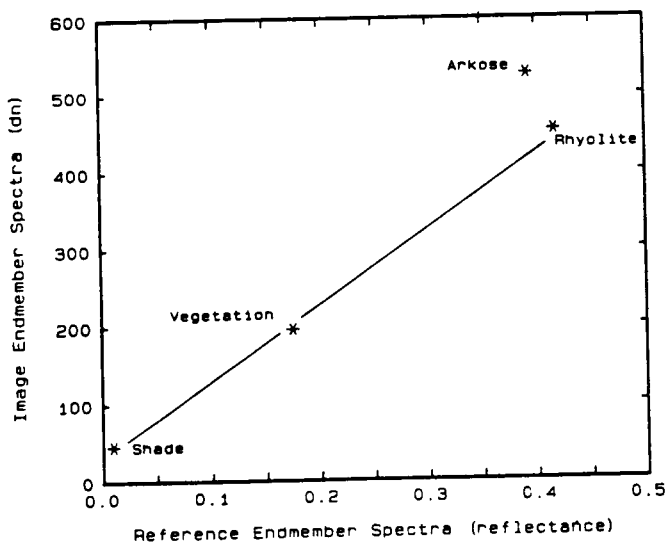

Figure 6. The departure of the reference arkose spectrum from that of the unmixed image arkose endmember spectrum is inferred from the deviation of the arkose endmember from a linear calibration from the other endmembers.

absorption feature can be accomplished by spectrally unmixing the background continium spectrum from that of the arkose (Shipman and Adams 1987).

In summary, we have found that the Tucson AIS-2 image is consistent with each of our initial hypotheses; 1) that the AIS-2 instrument calibration is nearly linear, 2)the spectral variance is caused primarily by sub-pixel mixtures of spectrally distinct materials and shade, and 3) that sub-pixel mixtures can be treated as linear mixtures of pure endmembers. In addition, we have found that the image can be characterized by relatively few spectral endmembers using the AIS-2 high resolution spectra. The resulting patterns in fractions, gains, offsets, and overall fit of Equation 1 to the data make possible the separation of surface effects from those of the instrument, atmosphere, and solar spectrum.

REFERENCES

Adams, J. B., M. O. Smith and P. E. Johnson. 1986. Spectral mixture modeling: A new analysis of rock and soil types at the Viking Lander I Site, J. Geophys. Res. 91, 8098-8112.

Shipman H. M., and J. B. Adams, Detectability of mineral on desert alluvial fans using reflectance spectra, J. Geophys. Res., in press 1987.

THE USE OF AIRBORNE IMAGING SPECTROMETER DATA TO DETERMINE EXPERIMENTALLY INDUCED VARIATION IN CONIFEROUS CANOPY CHEMISTRY

NANCY A. SWANBERG, TGS Technology, Inc. NASA/Ames Research Center, Moffett Field, California 94035; PAMELA A. MATSON, NASA/Ames Research Center, Moffett Field, California 94035

ABSTRACT

A study is underway to determine whether experimentally induced differences in forest canopy chemical composition can be detected using data from the Airborne Imaging Spectrometer (AIS). Treatments have been applied to an even-aged forest of Douglas-fir trees near Mt. Taylor, New Mexico.

Work to date has stressed wet chemical analysis of foliage samples and correction of AIS data. Plot treatments have been successful in providing a range of foliar nitrogen concentrations. Much time was spent investigating and correcting problems with the raw AIS data. Initial problems with groups of drop out lines in the AIS data were traced to the tape recorder and the tape drive. Custom adjustment of the tape drive led to recovery of most missing lines. Remaining individual drop out lines were replaced using averages of adjacent lines. Application of a notch filter to the Fourier transform of the image in each band satisfactorily removed vertical striping. The aspect ratio was corrected by resampling the image in the line direction using nearest neighbor interpolation. Future work will include examination of first and second difference AIS spectra from study plots at bands known to contain information about a given foliar constituent and exploration of multiple stepwise linear regression techniques for determining spectral bands correlated to foliar chemical composition. Acquisition of AIS or Airborne Visible and Infrared Imaging Spectrometer (AVIRIS) data prior to bud break and during the growing season has been requested for 1987.

INTRODUCTION

Biochemical composition of forest canopies is related to biogeochemical cycling in forest ecosystems. It has been suggested that fertile forest ecosystems which cycle large amounts of elements have greater potential for element losses to the atmospheric and hydrologic systems, while infertile systems with low nutrient turnover have low losses (Matson and Vitousek, submitted). One objective of this research is to correlate foliar biochemical ratios with nitrogen turnover rates and nitrous oxide evolution in forests with varying fertility. A second objective, which is the subject of this paper, is to determine whether experimentally induced differences in forest canopy nutrient and biochemical composition can be detected using data from the Airborne Imaging Spectrometer (AIS).

STUDY SITE

The study site is in a Douglas-fir forest near Mt. Taylor, New Mexico and was established by collaborators in the School of Forest Resources at Northern Arizona State University. Treatments include replicated control, fertilized, irrigated and saw dust-treated 25m x 25m plots. Monthly fresh foliage samples have been collected and are being analyzed for nitrogen, phosphorus, amino acids, lignin, starch, cellulose, and proteins. Preliminary wet chemical analysis indicates that foliage from fertilized plots exhibits markedly higher concentrations of nitrogen than those from other treatments. Ratios of amino acids:total nitrogen and concentrations of starch also differ among treatments and across seasons.

Table 1.0 shows N concentration in mg/g for eight of the study plots. Allometric equations for Douglas-fir at this site are being prepared at Northern Arizona State. These equations should provide reliable estimates of foliage mass. Nitrogen concentration will be multiplied by the foliage mass to obtain the total nitrogen content for each plot. Preliminary calculations done using allometric equations for Douglas-fir in Washington indicate that the nitrogen content of the plots ranges between 100.8 kg/ha and 205 kg/ha.

Table 1.0 Foliar nitrogen concentration of one and two year needles

SITE	TREATMENT	TOTAL N mg/g
C1	CONTROL	8.52
C2	CONTROL	9.09
I1	IRRIGATED	8.62
I2	IRRIGATED	9.52
S1	SAWDUST	10.02
S2	SAWDUST	10.22
N1	NITROGEN	14.08
N2	NITROGEN	14.54

REMOTE SENSING

Data collection

AIS-2 data at spatial resolutions of approximately 7m and 10m were acquired with the NASA C-130 aircraft over the study site on September 18-19, 1986. These data were obtained both in Tree mode with a useable range of 800-1600nm and in Rock mode with a useable range of 1600-2400nm. NS-001 Thematic Mapper simulator data, color infrared and natural color photography were also obtained.

Processing and Corrections

Upon initial inspection of the data large groups of drop-out lines were observed. This problem was reported to the NASA Ames Data Management facility. They had their tape drive adjusted specifically to read the high density tape containing the data of interest and were eventually able to recover most of the groups of lines that had been missing after the initial decommutation. (In a subsequent mission for these investigators at another site, a newer one inch on-board tape recorder was used to record the AIS data and a newer tape drive was used to decommutate the data, eliminating the problem.)

Examination of the newly decommutated data revealed individual drop out lines. Each pixel in these lines was replaced by the average of the corresponding pixels in the two adjacent lines. Vertical striping, striping in the along-track direction, was also observed. It was removed by applying a notch filter to the Fourier transform of the image in each band as described by Hlavka (1986).

Even after the lines were replaced and the image was destriped, it was difficult to locate the study site. The scene appeared blurry. After consultation with the NASA Ames Data Management Facility and the Jet Propulsion

Laboratory it was discovered that the image aspect ratio was incorrect due to "overscanning". The AIS had imaged the same ground area more than once, giving it a blurry appearance. The amount of "overscanning" was calculated using the following equation(1).

$$\text{number of times over-scanned} = \frac{\text{Aircraft altitude in ft. x AIS instantaneous field of view in radians}}{\text{Aircraft speed in ft/sec x integration time of the AIS sensors in sec.}} \quad (1)$$

The result of this calculation was used to determine the scale to which to resample the image in the line direction using nearest neighbor interpolation. Resampling corrected the aspect ratio and produced a sharp image from which to locate study sites.

FUTURE WORK

Much time was spent investigating and correcting problems with the raw AIS data. Now that the image is in a useable form, study plots will be located in the images and an average DN value will be extracted from a 3 x 3 pixel window in each band for each plot. These values will be used to create a spectrum for each plot. First and second difference transformations (the first order approximation of the first and second derivative) will be performed. These spectra will be examined at bands that the literature and previous studies indicate contain information about a given leaf constituent. Multiple stepwise linear regression techniques as described in Swanberg and Peterson (1987) and Wessman et al. (1987) will be explored as a possible means to identify spectral bands that are correlated to foliar chemical content.

AIS-2 data examined here were acquired in September. Since foliar chemical composition changes throughout the growing season, we have requested acquisition of AIS-2 or Airborne Visible and Infrared Imaging Spectrometer (AVIRIS) data before bud break as well as during the height of the growing season this year. We hope to observe spectral changes related to change in foliar chemical composition.

CONCLUSIONS

We have found that the experimental treatments applied to Douglas-fir forest have successfully changed foliar element content and biochemical concentrations. These treatments have provided a controlled test site with which we can examine AIS capabilities for determining canopy chemistry. Initial problems with AIS-2 data were with missing lines, vertical striping,

and the aspect ratio. These problems have been corrected and future work will include examination of first and second difference AIS spectra from study plots at bands known to contain information about a given foliar constituent and exploration of multiple stepwise linear regression techniques for determining spectral bands correlated to foliar chemical composition. Acquisition of AIS or AVIRIS data prior to bud break and during the growing season has been requested for 1987.

ACKNOWLEDGEMENTS

We thank C. Berger for her chemical analysis; C. Grier, T. Gower, and K. Elliot for their work in setting up the treatment plots and for collecting the foliage samples; and D. Peterson for assistance in planning and analysis. We are grateful for efforts of J. Myers and C. Mahoney for decommutating the AIS data and for examining the aspect ratio problems. We thank the NASA/Ames Research Center C-130 crew and the Jet Propulsion Laboratory AIS team for their superb cooperation and performance in the collection of this AIS data.

Funding for this study was provided through the Biospherics Research Program in the Life Science Division at NASA Headquarters.

REFERENCES

Hlavka, C. 1986. Destriping AIS data using Fourier filtering techniques. In Proc. 2nd AIS data Analysis Workshop, ed. G. Vane and A.F.H. Goetz. (Pasadena, CA: Jet Propulsion Laboratory). JPL Publ. 86-35. pp. 74-79.

Matson, P.A and P.M. Vitousek. Cross system comparison of soil nitrogen transforms and nitrous oxide flux in tropical forest ecosystems. Global Biogeochemical Cycles (submitted, 1987).

Swanberg, N.A. and Peterson, D.L. 1987. Using the Airborne Imaging Spectrometer to determine nitrogen content in coniferous forest canopies. Proc. IGARSS '87 Symp., Ann Arbor. MI. Inst. Electrical and Electronics Engineers 87 CH2434-9. p. 981.

Wessmann, C.A., Aber, J.D. and Peterson, D.L. 1987. Estimating key forest ecosystem parameters through remote sensing. Proc. IGARSS '87 Symp., Ann Arbor, MI. Inst. Electrical and Electronics Engineers 87 CH2434-9. pp. 1189-1193.

OVERVIEW OF AUSTRIAN AIRBORNE IMAGING SPECTROMETER (AIS) PROGRAMME AND FIRST RESULTS

C. BANNINGER, Institute for Image Processing and Computer Graphics, Research Centre Joanneum, Graz, Austria.

ABSTRACT

AIS data collected from eight test areas in Austria during the summer of 1986 are currently being evaluated for their usefulness in forest damage assessment, geobotany, alpine vegetation mapping, and land-use classification. Difficulties encountered in installing the SPAM spectral analysis software for use on our image display system and the necessity to adapt existing in-house programs for this task have impeded and delayed the analysis of the AIS data. Spectral reflectance curves obtained from a geobotanical test site show a marked increase in reflectance across most of the measured spectrum for metal-stressed spruce trees compared with non-stressed spruce trees.

INTRODUCTION

The deployment of the NASA C-130 research aircraft to Europe during the spring and summer of 1986 gave Austria the opportunity to acquire high spatial and spectral resolution data from several test areas in the eastern Alps for use in vegetation mapping and stress detection and urban and rural land-use classification. During a one week period in July, C-130 overflights of Austria collected airborne imaging spectrometer (AIS), Thematic Mapper Simulator (NS001), and Thermal Infrared Multispectral Scanner (TIMS) data from eight test sites situated in the Austrian provinces of Styria, Carinthia, and Upper Austria. Unsettled weather, cloud build up in the mountains, and heavy haze - common conditions at this time of the year in the Alps - necessitated overflights well before the preferred mid-day time period to minimise their effects on the data collection. The earlier than planned flights did, however, result in an increase in the amount of shadow in the data.

TEST SITE DESCRIPTIONS

All test sites flown as part of the Austrian AIS programme have as their principal objective the mapping of vegetation as to type, species, or condition. Five of the eight test sites are concerned with forest damage associated with air pollutants emitted by chemical, refining, pulp, and coal—burning plants or tree stress related to the presence of heavy metals in the underlying soil. The remaining three test sites pertain to alpine vegetation and soil mapping and

land-use classification of an urban-rural setting. FIGURE 1 shows the location of the test sites and TABLE 1 gives a brief description of their main vegetation cover or land type and the nature of their research work.

SENSOR SYSTEM CHARACTERISTICS

TABLE 2 lists the pertinent information on the AIS-2, NS001, and TIMS sensor systems. AIS-2 differs principally from AIS-1 in comprising a 64 by 64 detector element array (thereby doubling the swath width obtainable with AIS-1), a

TABLE 1 DESCRIPTION OF AUSTRIAN AIS TEST SITES

Test Site	Location	Description	Study Purpose
Burghausen	Upper Austria	Spruce (pine-larch-beech) forest	Assessment of tree damage related to chemical plant emissions.
Ranshofen	Upper Austria	Spruce (pine-larch-beech) forest	Assessment of tree damage related to aluminium plant emissions (fluorine)
Frohnleiten	Styria	Spruce (pine-fir-beech) and spruce-broad-leaved (fir) forests	Geobotany - heavy metal (Cu-Pb-Zn) stress
Koralpe	Carinthia	Spruce (pine-fir-larch-beech) forest	Assessment of tree damage related to pulp mill and coal-burning power plant emissions (SO2)
Klagenfurt	Carinthia	City-urban-rural setting	Land use classification
Hochobir	Carinthia	Spruce-Larch (fir-beech) forest	Geobotany - heavy metal (Pb-Zn) stress
Hochtor	Carinthia	High alpine terrain	Alpine vegetation and soil mapping
Gross-glockner	Carinthia	High alpine terrain	Alpine vegetation and soil mapping

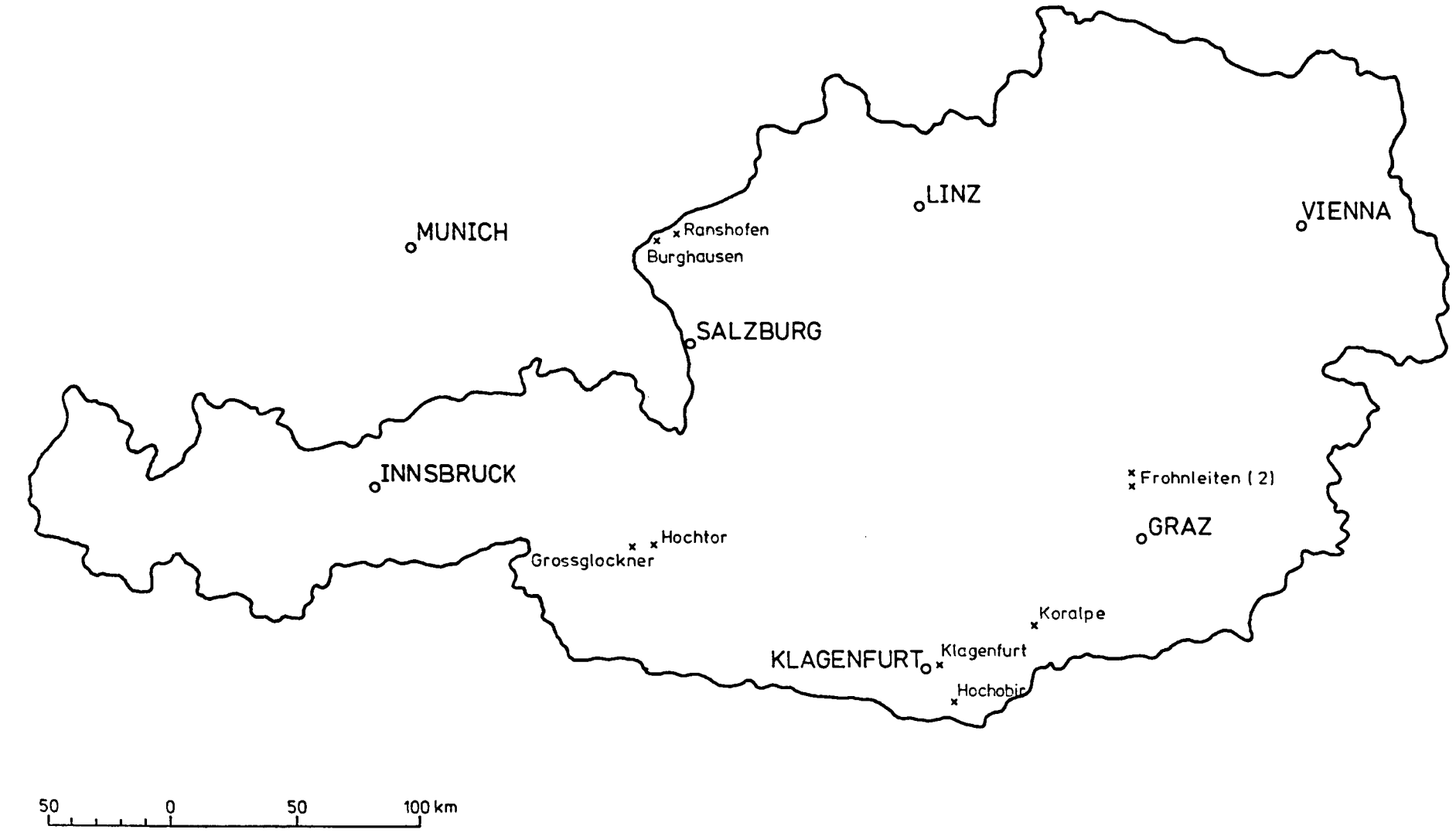

FIGURE 1. AUSTRIAN AIS TEST SITES

TABLE 2 Airborne Imaging Sepctrometer (AIS), Thematic Mapper Simulator (NS001), and Thermal Infrared Multispectral Scanner (TIMS) Sensor Characteristics

Sensor	Bands	Bandwidths (microns)	Comments
AIS-2	128 (contiguous)	Interval: 10.5 m Range: 0.78 - 2.53 Tree mode: 0.78 - 2.14 Rock mode: 1.19 - 2.53	64 x 64 detector element array swath: 512 m* pixel size: 8 m*
NS001	8 (discrete)	0.46 - 0.52 0.53 - 0.60 0.63 - 0.70 0.77 - 0.91 1.13 - 1.35 1.57 - 1.71 2.10 - 2.38 10.90 - 12.30	FOV: 5 km* IFOV: 10 m*
TIMS	6 (contiguous)	8.2 - 8.6 8.6 - 9.0 9.0 - 9.4 9.4 - 10.2 10.2 - 11.2 11.2 - 12.2	FOV: 4.6 km* IFOV: 10.0 m*

* 4000 m flying height above ground level.

set of blocking filters that reduces the problem of wavelength contamination caused by second order light, and the use of all 12 bits of the recorded data to increase the dynamic range of the detectors. The need to change the foreoptics of AIS-2 to accommodate the doubling of the sensor field of view (FOV) did result in a degradation of the instantaneous field of view (IFOV) and, more importantly, an approximate 1.8 reduction in the effective versus the nominal spatial resolution of the pixels.

DATA ACQUISITION

All sensor systems appeared to function normally during the data acquisition flights, except for jamming problems related to the Nikon 35 mm camera. AIS, NS001, and TIMS data and colour and colour-infrared photography were collected over each test site, with AIS data obtained in both the tree and rock modes for the Burghausen, Ranshofen, Frohnleiten, and Hochobir test sites, but only in the tree mode for the Koralpe and Klagenfurt sites and in the rock mode for the Hochtor and Grossglockner sites.

TABLE 3 AIS Test Site Data Acquisition Information

Test Site	Flight Date	Flight Time (Solar Time)	Atmospheric Conditions	AIS-2 Scan Modes	Nominal Pixel Spatial Resolution (metres)	
					Ground	Effective
Burghausen	16.07	12.00-12.15	Hazy	Tree Rock	6	11
Ranshofen	16.07	12.15-12.30	Hazy	Tree Rock	6	11
Frohnleiten	17.07	8.45-9.45	Hazy	Tree Rock	6/10	11/18
Koralpe	17.07	10.00	Wispy Clouds	Tree	10	18
Klagenfurt	17.07	10.30	Hazy	Tree	11	20
Hochtor	21.07	8.30	Clear-Cloudy	Rock	10.5	19
Hochobir	21.07	9.00-9.30	Heavy Clouds	Tree Rock	10-11	18-20
Grossglockner	21.07	10.00	Clear-Cloudy	Rock	10	18

Flying heights above the test sites resulted in nominal ground pixel sizes of between 6 and 11 metres, although the effective spatial resolution of the pixels is between 11 and 20 metres, due to the degradation of the optics.

Where possible, highways or water bodies are contained within each flight line to permit calibration of the response of each detector, using the flat-field correction method.

Data from the first priority test sites (Burghausen, Ranshofen, and Frohnleiten) are cloud free (although with considerable haze), while data from the remaining test sites vary from being hazy to heavily contaminated by clouds. The occurrence of storms and late morning cloud build up in the Alps during the time of the Austria overflights necessitated data acquisition times much earlier than the preferred mid-day period, thereby increasing the shadow component in the data - especially in the mountainous regions.

TABLE 3 summarises the principal data acquisition information from the eight test sites.

DATA ANALYSIS

Only a limited amount of analysis has been performed on the AIS data from the Austrian test sites, and this has been mainly confined to examining the quality of the data on our display system and obtaining spectral reflectance curves from some of the test sites, using raw, uncorrected data. We have not been able to install the SPAM spectral analysis software to operate on our system, because of software-display interface incompatibility. This means that either an extensive amount of program rewriting has to be done or existing in-house image processing programs need to be modified to operate on AIS data. Both approaches are a time consuming and costly affair, and a decision is still pending on the third option of purchasing an image processing system that is compatible with the TAE/VICAR2 (which SPAM is one component) software. The third option is presently the favoured approach, with select in-house image processing and analysis programs being modified to handle AIS data as an interim measure until a new image processing system is available.

Modification of some of our in-house image processing programs has allowed us to produce spectral reflectance curves from a number of the test sites and to do a preliminary visual analysis of the data. FIGURES 2 and 3 show the spectral plots from one of the Frohnleiten geobotanical test sites, where an almost pure Norway spruce forest is growing in soils containing high concentrations of copper, lead, and zinc. The spectral curves represent 2 by 2 pixel areas from stressed and non-stressed parts of the forest, and clearly show an increase in reflectance across most of the measured spectrum for the stressed compared with the non-stressed trees. This is in agreement with the expected response of stressed vegetation in the inter-water absorption region between approximately 1500 nm and 1800 nm, but is less in agreement for the near-infrared plateau region between 800 nm and 1350 nm. Similar results are obtained using 3 by 3 and 5 by 5 pixel windows. Differences in curve shape and slope can also be seen between the two spectra, but as only raw, noisy data have been used so far in the analysis, no attempt has been made to analyse these features, other than to note their presence for a closer examination when corrected data are available.

ACKNOWLEDGMENTS

Special thanks are extended to Dipl.-Ing. V. Kaufmann for making the necessary modifications to our image processing programs to permit the extraction of spectral reflectance curves from the AIS data.

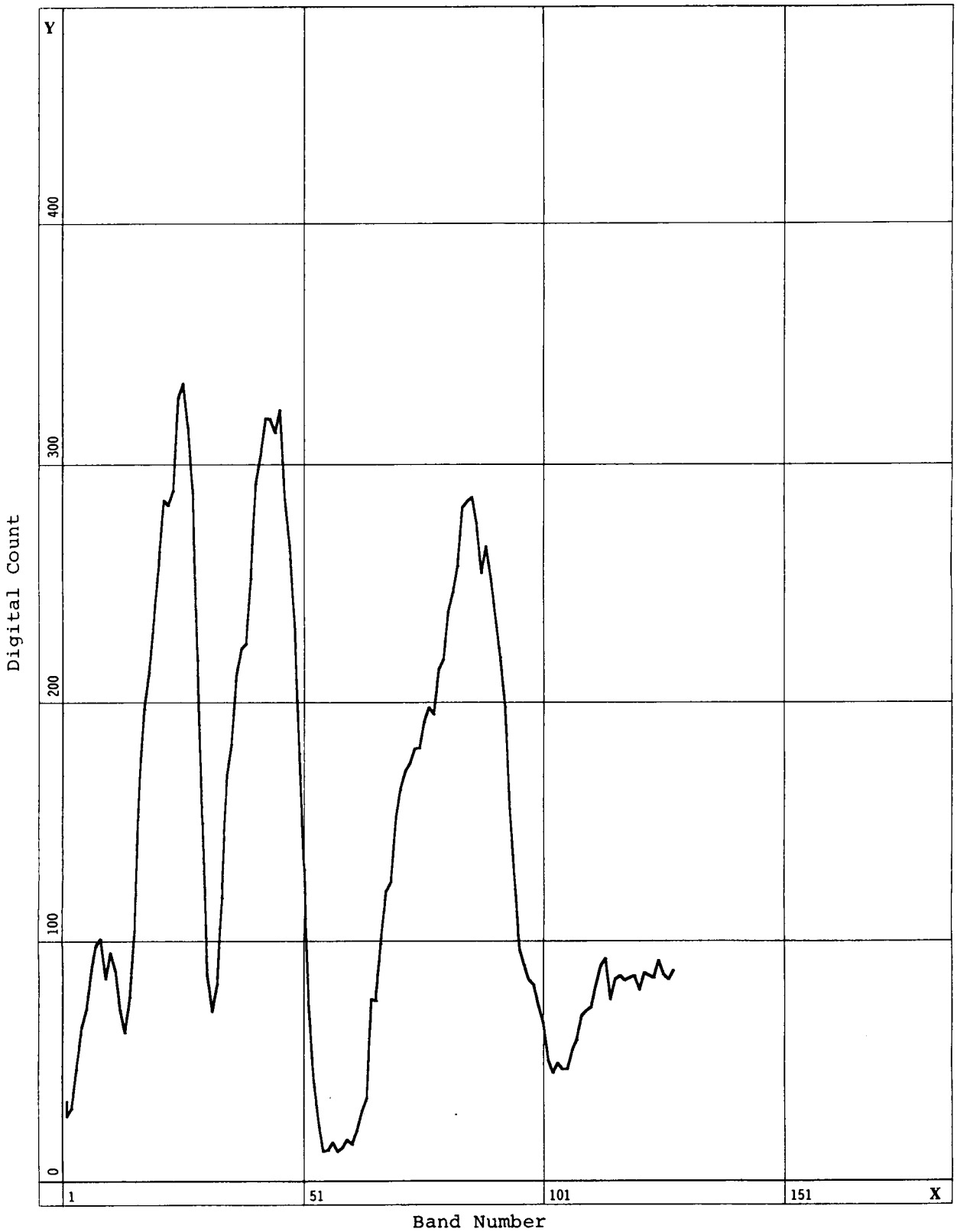

FIGURE 2. Non-Stressed Spruce Forest (Frohnleiten Test Site)

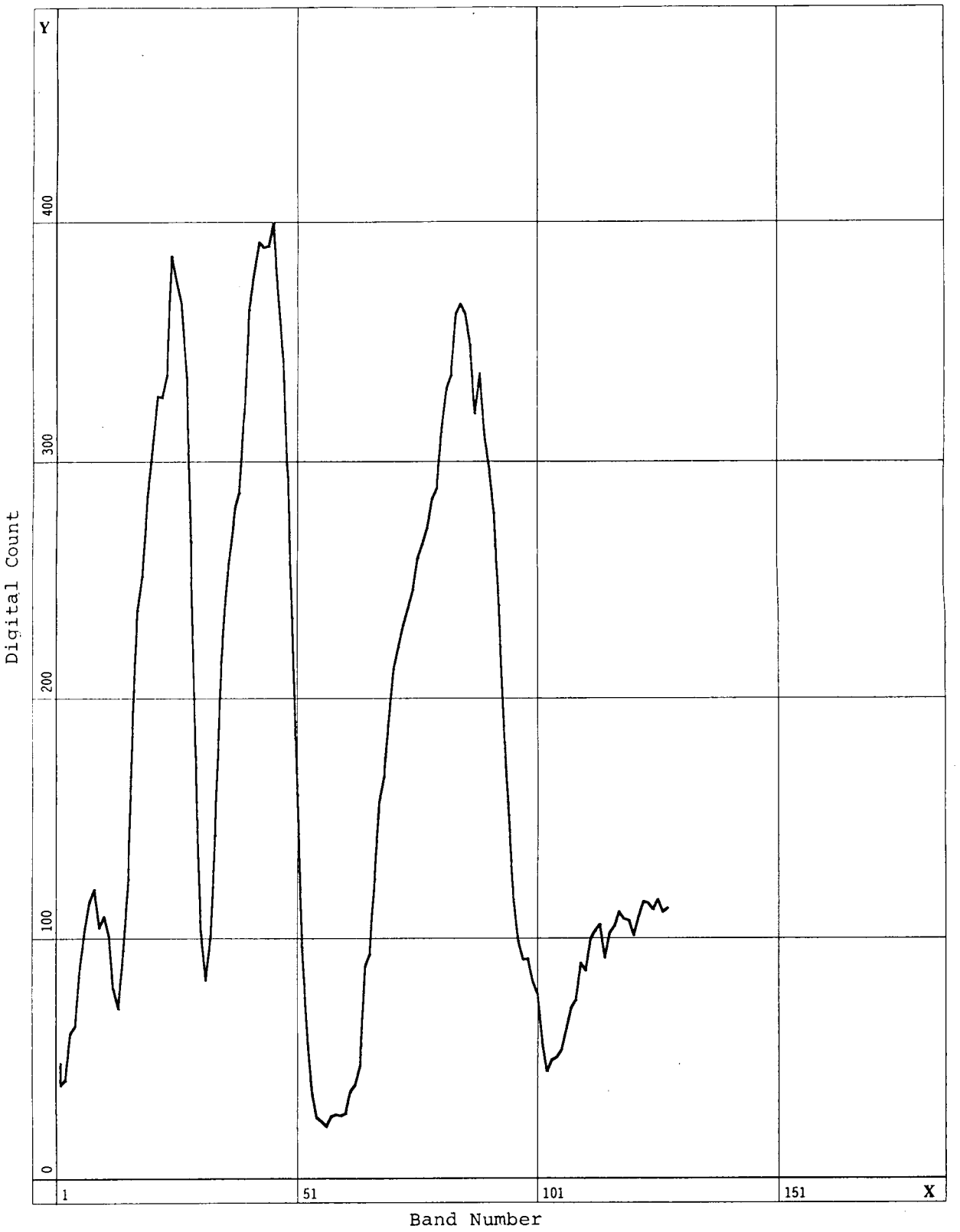

FIGURE 3. Stressed Spruce Forest (Frohnleiten Test Site)

AIS-2 SPECTRA OF CALIFORNIA WETLAND VEGETATION

MICHAEL F. GROSS, College of Marine Studies, University of Delaware, Newark, DE 19716, USA; SUSAN L. USTIN, Department of Botany, University of California, Davis, CA 95616, and Space Sciences Laboratory, University of California, Berkeley, CA 94720, USA; VYTAUTAS KLEMAS, College of Marine Studies, University of Delaware, Newark, DE 19716, USA.

ABSTRACT

Spectral data gathered by AIS-2 from wetlands in the San Francisco and Suisun Bays, California, on 11 September 1986 were analyzed. Spectra representing stands of green Salicornia virginica, green Sesuvium verrucosum, senescing Distichlis spicata, a mixture of senescing Scirpus acutus and Scirpus californicus, senescing Scirpus paludosus, senescent S. paludosus, mowed senescent S. paludosus, and soil were isolated. No difference among narrow-band spectral reflectance of the cover types was apparent between 0.8-1.6μm. There were, however, broad-band differences in brightness. These differences were sufficient to permit a fairly accurate decomposition of the image into its major cover type components using a procedure that assumes an additive linear mixture of surface spectra.

INTRODUCTION

The primary objective of our study is to compare AIS spectra of various wetland vegetation types. Ultimately, we hope to use imaging spectrometer data to identify vegetation types and their status (e.g. green, senescing, stressed). Gross and Klemas (1985, 1986) reported differences in the AIS-1 spectral response of Delaware wetland vegetation types, enabling them to be distinguished. Most of the spectral differences occurred between 1.4-1.9μm, and may have been influenced by second order overlap (Vane 1986). To continue these investigations, we analyzed AIS-2 data collected over intertidal wetlands in the Suisun and San Francisco Bays of California. The vegetation in the California marshes exhibited greater spatial and community heterogeneity than that in the Delaware marshes.

DATA ACQUISITION AND ANALYSIS

Three flightlines of AIS-2 data were acquired in Tree Mode (0.8-2.2μm, with the useful region [i.e. no second order overlap effects] approximately 0.8-1.6μm) on 11 September 1986 at about 21:00 GMT: one over salt marshes in the southern part of San Francisco Bay, and two covering the brackish Suisun Marsh in Suisun Bay. Within a few days preceding and following the date of flight, spectra of various wetland soils and of green, senescing, and senescent (dead) wetland vegetation species were obtained from field samples using a VIRIS (Visible/Infrared Intelligent Spectroradiometer). One to four samples of each cover type were obtained. In addition, accessible regions of the marsh were visited by car and on foot, permitting mapping of the various cover types and observations of site characteristics. Four days after the flight, photo-

graphs of the flightline areas were taken from a low-altitude aircraft and used to identify surface cover.

The AIS data were analyzed at the Space Sciences Laboratory of the University of California (Berkeley) using SPAM (Spectral Analysis Manager) software developed by the Jet Propulsion Laboratory. No radiometric calibration had been applied to the data by JPL. Observation of the raw data revealed substantial vertical striping and geometric distortions resulting from aircraft movements. Horizontal striping was not evident. We chose to analyze a portion of the flightline encompassing parts of Joice and Grizzly Islands in the Suisun Marsh (Fig. 1). This area was selected because it had been extensively groundtruthed and contained the majority of marsh cover types. The leveed wetlands in the study region are managed to optimize waterfowl habitat, such that tidal flooding and salinity are controlled, thus causing vegetation distribution and condition to differ between ponds. At the time of AIS data collection, dry summer weather and lack of tidal flooding had resulted in the senescence of much of the marsh vegetation.

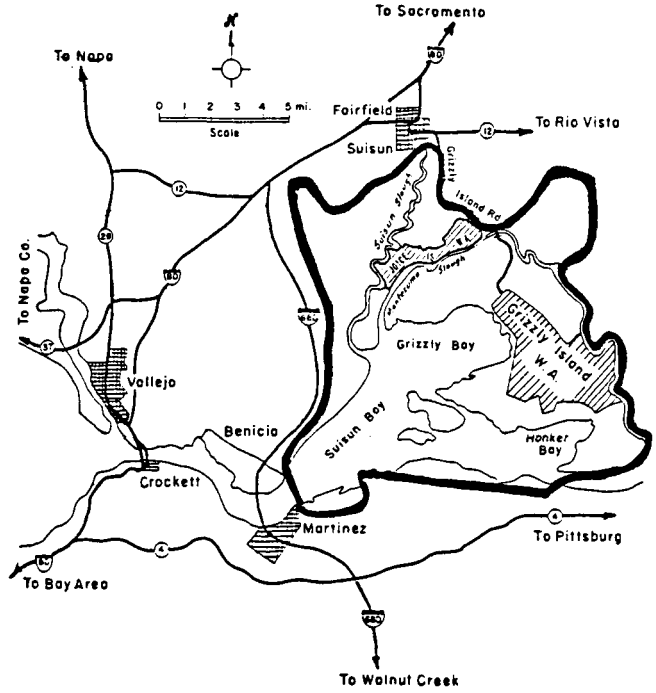

Fig. 1. Location of Suisun Marsh (area within thick solid line).

The area of interest was divided into two 512-line segments and one 400-line segment for analysis. One of the 512-line segments was free of large water bodies, but the other two contained significant portions of large, vertically oriented sloughs filled with water. Analysis of the raw data demonstrated that the vertical striping was too severe to permit a meaningful extraction of information. To destripe the image, a program that computes the mean data value for an entire scene in each spectral band and then adjusts the column mean in each band to match the corresponding scene mean value was employed. This program assumes that, over the entire length of the image segment, the mean brightness value is the

same for each of the 64 columns of data. This technique was effective only on the segment free of major vertical water features; we thus chose to concentrate our analysis on this part of the data. Wavebands beyond 1.58μm (bands 73-128) were avoided to minimize second order overlap effects.

RESULTS

Destriping the AIS data resulted in a significant improvement in the visual appearance of the data (Figs. 2 and 3) and in a substantial reduction in the noise of plotted spectra. To derive spectra of various cover types in the image, the mean spectrum of 2x2 to 5x5 pixel samples (n = 3-14) of distinct vegetation types or soil was computed and considered to represent the spectral response of the cover type. The eight distinct cover types identified were green Salicornia virginica (pickleweed), green Sesuvium verrucosum (purslane), senescing Distichlis spicata (saltgrass), senescing Scirpus acutus and Scirpus californicus (tules), senescing Scirpus paludosus (alkali bulrush), senescent S. paludosus, mowed senescent S. paludosus, and dry soil. A mean spectrum for the entire image was then approximated by computing the mean spectrum of seven evenly-spaced 10x64 segments from the image. These nine spectra were stored in a library.

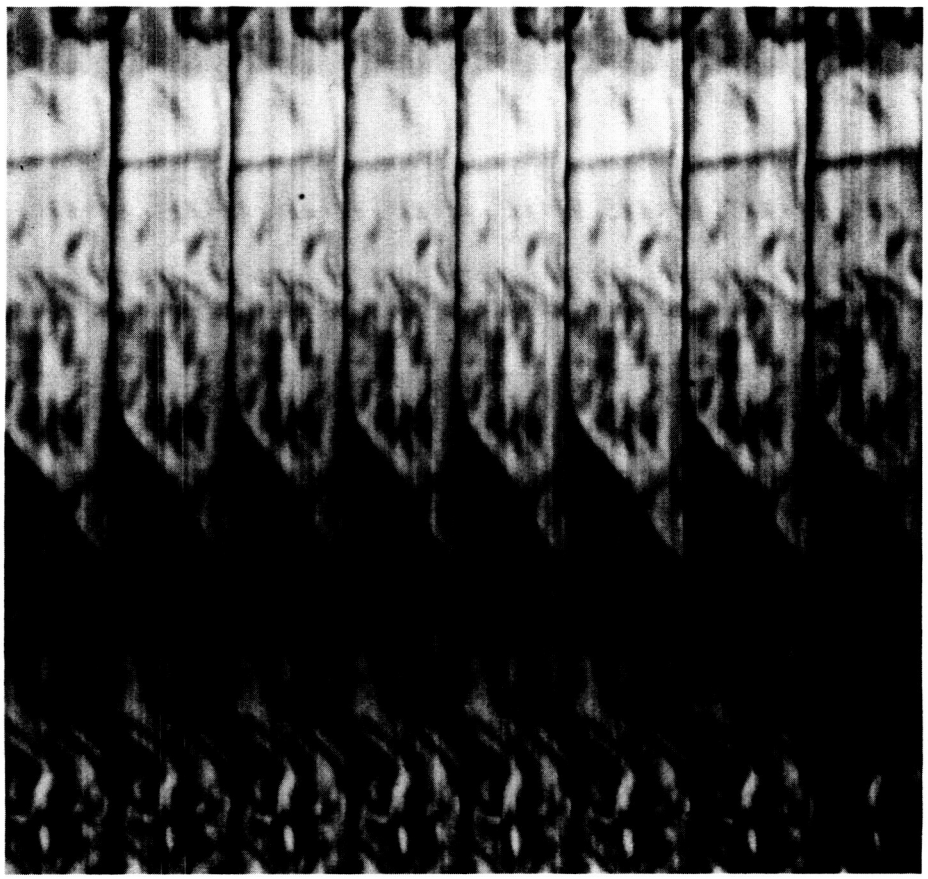

Fig. 2. Raw AIS-2 data, 1.27-1.35μm.

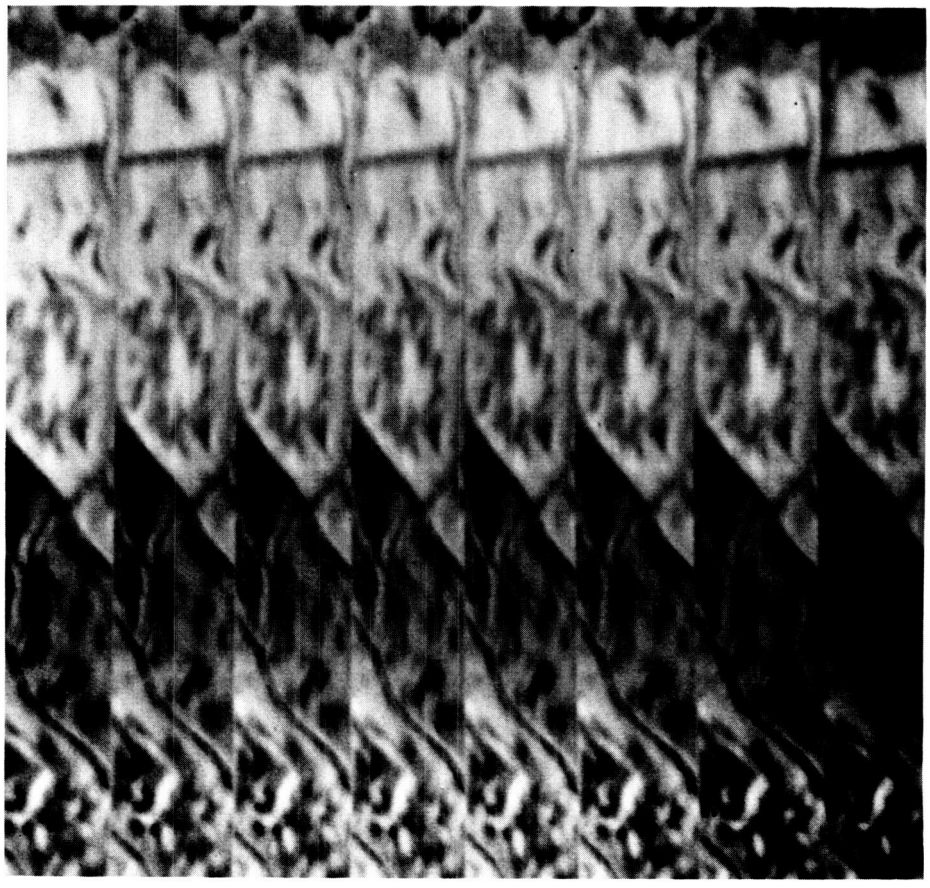

Fig. 3. Vertically destriped AIS-2 data, 1.27-1.35μm.

Spectra were displayed in both normalization modes (area and amplitude). Spectra were compared within four groups of wavebands separated by atmospheric absorption features: 0.80-97μm, 0.97-1.15μm, 1.15-1.44μm, and 1.44-1.58μm (Table 1). Figure 4 shows spectra from the cover types between 1.15-1.44μm, displayed in amplitude normalization mode. No narrow spectral band reflectance features were evident within any waveband segment; only broad-band differences in brightness were apparent.

The VIRIS data were also displayed in normalized amplitude mode, and the spectra were visually compared amongst themselves and with AIS spectra. Similar cover types exhibited generally similar VIRIS spectra. There were some broad-band differences in brightness between species, and may have been some narrow-band differences. However, the number of replicates (n = 1-5) was too small, the field of view of the instrument ($\approx 1 cm^2$) insufficient, and the level of noise (resulting from wind, variable irradiance conditions, and the instrument) too high, to ascertain whether such narrow-band differences were real.

To determine whether the observed AIS brightness differences were sufficient to permit discrimination of cover types, we ran the CLUSTER (unsupervised classification) program, with and without the "manual" option, several times using different noise and cluster thresholds. Although the algorithm did create several classes, their distribution

did not correspond closely to that of the cover types and appeared to be largely random. In addition, some classes were composed of vertical stripes resulting from unequal detector response.

Table 1. Relative brightness of eight wetland cover types, displayed in amplitude normalization and area normalization modes.

Cover Type	Display Mode	.80-.97μm	.97-1.15μm	1.15-1.44μm	1.44-1.58μm
Green *Salicornia virginica*	Amp.	<	<	<	=
	Area	=	<,>*	=	=
Green *Sesuvium verrucosum*	Amp.	<	<	<	=
	Area	=	=	=	=
Senescing *Distichlis spicata*	Amp.	=	=	=	=
	Area	=	=	=	=
Senescing *Scirpus acutus* and *Scirpus californicus*	Amp.	=	=	=	=
	Area	=	=	=	=
Senescing *Scirpus paludosus*	Amp.	=	=	=	=
	Area	=	=	=	=
Senescent *S. paludosus*	Amp.	=	=	=	=
	Area	=	=	=	=
Mowed Senescent *S. paludosus*	Amp.	>	>	>	=
	Area	=	=	=	=
Dry Soil	Amp.	=	=	=	=
	Area	=	=	=	=

*S. virginica had the lowest radiance between 0.98-1.04μm, but the highest radiance between 1.05-1.11μm. Relative brightness between cover types should be compared for similar display modes within a column. For example, between 1.15-1.44μm in amplitude normalization mode, mowed senescent S. paludosus was the brightest, S. virginica and S. verrucosum the darkest, and the other five spectra were intermediate and similar in brightness.

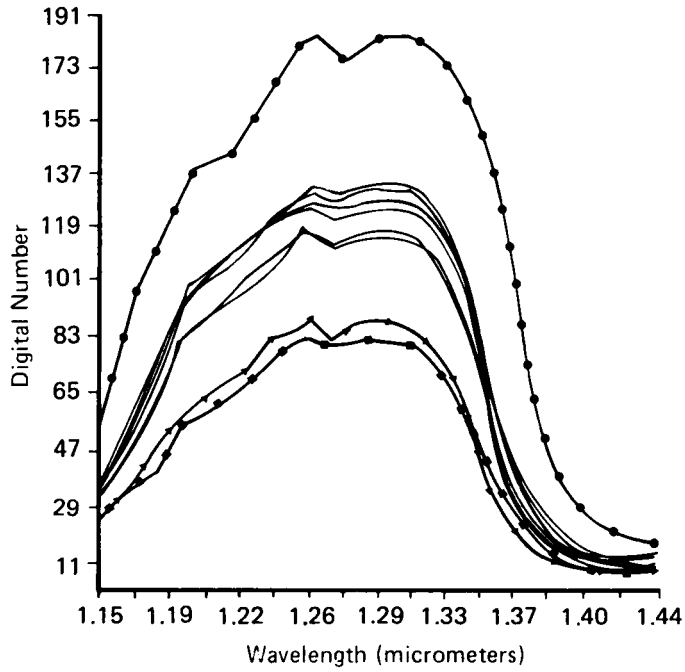

Fig. 4. Mean scene spectrum and spectra of eight cover types, shown between 1.15-1.44μm in amplitude normalization mode. -●-●-●- = mowed senescent S. paludosus, -▲-▲-▲- = S. verrucosum, -■-■-■- = S. virginica. The other six spectra are clustered between the first three spectra.

Better results were achieved with MIXTURE, a program that, when used in the area mode, assigns pixels to classes based on user-specified spectra (somewhat analogous to a supervised classification). The distribution of cover types assigned by the algorithm corresponded well to the actual distribution when spectra of only three cover types (green Salicornia, senescing D. spicata, and mowed dead S. paludosus) were specified (Fig. 5), as well as when all eight cover type spectra were specified. The relatively featureless residual image (column 5 in Fig. 5) supports the interpretation that the user-defined spectra encompassed most of the spectral variation within the image. When used in plot mode, MIXTURE breaks a selected segment of the scene into its surface components, by percent, based on user-defined component spectra. Use of this program yielded good correspondence with ground data when used on areas composed of only two dominant cover types (green S. virginica and senescent S. paludosus), but poor results on more complex parts of the image. The two vegetation types represent some of the greatest spectral divergence of those measured and suggest that the spectral mixing was

responding to changes in moisture content or to the architecture-related shadowing of the canopies.

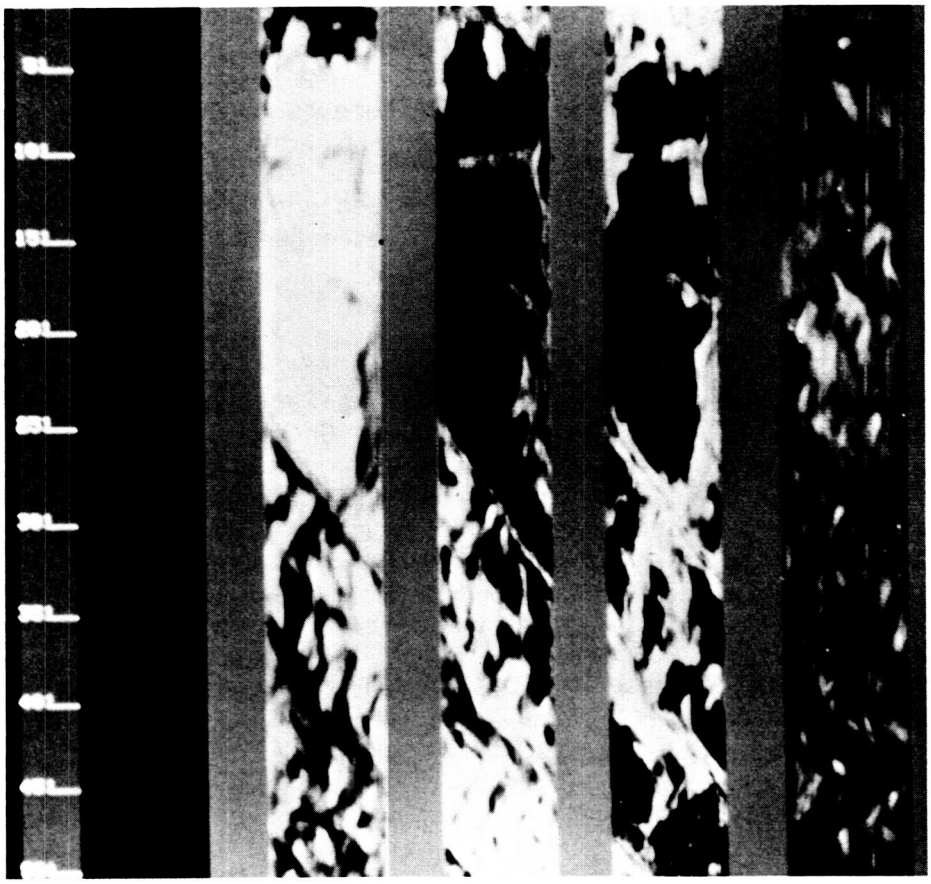

Fig. 5. Results of MIXTURE analysis, using three spectra (mowed dead S. paludosus [column 2], green S. virginica [column 3], senescing D. spicata [column 4]). Column 1 is blank, and column 5 is the residual, or pixels whose spectra do not match any of the three spectra.

DISCUSSION

No distinguishing narrow-band absorption or reflectance features were apparent among the soil or vegetation types at the wavelengths studied. In particular, we examined senescent vegetation spectra for evidence of cellulose features, but could identify only those also present in soil and succulent green vegetation spectra. Examination of the ground-gathered spectroradiometric measurements collected for this study revealed similar results. The only differences in AIS spectra were broad-band brightness differences, i.e. differences in radiance of particular cover types within broad wavebands. Despite the lack of distinct narrow-band spectral differences in cover types, it is encouraging that the broad-band brightness differences alone were sufficiently consistent to permit discrimination of various vegetation types. It is unfortunate that the data acquired beyond 1.6μm could not be used, since there is some evidence

that distinct spectral signature features may exist between 1.6 and 1.9μm (Gross and Klemas 1985, 1986; Spanner and Peterson 1986, Ustin et al. 1986, Wood and Beck 1986).

Our results suggest that, for vegetation studies, more consideration should be given to analysis techniques designed to maximize the extraction of the information contained in broad-band brightness differences. Given the apparent similarity in the shape of infrared spectra of various vegetation types, broad-band brightness differences apparently related to canopy moisture and/or architectural geometry may be the most important factor in vegetation studies using infrared data. We anxiously await AVIRIS data, which will be better calibrated and include information in narrow-band visible wavelengths that are expected to be more useful for vegetation analyses.

ACKNOWLEDGEMENTS

This research was supported by the NASA Earth Science and Applications Division Land Processes Program under Grant No. NAGW-950, and the Universities of Delaware and California. The authors wish to thank Paul Ritter at UC-Berkeley for assistance in analyzing the AIS data, Gordon Hoover of JPL for collecting and analyzing the VIRIS data, and Heather Froozandeh for secretarial expertise.

LITERATURE CITED

Gross, M.F. and V. Klemas. 1985. Discrimination of coastal vegetation and biomass using AIS data. Pp. 129-133 in Proc. AIS Data Anal. Wkshop., Jet Propulsion Lab., Pasadena, CA. JPL Publ. 85-41.

Gross, M.F. and V. Klemas. 1986. The use of Airborne Imaging Spectrometer (AIS) data to differentiate marsh vegetation. Remote Sens. Environ. 19(1):97-103.

Spanner, M.A. and D.L. Peterson. 1986. Analysis of AIS data of the Bonanza Creek Experimental Forest, Alaska. Pp. 144-152 in Proc. Second AIS Data Anal. Wkshop., Jet Propulsion Lab., Pasadena, CA. JPL Publ. 86-35.

Ustin, S.L., B.N. Rock and R.A. Woodward. 1986. Patterns of vegetation in the Owens Valley, California. Pp. 180-186 in Proc. Second AIS Data Anal. Wkshop., Jet Propulsion Lab., Pasadena, CA. JPL Publ. 86-35.

Wood, B.L. and L.M. Beck. 1986. Trace element-induced stress in freshwater wetland vegetation: Preliminary results. Pp. 171-179 in Proc. Second AIS Data Anal. Wkshop., Jet Propulsion Lab., Pasadena, CA. JPL Publ. 86-35.

Vane, G. 1986. Introduction. Pp. 1-16 in Proc. Second AIS Data Anal. Wkshop., Jet Propulsion Lab., Pasadena, CA. JPL Pub. 86-35.

TOWARD DETECTING CALIFORNIA SHRUBLAND CANOPY CHEMISTRY WITH AIS DATA

CURTIS V. PRICE, TGS Technology, Inc., NASA Ames Research Center, M.S. 242-4, Moffett Field, CA 94035, USA; WALTER E. WESTMAN, NASA Ames Research Center, M.S. 242-4, Moffett Field, CA 94035, USA.

ABSTRACT

AIS II data of coastal sage scrub vegetation from the Santa Monica Mountains were examined for fine spectral features that might be used to predict concentrations of certain canopy chemical constituents. A Fourier notch filter was applied to the AIS data and the TREE and ROCK mode spectra were ratioed to a flat field. Portions of the resulting spectra resemble spectra for plant cellulose and starch in that both show reduced reflectance at 2100 and 2270 nm. The latter are regions of absorption of energy by organic bonds found in starch and cellulose. Whether the relationship is sufficient to predict the concentration of these chemicals from AIS spectra will require testing of the predictive ability of these wavebands with large field sample sizes.

INTRODUCTION

Strong interest exists in determining the concentration of leaf chemical compounds in canopies using fine spectral features of Airborne Imaging Spectrometer (AIS) data (Spanner et al. 1985; Spanner & Peterson 1986; Swanberg & Peterson 1987; Wessman et al. 1987; cf. Westman & Price 1987). Our interest in this application of AIS is spurred by the observation that particular air pollutants can induce distinct chemical changes in leaves of some species, both in fumigation studies, and apparently along field gradients in these pollutants (Westman 1987). The ability to identify such chemical changes remotely might thus permit both the identification of air pollutants as stressors, and the separation of influence of different pollutants in a multipollutant atmosphere on the species of interest. The physical basis for the postulated relationship between leaf chemistry and reflectance lies in the narrow absorption features, induced by vibrational stretching frequencies of organic bonds, that are embedded in the reflectance spectrum.

We present progress in analyzing AIS data of the Santa Monica Mountains of Los Angeles, California. This coastal range experiences inputs of pollutants from urban sources, particularly at the eastern end. In combination with daytime offshore winds, these conditions create a predominant diurnal west-east gradient of decreasing pollutant exposure, particularly in photochemical oxidants (Westman 1987). Our study objectives include the derivation of spectral reflectance curves in the 800-2400 nm range from selected sites of coastal sage shrubland arrayed along the pollution gradient for comparison with canopy chemical data obtained from field sampling.

THE STUDY AREA AND POLLUTANT EFFECTS

Coastal sage scrub is a drought-deciduous, seasonally leaf-dimorphic shrubland type that occupies approximately 25% of the Santa Monica Mountains area, mostly at lower elevations in the western portion of the range. The location of the vegetation type in the Santa Monica Mountains has been mapped using Thematic Mapper Simulator data by Price and Westman (1987). The vegetation includes occasional individuals of evergreen habit, such as the laurel sumac, Rhus laurina. The latter often occurs as large clumps of 5-8 m diameter within the shrubland.

Ten species of coastal sage scrub were exposed for ten weeks to three levels each of ozone (0.1, 0.2, 0.4 ppm) and sulfur dioxide (0.05, 0.2, 0.5 ppm) alone and in combinations, and a filtered-air control, in fumigation chambers at the Statewide Air Pollution Research Center at the University of California, Riverside (Westman et al. 1985). The leaves remaining attached to the fumigated plants (5 plants in each of two replicates per treatment) were analyzed for plant pigments (chlorophylls a,b; total carotenoids), structural components (cellulose, fiber, lignin) and elemental content in five of the species (Artemisia californica, Rhus laurina, Eriogonum cinereum, Salvia mellifera, Encelia californica). Ozone treatment caused significant increases in leaf nitrogen, potassium and lead, and weaker trends toward increase in structural components and chlorophyll. Sulfur dioxide treatment induced significant rises in total sulfur. Combinations of the two pollutants caused a rise in sulfur and decline in carotenoids (Westman 1987). In the field, these sample species showed chemical changes from west to east that would be expected from the known rise in ozone levels toward the east: a rise in nitrogen and chlorophyll, and to a lesser extent in structural compounds (Westman 1987). These chemical changes may arise from accelerated leaf drop, and the consequent enrichment of the canopy in young, though stunted, leaves (Westman 1987). This and other hypotheses are currently being tested with additional field data.

METHODS

AIS-2 data were collected over 15 study sites in the Santa Monica Mountains on September 15, 1986 by the NASA Ames C-130 aircraft. TREE (800-2100 nm) and ROCK (1100-2400 nm) mode data were obtained for all sites.

The raw imagery contained intermittent striping, dropped lines, noisy data lines, and blank image columns. Gain differences between image columns occurred due to varying responses between detectors. Periodic gain changes also occurred within an image column due to changes in detector response over time. These effects were expressed as vertical and horizontal striping in the imagery, respectively. Loss of certain lines on some flightlines occurred during the process of decommutating the high-density tape to computer-compatible tape. Several image columns (column numbers 1164,1985,1986) were zero for all pixels in the flight lines. Also the first column in each band contained noise.

Striping in the imagery was eliminated by replacing noisy image lines that occurred intermittently in Bands 1-32 with an average of

neighboring lines, and then applying a Fourier notch filter to the imagery as described by Hlavka (1986). This method for destriping the data is superior to a column by column flat-field division in that horizontal striping is removed and the original intensity (DN) values are preserved.

A section of freeway (Interstate 5) near Griffith Park, at the eastern end of the Santa Monica Mountains, was used to obtain flat field spectra in TREE and ROCK mode. The spectra represent an average of three rows for all 64 columns of pixels . Wavelength calibration was performed using supplied values (Jet Propulsion Laboratory 1986) for all 128 bands in ROCK mode, and for bands 65-128 in TREE mode. Bands 1-64 of TREE mode were calibrated using the 935 nm atmospheric absorption band (Chahine 1983).

AIS data were collected over areas of Rhus laurina of different densities in the La Jolla Canyon region of the western Santa Monica Mountains. Two weeks later, field measurements were taken of Rhus laurina shrubs using the Barringer REFSPEC IIA, an integrating sphere ratioing spectroradiometer. The instrument was suspended 0.5 m above the canopy so that the measured target contained several leaves in the uppermost layer of canopy. The latter data were ratioed to reflectance from a barium sulfate plate observed under the same conditions.

To compare AIS spectra of vegetation to plant chemical constituents, we digitized spectral reflectance curves for starch (from corn), liquid water (the difference between water-soaked filter paper and dry filter paper; in Hruschka and Norris 1982), and cellulose (in Norris and Barnes 1976). We converted data from log (1/R) to R, where R is reflectance of dried, ground extract as measured by a Cary Model 14 monochromator against a ceramic standard. These curves were then overlaid upon destriped AIS spectra ratioed to flat field spectra.

RESULTS

Vegetation and flat-field spectra

The flat field (freeway) spectra are shown in Figure 1. The shapes of the TREE and ROCK mode peaks between 1150 and 1350 nm are not very similar. This disparity probably results from effects of the blocking filter at 1100 nm used for ROCK mode data acquisition. The two spectra also differ beyond 1600 nm, where second order effects alter the TREE mode response (Vane 1986). These differences are obvious in TREE mode as a peak in the 1600-1800 nm region and a flattening of the two carbon dioxide absorption features in the 2000-2100 nm region (Weisnet & Matson 1983).

Figure 2 compares flat-field corrected, destriped AIS spectra of Rhus laurina to similarly ratioed reflectance curves of the same species obtained with the field spectroradiometer (after deleting data in the atmospheric water absorption bands from the figure). The high noise in the field-derived spectra makes detailed comparison difficult, but some broad similarities in features appear to occur in the 900-1300 nm and 1500-1750 nm regions; second-order effects presumably explain the peak in TREE mode in a water absorption region near 1800 nm.

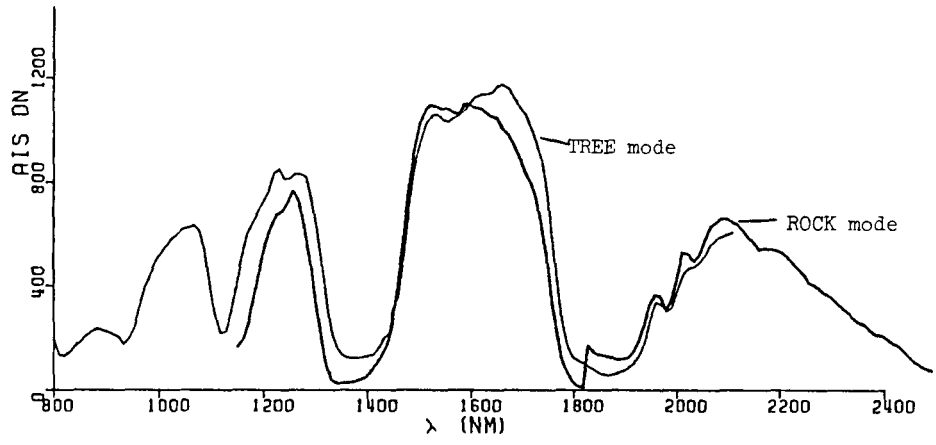

Fig. 1. Flat field spectra of AIS-2 data. A section of Interstate 5 at the east end of the Santa Monica Mountains was the area used.

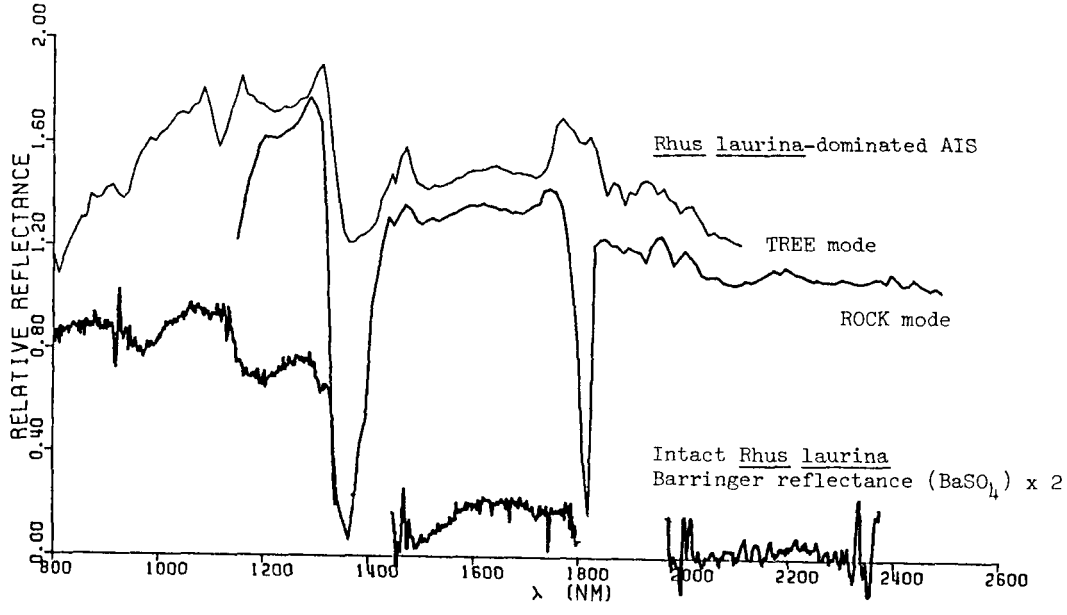

Fig. 2. AIS spectra over an area of dense Rhus laurina at La Jolla Canyon. The data were destriped and ratioed to a flat field. Lower curve is reflectance of Rhus laurina from the same location using a field spectroradiometer.

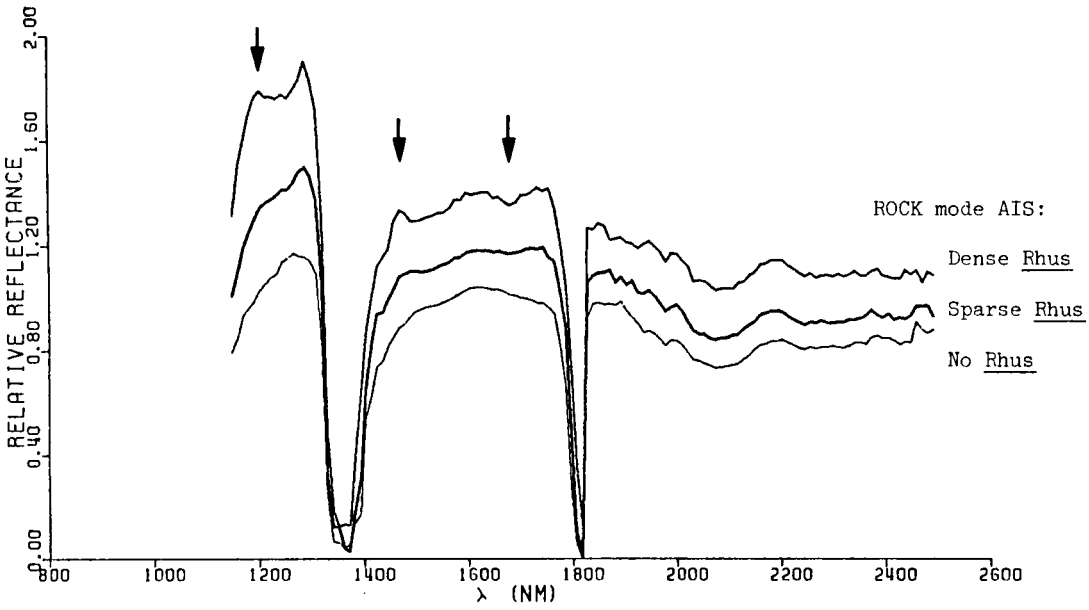

Fig. 3. AIS spectra for three areas dominated by Rhus laurina of different densities. AIS data are destriped, averaged over 3 X 3 pixels, and ratioed to a flat field. Note fine spectral variation between the three curves (arrows).

Figure 3 shows ROCK mode spectra extracted over coastal sage scrub of differing Rhus canopy closure. Each has been ratioed to flat-field spectra. The large differences in levels of reflectance between spectra are likely related to albedo (affected by sun and view angles), and possibly to leaf area index. Differences in fine spectral features (arrows) may arise from vegetation-induced spectral features independent of illumination angle. Further analysis is planned using log residual techniques to suppress the effects of varying scene illumination (Roberts et al. 1986).

Comparison to chemical spectra

Figure 4A compares the Rhus laurina-dominated spectra of Fig. 2 to reflectance curves for pure cellulose, starch and liquid water in filter paper. Liquid water has absorption peaks displaced 55-70 nm to longer wavelengths (1450 and 1940 nm, reported by Curcio and Petty 1951) compared to atmospheric water absorption maxima (1395, 1870 nm; Chahine 1983). These features can be seen in Figure 4A, and for plants in Figure 4B. The latter shows reflectance spectra from a canopy of intact seedlings of Pinus jeffreyi, measured with a Collins VIRIS spectroradiometer under artificial illumination (Westman and Price 1987).

The cellulose, starch, and water curves all show broad spectral features in Fig. 4A. The 1540 nm first overtone of an O-H stretching frequency, and a C-H first overtone at 1780 nm (bonds in starch and cellulose, and in the first case, water) occur in regions heavily influenced by water absorption. The AIS spectra cannot therefore be used with confidence to detect fine spectral features in these regions

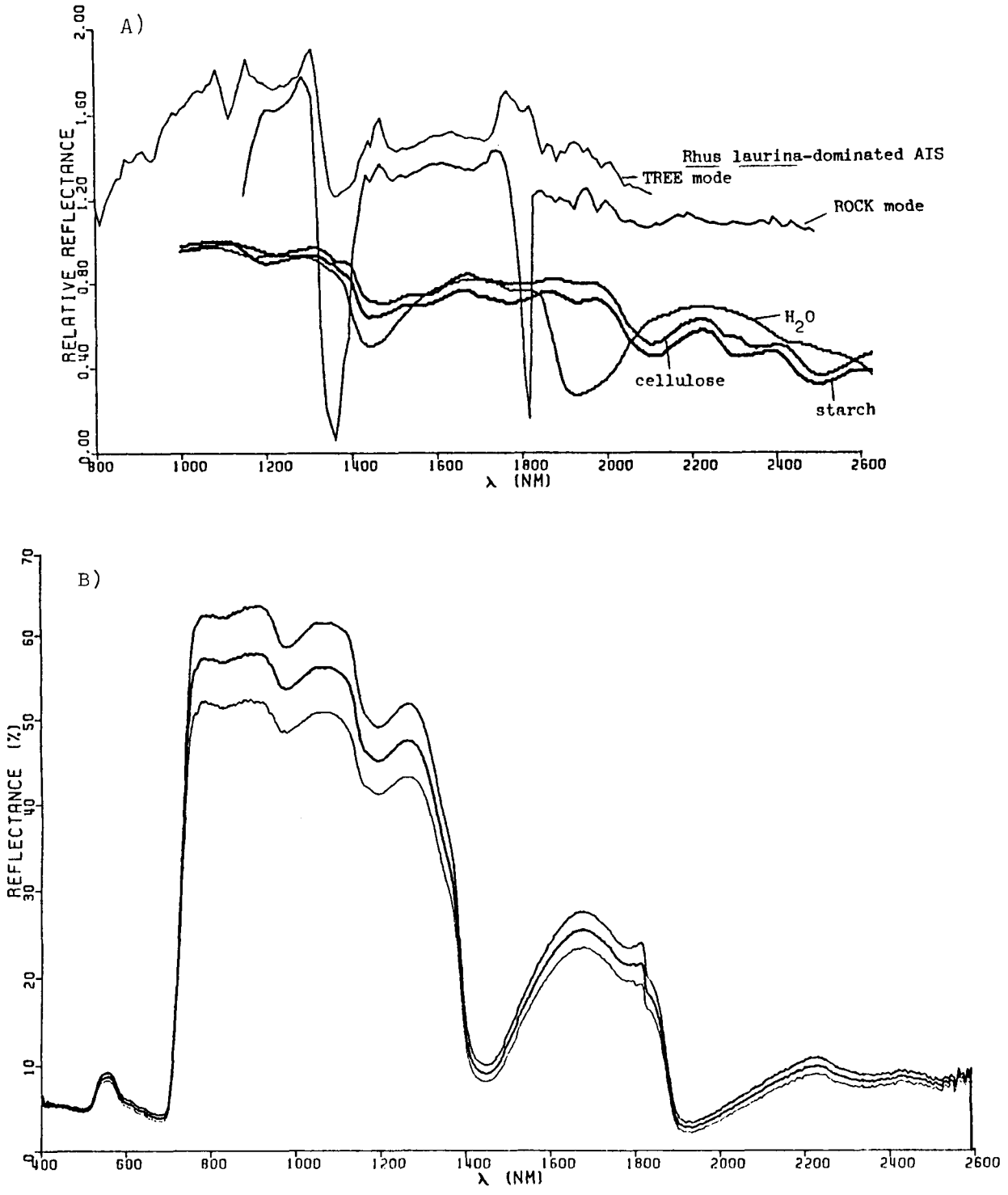

Fig. 4. A) Destriped AIS data of Rhus laurina-dominated areas, ratioed to flat field. Curves below are laboratory-derived reflectance curves for dried, ground extracts of starch and cellulose, and liquid water in soaked filter paper (adapted from Norris and Barnes 1976; Hruschka and Norris 1982). B) Reflectance of Pinus jeffreyi seedlings with Collins' VIRIS spectroradiometer. Upper and lower curves are standard errors.

because of the low signal/noise ratio resulting from absorption of much of the radiation by atmospheric water. The O=H bend/C-O stretch combinations at 2100 nm, and O-H stretch/C-C stretch combinations at 2270 nm (occurring in starch and cellulose) can be seen as absorption features in the pure cellulose and starch curves in a region where water absorption is less. These features at 2100 and 2270 nm in the cellulose and starch curves may or may not be responsible for the declines in reflectance in these regions in the AIS curve (ROCK mode). The green plant curve (Fig. 4B) shows a dip in the 2270 nm region, but not the 2100 nm region. The further dip in the starch and cellulose curves at 2500 nm is beyond the range of the AIS.

It does not appear possible, based on visual inspection, to determine whether the spectral features in the AIS curve are caused by absorption properties of the major plant chemical constituents, given present understanding. An understanding of the relative contributions of other features, including other chemical constituents, and other components of the scene, would be necessary for such a deterministic approach.

DISCUSSION

Each spectral region is influenced by many factors, but the combination of spectral features of any one chemical constituent are unique. In principal, therefore, reflectance at a combination of characteristic wavelengths could enable prediction of chemical concentrations. With the high level of intercorrelation that exists between chemical constituents in a leaf, and factors such as albedo or water content that affect large portions of a canopy reflectance spectrum, further intercorrelations between portions of the spectrum are introduced. For this reason, the potential range of wavelengths with high predictive power for a chemical constituent may be somewhat broader than implied by narrow stretching frequencies alone. Wessman et al. (1987) and Swanberg and Peterson (1987) report initial results in predicting leaf canopy chemistry from AIS spectra using stepwise regression to select wavelengths for prediction.

Research in the use of AIS spectra to predict canopy chemistry is in an exploratory stage. The spectra in Fig. 4 suggest that 2270 nm, and possibly 2100 nm, may be useful wavelengths to test in predictive models for the complex of glucose-based structural compounds such as starch, sugars and cellulose in plant canopies. Such deterministic approaches, as well as multivariate statistical approaches yet untried, remain for future testing.

ACKNOWLEDGEMENTS

Research was supported by NASA Earth Sciences Division under grant 677-21-35-08 and Life Sciences Division under grant 199-30-72-05. Research was conducted while one of us (W.E.W.) held a National Research Council research associateship at NASA Ames Research Center.

REFERENCES

Chahine, M.T. 1983. Interaction mechanisms within the atmosphere. In Manual of Remote Sensing, 2nd edn., ed. R. Colwell. (American Society of Photogrammetry, Falls Church, VA), pp. 165-201.

Curcio, J.A. and Petty, C.C. 1951. The near infrared absorption spectrum of liquid water. J. Optical Soc. Amer. 41: 302-305.

Hlavka, C. 1986. Destriping AIS data using Fourier filtering techniques. In Proc. 2nd AIS Data Analysis Workshop, ed. G. Vane and A.F.H. Goetz. (Pasadena, CA: NASA and Jet Propulsion Laboratory). JPL Publ. 86-35. Pp. 74-79.

Hruschka, W.R. and Norris, K.H. 1982. Least-squares curve fitting of near infrared spectra predicts protein and moisture content of ground wheat. Applied Spectroscopy 36: 261-265.

Jet Propulsion Laboratory. 1986. Supplement to the Science Investigator's Guide to AIS Data. (Pasadena, CA: Calif. Inst. Technology).

Norris, K.H. and Barnes, R.F. 1976. Infrared reflectance analysis of nutritive value of feedstuffs. Proc. 1st Intl. Symp. Feed Composition, Animal Nutrient Requirements and Computerization of Diets. Utah State Univ., Logan, Utah.

Price, C.V. and Westman, W.E. 1987. Vegetation mapping and stress detection in the Santa Monica Mountains, California. Proc. IGARSS '87 Symp., Ann Arbor, MI. Inst. Electrical and Electronic Engineers 87 CH2434-9. Pp. 1195-1200.

Roberts, D.A., Yamaguchi, Y. and Lyon, R.J.P. 1986. Comparison of various techniques for calibration of AIS data. In Proc. 2nd AIS Data Analysis Workshop, ed. G. Vane and A.F.H. Goetz. (Pasadena, CA: NASA and Jet Propulsion Laboratory). JPL Publ. 86-35. Pp. 21-30.

Spanner, M.A., Peterson, D.L., Acevedo, W. and Matson, P. 1985. High resolution spectrometry of leaf and canopy chemistry for biogeochemical cycling. In Proc. AIS Data Analysis Workshop, ed. G. Vane and A.F.H. Goetz. (Pasadena, CA: NASA and Jet Propulsion Laboratory). JPL Publ. 85-41. Pp. 92-99.

Spanner, M.A. and Peterson, D.L. 1986. Analysis of AIS data of the Bonanaza Creek Experimental forest, Alaska. In Proc. 2nd AIS Data Analysis Workshop, ed. G. Vane and A.F.H. Goetz. (Pasadena, CA: NASA and Jet Propulsion Laboratory). JPL Publ. 86-35. Pp. 144-152.

Swanberg, N.A. and Peterson, D.L. 1987. Using the Airborne Imaging Spectrometer to determine nitrogen content in coniferous forest

canopies. Proc. IGARSS '87 Symp., Ann Arbor. MI. Inst. Electrical and Electronic Engineers 87 CH2434-9. P. 981.

Vane, G. 1986. Introduction. In Proc. 2nd AIS Data Analysis Workshop, ed. G. Vane and A.F.H. Goetz. (Pasadena, CA: NASA and Jet Propulsion Laboratory). JPL Publ. 86-35. Pp. 1-16.

Weisnet, D.R. and Matson, M. 1983. Remote sensing of weather and climate. In Manual of Remote Sensing, 2nd edn., ed. R. Colwell. (American Society of Photogrammetry, Falls Church, VA), pp. 1305-1369.

Wessmann, C.A., Aber, J.D. and Peterson, D.L. 1987. Estimating key forest ecosystem parameters through remote sensing. Proc. IGARSS '87 Symp., Ann Arbor, MI. Inst. Electrical and Electronics Engineers 87 CH2434-9. Pp. 1189-1193.

Westman, W.E. 1987. Detecting early signs of regional air pollution injury to coastal sage scrub. In G.M. Woodwell, ed. Biotic Impoverishment: Changes in the Structure and Function of Natural Communties under Chronic Disturbance. Cambridge Univ. Press, Cambridge, England. In press.

Westman, W.E., Preston, K.P. and Weeks, L.B. 1985. Sulfur dioxide effects on the growth of native plants. In Sulfur Dioxide and Vegetation -- Physiology, Ecology, and Policy Issues, ed. W.E. Winner, H.A. Mooney & R.A. Goldstein. Stanford Univ. Press, Stanford, CA. Pp. 264-280.

Westman, W.E. and Price, C.V. 1987. Remote detection of air pollution stress to vegetation: laboratory-level studies. Proc. IGARSS '87 Symp., Ann Arbor. MI. Inst. Electrical and Electronic Engineers 87 CH2434-9. Pp. 451-456.

MEASURING NEAR INFRARED SPECTRAL REFLECTANCE CHANGES FROM WATER STRESSED CONIFER STANDS WITH AIS-2

GEORGE RIGGS, School of Forestry, University of Montana, Missoula, MT 59812 USA; STEVEN W. RUNNING, School of Forestry, University of Montana, Missoula, MT 59812 USA

ABSTRACT

AIS-2 data was acquired over two paired conifer stands in West Germany for the purpose of detecting differences in spectral reflectance between stressed and natural canopies. Water stress was induced in a stand of Norway spruce near Munich and white pine near Frankfurt by severing the sapwood near the ground. Water stress during the AIS flights was evaluated through shoot water potential and relative water content, measurements. Preliminary analysis with raw AIS-2 data using SPAM indicates that there were small, inconsistent differences in absolute spectral reflectance in the near infrared .97-1.3um between the stressed and natural canopies.

INTRODUCTION

Recent theory and laboratory results have suggested that an increase in near infrared leaf reflectance occurs as leaf water content decreases with increasing plant water stress (Ripple 1986). Additionally, some theories have related leaf water stress to canopy air pollution damage (Rock et al. 1986). This study was designed to test the ability of the AIS-2 to discriminate an induced water stress in two pairs of conifer stands as part of a larger project in West Germany studying remote sensing of air pollution damage to the Black Forest. The paired plot study design was produced by inducing stress on half of the study plot leaving the remaining half as control. This experimental design allowed a rigorous comparison of reflectance differences with variables such as tree species and age, canopy illumination, sun-angle, sensor angle and atmospheric effects all equal, hence eliminating them from the comparative analysis.

BACKGROUND WATER RELATIONS

Ecologically significant measures of the water status of vegetation are leaf water potential and relative water content (RWC). Leaf water potential is a measure of the energy status of water in plant tissue and RWC is a measure of water content in the leaf tissues relative to that occuring at saturation water content. Water stress in plants is measured as a decrease in leaf water potential from 0 bars and as a decrease in RWC from 100%. Leaf water potential is easily measured on a conifer shoot with a pressure chamber apparatus in the field (e.g. Ritchie and Hinckley, 1975), expressed as a pressure (-bars). RWC is calculated as (fresh wt-dry wt)/(saturation wt-dry wt) and expressed as a percentage.

METHODS & STUDY SITES

Water stress can be rapidly induced, in one hour to one day depending on tree size, by severing the stem sapwood through which water flows from the roots to the canopy. Complete severing of the sapwood causes a rapid increase in the level of leaf water stress which is then maintained until the death of the tree 30 or more days later (Brix and Mitchell, 1985; Running, 1980).

The study was located at two sites in West Germany with the aid of our German colleagues who located and made available the forest stands, arranged for the cutting of the trees and assisted in the collection of field data. A 50x50m plot of trees was stressed by either girdling of the sapwood or complete severing of the trunk.

One stand was of Norway spruce located near Munich and the other was a plantation of white pine in the Frankfurt Forest. The Norway spruce were approximately 30m in height and about 60cm in diameter, with a closed canopy and 5-10 cm ring of sapwood. Girdling was done with chainsaws on 2 July with the AIS flight occurring 13 days later on 15 July.

The Frankfurt Forest site was prepared with a much greater physical effort. The white pine stand was a high density plantation approximately 7m in height, and 15-20cm in diameter, most of which was sapwood. For this reason the trees were completely severed by cutting the trunk about 1m above ground and strapping trunks upright with steel banding to the stumps. Severing of the 2400 trees was begun 2 July and was completed 7 July. AIS flights were 15 and 21 days after severing of the Frankfurt plot.

Shoot water potentials were collected during or the day after AIS-2 overflights to measure the difference in stress between cut trees and adjacent uncut trees (Table 1). Shoot water potentials were related to relative water content so that an estimate of RWC near the time of AIS flight could be made (Fig. 1).

Table 1. Water stress measurments taken at the time of AIS flights. Shoot water potentials are averages of 5-7 measurements, and RWC the average from 5 samples.

	Days after cutting	Shoot water potential (bars)	RWC (%)
Munich			
Girdled trees	13	-21.0	86
Control trees	13	-9.1	91
Frankfurt			
Severed trees	16	-19.5	79
Control trees	16	-13.3	89

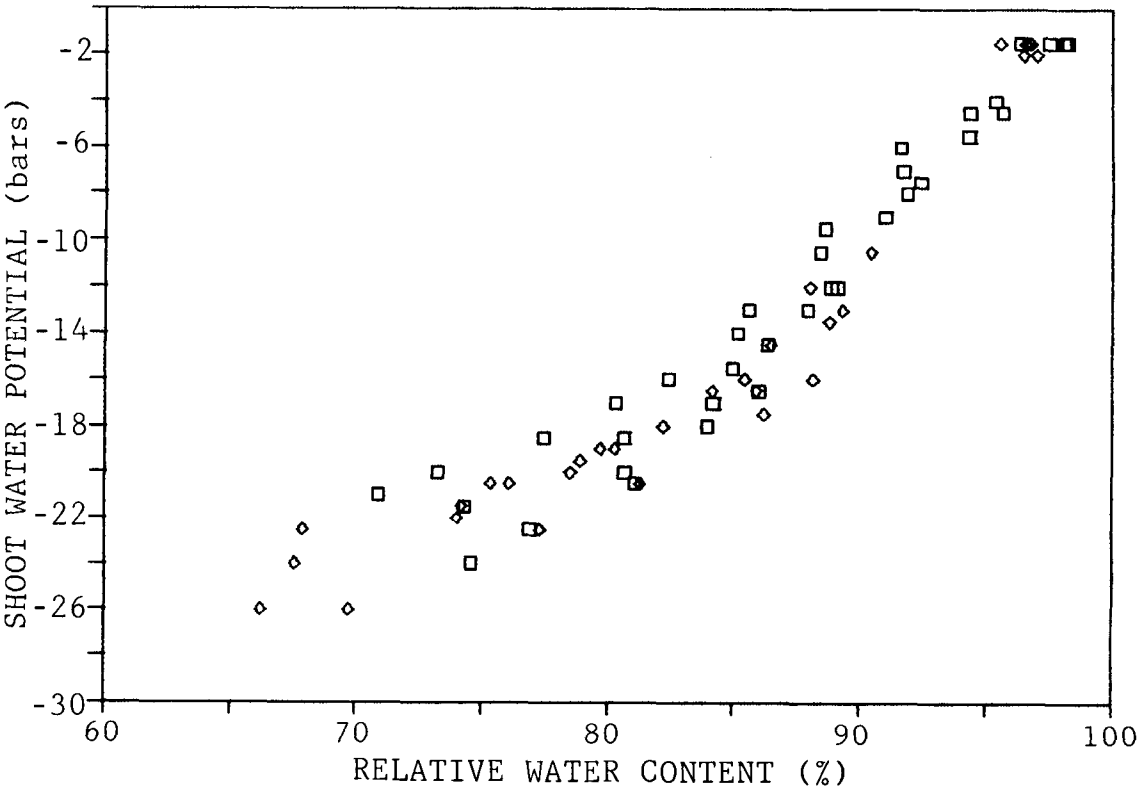

Fig. 1. Relationship between shoot water potential and RWC for severed (□) and control (◇) white pines on the Frankfurt site. Measurements from 5 samples of each treatment collected the day after AIS-2 flight.

AIS DATA ANALYSIS

AIS data was collected in "tree mode" 0.8-2.2um with an approximate ground pixel size of 6.5m. In "tree mode" the usable range of AIS data ends at approximately 1.6um due to second order light contamination. Analyisis of AIS data was begun using the Spectral Analysis Manager (SPAM) at JPL. Quality of AIS data was very good and the raw data, without normalizations or atmospheric corrections, was used.

SPAM was used to plot average spectral curves for stressed and control trees, constructed from 5 to 7 pixels selected from a plot.

RESULTS AND DISCUSSION

Spectral plots of the white pine at Frankfurt taken 21 days after severing show a slightly higher reflectance from the control trees compared to the severed trees in the 0.97-1.3um region, contradicting expected patterns (Fig. 2). When a log residual normalization to remove common atmospheric effects was done, spectral separation was improved across the spectrum. Spectral plots of the Norway spruce, Munich site, were obtained from two AIS flights at approximately 1030hr and 1330hr 13 days after girdling of the trees. For the 1030hr flight (Fig. 3) the girdled trees had greater reflectance than the

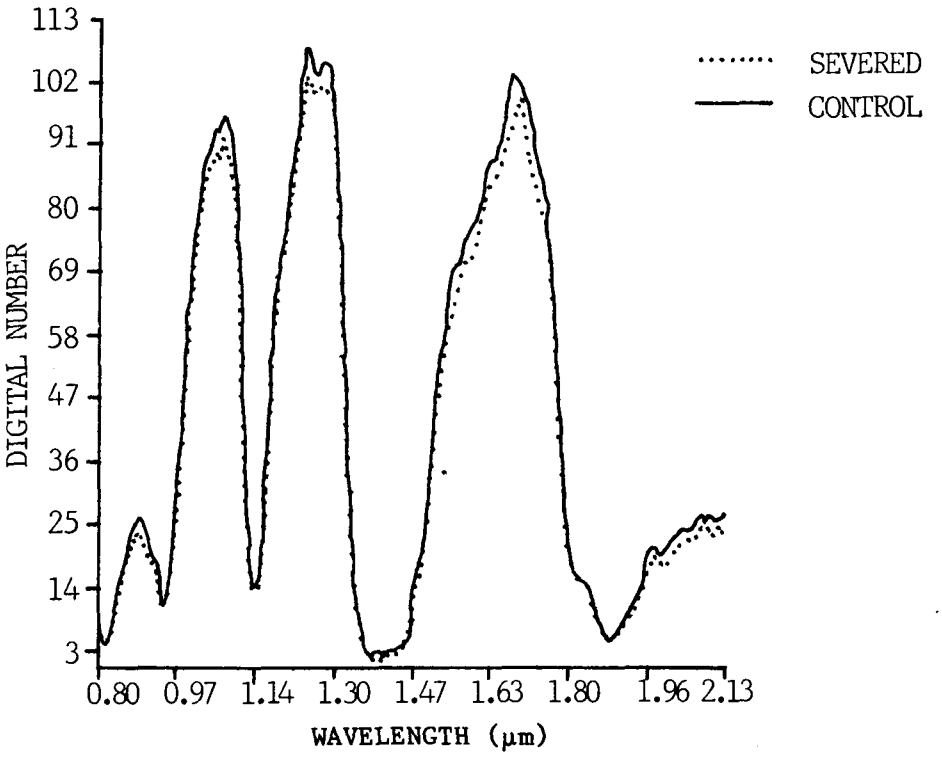

Fig. 2. Spectral reflectance of severed and control white pines at the Frankfurt site from AIS flight 21 days after severing. Estimated difference of 6 bars in shoot water potential and 10% absolute difference in RWC between severed and control trees.

control trees at the peaks of reflectance in the infrared. The difference in shoot water potential at that time was 12 bars, and 5% in RWC. However, for the 1330hr overflight reflectance from the girdled canopies was lower than that from the control, a reversal of reflectance differences seen for the 1030hr flight. The difference in shoot water potential at this time was 7 bars, and 4% in RWC.

SUMMARY

Anaylsis of raw AIS-2 data to date has found small differences in the amplitude of reflectance in the near infrared region, .97-1.3um, between stressed and control canopies. For white pine, reflectance from the stressed canopy was slightly lower than the control canopy. For Norway spruce, control canopy reflectance was greater than the stressed canopy in the morning, but this relationship was reversed in the early afternoon. At this time our results do not consistently support the current hypothesis that near infrared reflectance increases with leaf water stress. We will next analyze the NS001 TM simulator data and the TIMS data to attempt to find consistency in the spectral response of these canopies to the induced water stress.

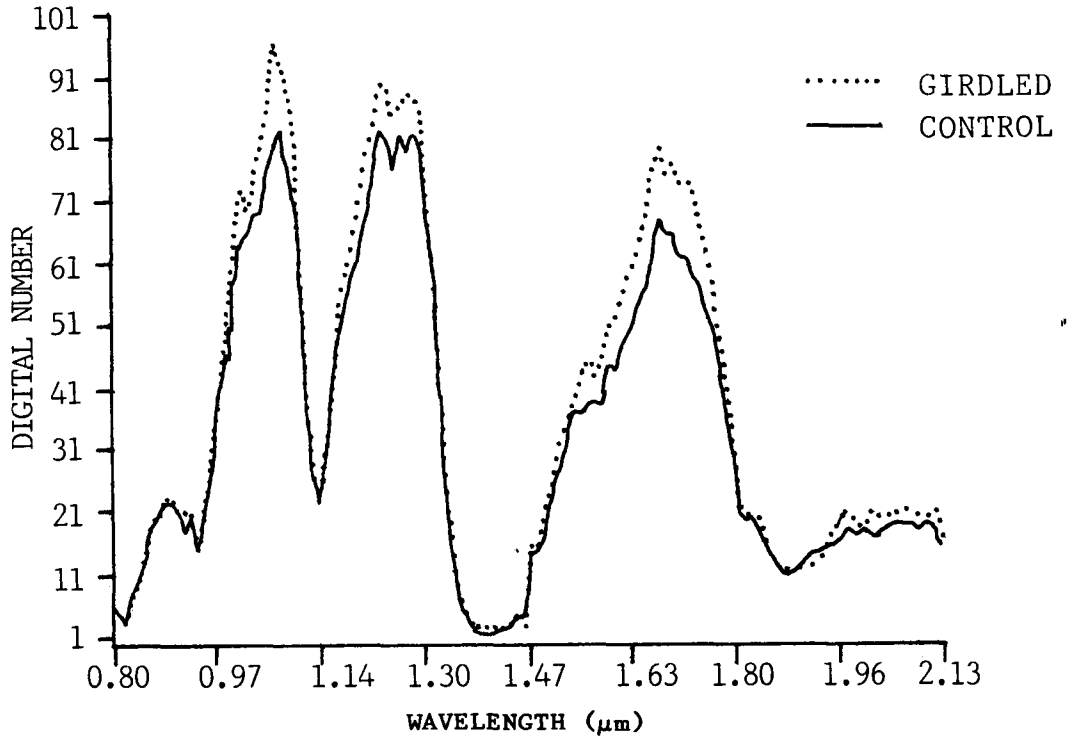

Fig. 3. Spectral reflectance of girdled and control Norway spruce at the Munich site from morning AIS flight 13 days after girdling. A difference of 12 bars in shoot water potential between girdled and control trees was measured in the field at time of overflight.

ACKNOWLEDGMENTS

We thank Barry Rock for his support and assistance in this research. Funding for this research was provided for by the NASA Graduate Student Researchers Program and NASA Grant #NAGW 829. Special thanks to our German colleagues; Georg Kritikos, Barbara Koch, Manfred Schramm and Martin Lamberty for their efforts in making available the study sites and assistance in the field.

REFERENCES

Brix, H. and A.K. Mitchell. 1985. Effects of disrupting stem sapwood water conduction on the water status in Douglas-fir crowns. Canadian Journal Forest Research 15:982-985.

Ripple, W.J. 1986. Spectral reflectance relationships to leaf water stress. Photogrammetric Engineering and Remote Sensing 52:1669-1675.

Ritchie, G.A. and T.M. Hinckley. 1975. The pressure chamber as an instrument for ecological research. Advances in Ecological Research. 9:165-254.

Rock, B.N., J.E. Vogelmann, D.L. Williams, A.F. Vogelmann, and T. Hoshizaki. 1986. Remote detection of forest damage. BioScience 36:439-445.

Running, S.W. 1980. Relating plant capacitance to the water relations of Pinus contorta. Forest Ecology and Management. 2:237-252.

ABUNDANCE AND DISTRIBUTION OF ULTRAMAFIC MICROBRECCIA IN MOSES ROCK DIKE: QUANTITATIVE APPLICATION OF AIS DATA

MUSTARD, JOHN F. and CARLE M. PIETERS, Department of Geological Sciences, Box 1846, Brown University, Providence RI 02912.

Our investigation of Moses Rock dike using data collected with the Airborne Imaging Spectrometer (AIS) is near completion. Our results are presented and discussed in the articles in professional journals listed at the end of this abstract. These manuscripts include detailed desription and discussion of the nature of the geologic problems, the Moses Rock field site, calibration of AIS data, mineral identification from the AIS data, analytical models for determining abundance estimates from bidirectional reflectance spectra and application of the analytical mixing model to the AIS data. We will be happy to send reprints of these articles to any interested parties. The following is a short summary of these investigations concerning Moses Rock dike.

Moses Rock dike is a Tertiary diatreme containing serpentinized ultramafic microbreccia (SUM) (derived from the mantle) located on the Colorado Plateau in Utah. Field evidence indicates that SUM was emplaced first followed by breccias derived from the Permian strata exposed in the walls of the diatreme and finally by complex breccias containing basement and mantle derived rocks. SUM is found primarly dispersed throughout the matrix of the diatreme. A major objective in examining Moses Rock dike with AIS was to map the distribution and abundance of SUM in the matrix to better understand the nature of the eruption which formed this explosive volcanic feature.

AIS data were collected in July of 1984 and 1985. These data were calibrated by dividing the entire suite of raw AIS data by data from an internal standard area and then multiplying this relative reflectance data by the absolute bidirectional reflectance of a carefully selected sample from the standard area which was measured in the laboratory. From the calibrated AIS data the minerals serpentine, gypsum, and illite as well as desert varnish and the lithologies SUM and various sandstones were identified. Six endmembers (SUM, two types of sandstone, gypsiferous soil, clay–rich soil, desert varnish) were chosen to represent the dominant lithologies of the surface in the Moses Rock dike region. Spectra of these endmembers were used in an intimate mixture model to deconvolve the AIS spectral data into surface abundance coefficients for each component using a nonnegative least squares inverse algorithm. The results of these calculations of surface compositions are consistent with field observations and investigations.

SUM distribution and abundance in the matrix of the diatreme were examined in detail and two distinct sytles of SUM dispersion were observed. One style is characterized by high to moderate SUM abundance surrounded by halos of lesser SUM abundance. The dispersion halos grade steeply into regions of the matrix with little or no SUM. The second style is characterized by moderate SUM abundances and broad dispersion halos with SUM distributed across the entire width of the diatreme. These dispersion styles indicate that SUM, which is emplaced early, becomes reincorporated into the turbulent flow of the diatreme by abrasion and comminution by material carried along in the erupting medium. This eroded SUM is then dispersed throughout the matrix by eddy diffusion. The first style represents either an early arrested phase of the eruption sequence or a region of the diatreme where flow velocites were less intense than regions represented by the second styles. Since both styles are observed at the same erosion level this indicates that the duration or intensity of eruption varied along strike at Moses Rock dike.

(1) Mustard, J. F. and C. M. Pieters, Quantitative abundance estimates from bidirectional reflectance measurements, *Proc. Lunar Planet. Sci. Conf. 17th.* in *J. Geophys. Res.*, *92*, E617–E626, 1987.

(2) Mustard, J. F. and C. M. Pieters, Abundance and distribution of ultramafic microbreccia in Moses Rock dike,: Quantitative application of mapping spectrometer data, *J. Geophys. Res.* in press, 1987.

(3) Pieters, C. M. and J. F. Mustard, Exploration of crust/mantle material for the earth and moon using reflectance spectroscopy, *Special AIS issue of Remote Sensing of Environment*, in press, 1987.

(4) Mustard, J. F. and C. M. Pieters, Abundance estimates derived from reflectance spectra of tricomponent mixtures, *abstr.*, *EOS Trans. Am. Geophys. Un.*, *68*, p. 467, 1987.

EVALUATION OF AIS-2 (1986) DATA OVER HYDROTHERMALLY ALTERED GRANITOID ROCKS OF THE SINGATSE RANGE (YERINGTON) NEVADA AND COMPARISON WITH 1985 AIS-1 DATA.

R.J.P. LYON, Applied Earth Sciences Department, Stanford University, Stanford, CA 94305, USA

ABSTRACT

The 1986 AIS-2 flights on 29 September 1986 along two subparallel lines (bearing 013°) over the western flanks of the Singatse Range, were designed to traverse three major rock assemblages--the Triassic sedimentary sequence; the granitoid rocks of the Yerington batholith (Ann Mason and MacArthur) and the Tertiary ignimbritic ash-flow and ash-fall tuffs. Both Ann Mason and MacArthur sites are hydrothermally altered to a quartz-sericite-tourmaline mineralogy (Dilles, 1983; Proffett and Dilles, 1984; Einaudi, 1977).

The original AIS-2 data set showed numerous line-dropouts and a considerable number of randomly distributed, dark pixels. A second decommutation of the master tape (at NASA/ARC) produced a much better product, reducing the dropout essentially to near zero and the dark pixels by about 75%. These were further removed by a spatially-active 3 x 3 filter, which replaced a "bad" pixel by the average of its eight neighbors, if that pixel deviated from this local average by 30 DN.

Vertical striping was removed by histogram-matching, column by column. Finally, a "log-residual" spectrum was calculated which showed the departure of a 2 x 2 pixel area from the spatially- and spectrally-averaged scene.

A 1:1 correlation was found with the log-residual AIS-2 data and a large open pit area of gypsum. An area with known sericite agreed with the overflight data, and an area known to be free of any significant amount of O-H-bearing minerals showed no evidence of any in the AIS-2 log-residuals.

INTRODUCTION

AIS-2 imagery was obtained along four almost N-S lines (bearing 013°) over the western flank of the Singatse Range, near Yerington, approximately 120 miles SE of Reno, Nevada. Concurrent 35 mm Nikon B/W photography was taken to aid in ground location, with airborne video as an adjunct.

The four 1986 flight lines (flight 86-009-09, 29 September 1986) were flown between 9,000 ft. and 12,000 ft. above ground level (2.74 Km to 3.66 Km). The 013° bearing for the 15 Km lines was chosen to traverse the strike length of the Triassic limestone sequences (Ludwig area) at the south end; the Jurassic granitoid rocks of the Yerington batholith (Ann Mason area); and the Singatse Peak Tertiary ignimbritic tuffs. At the

northern end (in the MacArthur area) a repeated section of the granitoid rocks was also traversed. A total of 14 "parent" rock types was sampled - 5 Triassic sediments, 3 granitoid types, and 6 members of the ignimbritic sequence. In addition, two sequences of "hydrothermally-altered" granitoids were overflown.

This paper deals initially with the processing of the 1986 data and then covers some of the geological results relating the airborne data to ground-measured VIRIS spectra taken from underneath the flight lines.

DATA QUALITY

The 1986 AIS-2 data sets as supplied initially contained severe line-dropouts and extensive ("pepper and salt") randomly-placed (usually dark) anomalous single pixels. All attempts to remove these pixels proved fruitless. We requested and received from NASA/ARC, a second attempt at decommutating the master tape which was of decidely better quality (see Fig. 1).

The imagery was still badly striped (vertically) and software had to be developed (Table 1) to take care of these artifacts.

Table 1

SOFTWARE PROGRAMS - STANFORD

INPUT:	AIS32	Reads AIS-1 and AIS-2 tapes, displays image data, writes 80-line disk file (of channels 1-128; 76-117; or 97-128).
PROCESSING:	DEST32	Removes the vertical striping from an AIS image, forcing histogram for each vertical line to be equal.
	DESPIKE	Removes isolated bad pixels from an AIS image. Works in the spatial domain. Compares pixel to its 8 neighbors, replaces by average if outside tolerance (generally 30 DN).
	DESTAP	Destripes a whole flight-line; writes output to a second tape.
	ANDY32	Applies "log-residual" correction to an AIS image file.
	ANDYTAP	Same as ANDY32, but builds its averages from readings from the flight-line data from tape.
DISPLAY:	MULTI32	Displays as many channels as possible of an AIS file, in monochrome.
	TVAIS32	Displays a color-composite image of 3 AIS channels, and graphs the spectra of selected pixels.

DATA PROCESSING

Data Omission

This year we elected only to process the 2.2 micron region of the data (compare with Lyon, 1986), and further to concentrate only on those channels (#76-117) with a high radiance level.

We also deleted the last 11 channels (#118-128) to avoid possible "second-order" grating effects (noted in AIS Workshop II Report, p. 7, footnote C). The remaining 42 channels proved to be very useful in data analysis and less noisy than those we had omitted.

Image Extraction and Viewing

With the advent of the 64-pixel swath of AIS-2, we had to change the dimension statement of our software (Table 1). In addition, because of the size of our display screen (640 x 480 pixels) and with our desire initially to view as many channels of the 42 as possible, we again selected for display, 32 windows of 80 flight-line segments.

MULTI32 (Table 1) can be used to display any 32 continuous channels at once for these 80 flight-line segments, using either raw, destriped, despiked, or log-residual image data.

TVAIS32 will use any three channels (those selected from the MULTI32 display with maximum spectral contrast) and display them (2X enlarged) side by side, with their color-composite image on their left (Fig. 2A). A second aspect of TVAIS32 is the graphical mode. The 3-band color image is retained, and the three individual monochrome images are suppressed, being replaced by a spectrum (of 42 channel-elements) drawn horizontally across the screen, tied to the specific 2 x 2 pixel area from which their average graph was taken. This graphical display can be keyed to ground localities from which sample-spectra have been taken (Figs. 2B,D), or overlain onto geological maps, etc.

Our strategy for field correlation using the AIS imagery is based on the need to locate on the ground these specific pixels whose graphs show significant mineral information. While the 80 lines by 64 pixel segments may seem small, they cover 1.6 x 1.3 Km at a 20 m pixel size.

Image Restriping

Severe vertical striping was obvious in the raw imagery. The program DEST32 removed most of this by forcing the histogram of each column of pixels to be equal. Some intermittently (vertical) noisy columns still retained their bad data even after this action (noted especially in channel 97 (see Figs. 1C,D).

Image Despiking

The program DESPIKE operates on a 3 x 3 matrix in the spatial domain, and examines the central pixel DN, by comparing it to that of its eight neighbors. If the center pixel has a DN value differing from the 8-pixel mean, over a "tolerance" of 30 DN, it is replaced by that average, and the kernel moves forward. All 42 channels are so processed. The tolerance, however, cannot be made too small as it would soon give the kernel the effect of a 3 x 3 smoother. As the random spikes have non-zero DN with a

clear distribution in greyness, some "noise" is left in the data, if it is within the 30 DN tolerance.

This problem is markedly enhanced by the "log residual" processing and leads to significant levels of noise in that final product (Figs. 1E,F).

Log-Residual Processing

This algorithm has been borrowed from Dr. A. A. Green, CSIRO, Australia, but we have modified it slightly from its original expression (Green and Craig, 1985). Both these formulations also differ from a later "JPL log-residual" which appears only to use the first two items (A,B), of equation 4. The "offset" term (D) is probably used in all three forms in actual utilization by manipulation of the display system.

Our version of this statistically-based method (Roberts, et.al., 1986, p. 22) uses the relationship

$$DN_{s,\lambda} = T_s R_{s,\lambda} E_\lambda \qquad (1)$$

where $DN_{s,\lambda}$ = radiance , or the DN of each channel (λ) for each spatial pixel$_{(s)}$ in the data; T_s = a topographic factor for slope orientation effects; R_s is the desired "reflectance" for each channel at each spatial pixel, and E_λ is a measure of the average irradiance.

$$\underline{\text{"TOPOGRAPHIC"}} \text{ term } \quad T_s = \frac{1}{128} \sum_{1}^{128} \log (DN_{s,\lambda}) \qquad (2)$$

in the spatial domain

$$\underline{\text{"IRRADIANCE"}} \text{ term } \quad E = \frac{1}{N} \sum_{1}^{N} \log (DN_{s,\lambda}) \qquad (3)$$

in the spatial and spectral domain <u>for each λ</u>

Equation (1) in a logarithmic form, can be rearranged as follows:

$$\log(R_{s,\lambda}) = \underset{\text{"A"}}{\log(DN_{s,\lambda})} - \underset{\text{"B"}}{\text{Avg.}(\log_\lambda)} - \underset{\text{"C"}}{\text{Avg.}(\log_s)} + \underset{\text{"D"}}{\text{offset}} \qquad (4)$$

This also can be thought of as

Output spectrum = raw spectrum - average spectrum - pixel brightness + image brightness

where all are in logarithmic form (see Fig. 4).

RESULTS

Anhydrite (gypsum)

AIS-2 Run 604 at lines 650-730 crossed over the Ludwig open pit in the Triassic anhydrite (gypsum) beds. The open area of the pit, together

with the (white) spoil dumps gave a relatively pure, large target for analysis, covering two patches about 15 x 15 pixels each.

Figures 1A-F show the several steps of the processing and analysis. Figures 1A,B are a portion of the RAW data seen in a MULTI32 presentation. Figures 1C,D represent the same data after "cleaning-up" with DEST32 and DESPIKE operations. Figures 1E,F show the result of the ANDY32 log-residual process, now revealing the two dark patches (between the letters A,B,C) in channels 76, 77, and 78 corresponding to the low reflectance of gypsum in those wavelengths (1945, 1956, 1966 um). Figures 2A,B complete the analysis with a graphical presentation of selected 2 x 2 pixel areas emphasizing this lowered reflectance. A second broad low appears centered at channel 100 (2200 um).

Figure 2B should be compared with Figs. 5B and 6B, both showing ground spectra of the pit area taken with the GER VIRIS field grating spectrometer. Only the area of the spectrum from 1945 to 2380 um is used by channels 76-117 of AIS-2. This area is stippled on Fig. 5B and enlarged to cover all of Fig. 6B, so that a direct comparison may be made between the AIS-2 "residual-reflectance" and the ground equivalent. The second broad low appears at 2220 um in the ground spectrum (Fig. 6B).

Limestone

AIS-2 Run 602 lines 100-180 passed directly along the strike length of the Mason Valley limestone, a steeply-dipping formation on the west flank of the vertically-plunging Ludwig anticline. In our field spectral work we have noted that on many limestone outcrops the surfaces do not show "limestone" (calcite) spectra, but these are rather more clay-like. Figures 5F and 6F are examples of this and show O-H absorbance more typical of a mixed-layer illite-chlorite phase. Other spectra show a montmorillonite clay to be the surface composition. This is probably residual clay from dissolution of the limestone, or "mud" from summer thunder storms.

Figure 2C shows the log-residual results using MULTI32 with absorptions (black) at channels 107-112 (2275-2329 um), much shorter than channel 113-114 typical of calcite. This may reflect more of a magnesian-rich carbonate (dolomite), although the ground VIRIS spectra of Fig. 6D show the typical very sharp peak at 2339 um (channel 113) of calcite.

Hydrothermal Alteration

AIS-2 Run 604 at lines 1310-1390 crosses almost at right angles over the thin, WNW-trending zones of hydrothermally-altered quartz monzonite of the Yerington batholith, immediately south of the creek bed along which runs the E-W Mickey Pass road. This area is called Ann Mason. (The same run at its northern end also passes over the MacArthur zone of comparable mineralization).

Figures 3A,B show the log-residual displayed with MULTI32, with a darkened strip (in the lower half of each image) in channels 97-101 (2169-2211 um), with a secondary darkening of channels 109-115 (2300-2360 um). Sericite is a major component of this alteration at this site (Dilles, 1983) and our field VIRIS spectra show a minimum at 2204 (channel 100) and another at 2355 um (channel 114, Fig. 6E). Alunite (Fig. 6A) with a minimum at 2173 (channel 97) would be a better match with the AIS-2 data

(channel 97-101) but is unknown from any ground samples within several miles of this locality.

AIS-2 Run 604 at lines 1225-1305 shows the total absence of any O-H in the log-residuals display (Fig. 3C) using MULTI32. This is in agreement with field observations and is confirmed also by a lack of absorptions in the 2.2 um channel of the NS 001 TMS scanner, flown concurrently with the AIS-2.

CONCLUSIONS

1. AIS-2 has severe vertical striping but this can be removed by histogram-matching, column by column.

2. AIS-2 shows random low-valued (but non-zero) pixels, generally located in the darker (lower radiance) areas. Some 1-2% are brighter than average (but are not 255 DN). Most of these can be removed by a 3 x 3 (spatial) mean-matching kernel, with a "replacement" tolerance of 30 DN.

3. AIS-2 can be directly related to ground-acquired VIRIS spectra, if the "outcrop" shows a significant percentage of ("lag") rock fragments, or has been bulldozed clear of surface debris. Fine dust-silt between (and under) the surface fragments invariably has a VIRIS spectrum of a montmorillonite clay. Some mixed-layer ("illites") show also in this fine material.

4. Significantly, AIS-2 flight data from over rocks known to show no O-H in surface VIRIS spectra, do not show any AIS-2 minima attributable to O-H. This was not so clear in the 1985 AIS-1 data due to a higher noise component (see Fig. 3D).

5. Direct confirmation of dolomitic limestone outcrops with calcite/dolomite spectra from the AIS-2 data (Mason Valley limestone) is occasionally possible (Fig. 3A,B).

REFERENCES

Dilles, J.H., 1983, The petrology and geochemistry of the Yerington batholith and the Ann-Mason porphyry copper deposit, western Nevada, Unpublished Ph.D. thesis, Applied Earth Sciences Department, Stanford University, 600 pp.

Einaudi, M.T., 1977, Petrogenesis of the copper-bearing skarn at the Mason Valley mine, Yerington district, Nevada: Econ. Geol. 72, p. 769-795.

Green, A.A., and Craig, M.D., 1985, Analysis of aircraft spectrometer data with logarithmic residuals: Proc. AIS Data Analysis Workshop, April 8-10, 1985, G. Vane & A.F.H. Goetz, eds., Jet Propulsion Lab, Cal. Tech., Pasadena, California, p. 111-119.

Lyon, R.J.P., 1986, Comparison of the 1984 and 1985 AIS data over the Singatse Range (Yerington) Nevada: Proc. Second AIS Data Analysis Workshop, May 6-8, 1986, G. Vane & A.F.H. Goetz, eds., Jet Propulsion Lab, Cal. Tech., Pasadena, California, p. 86-95.

Proffett, J.M., Jr., and Dilles, J.H., 1984, Geological Map of the Yerington district, Map 77, published by the Nevada Bureau of Mines and Geology, University of Nevada, Reno, Nevada. One page map in folder.

Roberts, D.A., Yamaguchi, Y., and R.J.P. Lyon, 1986, Calibration of various techniques for calibration of AIS Data: Proc. Second AIS Data Analysis Workshop, May 6-8, 1986, G. Vane & A.F.H. Goetz, eds., Jet Propulsion Lab, Cal. Tech., Pasadena, California, p. 21-30.

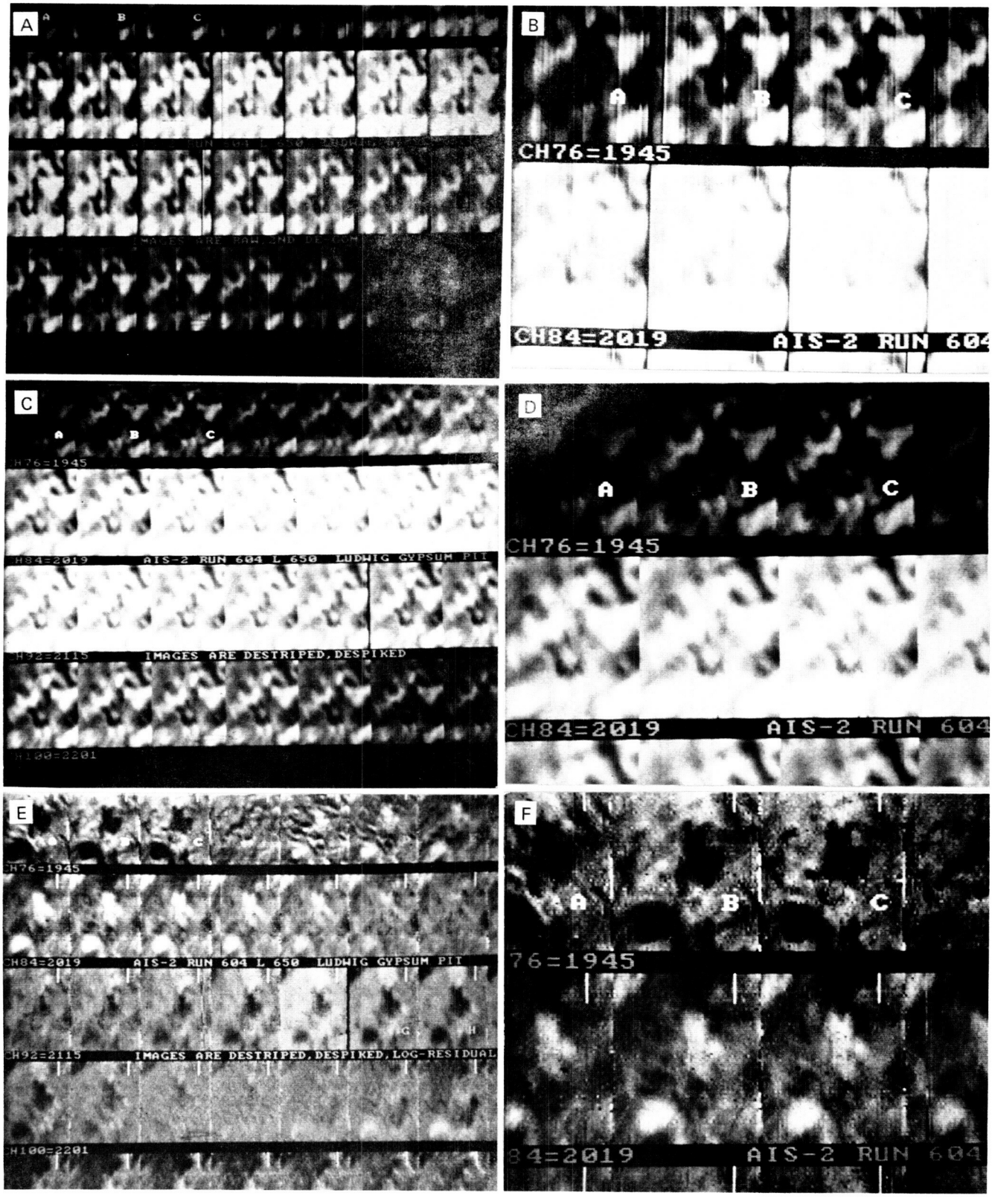

Figure 1. 64 pixel x 80 line flight segments, Run 604 lines 650-730, 29 September 1986. 32 contiguous channels (from #76-117) may be viewed using MULTI32. A. Raw AIS-2 data, 2nd decom.; B. 2X mag.; C. Destriped and despiked; D. 2X mag.; E. Log-residual "reflectance"; and F. 2X mag.

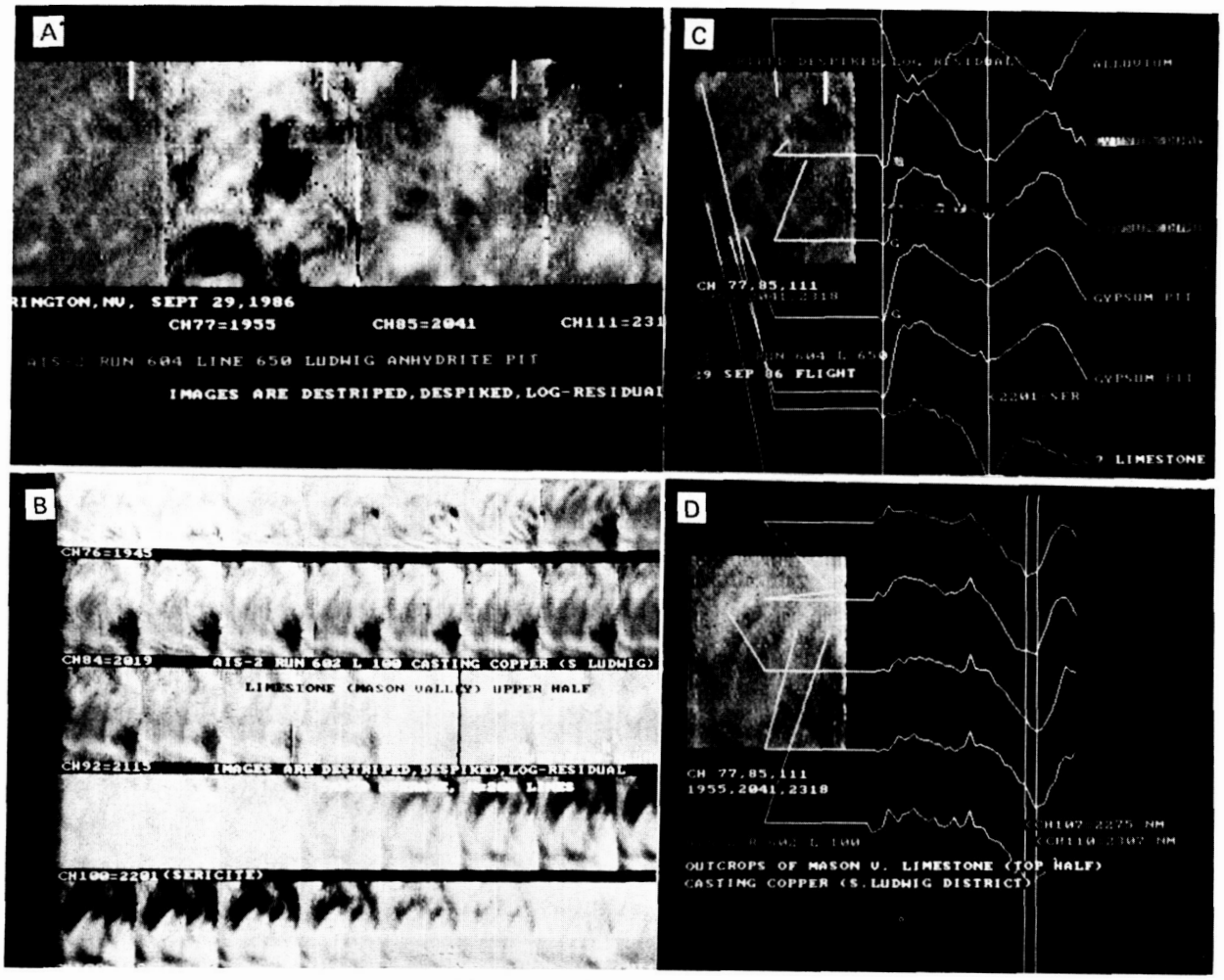

Figure. 2. Run 604, lines 650-730. TVAIS32 display of 64 x 80 flight segments. A. (left) B/W view of color composite. Three monochromes to right are CH 77,85,111. Selected to show max. spectral contrast. B. Same data (left) B/W view of color composite. Spectra (of 42 channels) keyed to specific pixel sites. Note steep rise (G) at CH 76-79 typical of gypsum. Broad "valley" at 2201 um is also gypsum. C. MULTI32 display, Run 602, lines 100-180, over limestone. Note black areas in CH 106-111 (C) and major absorptions at 2275,2307 (D).

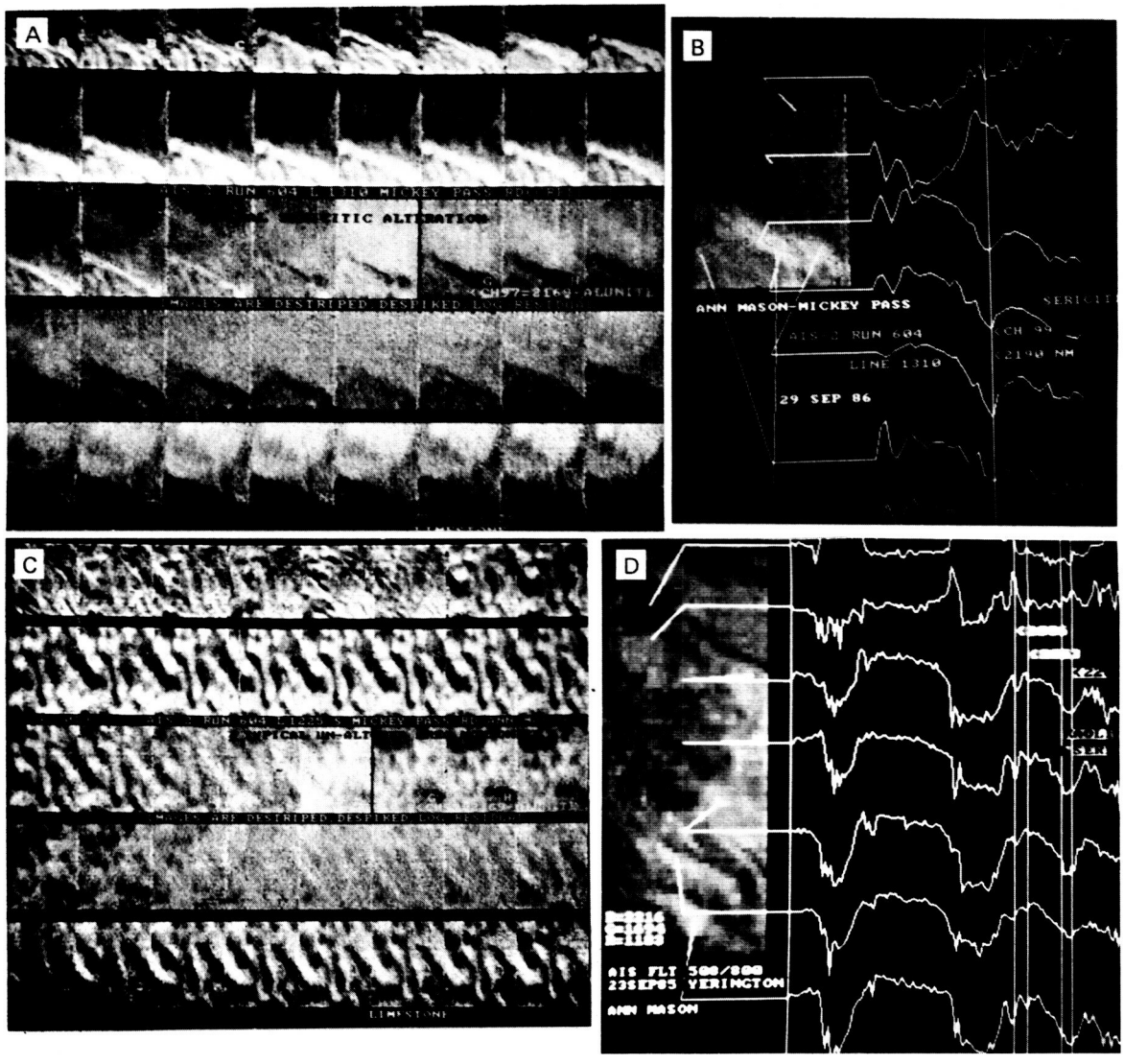

Figure 3. A. MULTI32 display, Run 604, lines 1310-1390, over area (Ann Mason) of typical sericitic alteration (lower half, oblique strip). Dark channels are 97-102, and 108-115. B. Graphs show CH 99, 2190 um minima. C. Similar display, Run 604, lines 1225-1305, same rock type but without significant sericite alteration on ground examination. D. 1985 AIS-1 graphical display of an area close to A,B above. Note high noise content (128 channels).

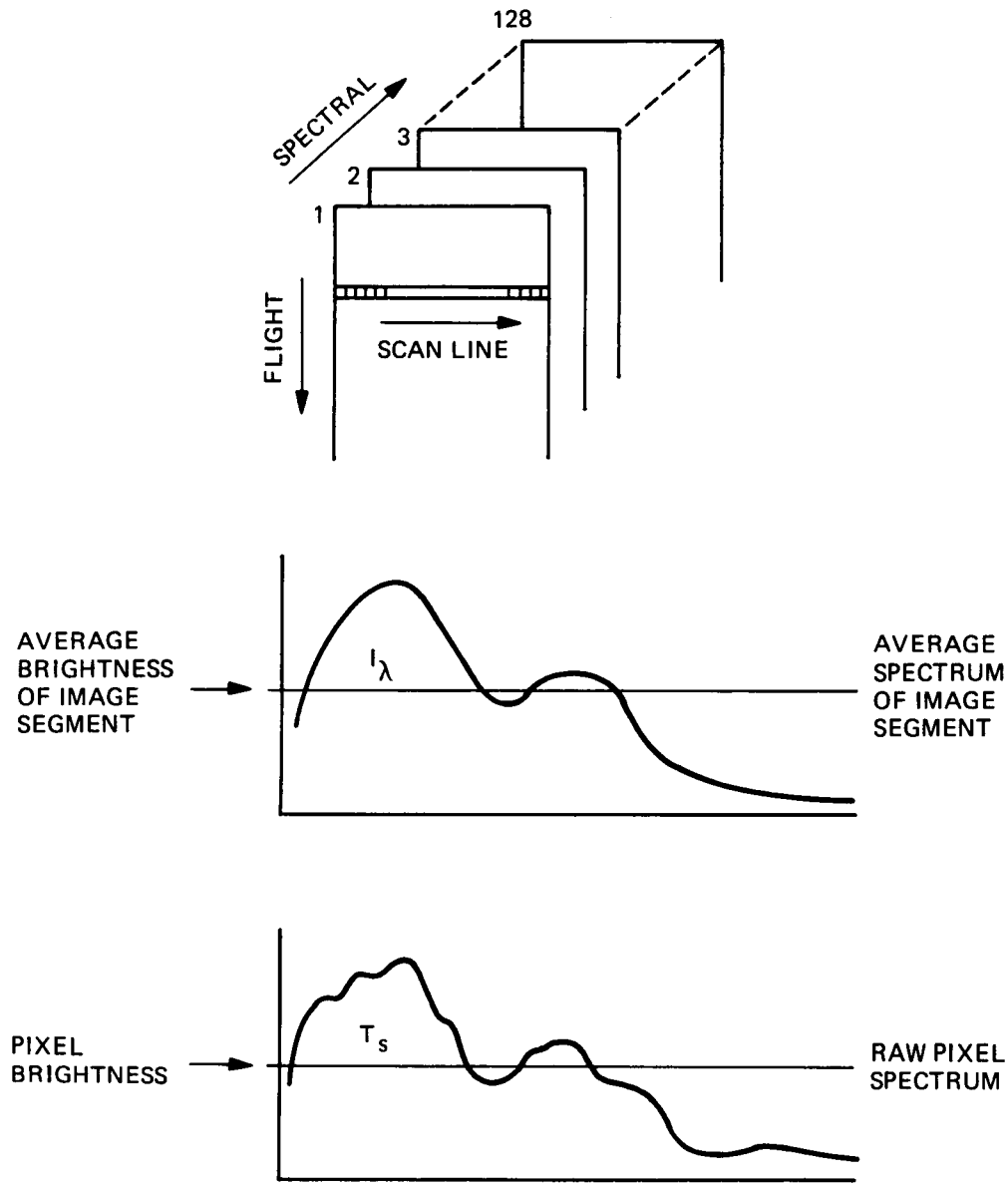

Figure 4. Diagrammatic representation of the log-residual "reflectance" processing.

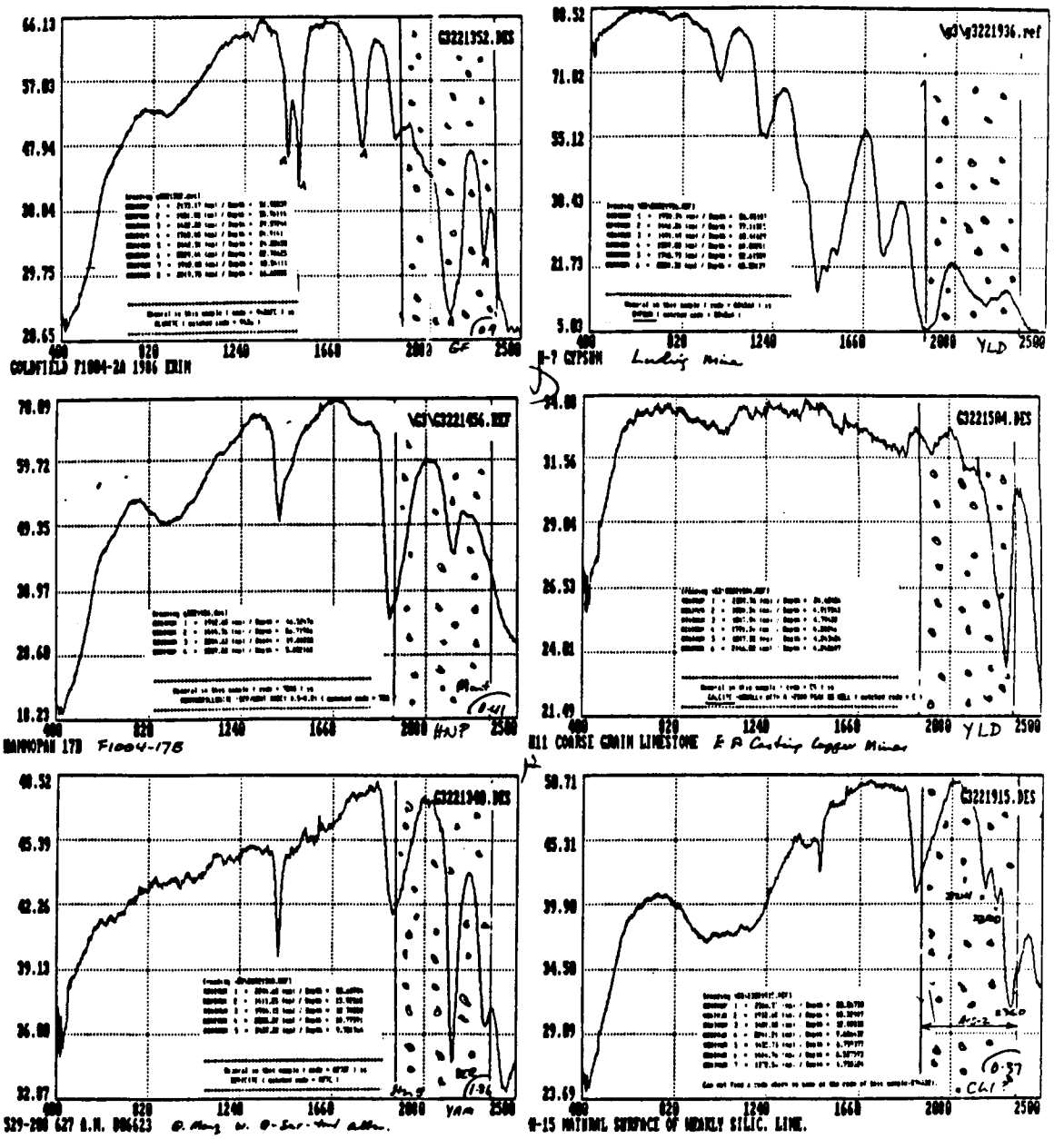

Figure 5. VIRIS ground spectra, full spectrum 400-2500 um. A. Goldfield, Nevada, alunite; B. Yerington (Ludwig) gypsum; C. Hannapah, Nevada, montmorillonite; D. Ludwig limestone; E. Ann Mason sericite; F. Natural surface of Ludwig limestone - note O-H features.

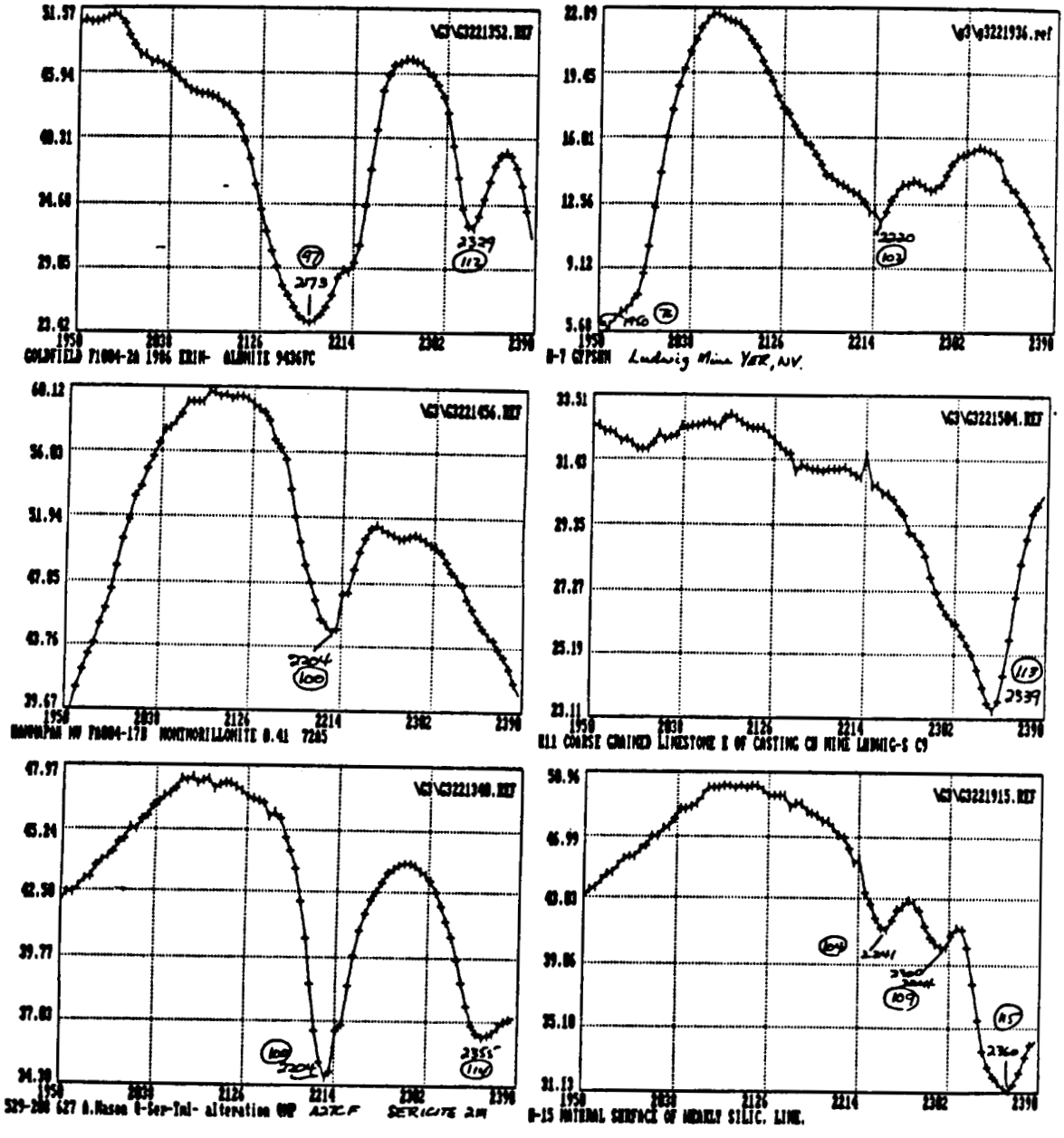

Figure 6. VIRIS ground spectra, portion equivalent to CH 76-117 of AIS-2 (1950-2390 um). A. Alunite; B. Gypsum; C. Mont-morillonite; D. Fractured surface limestone; E. Sericite; F. Natural surface of limestone.

N88-13768

PRELIMINARY RESULTS FROM AN INVESTIGATION OF AIS-1 DATA OVER AN AREA OF EPITHERMAL ALTERATION: PLATEAU, NORTHERN QUEENSLAND, AUSTRALIA.

STEVE MACKIN, TIM MUNDAY, & SIMON HOOK, Department of Geological Sciences, University of Durham, Durham DH1 3LE, England.

ABSTRACT:

AIS-1 data were acquired over the eastern edge of the Seventy Mile Range, north Queensland, Australia, as part of the US/Australia Joint Scanner Project. The area includes undifferentiated sequences of acid to intermediate volcanics and intrusives; meta-sediments; and a series of partially lateritised sedimentary rocks.

The study area exhibits a considerable spectral variability, after the suppression of striping effects commonly observed in AIS-1 data. Log residual, and Internal Average Relative Reflectance (IARR) analytical techniques were used to enhance mineralogically related spectral features. Both methods produce similar results, but did not visually highlight mineral absorption features due to processing artifacts in areas of significant vegetation cover. The enhancement of mineralogically related absorption features was achieved using a hybrid processing approach based on the relative reflectance differences between vegetated and non-vegetated surfaces at 1.2um & 2.1um. The result is an image with little overall contrast, but which enhances the more subtle spectral features believed to be associated with clays and epidote.

The AIS data was subject to interactive analysis using the SPAM package. Clear separation of clay and epidote (?) related absorption features was apparent, and the identification of kaolinite proved possible despite the presence of spectral effects caused by vegetation and second order overlap.

INTRODUCTION:

As part of the US/Australia Joint Scanner Project, two AIS flight lines were flown over the Plateau site in northern Queensland, Australia. The study area is located approximately 150 km SSW of Townsville (Figure 1). This paper describes some preliminary results arising from the analysis and interpretation of data from one of the two flight lines, which covers part of the Horse Creek Block (Figure 1). Limited ground data were available for this area, enabling us to evaluate a variety of processing techniques for highlighting mineralogically related absorption features.

GEOLOGICAL AND ENVIRONMENTAL SETTING:

The study area experiences a tropical climate, with warm dry winters and hot wet summers. Vegetation consists primarily of open Eucalypt and acacia woodland. Grasses, particularly spear grass (Heteropogon contortus), are the dominant understorey. The vegetation density is varied, and species distribution irregular.

The regional geological setting of the site is reviewed by Wyatt et al. (1971). The geology of the Horse Creek Block itself, is summarised in Figure 1. In the NE the area is dominated by Tertiary sandstones. Isolated mesas of lateritised Tertiary sediments are present throughout this part of the surveyed area. The Cambro-Ordovician Mount Windsor volcanics, of andesitic composition, outcrop in a north-south trend running across the central part of the block. Silicious shales and cherts of an equivalent age (the Cape River Beds) are present to the east of the flight line. Isolated outcrops of late Tertiary/early Quaternary shale and sandstone of the Campse beds are also present.

The Cambro-Ordovician volcanics and meta-sediments are intruded by a small leucogranite and an altered rhyolite body of a similar size. Both these intrusives are believed to be Permo-Carboniferous in age. The rhyolite has a mineralised brecciated margin with pervasive quartz-sericitic and minor kaolinitic and chloritic alteration. Laboratory spectra and corroborative XRD analysis of weathered samples from the rhyolite and the adjacent host volcanics, indicate the presence of kaolinite, sericite, chlorite, carbonate and epidote minerals (Figure 2).

AIS-1 DATA QUALITY AND PREPROCESSING:

Calibrated AIS-1 data from the Plateau site exhibit the effects of a time dependent, non-uniform individual detector response, and a vibrating detector array (Vane 1986). In the imagery these are manifest as vertical and horizontal striping respectively. Two radiometric correction techniques were applied to the data to suppress the striping.

Vertical striping and data "spikes" were removed in two steps. Firstly, the effects of extreme column values, due to dead detector elements, and spectral "spikes" or discontinuities, such as those that occur at boundaries between different grating positions, were removed by averaging in the spectral direction. Secondly, the data were spatially averaged, tying the individual column means to the overall band mean to suppress the vertical striping.

Horizontal stripes in the imagery, arising from a vibrating detector array at the focal plane of the spectrometer, were removed by spatial averaging within a moving window of lines down the image. Residual striping

remained after both techniques had been applied to the data.

The AIS data for the Plateau area also exhibits the effects of spectral contamination in the 1.6 to 2.4μm region due to a second order overlap from shorter wavelengths between 0.8 and 1.2μm. The cause of this problem, as described by Vane (1986), is related to a switch in the position of a blocking filter, and the efficiency of the diffraction grating in second order. The presence of a contribution in second order to that in first order between 1.6 and 2.4 is seen in variations in the CO2 absorption bands at 2.0 and 2.06μm down the flight line, and as a broad absorption feature around 2.28μm, particularly where vegetation is present. These effects are similar to those described by Huntington et al. (1986) for other Australian AIS-1 data sets.

AIS DATA ANALYSIS FOR THE HORSE CREEK BLOCK SUBSCENE:

1. Data Normalisation and Image Enhancement:

Examination of the raw radiance data for the Horse Creek Block sub-scene revealed no apparent mineralogical information. This has been ascribed to the diminution of mineralogical absorption features due to a combination of atmospheric effects, weathering, and the presence of vegetation cover (Huntington et al. 1986). Several processing methods were examined for the suppression of background and atmospheric effects, and the enhancement of subtle mineral related spectral features. These included the log residual technique (Green and Craig 1985), and the Internal Average Relative Reflectance (IARR) method (Kruse et al. 1985).

Both the log residual and IARR processing methods require the normalisation of the data prior to spectral curve averaging which produces a standard or reference curve for the whole scene. The standard curve is then divided into the the normalised pixel curve to produce a residual relative reflectance curve for each pixel. The results produced from either method are essentially the same. Both have the advantages of :

i) requiring no ground data for their implementation;
ii) being computationally simple to implement;
iii) producing output in the form of relative reflectance suitable for use with the SPAM package;
iv) being applicable to different terrains and environments.

However, they also exhibit several disadvantages, including:

i) the removal, or even suppression, of the spectral response of dominant cover types which may be important;
ii) the creation of spectral "artifacts" which could be interpreted as real absorption features and/or spectral highs;
iii) the apparent suppression of more subtle mineral absorption features in the 2.2μm wavelength region when vegetation is present (Huntington et al 1986, & Cocks and Green 1986).

Although the first two drawbacks mentioned above cannot be corrected for (only recognised and accepted as possible sources of error), the third problem can be overcome.

Figure 3 shows a fanned set of AIS data (covering bands 100 to 112, between 2.14 and 2.26μm) for the area depicted in Figure 1. These images have been processed by the log residuals method using all 128 bands. The lack of observable mineral related absorption features around the 2.2μm wavelength region is apparent, particularly in the area coincident with, and adjacent to, the rhyolite. This contrasts with what might have been expected given the nature of the spectral features depicted in Figure 2. A similar problem was reported by Huntington et al. (1986) for another Australian AIS data set processed in the same way.

Vegetation and rock components within the scene behave very differently at 1.2μm and 2.1μm. The differences between these two spectral regions are more marked for a vegetated surface than for one which is bare. Vegetation gives a high response at 1.2μm relative to that at 2.1μm. This contrasts with only a slightly higher response at 1.2μm relative to 2.1μm for bare surface materials. Normalising the data using log residuals or the IARR method, forces bare surfaces to give a higher spectral response in the region around 2.2μm when compared with one which is vegetated. In effect, subtle spectral features are masked by sharp contrasts between vegetated and bare surfaces. In Figure 3, the darker grey levels represent areas of dense vegetation cover, whilst lighter areas correspond to partially vegetated and bare surfaces. Subtle mineral absorption features, whilst being present, are not very apparent.

Two alternative methods were utilised in an attempt to suppress the marked contrasts between different cover types and to enhance the more subtle spectral features of interest.

The first of these has been outlined by Huntington et al. (1986), and represents an extension of the log residuals technique. Instead of processing all 128 spectral bands of the AIS data, those covering the atmospheric water absorption bands were excluded from the analysis. The remaining spectral bands in the three atmospheric windows were then processed separately using the log residuals method. This approach does remove the relationship between

the 1.2 and 2.1μm regions as described above, to enhance mineral related absorptions. However, absorptions relating to vegetation are still present and although the major mineral absorption features are more apparent, they may still be confused with those corresponding to vegetation.

A second technique, a hybrid approach, known as Ratio Group Normalising (RGN), was also tried which attempts to normalise the data relative to several standard curves rather than one individual curve. Pixels were grouped into ten classes based upon a simple ratio of bands 1 and 97, and then standard curves were generated for each group using the IARR method of Kruse et al. (1985). Grouping was based on a division of the ratio range generated by all pixels, into ten equally spaced increments. The main advantage offered by this approach is that standard curves are generated for pixels with spectral curves of the same general order of magnitude. This has the effect of enhancing the more subtle absorption features contained in the data. However, problems can arise when a particular ratio grouping may contain a single or predominant land cover type. The technique would lead to the suppression of spectral features relating to that cover type.

A fanned AIS data set processed using the RGN method is depicted in Figure 4. The images cover the same spectral bands and the same area as shown in Figure 3. In contrast to the data processed using log residuals on 128 bands, subtle absorption features are more apparent. For example, the area corresponding to the rhyolite shows an absorption centred around 2.2μm (see Fig. 4). Vegetation related spectral features have also been suppressed. It should be noted that the ratio groupings seem to be correlated to varying vegetation/bare surface proportions. Pixels falling in the high ratio value groups correspond to heavily vegetated surfaces, whilst low ratios relate to areas of sparse vegetation cover. The role of dead vegetation in this simple model remains undetermined. Further work is required to confirm the utility of the ratio grouping method.

2. Spectral Feature Analysis:

Output from the data normalising and enhancement processing was analysed extensively using the NASA/JPL SPAM (SPectral Analysis Manager) package configured to run on an I2S Model 75 image processing system running S600 software.

The initial phase of analysis involved automatic clustering of IARR processed AIS data over the 2.12 to 2.41μm wavelength range. The intention was to flag areas with more subtle spectral features which might be related to certain mineral groupings. In the subscene covering part of the Horse Creek Block, three main spectral clusters were observed, giving mean class curves as indicated in colour slide 1 (see pocket at the end of proceedings). Two of the three curves show absorption features with minima around 2.2μm (yellow), and 2.3um (purple).

Using the SPAM 'FIND' function, pixels with curves matching (in amplitude terms) those determined by SPAM 'CLUSTER', were flagged in the image. The result is also shown in colour slide 1 (see pocket at the end of proceedings). The rhyolite, and some adjacent areas of altered andesite, are highlighted as having absorptions centred around 2.2 and 2.3μm respectivly, which is as expected. Areas of dense vegetation cover are also flagged (as light blue) in the image (see colour slide 1). These results suggest that a preliminary analysis of AIS data using an unsupervised cluster may identify areas that warrant further more detailed investigation.

Average spectral curves generated from 3 x 3 pixel areas on the rhyolite, and over the altered andesite, were compared with mineral spectra held in the SPAM library. Close correspondence was noted between that for the rhyolite and Kaolinite. ORD (kaolinite), as shown in colour slide 2 (see pocket at the end of proceedings). The rhyolite curve is shown in yellow, and the Kaolinite.ORD curve in blue. A closer match was also noted with Kaolinite.F.1.(kaolinite, mica, quartz) and the rhyolite (not shown). The slight displacement in the position of the rhyolite minima relative to the library spectra may be linked to the vibrating detector array in the AIS spectrometer (see Cocks and Green 1986).

A mean spectral curve for an area mapped as epidote altered andesite was closely tied with a library curve for Calcite.C.2 (Figure 5), rather than one for epidote as might have been expected. However, this apparent mismatch could, in part, be accounted for by spectral contamination due to second order overlap. Much of the andesite is covered by open Eucalypt woodland with a dry grass understory of varying density. The spectral curve shown in Figure 5 is likely to represent a mixture of a first order absorption relating to the mineralogy, a broad cellulose linked absorption feature around 2.25μm commonly found in dry vegetation (Figure 6), and a "pseudo" absorption at about 2.28μm which represents the second order contribution from a water absorption feature in vegetation at 1.14um (see Figure 6). The latter component has been described elsewhere by Huntington et al. (1986). The combined effect of these elements could explain the broad nature of the absorption shown in the AIS data.

CONCLUSIONS:

Although only a preliminary analysis of the AIS data for the Plateau site has been carried out, we can draw several conclusions from this work.

1. The time-varying detector response, a vibrating detector array, and contamination from spectral order overlap severely degrade the radiometric quality of data acquired over the Plateau site.

2. Mineral related absorption features in the 2.0 to 2.4μm region become apparent when background and atmospheric effects are suppressed. Log residuals computed on data for this atmospheric window only, rather than on all 128 bands, are partially effective for such purposes. An alternative, computationally simple approach known as the Ratio Group Normalising method, successfully enhances subtle mineral related absorption features when all 128 bands are utilised.

3. Preprocessed, corrected (normalised) AIS data is effectively analysed using SPAM.

4. Clear separation of major mineral groupings is possible using normalised AIS data. In certain limited cases, the identification of particular clay mineral species (eg. kaolinite) is possible using these data.

5. Second order spectral contamination, combined with absorption features specific to dry vegetation, mask absorptions diagnostic of some minerals. These problems are particularly acute in the case of pixels with appreciable amounts of vegetation cover.

6. Further work is necessary to evaluate various methods designed to suppress the effects of second order spectral contamination. Similarly, additional study is required to elaborate on the spectral mixing processes that occur in the heavily weathered, partially vegetated environment, characterised by the Plateau site.

ACKNOWLEDGEMENTS:

We would like to thank Esso Minerals Australia Ltd., and particularly Dave Tucker and Eric Swarbrick, for their help whilst in Australia. The kind assistance of colleagues at CSIRO and JPL over the past year, is also greatly appreciated. We would also like to thank BP Minerals Int. Ltd., notably Mike Davies and Kathy Bowden, for their considerable support re. the installation of SPAM. S.M. is currently supported by a NERC Studentship (GT4/86/GS/28). This work is being carried out under the auspices of a NERC Special Topic Research Grant (GST/02/126) which T.J.M. and S.J.H. gratefully acknowledge.

REFERENCES:

Cocks, T. C. and Green, A. A. 1986. Airborne spectroradiometry: The application of AIS data to the detection of subtle mineral absorption features. Proc. 2nd

Airborne Imaging Spectrometer Data Analysis Workshop, May 6-8, 1986, JPL Publication 86-35, pp. 52-62.

Green, A. A. and Craig, M. D. 1985. Analysis of aircraft spectrometer data with logarithmic residuals. Proc. of the Airborne Imaging Spectrometer Data Analysis Workshop, April 8-10, 1985, JPL Publication 85-41, pp. 111-119.

Huntington, J. F., Green, A. A., Craig, M. D. and Cocks, T. D. 1986. Preliminary geological investigation of AIS data at Mary Kathleen, Queensland, Australia. Proc. 2nd Airborne Imaging Spectrometer Data Analysis Workshop, May 6-8, 1986, JPL Publication 86-35, pp. 109-131.

Kruse, F. A., Raines, G. L., and Watson, K. 1985. Analytical techniques for extracting geological information from multichannel airborne spectroradiometer and imaging spectrometer data. Proc. Int. Symp. Remote Sensing of Environment: 4th Thematic Conf. Remote Sensing for Exploration, April 1-4, 1985, pp. 309-324.

Vane, G. 1986. Introduction to the proceedings of the second airborne imaging spectrometer (AIS) data analysis workshop. Proc. 2nd Airborne Imaging Spectrometer Data Analysis Workshop, May 6-8, 1986, JPL Publication 86-35, pp. 1-16.

Wyatt, D. H., Paine, A. G. L., Clarke, D. E., Gregory, C. M., and Harding, R. R. 1971. Geology of the Charters Towers 1:250,000 Sheet Area, Queensland. Bureau of Mineral Resources, Report No. 137, 85pp.

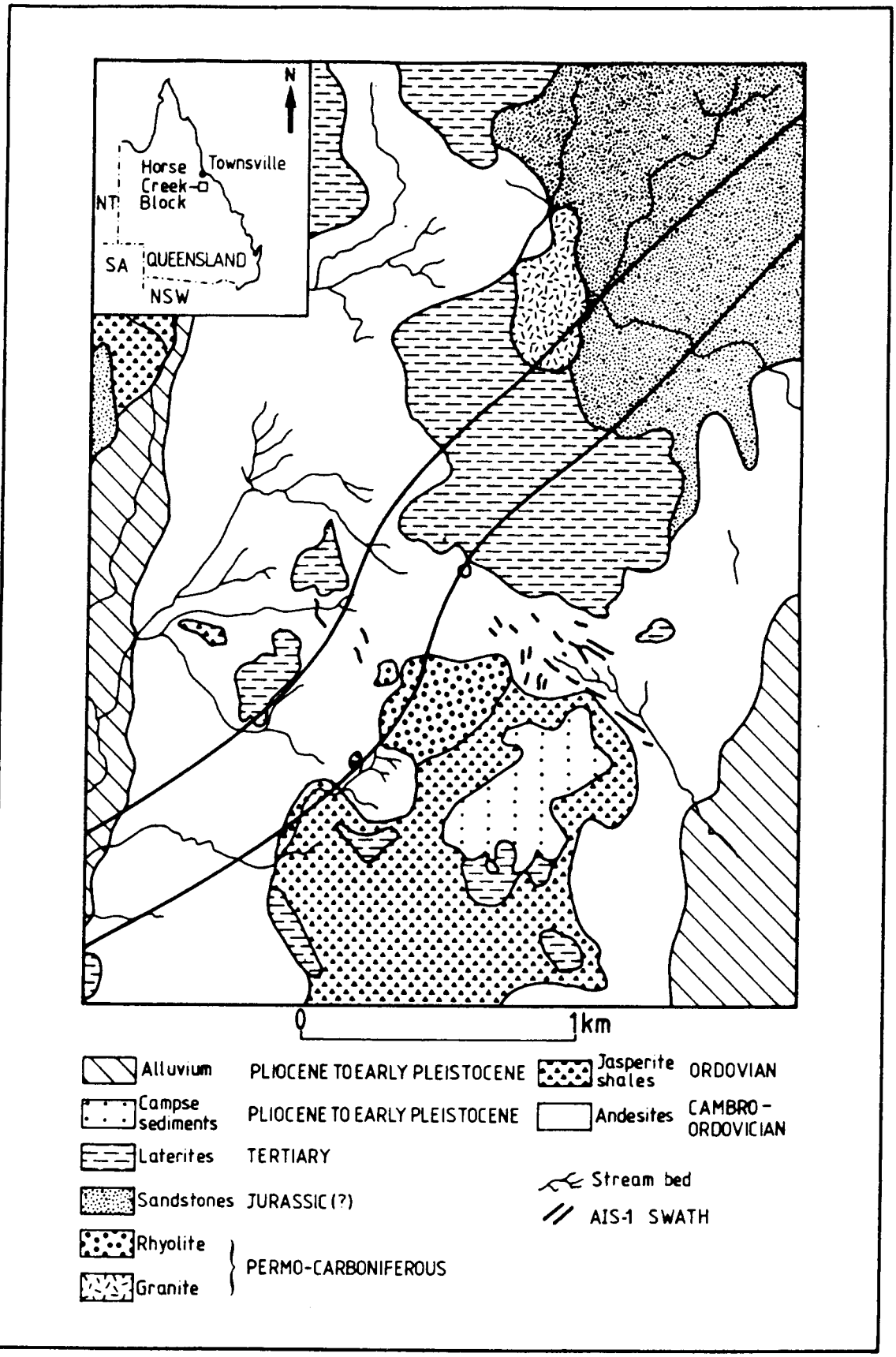

Figure 1: Generalised geology of the Horse Creek Block, northern Queensland, Australia.

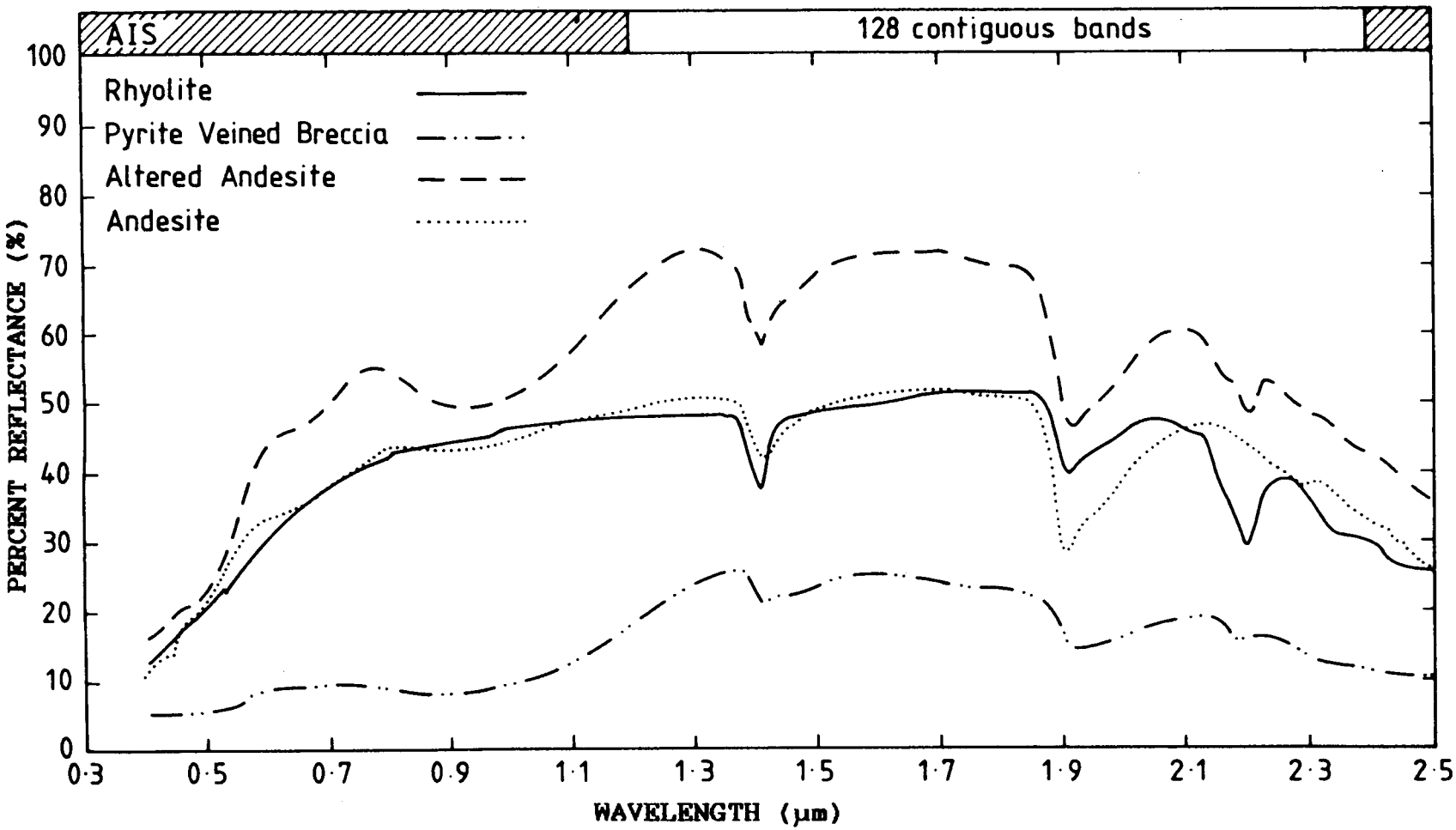

Figure 2: Laboratory spectra (0.4 - 2.5µm) taken from weathered surfaces of four samples acquired in the Horse Creek Block

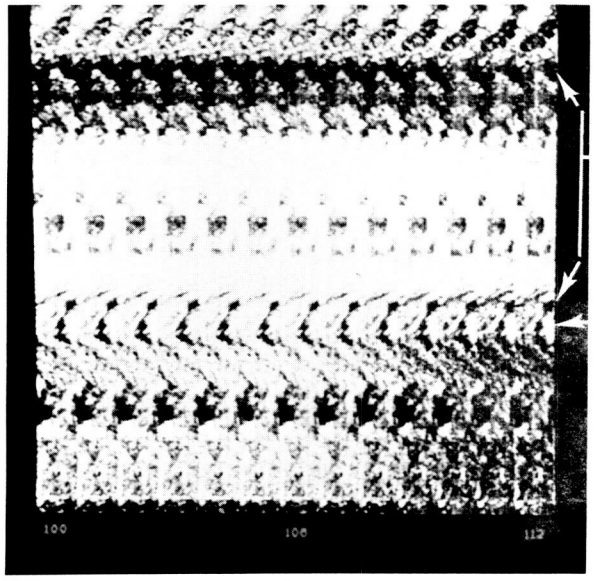

Figure 3: Fanned set of log residual images covering bands 100 to 112 (2.14 - 2.26μm), computed from all 128 AIS channels.

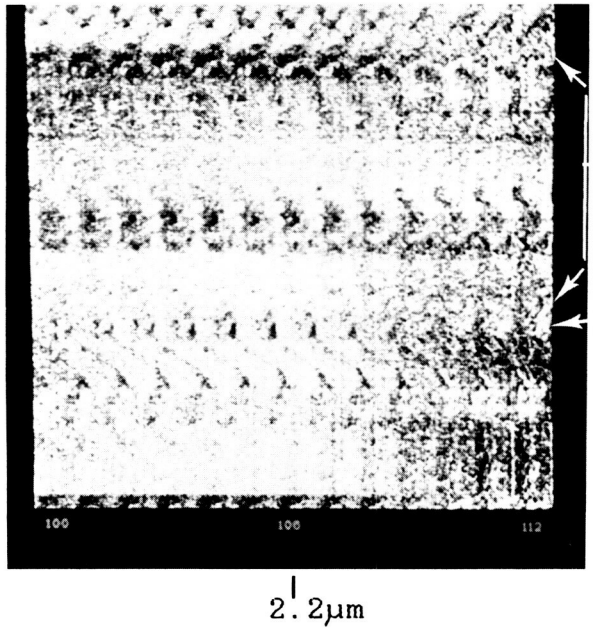

Figure 4: Fanned set of Ratio Group Normalised images covering bands 100 to 112 (2.14 - 2.26μm), computed from all 128 AIS channels.

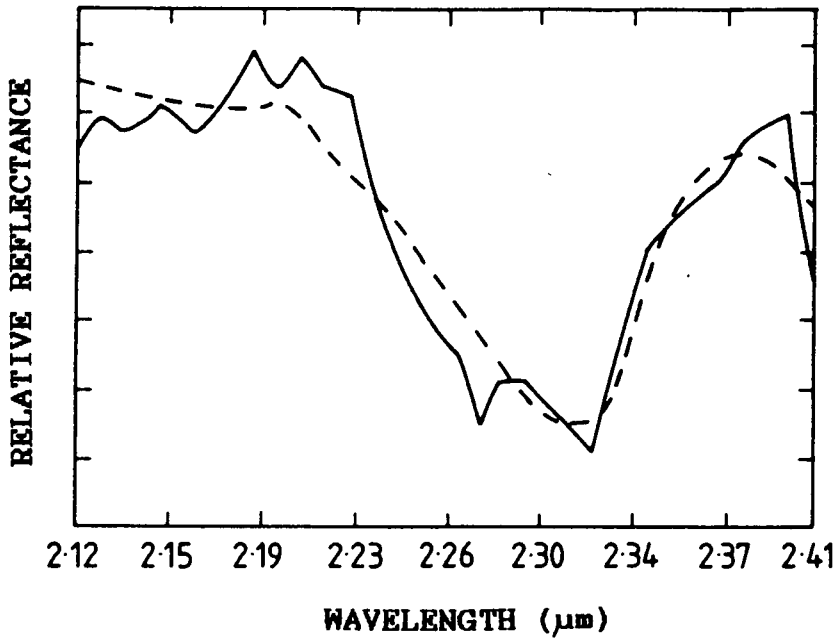

Figure 5: Plot of averaged AIS spectral curve from area of epidote altered andesite (solid line), matched with SPAM library curve for Calcite.C.2 (dashed line).

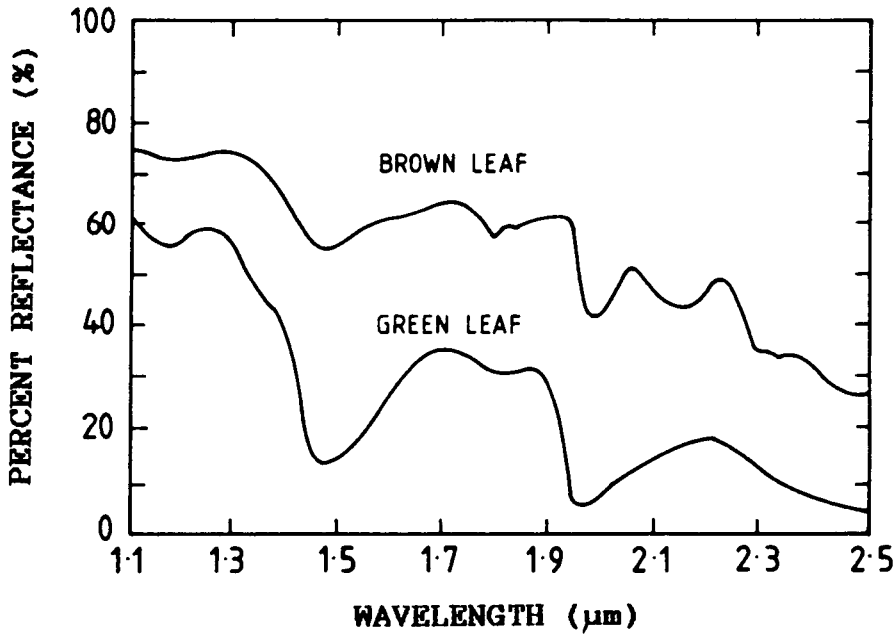

Figure 6: Representative spectral curves for green and dry vegetation. Note the steep drop off in the curve for dry vegetation around 2.25μm. This is related to a cellulose absorption feature.

CAUSES OF SPURIOUS FEATURES IN SPECTRAL REFLECTANCE DATA

ROGER N. CLARK and TRUDE V.V. KING, U.S. Geological Survey, MS964, Box 25046 Federal Center, Denver, CO 80225

ABSTRACT

Several techniques are becoming common in the analysis of imaging spectrometer data that can lead to spurious absorption features or to changes in the position, width, and shape of actual absorption features. It is a common practice to calibrate AIS or other imaging spectrometer data by averaging each pixel along the flight line. The average is used to calibrate the spectral data by dividing the spectrum at each pixel by the average. If some pixels in the data set contain an absorption, then the average will also show an absorption. Some AIS data has had problems with wavelength stability from one scan line to the next (e.g. Vane, 1986 and references therein) which can produce spurious features with some analysis methods. If a pixel has a spectrum with an absorption having a different position or width than the spectrum used in a ratio, then the ratio can produce a spurious absorption at a different position and width than the true absorption feature. An average spectrum ratioed to each pixel will produce band shifts, and changes in width or shape. If continuum removal is performed by subtraction rather than division, band positions can also be shifted.

SPURIOUS BAND SHIFTS AND FEATURES

Consider two spectra that are to be ratioed. In the analysis of imaging spectrometer data, the spectrum on the numerator would likely be a spectrum from an individual pixel or a small group of pixels having similar spectral features. The spectrum on the denominator usually represents some form of calibration data set. The calibration could consist of an average of all pixels in the scene or the log residual (e.g. Green and Craig, 1985). In cases such as these the denominator spectrum could have residual features in the spectra due to the minerals on the surface. The denominator spectral features can be different than those in the numerator if there is a wavelength instability in the instrument from pixel to pixel, or if there are minerals with slightly different absorptions that when combined will have features that are broadened and/or shifted from the spectral features in individual spectra.

The denominator spectrum could also result in spectral errors if the calibration for the imaging spectrometer data was based on field spectrometer and/or laboratory spectra of samples for which the spectral resolution and/or wavelength calibration was different than that of the imaging system. Errors could also occur if the small spot(s) measured by the field spectrometer or the laboratory samples were not spectrally representative of the much larger pixel(s) measured by the imaging instrument.

Example of the spectral errors produced by the above mechanisms are shown in Figures 1, 2 and 3. If the denominator spectral feature is shifted from the numerator spectrum, a "dip/rise" is observed (Figure 1). The resulting absorption band is shifted in wavelength, as in the case of Figure 1, to shorter wavelengths. If the demoninator spectrum has a broader feature than the numerator spectrum, but no wavelength shift, then the ratio shows a feature at the same position but it is narrower than the characteristic absorption of the mineral (Figure 2).

If the denominator and numerator spectra have an absorption edge as in hematite at visual wavelengths and there is a wavelength shift or instability, then the ratio can produce absorption features that are not real (Figure 3). In Figure 3, the strongest spurious feature is located at 0.56 μm.

BAND POSITION MEASUREMENTS

In the analysis of band positions, a strongly sloping continuum influences the wavelength of minimum reflectance. For example, in lunar spectra, the slope of the continuum is often so strong the 1-μm pyroxene absorption has no minimum in reflectance. Thus, it is a common practice to remove the continuum to find the correct band center (see Clark and Roush, 1984 and references therein). Clark and Roush (1984) showed that for reflectance spectra, it is theoretically correct to remove the continuum by division, not subtraction.

While the analysis of imaging spectrometer data is increasingly done by computer, "paper and pencil techniques" are still common when trying to understand individual spectra. A common practice to remove a continuum graphically is to draw a continuum and then draw a parallel line that is tangent to the lower part of the curve (Figure 4A). In this case, the tangent occurs near 1.35 μm. However, this method is a subtraction method. Figure 4B shows the spectrum with the continuum subtracted while Figure 4C shows it with the continuum removed by division. The division method shows a minimum near 1.1 μm. The continuum removal methods are not comparable.

CONCLUSIONS

Spurious features can be produced in the spectral data from imaging spectrometer instruments if there are instrumental wavelength instabilities or from various calibration techniques. Spurious features could cause misidentification of minerals or plant species. If there are wavelength instabilities in the instrument, the wavelengths should be registered (e.g. by using known absorption bands such as atmospheric lines that do not shift) before any other operations are performed on the data.

The analysis of band positions should use the same methods. If laboratory comparison data were analyzed for band position with one method, and imaging spectrometer data with another, there could be

misidentification of species. As the composition of mixture changes, the continuum slope could change and the band position would appear to change if analyzed by the subtraction method. Similarly, the shape of a band and its continuum can change as a function of grain size, again causing a spurious band shift if analyzed by the subtraction method.

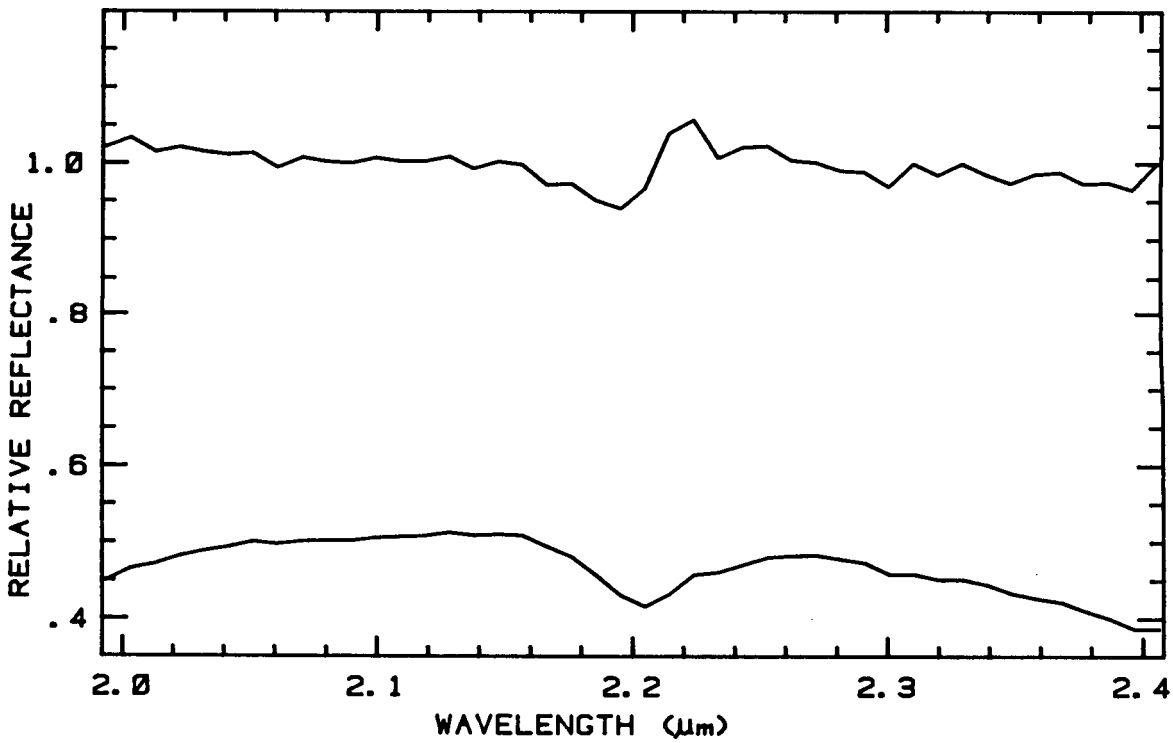

Figure 1. This figure shows one of the possible spectral errors that can result from pixel shifting in calibration images. The lower spectrum in this figure is a laboratory spectrum of montmorillonite convolved to AVIRIS spectral resolution. The upper spectrum represents the laboratory spectrum of montmorillonite convolved to AVIRIS spectral resolution divided by the same spectrum which has been shifted one data channel to the right (longer wavelengths). This (upper) spectrum results in a dip/rise feature near 2.2-μm region which is not representative of the characteristic absorption feature of montmorillonite. The presence of these features could lead the analyst to incorrectly identify mineralogy.

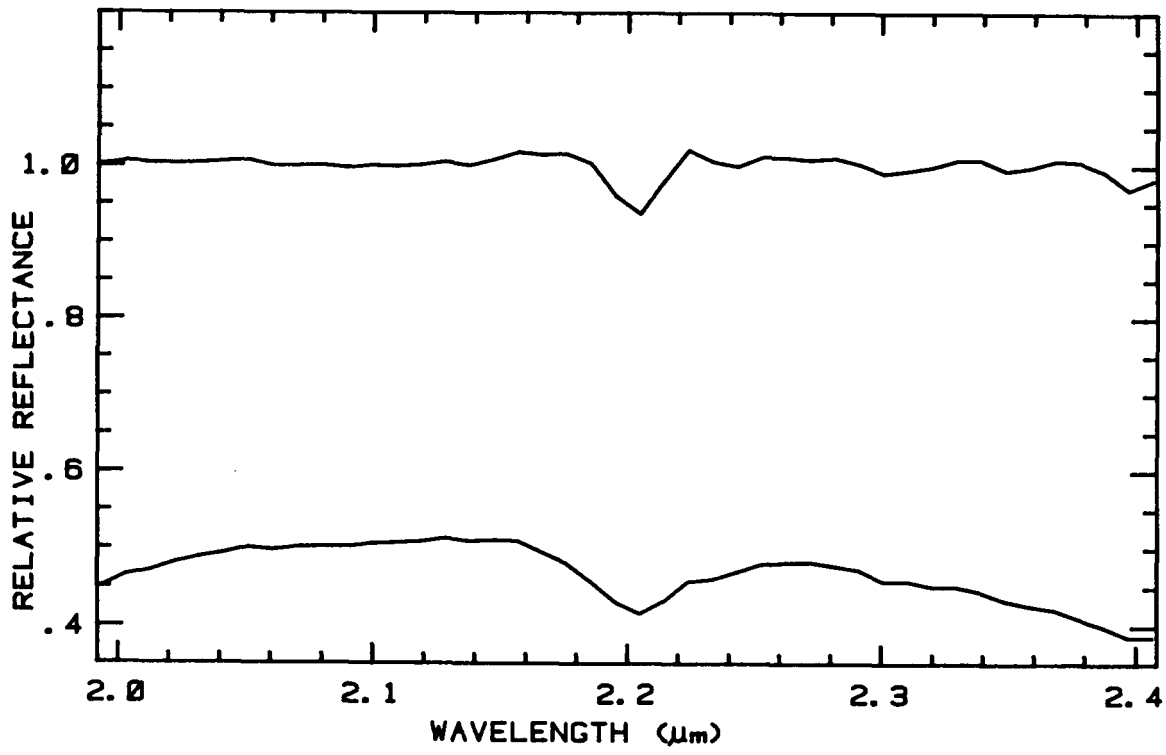

Figure 2. This figure shows that the width of an absorption band can be altered by incorrectly determining calibration images. The lower spectrum in this figure represents a standard laboratory montmorillonite that has been convolved to AVIRIS spectral resolution. The upper spectrum results from dividing the laboratory montmorillonite convolved to AVIRIS resolution by the average of the montmorillonite (AVIRIS resolution) and the same spectrum shifted two data channels to the right plus the montmorillonite (AVIRIS resolution) shifted two data channels to the left (short wavelength). The resulting spectrum shows that the minimum of the 2.2-μm absorption has not shifted, but the absorption feature is narrower than in the standard montmorillonite (AVIRIS spectral resolution) spectrum.

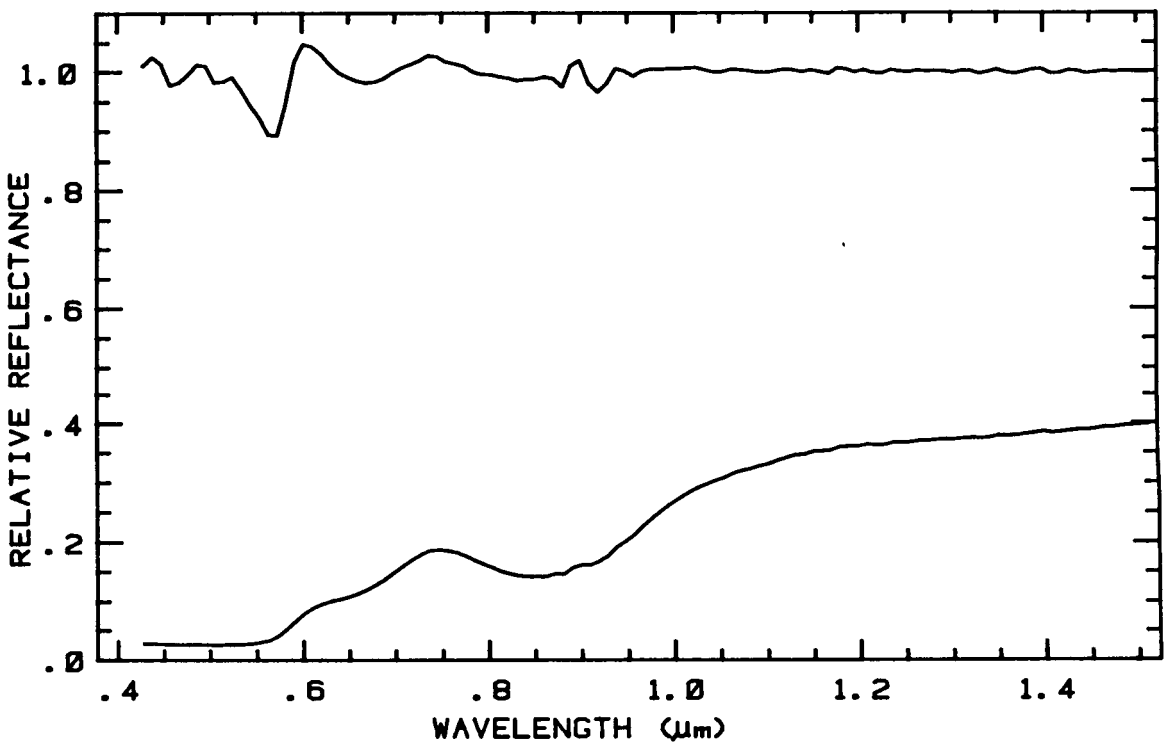

Figure 3. The upper spectrum in this figure shows an additional type of spectral error that can result from using incorrect calibration files in the data reduction process. The lower spectrum represents a laboratory sample of hematite that has been convolved to AVIRIS spectral resolution. The upper spectrum results from dividing the laboratory hematite (AVIRIS resolution) by the average of the same hematite spectrum plus ones that have been shifted two data channels to the left and right. Spurious features are produced at wavelengths less than 1 μm. The strongest spurious feature is located at 0.56 μm. The position and widths of the absorption features in the upper spectrum would not allow for the correct identification of hematite.

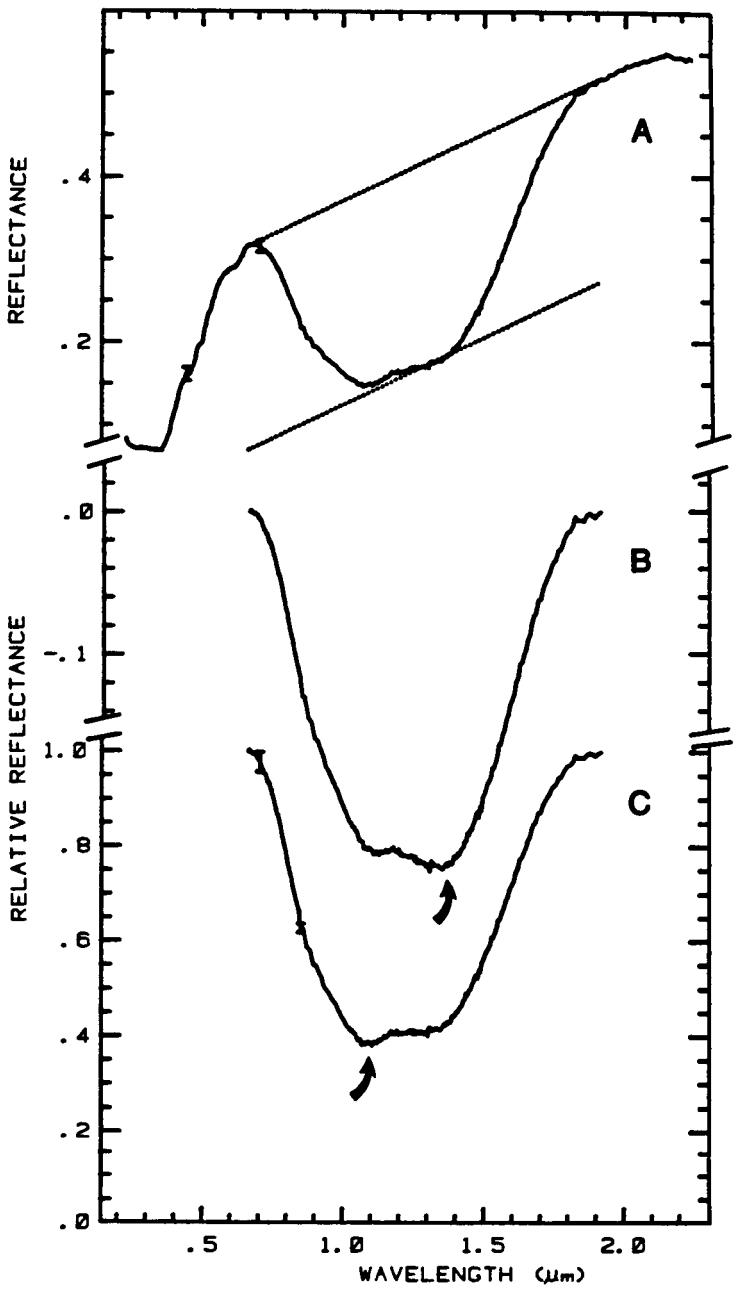

Figure 4. This figure illustrates differences in band center determinations depending on the method used in continuum removal in the data reduction process. Figure 4A shows a spectrum of olivine using a graphical method for continuum removal. The upper line is a straight line continuum whose end-points are defined by the reflectance on either side of the absorption band. The bottom line is drawn parallel to the upper continuum line and is tangent to the absorption feature. Figure 4B shows the resulting spectrum when the continuum is removed by subtracting the continuum from the original olivine spectrum. This method determines that the band center is located at 1.35 μm. Figure 4C illustrates the spectrum of olivine with the continuum divided. This method is the correct method for band center determination. This method determines that the band center occurs at 1.05 μm.

REFERENCES

Clark, R.N. and T.L. Roush (1984) Reflectance Spectroscopy: Quantitative Analysis Techniques for Remote Sensing Applications, *J. Geophys. Res.*, 89, 6329-6340.

Green, A.A. and Craig, M.D. (1985) Analysis of aircraft spectrometer data with logarithmic residuals, in Proceedings of the Airborne Imaging Spectrometer Data Analysis Workshop, April, 1985, (G. Vane and A. Goetz, eds.) JPL Publication 86-35, 111-119.

Vane, G., 1986, Introduction to the proceedings of the second airborne imaging spectrometer (AIS) data analysis workshop, JPL Publication 86-35, 1-16.

AUTOMATIC CONTINUUM ANALYSIS OF REFLECTANCE SPECTRA

ROGER N. CLARK, TRUDE V.V. KING, and NOEL S. GORELICK, U.S. Geological Survey, MS964, Box 25046 Federal Center, Denver, CO 80225

ABSTRACT

A continuum algorithm based on a "Segmented Upper Hull" method (SUH) is described. An upper hull is performed on segments of a spectrum defined by local minima and maxima. The segments making a complete spectrum are then combined. The definition of the upper hull allows the continuum to be both concave and/or convex, adapting to the shape of the spectrum under study. The method performs multiple passes on a spectrum by segmenting each local maximum to minimum and performing an upper hull. The algorithm naturally adapts to the widths of absorption features, so that all features are found, including the nature of doublets, triplets, etc. The algorithm is also reasonably fast on common minicomputers so that it might be applied to the large data sets from imaging spectrometers.

INTRODUCTION

Data from imaging spectrometers requires fast analysis of the continuum and features in a spectrum. To date, analyses of such data have not employed the analysis techniques used on reflectance spectra obtained in the laboratory. For laboratory spectra, the analyst chooses continuum tie points and uses an algorithm to derive the continuum based on straight line segments or a curve such as a cubic spline. Some researchers have used the "upper convex hull" method (Green and Craig, 1985) for automatic determination of a continuum on Airborne Imaging Spectrometer (AIS) data. However, the upper convex hull is limited to spectra having certain characteristics (which happened to be common in the limited spectral coverage in AIS data) and is not always applicable. For example, in snow (water ice), the continuum in the near infrared is concave (e.g. Clark, 1981) and cannot be analyzed using the upper convex hull. Other spectra appear to have portions of the spectrum requiring a concave continuum (e.g. see alunite, Figure 1A, 1.3 to 2.2 μm and the examples of kaolinite in Green and Craig [1985] in the 2.2-μm region). As imaging spectrometer data with greater spectral coverage become available, more sophisticated continuum analysis is necessary. A continuum analysis should adapt to different types of absorptions present in a spectrum, such as very broad bands like that in olivine near 1 μm to the very sharp absorptions seen in OH-bearing minerals, and spectra with combinations of both sharp and broad absorptions.

AUTOMATIC CONTINUUM ANALYSIS

We approached the problem by analyzing how a spectroscopist chooses a spectrum, and modified it to use a method that can be both

fast and consistent in a computer algorithm. The algorithm is best described by example.

First the upper hull is determined (Figure 1A) on the original spectrum. The upper hull is derived by first finding the maximum in the entire spectrum (the "global maximum"), and then finding the line segments that bound the spectrum so that all points lie on or below the hull. The spectrum is divided into two segments on each side of the global maximum and treated independently. The local maximum away from the global maximum is found next for a spectral segment. A line is then computed between the global maximum and the local maximum. The data are divided by the continuum and checked to see if any points have values greater than 1. If a point does, this a relative peak and is marked as a new continuum tie point, and a new continuum is computed. This process is repeated until no points fall above the continuum. The local maximum becomes the new global maximum and the process of finding the next local minimum and local maximum is repeated until each end of the spectrum is reached. The method allows the continuum to be both concave and convex, but does not allow the slope to change sign or equal zero except at the global maximum.

An example of an upper hull is shown in Figure 1A and the continuum removed data in Figure 1B. Note how the hull follows local maxima to produce a continuum that is both convex and concave. The upper convex hull would have produced a straight line from 1.3 to 2.26 μm having major minima near 1.4, 1.8 and 2.2 μm and between them local maxima all below the continuum. The SUH presented here greatly reduces this problem. Also, the SUH method can be extended to analyze the fine structure that occurs in many absorption features.

Next, the continuum removed spectrum (e.g. Figure 1B) is divided into spectral segments bounded by continuum tie points (where data = 1.0 in the continuum removed spectrum). An example of tie points are labeled a and c in Figure 2A. Then, the minimum between the two tie points is found (labeled b in Figure 2A). The segment a-b is treated as an isolated spectrum and the upper hull derived. Segment b-c is treated likewise. Thus, there are two "Segmented Upper Hulls" that converge on the local minimum. The local maxima closest to the minimum on each side (labeled x and y on Figure 2A) are connected by a straight line. The data are divided by the continuum and checked to see if any points fall above the continuum and if so, the continuum tie points adjusted.

If there are no local minima between the data = 1.0 continuum tie points and the minimum, then the continuum was fully removed in the last iteration. Therefore, the continuum is defined to follow the data through the band (e.g. Figure 2A, bands near 1.75 and 2.3 μm).

The continua derived for the segments are spliced together and the spectrum is divided by the resulting continuum (Figure 2B, solid line). This continuum removed spectrum is then treated as a new spectrum and again fed to the SUH routine. The iterative process continues until a straight line is derived (e.g. Figure 2C).

The SUH routine will naturally follow the maximum data points, thus each small minimum due to noise fluctuations could be treated as a band. We chose to reject any minimum below a threshold and force the continuum to follow these small variations. The threshold is chosen in one of two ways: the standard deviation error bar value if it exists (as it does from our lab spectrometer) or a constant value chosen by the user (we chose a default of 1%).

The iterative SUH routine has been tested on laboratory spectra and laboratory spectra convolved to AVIRIS sampling intervals and resolution. The greatest number of iterations was found to be 3 in the case of alunite. The upper hull on the original spectrum counts as the first iteration. Three iterations take about ½ second of cpu time on an HP9000/500 series cpu (where processing speed is between a VAX 750 and 780 VMS system with floating point accelerator) on complicated spectra like the alunite. However, we have yet to optimize the code, so this value represents an upper limit to the possible compute time. The alunite analysis produced 17 minima between continuum tie points.

Our next step is to analyze each minimum for band position, width, asymmetry, depth and continuum level. That algorithm is already written and will be integrated with the SUH routine. The resulting output of the combination will be a list of spectral features. The continuum removal plus feature analysis is estimated to take less than 1.5 seconds of cpu time per AVIRIS spectrum on the HP9000, so that an entire AVIRIS 550x550 pixel scene can be analyzed in about 5 days of cpu time.

CONCLUSIONS

A fast, reliable continuum analysis routine has been formulated using the upper convex hull routine on segments of a spectrum. The speed of the routine is such that it is feasible to run on existing minicomputers on large amounts of data such as from AVIRIS.

Correlation of the feature analysis with a database of known features derived from laboratory spectra will result in maps of mineral occurrence. The non-selective nature of the algorithm will also select absorptions due to vegetation, atmospheric absorptions and any other natural or unnatural objects in the scene. The algorithm is not sensitive to the strength of the absorptions (except that they must be above the noise level) so that if features due to a particular mineral are present but weak due to low abundance or masking by opaques, it can still be identified. The algorithm might also be used on spectra in other wavelength regions such as the mid-infrared.

Images could be produced using "spectral intensity" (the depths of the absorption bands relative to those of the pure mineral) of specific minerals. The spectral intensity is correlated to the abundance and grain sizes of the minerals in the optical surface.

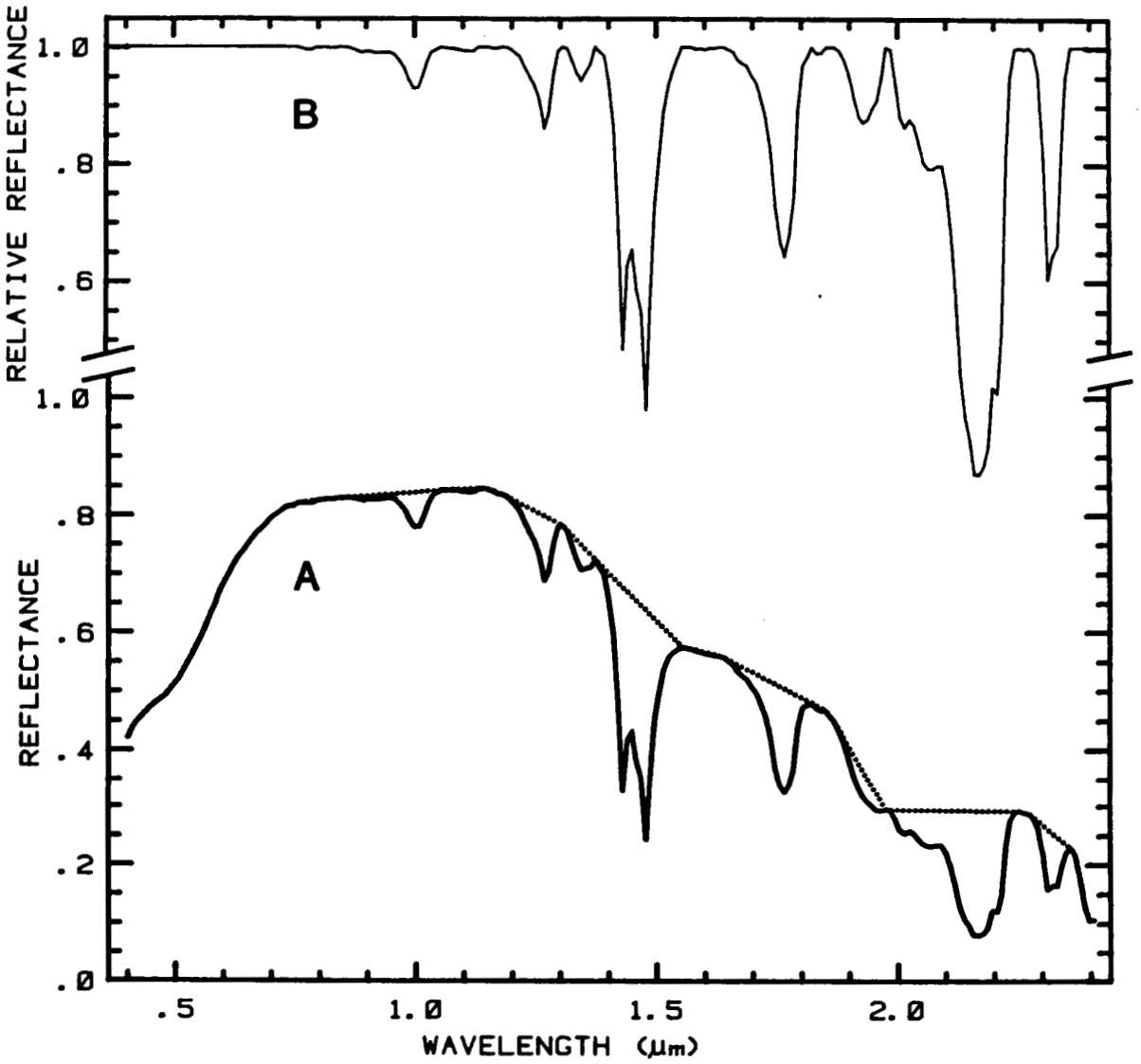

Figure 1. The reflectance spectrum of alunite convolved to AVIRIS resolution is shown with the upper hull (dotted line in A) and the reflectance divided by the upper hull continuum (B).

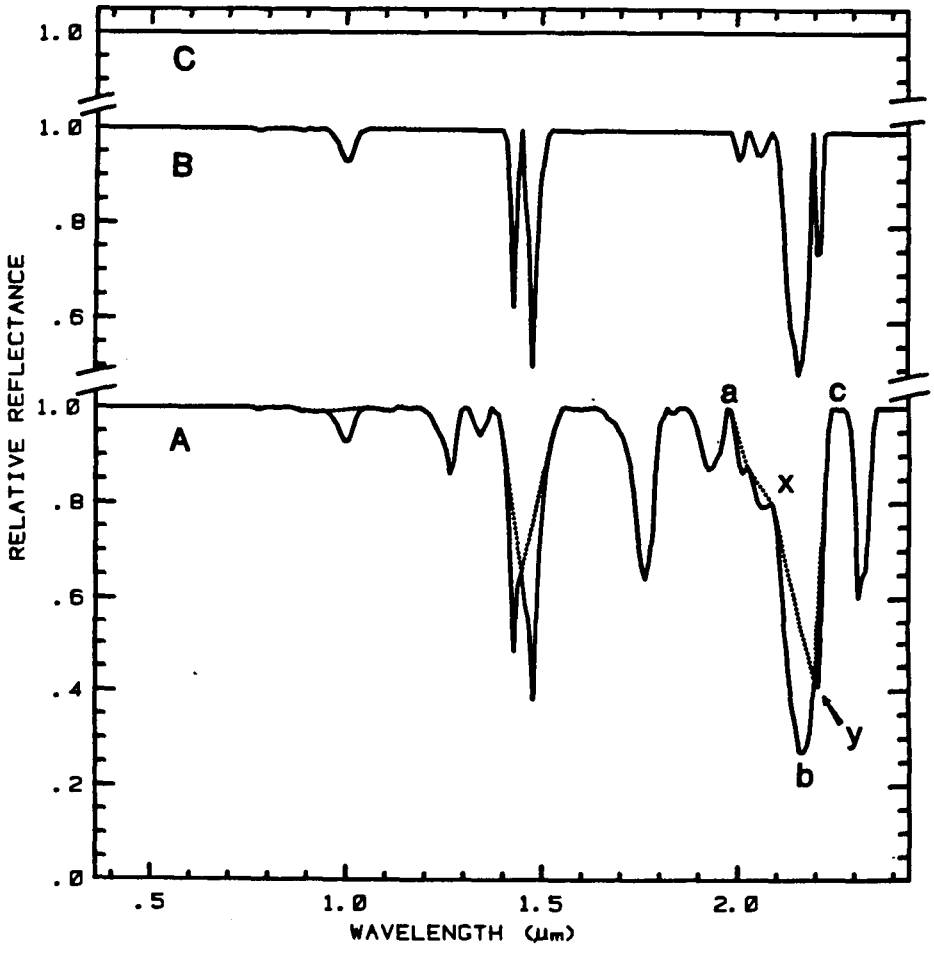

Figure 2. The "Segmented Upper Hull" (SUH) is shown for the second iteration (A, dotted line) compared to the continuum removed first iteration (A, solid line). The third iteration SUH is shown in B, but it overlies the continuum removed second iteration data so when the third iteration SUH is divided into the data a straight line is derived (C). Each iteration analyzes finer structure associated with the complex absorption bands until the continuum removed data equals 1.0.

REFERENCES

Clark, R.N. (1981) Water frost and ice: The near-infrared spectral reflectance 0.65-2.5 μm, *J. Geophys. Res.*, **86**, 3087-3096.

Green, A.A. and Craig, M.D. (1985) Analysis of aircraft spectrometer data with logarithmic residuals, in Proceedings of the Airborne Imaging Spectrometer Data Analysis Workshop, April, 1985, (G. Vane and A. Goetz, eds.) JPL Publication 86-35, 111-119.

ANALYSIS OF AIRBORNE IMAGING SPECTROMETER DATA FOR THE RUBY MOUNTAINS, MONTANA, BY USE OF ABSORPTION-BAND-DEPTH IMAGES

DAVID W. BRICKEY, JAMES K. CROWLEY, and LAWRENCE C. ROWAN,
U.S. Geological Survey, Mail Stop 927, Reston, Virginia 22092

ABSTRACT

Airborne imaging spectrometer-1 (AIS-1) data were obtained for the Ruby Mountains of southwestern Montana, an area of amphibolite-grade metamorphic rocks that have moderate rangeland vegetation cover. Although rock exposures are sparse and patchy at this site, soils are visible through the vegetation and typically comprise 20-30 percent of the surface area. Channel-averaged low-pass spatially filtered data were used to construct band-depth images for diagnostic soil/rock absorption bands. Sets of three such images were combined to produce color-composite band-depth images. This relatively simple approach did not require extensive calibration efforts and was effective for discerning a number of spectrally distinctive rocks and soils, including soils having high talc concentrations. The results show that the high spectral and spatial resolution of AIS-1 and future sensors holds considerable promise for mapping mineral variations in soil, even in moderately vegetated areas.

INTRODUCTION

The Ruby Mountains in southwestern Montana are underlain by Precambrian metasedimentary rocks. Many different lithologies are present, including dolomitic and calcitic marbles, hornblende gneiss, as well as other varieties of gneiss and schist, volcanic flows, diabase dikes, and alluvium (Heinrich, 1960). Numerous mineral species having diagnostic near-infrared spectral absorption features occur in the area (Table 1). The rangeland vegetation, including grasses, forbs, and shrubs, comprise 70-80% of the surface cover, soils the other 20-30%.

The chief objectives in selecting this study area were to assess the use of AIS-1 data for detecting minerals present in metamorphic rocks and to develop image processing techniques for dealing with moderate amounts of rangeland vegetation and limited rock exposures. Absorption-band-depth (ABD) images provided a relatively simple but effective approach for identifying a number of rocks and minerals present along the AIS-1 flight lines.

DATA COLLECTION AND ANALYSIS

Four flight lines of AIS-1 data were acquired in July 1985 covering approximately 100 km of groundtrack. This paper focuses on a portion of

one of the flight lines, nearly 6-km in length along an area with about 300 m of relief, which was sampled intensively during August 1986. Figure 1 is a geologic map for the area covered by the 6 km data set.

Table 1. AIS-1 wavelengths used in generating ABD images

Channel Combination	Wavelength		Minerals detected
1	2.151-2.179 μm	shoulder 1	Dolomite, talc, tremolite, Mg-mica
	2.347-2.366 μm	shoulder 2	
	2.300-2.319 μm	minimum	
2	2.328-2.347 μm	shoulder 1	Talc, tremolite, Mg-mica
	2.394-2.403 μm	shoulder 2	
	2.366-2.384 μm	minimum	
3	2.123-2.142 μm	shoulder 1	Illite, muscovite, illite/smectite, vermiculite, kaolinite
	2.263-2.282 μm	shoulder 2	
	2.189-2.207 μm	minimum	
4	2.291-2.310 μm	shoulder 1	Calcite, antigorite
	2.366-2.384 μm	shoulder 2	
	2.338-2.347 μm	minimum	
5	2.263-2.282 μm	shoulder 1	Dolomite, talc, tremolite, Mg-mica
	2.347-2.366 μm	shoulder 2	
	2.319-2.328 μm	minimum	
6	2.328-2.338 μm	shoulder 1	Talc, tremolite
	2.366-2.384 μm	shoulder 2	
	2.347-2.366 μm	maximum	
7	2.133-2.151 μm	shoulder 1	Same minerals as channel 3 above
	2.198-2.217 μm	minimum	

The AIS data were vertically de-striped and normalized for topographic and albedo effects by using an equal energy procedure (Jet Propulsion Laboratory, 1985). A 3x3 box filter was then applied to reduce high-frequency noise in the spatial dimension. A relative reflectance data set was generated from the box-filtered data by using the whole-image average spectrum as a divisor. ABD images were produced by using 2 to 3 channels from both shoulders and 2 to 3 channels from the minimum of each absorption feature so as to increase the signal to noise. The sum of all the channels for the shoulders was divided by the sum of the channels for the minimum to produce an ABD image. Table 1 lists the wavelengths of channels used in constructing the ABD images.

RESULTS AND DISCUSSION

Figure 1 is an index map to be used in conjunction with color slides nos. 3 and 4 located in the pocket at the end of the proceedings. The first slide is a color-composite ABD image generated

from the box-filtered AIS data by use of channel combinations 1, 2, and 3 in table 1 as red, green, and blue (RGB), respectively. Note that combinations 1 and 3 both utilize channels that are widely separated in wavelength to define the band shoulders. This slide is referred to henceforth as the "wide-band" image. The second slide uses channel combinations 4, 5, and 2, as RGB (table 1) and is referred to as the "narrow-band" image. This second image was generated from the box-filtered relative reflectance data set.

Comparing the wide-band with the narrow-band images reveals several differences that merit explanation. Site A (fig. 1) on the wide-band image shows a pronounced orange anomaly that is completely absent in the narrow-band image. The anomaly results from high digital number (DN) values in the dolomite and MgOH images (channel combinations 1 and 2, table 1). However, there is no dolomite at this location. Instead, the high DN values probably result from a soil rich in Mg-mica and an especially heavy rangeland vegetation cover. The vegetation gives an anomalous "dolomitic" component in the wide-band image, which is eliminated in the narrow-band image. Figure 2 illustrates schematically that without a continuum removal, a vegetation spectrum appears to have an absorption feature at 2.32 μm. This highlights a general problem in the use of widely separated channels to define absorption band shoulders--the resulting ABD images may lose their specificity for distinguishing materials. On the other hand, because the spectral content is less constrained, wide-band images show more spatial detail over the entire image area. Narrow-band images tend to be spectrally flat, except for local areas that exhibit the absorption features defined by the channel selections.

Sites B and C (fig. 1) contain exposures of calcitic and dolomitic marble, respectively. The principal absorption band centers for these units are offset by only 20 nm and thus provide a fairly rigorous test of AIS spectral discrimination. The wide-band image does not discriminate successfully between the two carbonate minerals. However, the narrow-band image generated from the box-filtered relative reflectance data does separate the calcitic (orange pixels) from the dolomitic minerals (yellow-green pixels). AIS relative reflectance spectra for pixel blocks at sites B and C are shown in figure 3. Also shown in the figure is an AIS relative reflectance spectrum for site D, which had substantial amounts of talc in the soil. The diagnostic talc absorption band at 2.38 μm is apparent in the site D spectrum, as is the MgOH band near 2.31 μm, located essentially at the same wavelength as the major absorption band for dolomite. Because only a few AIS channels are suitable for defining the narrow 2.38-μm feature, separating talc from dolomite provides a rigorous test of the band-depth approach. An ABD image was made by use of a larger number of channels to examine the talc maximum in reflectance near 2.34 μm (table 1, channel 6). However, this feature is not very distinct in the natural soils and the image showed no improvement. Sites E and F (fig. 1) are tremolite-bearing dolomitic marble units that produce a talc-like signature on the two composite ABD images. Talc and tremolite are very similar in the 1.2- to 2.4-μm wavelength range covered by the AIS data and cannot be distinguished; however, they are separable in the 0.4- to 1.2-μm region.

Laboratory spectra for soils in the study area exhibit considerable spectral variation in the 2.1- to 2.4-μm wavelength range. However, because the absorbing soil minerals generally are intermixed with spectrally featureless quartz and feldspar impurities, the spectral differences between soils as seen in the noisy AIS-1 data are very subtle. For example, the most pronounced talc absorption feature shown in laboratory spectra for talc-rich soils collected from site D (fig. 1) has a total band depth of less than 5 percent reflectance. Because the ABD images were able to distinguish features having such low spectral contrast, it appears likely that improved signal to noise will eventually permit other soil types to be detected in areas that have comparable rangeland vegetation cover. Images were produced to examine soil AlOH absorption bands near 2.2-μm (table 1, channels 3 and 7); however, only broad surface areas exhibiting weak absorption were discernable (site G; fig. 1). The strongest 2.2-μm features were observed for a well-exposed, weathered, feldspar-rich pegmatite, shown in the wide-band image at site H (fig. 1).

Simple ratios of channels or groups of channels may be better suited for resolving some spectral features. Laboratory spectra for many soils collected in the study area produced 2.2-μm AlOH absorption bands that lacked a strong rise from the band center to longer wavelengths. This characteristic shape probably was caused by the presence of vermiculite in many soil samples. Channel combination 7, a ratio image of one set of channels divided by another set, improved discrimination of this type of feature. Because of the mineralogical complexity of the soils in the study area, it would have been difficult to predict the form of the 2.2-μm soil feature without field sampling.

CONCLUSIONS

Absorption-band-depth images created from relative reflectance AIS-1 data provide a simple but effective approach for distinguishing some metamorphic rocks and minerals. The use of such images requires that assumptions be made regarding the absorption features present in a study area. Such assumptions can be misleading, especially in situations involving complex mineral mixtures that produce unfamiliar spectral reflectance curves. On the other hand, narrow ABD images are extremely specific and may facilitate the digital enhancement of subtle soil spectral features in rangeland-type vegetated areas.

REFERENCES

Heinrich, E.W., 1960, Geology of the Ruby Mountains and nearby areas in southwestern Montana: in Pre-Beltian Geology of the Cherry Creek and Ruby Mountains Areas, Southwestern Montana: Montana Bureau of Mines and Geology Memoir 38, p. 15-40.

Jet Propulsion Laboratory, 1985, Science Investigators Guide to AIS Data: Jet Propulsion Laboratory, Pasadena, California, p. III-2.

Acknowledgments: The authors would like to thank Fred Kruse and Dennis Krohn for their assistance and sharing of software used to process the AIS data in this study.

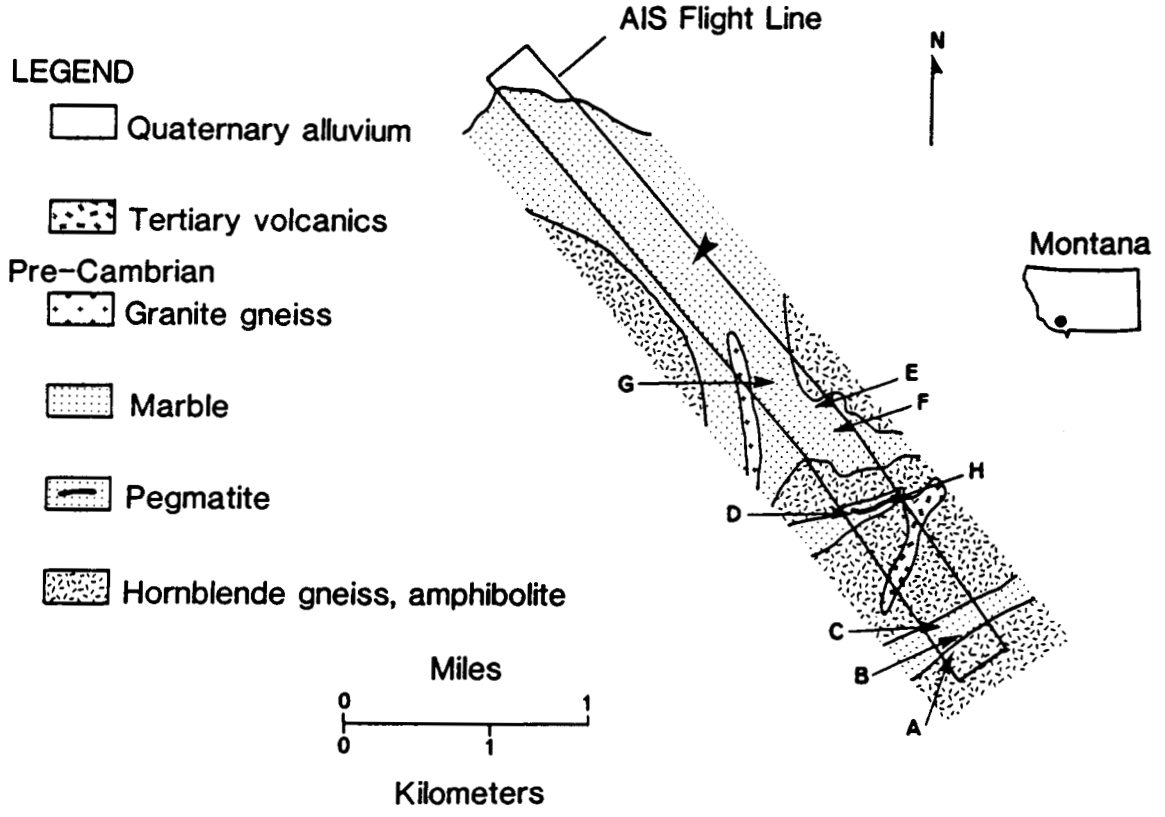

Figure 1. Geologic map of the Ruby Mountains study area. The lettered arrows indicate field sites that are discussed in the text. Also refer to slide nos. 3 and 4, located in the pocket at the end of these proceedings. The large arrow shows the northwest limit of the slide coverage. After Heinrich (1960).

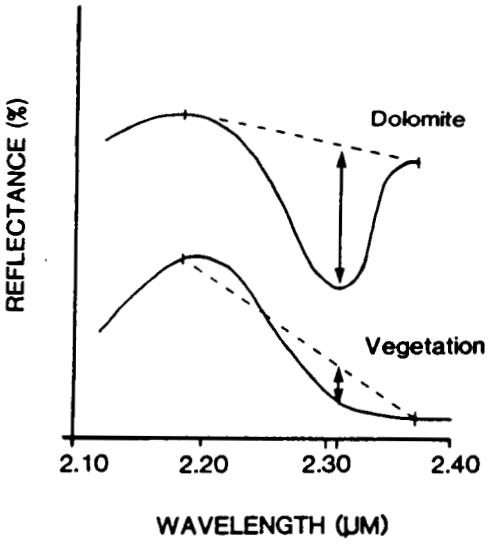

Figure 2. Schematic diagram showing the apparent "dolomite" component produced by rangeland vegetation in a band depth image in which separated shoulder channels were used.

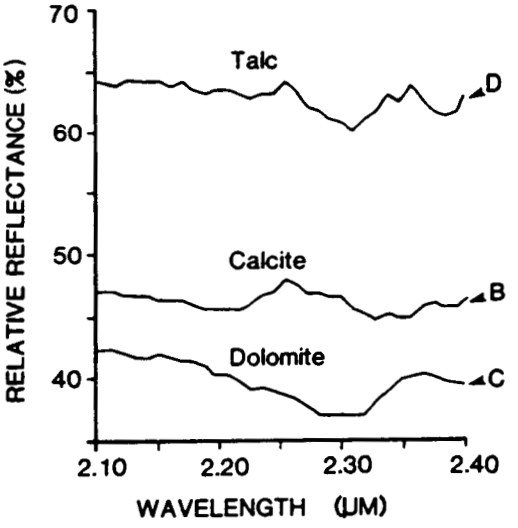

Figure 3. AIS spectra produced from the relative reflectance data set for field sites B, C, and D (refer to fig. 1).

S17-43
111675
P.11

N88-13772

MAPPING HYDROTHERMALLY ALTERED ROCKS IN THE NORTHERN GRAPEVINE MOUNTAINS, NEVADA AND CALIFORNIA WITH THE AIRBORNE IMAGING SPECTROMETER

FRED A. KRUSE
Cooperative Institute for Research in Environmental Sciences (CIRES)
Center for the Study of Earth from Space (CSES)
University of Colorado, Boulder Colorado 80309

ABSTRACT

Seven flightlines of Airborne Imaging Spectrometer (AIS) data acquired during 1984, 1985, and 1986 were analyzed for an area of hydrothermally altered rocks in the northern Grapevine Mountains, Nevada and California. The data were reduced to reflectance relative to an average spectrum, and an automated procedure was used to produce a color coded image displaying absorption band information. Individual spectra were extracted from the AIS images to determine the detailed mineralogy.

Two alteration types were mapped based upon mineralogy identified using the AIS data. The primary alteration type is quartz-sericite-pyrite alteration which occurs in northwest-trending zones in quartz monzonite porphyry. The AIS data allow identification of sericite (muscovite) based upon a strong absorption feature near 2.21μm and weaker absorption features near 2.35 and 2.45μm. The second alteration type occurs as a zone of argillic alteration associated with a granitic intrusion. Montmorillonite was identified in this zone based upon a weak to moderate absorption feature near 2.21μm and the absence of the two absorption features at longer wavelengths characteristic of sericite. Montmorillonite could be identified only where concentrations of sericite were low enough that the sericite spectrum did not mask the montmorillonite spectrum.

INTRODUCTION

Alteration mapping is a time consuming process that usually involves extensive field work, laboratory analysis of thin sections, and X-ray studies. Additionally, most conventional studies of hydrothermal alteration do not recognize weathering products of altered rocks and seek to characterize only the altered bedrock. The determination of the relationship of minerals formed by near-surface weathering of alteration minerals to the original alteration patterns is necessary to allow use of these secondary minerals to locate new orebodies. High spectral resolution remote sensing provides us with a tool to start determining these relationships. This study discusses techniques for processing Airborne Imaging Spectrometer (AIS) data, and presents results for a study area in the northern Grapevine Mountains, Nevada and California. A total of seven AIS flightlines were analyzed (Figure 1).

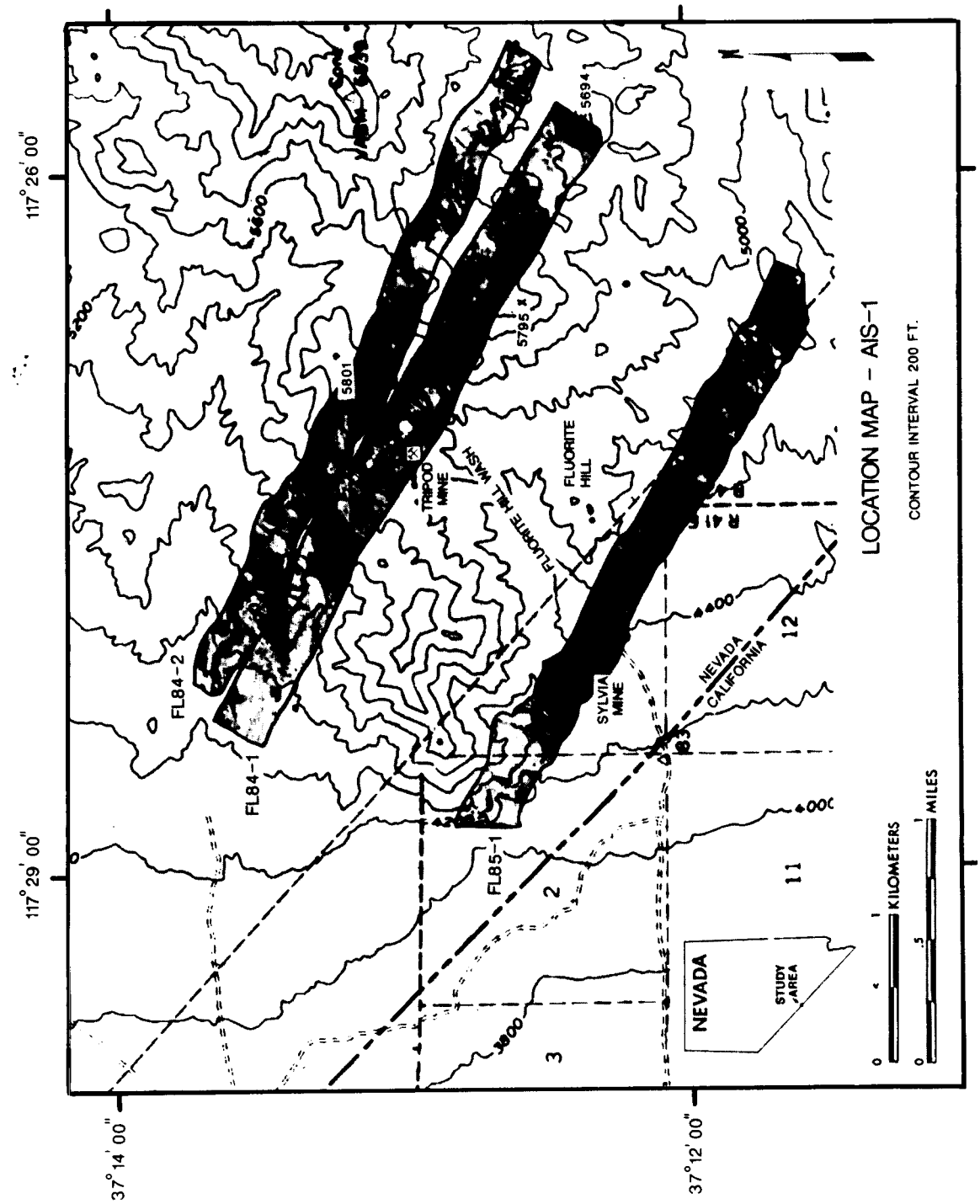

Figure 1a. 1984-85 AIS-1 flightline locations.

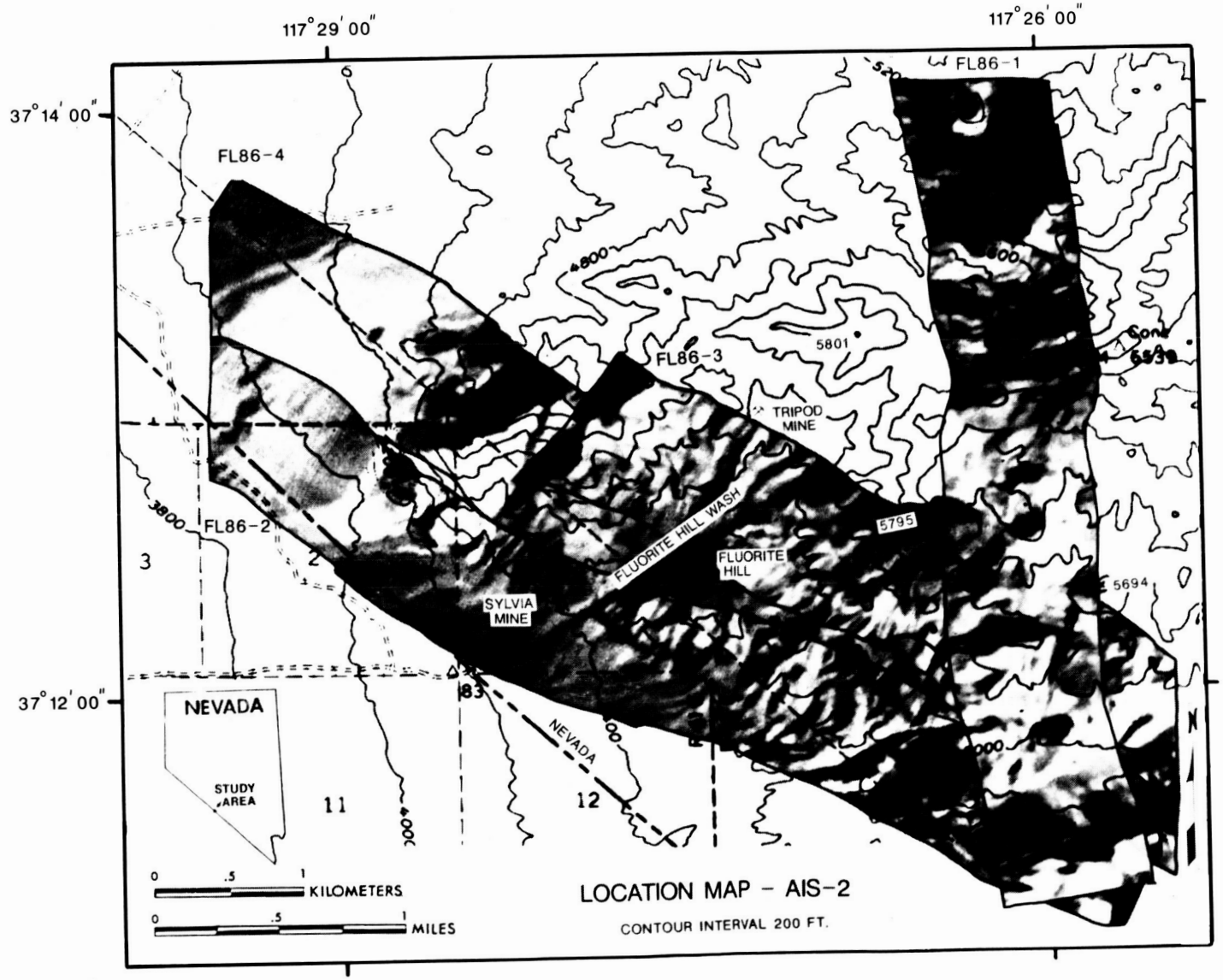

Figure 1b. 1986 AIS-2 flightline locations.

The AIS is an experimental sensor designed to test two dimensional, near-infrared area array detectors. It images 32 (AIS-1, 1983-1985) or 64 (AIS-2, 1986) cross-track pixels simultaneously, collecting data in 128 contiguous narrow channels (AIS-1 [9.3nm], AIS-2 [10.6nm]) from approximately 1.2 to 2.5μm (Vane and others, 1983; Goetz and others, 1985; Vane, 1986). The area array detector is composed of a 32 X 32 element (AIS-1) or 64 x 64 element (AIS-2) HgCdTe detector sandwiched with a silicon charge-coupled device multiplexer (Rode and others, 1982; Wellman and others, 1983; Goetz and others, 1985). The spectrometer is stepped through four grating positions (AIS-1) or two grating positions (AIS-2) in the time it takes to advance one pixel on the ground to obtain the 128 spectral bands. The AIS-1 was flown on a NASA C-130 aircraft at an altitude of approximately 4,500 meters above mean terrain, resulting in an average ground pixel size of about 10.9 X 10.9 meters and a swath width of about 350 meters. The AIS-2 was flown at a similar altitude; but the revised instrument characteristics resulted in an average ground pixel of about 14.4 X 14.4 meters and swath width of about 920 meters.

The basic analysis approach for these data was to identify individual minerals using reflectance information, and to use mineral assemblages and distribution information to develop a better understanding of the weathered surfaces of the hydrothermally altered rocks. The research results are an example of the use of airborne spectroscopy for alteration mapping.

PREPROCESSING

Several preprocessing steps are required to prepare AIS data for analysis. Cosmetic processing is necessary to correct for dropped lines and vertical striping. Normalization is required to remove albedo effects. Individual bad lines (data drop outs) were removed by replacing the bad lines with the average of the two adjacent lines. Additionally, even though JPL had applied radiometric corrections to the data, a pronounced vertical striping pattern was still observed in the images, presumably caused by varying DC offsets in detectors in the pixel direction. The DC offsets were corrected using the procedures described by Dykstra and Segal (1985). Albedo differences were removed from the images using an "equal area normalization" as described in the Airborne Imaging Spectrometer Science Investigator's Guide (JPL, 1984, 1985). This allowed extraction of spectral information that had been masked by brightness variation.

Ideally the aircraft data should next be calibrated to absolute reflectance so that individual spectra can be compared directly with laboratory data for mineral identification. However, this requires *a priori* knowledge,

therefore, the approach taken was to use the properties of the data themselves to calculate an approximation of the reflectance. This approximation is defined here as "internal average relative (IAR) reflectance". IAR reflectance is calculated by determining an average spectrum for a single flightline or in this case for all flightlines acquired on an individual mission. Each spectrum (pixel with 128 channels) in the flightline is then divided by the average spectrum (Figure 2). The resulting spectra represent reflectance relative to the average spectrum and resemble laboratory spectra acquired of the same materials. One thing to remember when looking at an IAR reflectance spectrum, however, is that the average spectrum used to calculate the IAR reflectance spectrum may itself have spectral character related to mineral absorption features. This can adversely affect the appearance of the IAR reflectance spectra and limit their usefulness in comparisons with laboratory spectra. The average spectrum for the flightlines analyzed in this study did not contain any obvious mineral absorption features. The IAR reflectance technique has the added advantage of effectively removing the majority of atmospheric effects, since the average spectra contains contributions from the atmosphere, however, if the flight crosses an area that has wide variation in ground elevation, or the atmosphere is not uniform across the flight, the global average will not completely remove the effects of the atmosphere. A technique similar to the IAR reflectance procedure (logarithmic residuals) has been successfully demonstrated by Green and Craig (1985) and Huntington and others (1986).

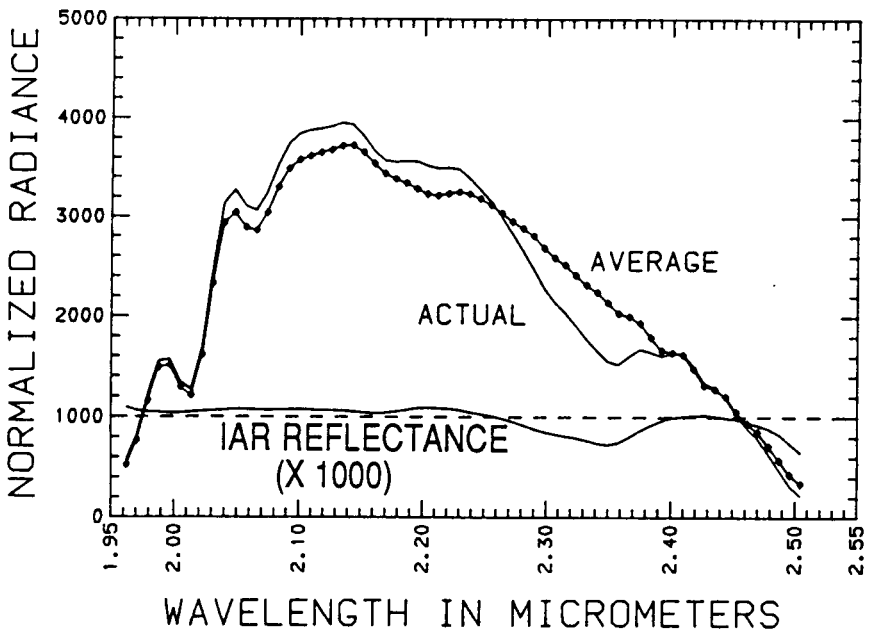

Figure 2. IAR Reflectance

DATA ANALYSIS

Once the IAR reflectance spectra are calculated then the data are ready for spectral analysis. Only the channels between 2.1 and 2.5μm were used for this analysis (the number of channels in this wavelength range varied between the 1984, 1985, and 1986 data sets). This region contains many of the characteristic absorption bands that allow mineralogical identification and generally avoids atmospheric absorption problems.

The image representation of IAR reflectance is shown in Figure 3. Dark areas in the IAR reflectance image (Figure 3B) represent absorption features. Color coded stacked spectra showing all of the spectra along a flightline (Marsh and McKeon, 1983; Kruse and others, 1985a, 1985b; Huntington and others, 1986) and a single-band color coded IAR reflectance image are shown in **slide 5.** A color coded spectrum (A) and the corresponding (idealized) spectral plot (B) show the relationship between the colors and the spectral features. The image on the left (C) consists of color-coded, stacked relative reflectance spectra. The x-axis represents the spectral direction (1.2 to 2.337μm), and the y-axis represents the flightline direction. Each line in the image represents a spectrum. The image on the right (D) is a color-coded single-band image for 2.21μm. The color bar in the upper right corner shows the colors for spectral features on both images. Black, purples and blues represent reflectance lower than the average spectrum (absorption features), green and yellow represent reflectance similar to the average, and oranges, reds, and whites represent reflectance higher than the average spectrum. The mineral absorption bands can be clearly seen in these images.

Algorithms were developed to identify automatically the strongest absorption feature in the 2.1 to 2.5μm portion of each AIS spectrum. Removal of a continuum (Clark and Roush, 1984) was used to place all of the spectra on a common reference plane (Figure 4). The continuum was calculated using a second order polynomial fitted to selected channels (channels without known absorption features) in the IAR reflectance spectra. The continuum was removed by dividing the polynomial function into the AIS data. The strongest absorption feature was defined as the wavelength position of the channel with the maximum depth from the continuum (Figure 5). Once the band position was identified, then the band depth and band width were calculated as the distance from the continuum at the band position, and the full width at one half the band depth respectively (Figure 5).

The next step was to put this information into a form that could be easily interpreted. The goal was to compress the spectral information into a single color-composite image representative of the data. This goal was accomplished using an intensity, hue, saturation (IHS) color transform (Raines, 1977; Raines and Knepper, 1983; Kruse and Raines, 1984) to map the three band parameters into red, green, blue (RGB)

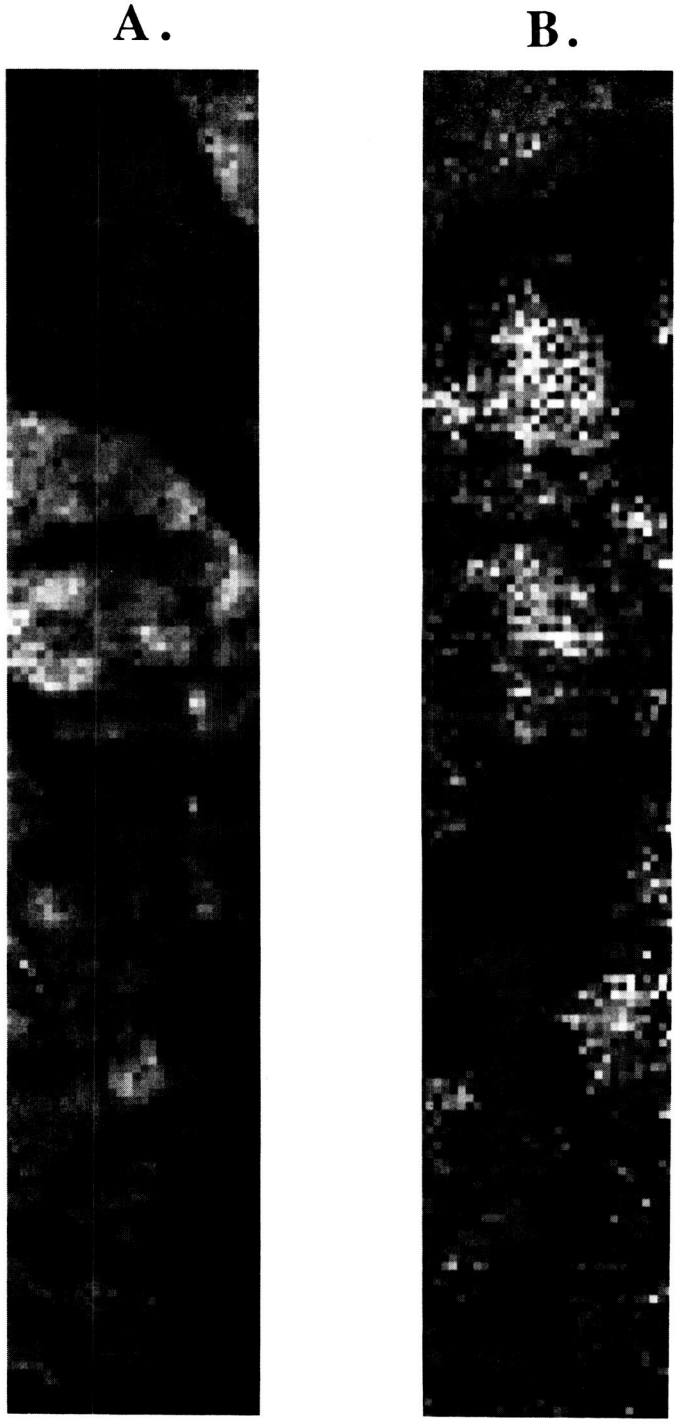

Figure 3. A. AIS-1 raw data - Dark areas represent dark rocks and shadows.
B. AIS IAR reflectance image - Dark areas represent absorption features at 2.21μm.

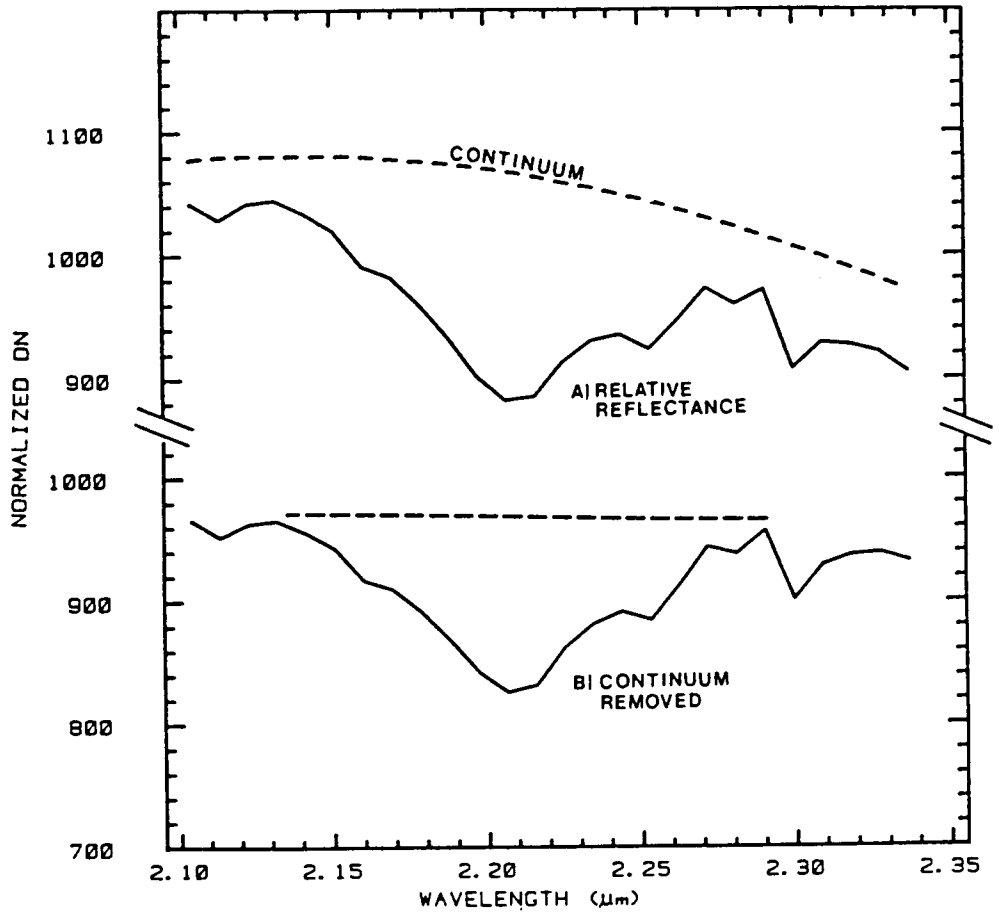

Figure 4. AIS continuum removal by division of 2nd order polynomial into each spectrum.

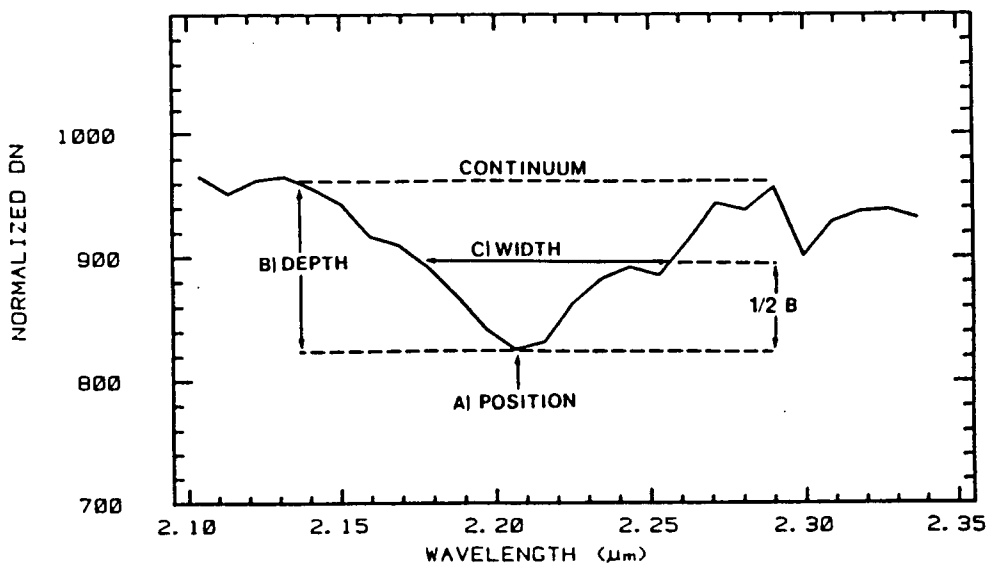

Figure 5. Absorption band parameters.

color space. The band position was mapped into hue, the band depth was mapped into intensity, and the band width was mapped into saturation. Transformation of the IHS encoded spectral information into the RGB color space produced an image in which all of the absorption band information for the strongest absorption feature between 2.1 and 2.4μm in each pixel was present in the color variation (Kruse and others, 1986; Kruse, 1987). This color variation was then mapped onto a single-band AIS image in which colored areas represent areas with absorption features deeper than a preselected cutoff value, and areas without absorption features are shown as the gray scale image **(See slide 6)**. This type of image is here termed an "IHS-coded absorption band image."

RESULTS

Several minerals were identified. Sericite (muscovite) was identified by absorption features at 2.206, 2.346, and 2.445μm (Figure 6). Sericite must be identified using slightly different criteria in the three different AIS data sets (1984 AIS-1, 1985 AIS-1, 1986 AIS-2). In the 1984 data, the cutoff wavelength of 2.337μm prevents observation of the 2.346 and 2.445μm absorption features. However, the decreasing reflectance between 2.3 and 2.337μm is characteristic (Figure 6A). In the 1985 data, the cutoff wavelength of 2.4μm prevents observation of the 2.445μm absorption feature, however, the 2.346μm absorption feature is clearly seen (Figure 6A). The 1986 data include the necessary wavelength range to observe both the 2.345 and 2.445 absorption features, however, in many cases neither of these bands is fully resolved. Instead, a broad band is observed in the data covering the full range between about 2.3 and 2.48μm (Figure 6B).

Montmorillonite could be differentiated from sericite in the 1984 AIS-1 data based upon the characteristics of the 2.3 to 2.337μm portion of the spectra (Figure 7). Areas with sericite show decreasing reflectance in this region caused by the absorption feature near 2.35μm, while montmorillonite spectra remain fairly level in this region. No montmorillonite spectra were found in the 1985 or 1986 data. Spectra characteristic of montmorillonite were found in the 1984 data that covers an area of argillic/sericitic alteration. Areas of mixed montmorillonite and sericite could not be distinguished from those having only sericite because even small amounts of sericite mask the montmorillonite spectra.

Examination of the carbonate spectra from the 1984 data indicates that discrimination of calcite from dolomite is difficult because of the wavelength cutoff for that data set at approximately 2.34μm. The spectral range of the 1985 data extends to approximately 2.4μm and the 1986 data to 2.52μm, so these data do allow identification of calcite and dolomite (Figure 8) based on the presence of absorption features near

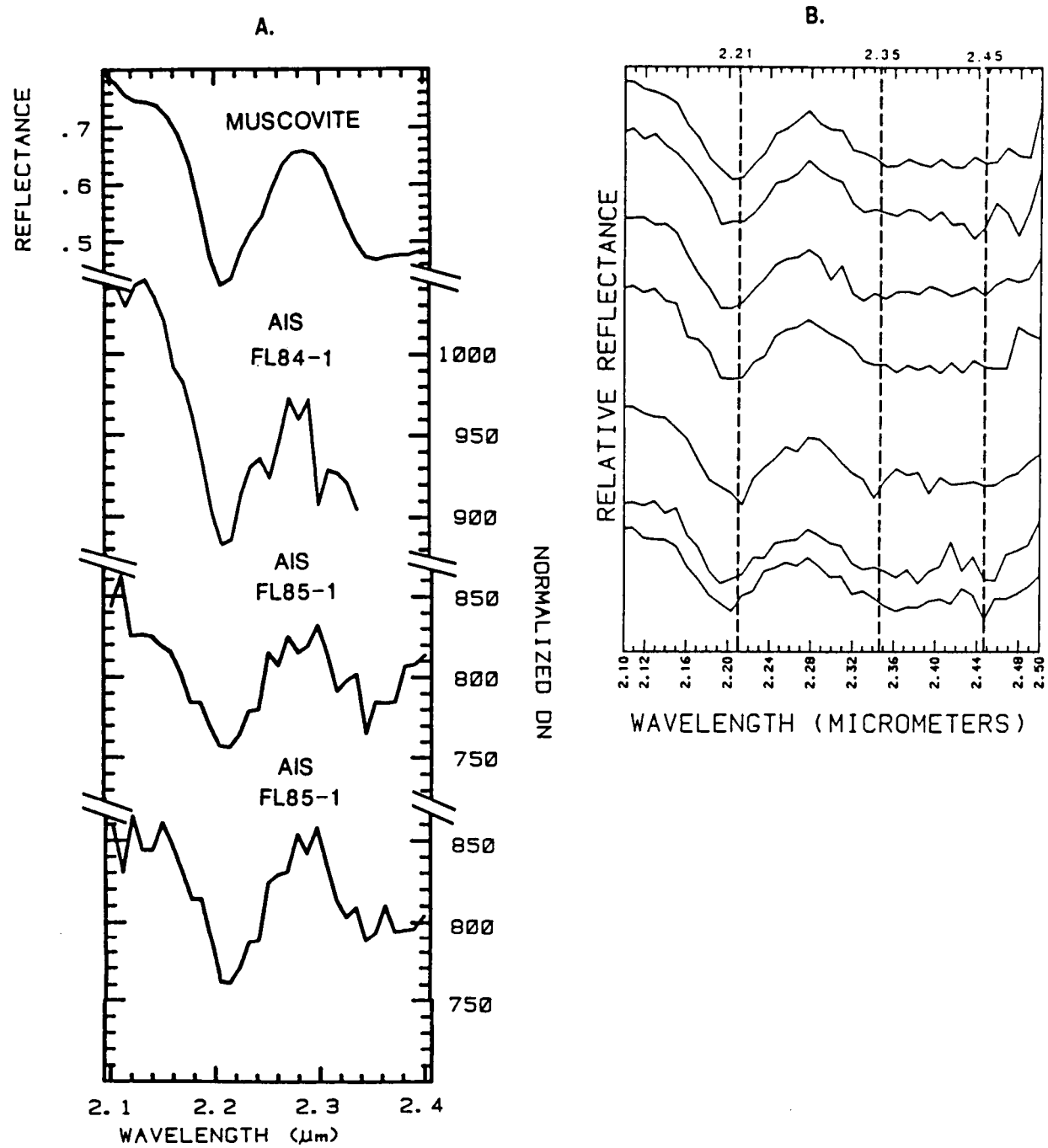

Figure 6. A. Laboratory spectrum for muscovite and AIS-1 spectra for sericite.
B. AIS-2 spectra for sericite.

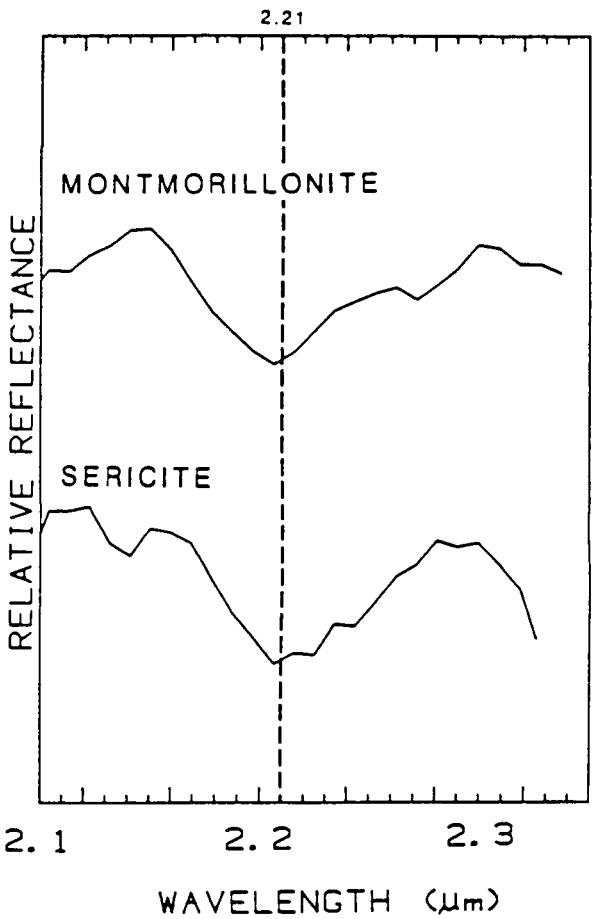

Figure 7. Comparison of AIS-1 spectra for montmorillonite and sericite.

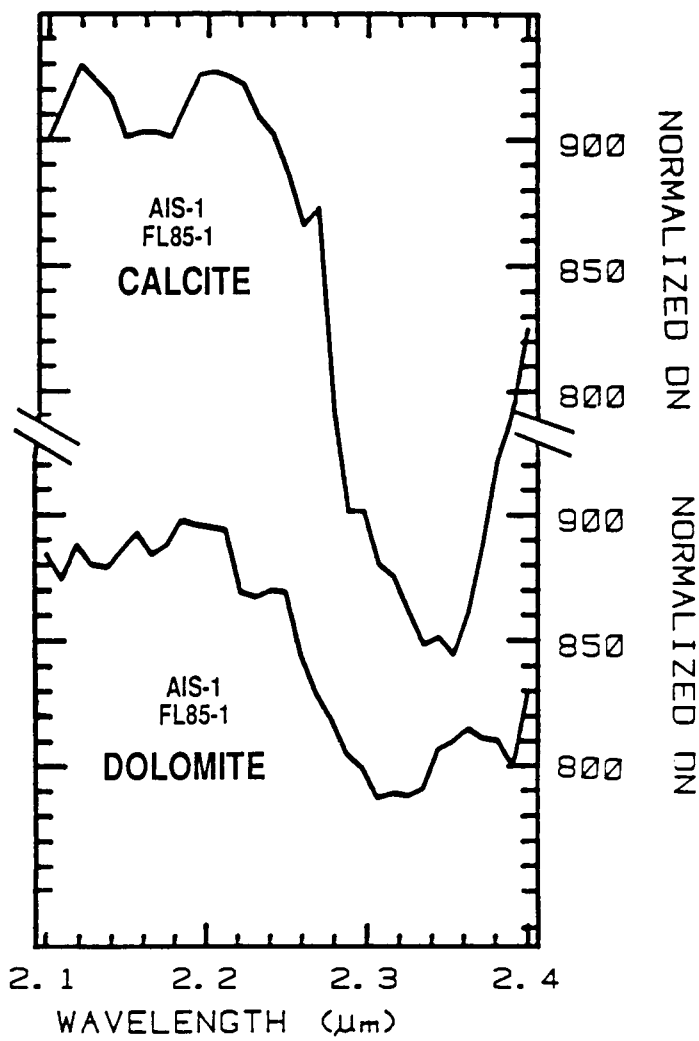

Figure 8. Comparison of AIS-1 spectra for calcite and dolomite.

2.34 and 2.32μm, respectively (Gaffey, 1984). For carbonate-derived alluvium the spectra have an absorption feature near 2.34μm, however, the feature is shallower and much broader.

Several spectra having some characteristics similar to epidote, tremolite, and actinolite were observed in the data. Low signal-to-noise ratios, however, precluded positive identification. The inability to precisely locate single pixels on the ground (and probable within pixel mixing) prevented independent confirmation of these minerals, although they are known to occur in the study area. Additionally, an unknown mineral with a broad absorption band near 2.43μm was observed in the volcanic rocks south of the study area (Figure 9). This area was not field checked and the mineral remains unidentified although the spectra somewhat resemble laboratory spectra of several zeolite minerals.

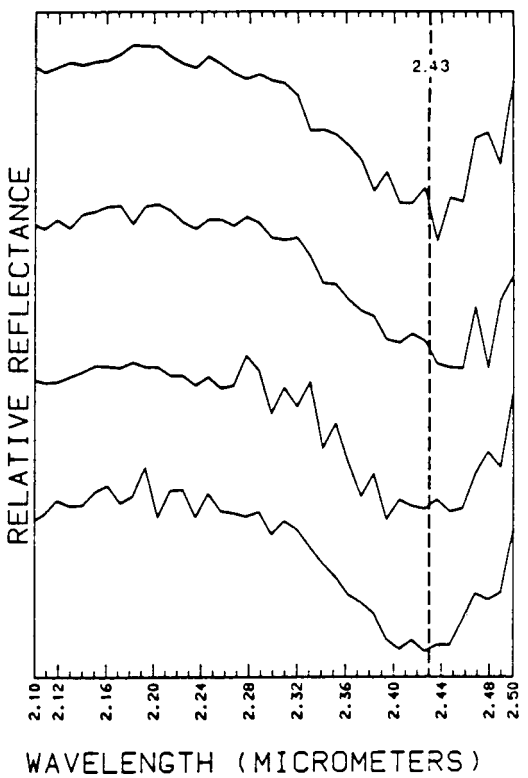

Figure 9. AIS-2 spectra of unknown mineral with broad absorption band near 2.43μm

The absorption feature map and individual spectra were used to identify minerals and the color-coded density-sliced images and individual spectra were used to estimate alteration intensity based upon the strength of absorption features. Figure 10 gives a good picture of the alteration in the study area. The strongest alteration found using the AIS data is the northwest-trending zone of strong sericite alteration just southeast of Fluorite Hill. Additionally, the AIS data show that this zone of strong alteration is surrounded by an envelope of weak sericite alteration. The AIS alteration map also shows a zone of strong sericite alteration just northeast of the Tripod Mine.

The AIS data allow identification and mapping of carbonate minerals (Figure 10). Dolomite (yellow **on slide 6)** was mapped by an absorption feature near 2.32μm and calcite **(reds on slide 6)** was mapped by an absorption feature near 2.34μm. The occurrence of spatially mixed calcite and dolomite pixels was mapped as mixed calcite and dolomite. Carbonate mineralogy generally was confirmed by X-ray diffraction within the limitations of sampling ~15m pixels. Finer spatial resolution is required to resolve the individual limestone and dolomite beds.

The AIS alteration map (Figure 10) was field checked during 1986 and generally shows good correspondence with field mapping (Figure 11). The minerals mapped using the AIS data accurately represent the surface conditions mapped in the field and verified by petrological and X-ray diffraction studies. Both the field mapping and the mineralogical map produced from the AIS data show a linear, northwest-trending zone of strong sericitic alteration surrounded by a halo of weaker alteration. The AIS map is more detailed than the field map, particularly in areas of moderate to weak sericitic alteration, where the AIS map resolves very small areas of more intense alteration (south of Fluorite Hill) surrounded by a broader halo. During field mapping, these small areas were not mapped and the entire area was mapped as moderate sericitic alteration. In one area of weakly sericitized rock (VWS, Figure 11), X-ray diffraction analysis demonstrated that the predominant soil clay mineral is montmorillonite. Although this soil contains less sericite than montmorillonite, the spectral character of the sericite dominates the near-infrared spectra and montmorillonite was not identified using field, laboratory, or aircraft spectra; X-ray diffraction was required to identify the montmorillonite.

ACKNOWLEDGEMENTS

This research was conducted in partial fulfillment of the requirements of the Ph. D. degree at the Colorado School of Mines, Golden, Colorado. I would like especially to thank Dr. Keenan Lee (thesis advisor) who provided valuable guidance throughout the study. This work was funded in part by the U.S. Geological Survey, Denver, Colorado.

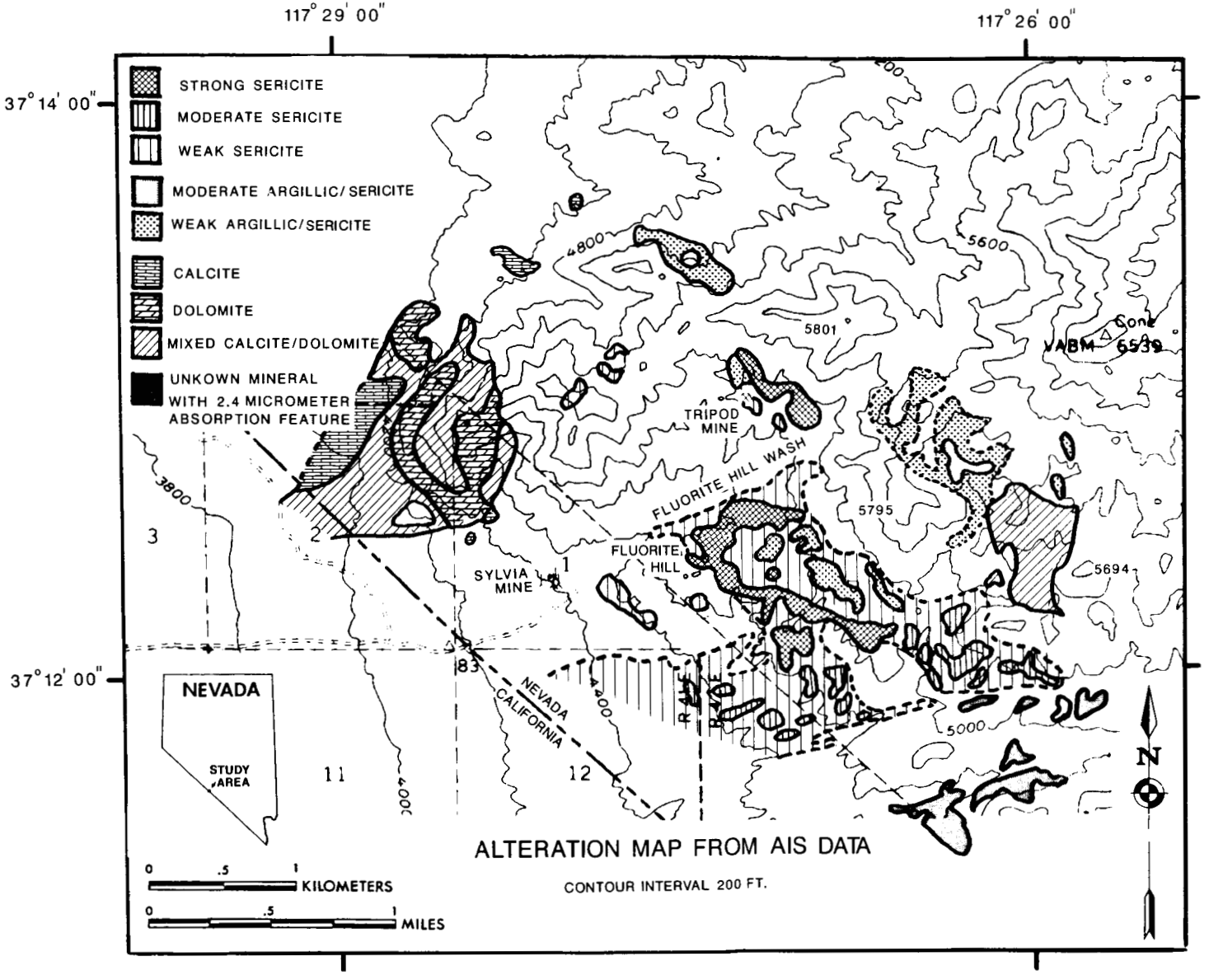

Figure 10. Map of mineral distribution from the AIS data.

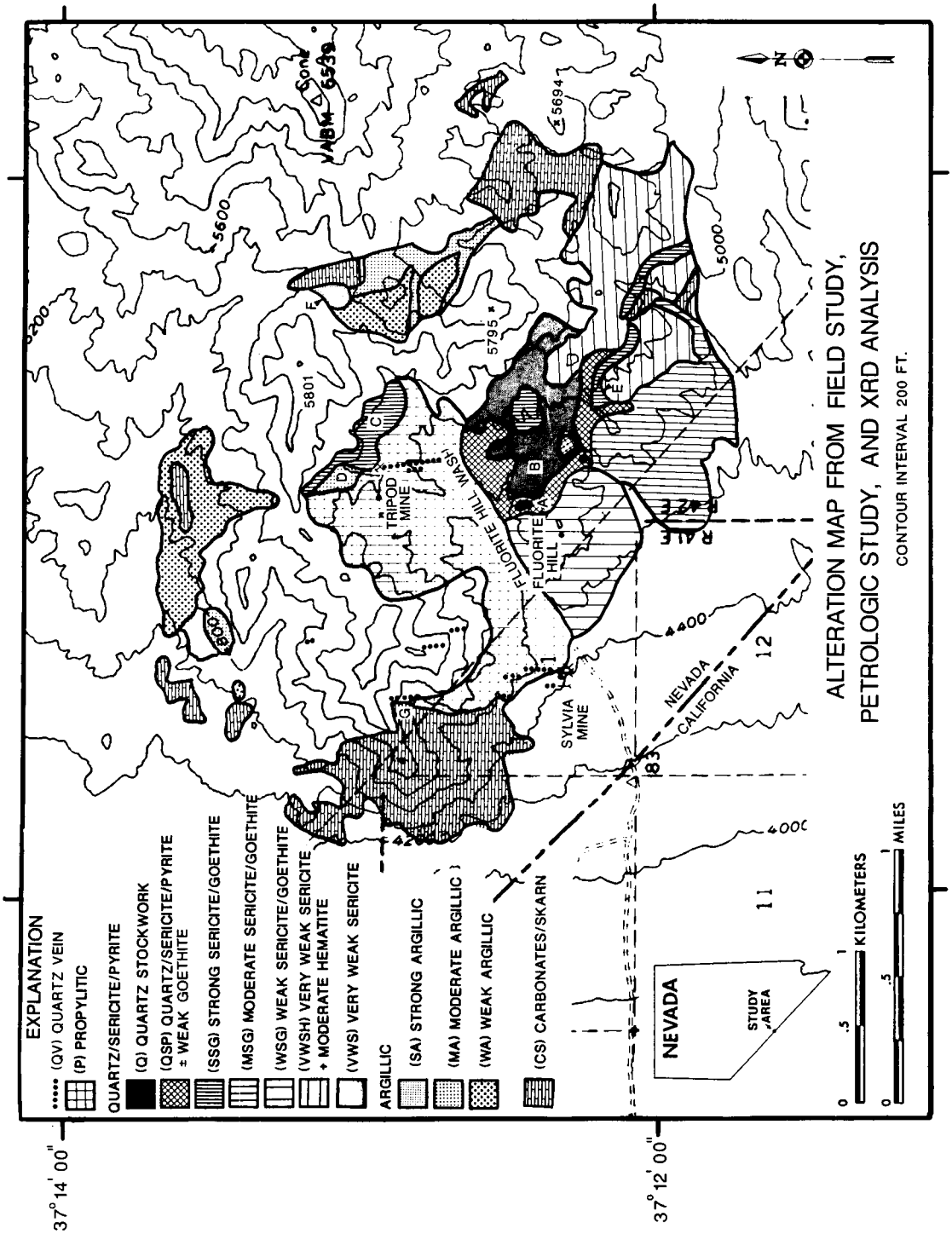

Figure 11. Alteration map from field study, petrologic study, and XRD analysis.

REFERENCES

Clark, R. N., and Roush, T.L., 1984, Reflectance spectroscopy: Quantitative analysis techniques for remote sensing applications, Jour. Geoph. Res., v. 89, no. B7, p. 6329-6340.

Dykstra, J. D., and Segal, D. B., 1985, Analysis of AIS data of the Recluse Oil Field, Recluse, Wyoming: *in* Proceedings, AIS workshop, 8-10 April, 1985, JPL Publication 85-41, Jet Propulsion Laboratory, Pasadena, California, p. 86-91.

Gaffey, S. J., 1984, Spectral reflectance of carbonate minerals and rocks in the visible and near infrared (0.35 to 2.55μm) and its applications in carbonate petrology: Unpublished Ph. D. dissertation, University of Hawaii, 236 p.

Goetz, A. F. H., Vane, Gregg, Solomon, J. E., and Rock, B. N., 1985, Imaging spectrometry for earth remote sensing: Science, v. 228, p. 1147-1153.

Green, A. A., and Craig, M. D., 1985, Analysis of aircraft spectrometer data with logarithmic residuals: *in* Proceedings, AIS workshop, 8-10 April, 1985, JPL Publication 85-41, Jet Propulsion Laboratory, Pasadena, California, p. 111-119.

Huntington, J.F., Green, A.A., and Craig, M. D., Preliminary Geological Investigation of AIS Data at Mary Kathleen, Queensland, Australia: *in* Proceedings, AIS workshop, 6-8 May, 1986, JPL Publication 86-35, Jet Propulsion Laboratory, Pasadena, California, p. 109-131.

Jet Propulsion Laboratory, 1984, Airborne Imaging Spectrometer, Science Investigator's Guide to AIS DATA, Jet Propulsion Laboratory, Pasadena, California, 15 p.

Jet Propulsion Laboratory, 1985, Airborne Imaging Spectrometer, Science Investigator's Guide to AIS DATA, Jet Propulsion Laboratory, Pasadena, California, 14 p.

Kruse, F. A., 1987, Use of high spectral resolution remote sensing to characterize weathered surfaces of hydrothermally altered rocks: Ph. D. thesis (unpublished), Colorado School of Mines, Golden, 139 p.

Kruse, F. A., Knepper, D. H., and Clark, R. N., 1986, Use of Digital Munsell Color Space to Assist Interpretation of Imaging Spectrometer Data -- Geologic Examples From the Northern Grapevine Mountains, California and Nevada: *in* Proceedings, AIS workshop, 6-8 May, 1986, JPL Publication 86-35, Jet Propulsion Laboratory, Pasadena, California, p. 132-137.

Kruse, F. A., and Raines, G. R., 1984, A technique for enhancing digital color images by contrast stretching in Munsell color space: *in* Proceedings, International Symposium on Remote Sensing of Environment, Third Thematic Conference, "Remote Sensing for Exploration Geology", Colorado Springs, Colorado, 16-19 April, 1985, University of Michigan, Ann Arbor, p. 309-324.

Kruse, F. A., Raines, G. L., and Watson, Kenneth, 1985a, Analytical techniques for extracting geologic information from multichannel airborne spectroradiometer and airborne imaging spectrometer data: *in* Proceedings, International Symposium on Remote Sensing of Environment, Fourth Thematic Conference, "Remote Sensing for Exploration Geology", San Francisco, California 1-4 April, 1985, Ann Arbor, Environmental Research Institute of Michigan, p. 309-324.

Kruse, F. A., Raines, G. L., and Watson, Kenneth, 1985b, Analytical techniques for extracting mineralogical information from multichannel airborne imaging spectrometer data (Abs.): *in* Proceedings, AIS workshop, 8-10 April, 1985,JPL Publication 85-41, Jet Propulsion Laboratory, Pasadena, California, p. 105.

Marsh, S. E., and McKeon, J. B., 1983, Integrated analysis of high-resolution field and airborne spectroradiometer data for alteration mapping: Econ. Geol., v. 78, no. 4, p. 618-632.

Raines, G. R., 1977, Digital color analysis of color ratio composite Landsat scenes: *in* Proceedings, Eleventh International Symposium on Remote Sensing of Environment, University of Michigan, Ann Arbor, p. 1463-1472.

Raines, G. R., and Knepper, D. H., Jr., 1983, A hue-saturation- intensity transform to improve hydrothermal alteration mapping: in International Geoscience and Remote Sensing Symposium Digest, 1983: Institute of Electrical and Electronic Engineers, v. 2, p. 1.1-1.3.

Rode, J. P., Vural, K., Blackwell, J. D., Cox, F. A., and Lin, W. N., 1982, Characterization of a 32 X 32 HgCdTe focal plane: Proceedings of the IRIS Specialty Group on Infrared Detectors, San Diego, California.

Vane, Gregg, 1986, Introduction to the Proceedings of the 2nd Airborne Imaging Spectrometer (AIS) Data Analysis Workshop: *in* Proceedings of the 2nd Airborne Imaging Spectrometer (AIS) Data Analysis Workshop, G. Vane and A.F.H. Goetz, editors, JPL Publication Number 86-35, Jet Propulsion Laboratory, Pasadena, California, p. 1-16.

Vane, Gregg, Goetz, A. F. H., and Wellman, J. B., 1983, Airborne imaging spectrometer: A New Tool for Remote Sensing: IEEE Transactions on Geoscience and Remote Sensing, v. GE-22, no. 6, p. 546-549.

Wellman, J. B., Goetz, A. F. H., Herring, M., and Vane, Gregg, 1983, An imaging spectrometer experiment for the shuttle: Proceedings 1983 International Geoscience and Remote Sensing Symposium (IGARS), IEEE cat No. 83CH1837-4.

Appendix A

Agenda

AGENDA

THIRD AIS DATA ANALYSIS WORKSHOP

JUNE 2, 3, and 4, 1987
JET PROPULSION LABORATORY
PASADENA, CALIFORNIA

TUESDAY, JUNE 2

8:00 Shuttle Bus Leaves Holiday Inn for JPL

8:30 Registration at JPL Visitors' Center

9:00 Workshop Welcome: Gregg Vane, AVIRIS/AIS Program Manager

9:15 NASA Headquarters Welcome: Diane Wickland, NASA Terrestrial Ecosystems Program Manager

9:30 HIRIS Project Overview: David Norris, HIRIS Project Manager

10:00 BREAK

10:30 AIS 1986 Operations: Gregg Vane

11:00 AVIRIS Status: Gregg Vane

11:30 PIDAS Overview and Results from Field Testing at Cuprite: Alex Goetz, Director, Center for Earth Observations and Remote Sensing, University of Colorado

12:00 LUNCH

SESSION 1: CALIBRATION AND DATA ANALYSIS TECHNIQUES

1:00 Correcting AIS Measurements for the Atmosphere: A Comparison of Methods: James E. Conel, Carol J. Bruegge, Brian Curtiss, Robert O. Green and Gregg Vane

2:00 Airborne Imaging Spectrometer Signatures of Clay, Zeolite and Carbonate Mineral Localities: Sandra Feldman and James V. Taranik

2:30 BREAK

3:00 Land Cover/Use Classification of Cairns, Queensland, Australia: A Remote Sensing Study Involving the Conjunctive Use of the Airborne Imaging Spectrometer, the Large Format Camera and the Thematic Mapper Simulator: Matthew Heric, William Cox and Daniel K. Gordon

3:30 A Model for Calibrating AIS Images Using Spectral Endmembers: M.O. Smith, D.A. Roberts, A.R. Gillespie, S.C. Willis and J.B. Adams

4:00 Spectral Unmixing to Remove the Background Component From High Resolution Spectra of Rock and Soil: H. Shipman and J.B. Adams

4:30 DISCUSSION OF THE DAY'S PRESENTATIONS

5:15 Shuttle Bus Returns to Holiday Inn

6:00 JPL-Hosted Working Dinner for Workshop Attendees and Spouses at the Holiday Inn (no-host bar)

WEDNESDAY, JUNE 3

8:30 Shuttle Bus Leaves Holiday Inn for JPL

SESSION 2: BOTANICAL RESEARCH

9:00 Progress in Studies of AIS Imagery for Biochemical Contents of Canopies: David Peterson, Walter Westman, Nancy Swanberg John Aber

9:30 Remote Detection of Forest Decline Damage Using High Resolution Imaging Spectrometer Data: Barry Rock, Karin Herrmann, Tak Hoshizaki and John Miller

10:00 BREAK

10:30 The Use of Airborne Imaging Spectrometer Data to Determine Experimentally Induced Variation in Coniferous Canopy Chemistry: Nancy A. Swanberg and Pamela A. Matson

11:00 A First Look at the Austrian AIS Data: Cliff Banninger

11:30 Effects of Ozone Exposure on Simulated AVIRIS Spectra of Douglas Fir, Ponderosa Pine and Lodgepole Pine: Brian Curtiss and Susan Ustin

12:00 LUNCH

1:00 Discrimination of San Francisco Bay Wetlands Vegetation with AIS Data: Michael F. Gross, Vic Klemas and Susan Ustin

1:30 Analysis of AIS Data of Vegetation Subjected to Air Pollution Gradients in Southern California: Curtis Price and Walter Westman

2:00 Preliminary Analysis of AIS-2 Data for Spectral Reflectance Changes from Water Stressed Conifer Stands: George Riggs and Steven W. Running

2:30 BREAK

SESSION 3: GEOLOGICAL RESEARCH

3:00 Abundance and Distribution of Ultramafic Microbreccia in Moses Rock Dike: Quantitative Application of AIS Data: John F. Mustard and Carle M. Pieters

3:30 Relationship of 1986 AIS-2 to 1984/5 AIS-1 Datasets Flown Over Hydrothermally-Altered Granitoid Rocks of the Singatse Range (Yerington) NV.: Ron J.P. Lyon

4:00 Preliminary Results from an Investigation of AIS-1 Data Over an Area of Epithermal Alteration: Plateau, North Queensland, Australia: Steve Mackin, Tim Munday and Simon Hook

4:30 DISCUSSION OF THE DAY'S PRESENTATIONS

5:15 Shuttle Bus Returns to Holiday Inn

THURSDAY, JUNE 4

8:30 Shuttle Bus Leaves Holiday Inn for JPL

9:00 Causes of Spurious Features in Spectral Reflectance Data; and, Automatic Continuum Analysis of Reflectance Spectra: Roger N. Clark and Trude V.V. King

9:30 Analysis of Airborne Imaging Spectrometer Data for the Ruby Mountains, Montana, Using Images of Absorption and Depth: David W. Brickey, James K. Crowley and Lawrence C. Rowan

10:00 Mapping Hydrothermally Altered Rocks in the Northern Grapevine Mountains, Nevada and California, with the Airborne Imaging Spectrometer: Fred A. Kruse

10:30 BREAK

11:00 WORKSHOP WRAPUP AND PLANS FOR THE FUTURE

12:00 LUNCH

1:00 SPAM Demonstrations at the AVIRIS Ground Data Processing Facility, PIDAS Demonstrations, and Tour of the AVIRIS Instrument and Calibration Facilities

5:15 Shuttle Bus Leaves for Holiday Inn

Appendix B

List of Workshop Attendees

C-3

ATTENDEES

Name	Affiliation
Adams, John B.	University of Washington
Adams, Steven	JPL
Albee, Arden	California Institute of Technology
Alger, George	NASA/Ames Research Center
Balick, Lee	EG&G Energy Measurements Inc.
Baltuck, Miriam	NASA HQ
Banninger, C.	Institute for Image Processing and Computer Graphics, Austria
Barge, Lisa	JPL
Bartholomew, M. J.	JPL
Bauer, Marvin E.	University of Minnesota
Beaver, Dennis	Battelle Pacific NW Laboratory
Brickey, David W.	USGS
Brill, Russ	JPL
Carrere, Veronique	JPL
Clark, Roger N.	USGS
Conley, Joseph M.	JPL
Cox, William	Autometric
Curtiss, Brian	University of Colorado
Davis, Philip	USGS
Defeo, Nancy	JPL
Del Vecchio, J. J.	U.S. Army Engineer, Topographic Lab
Dozier, Jeff	UCSB and JPL
Drake, Nick	University of Reading, England

ATTENDEES (Cont'd)

Name	Affiliation
Dwyer, John	EROS Data Center/USGS
Elvidge, Chris	JPL
Evans, Diane	JPL
Feldman, Sandra C.	University of Nevada - Reno
Gabell, Andy	CSIRO, Australia
Gambino, Larry	U.S. Army Engineer, Topographic Lab
Geissler, Paul	University of Arizona
Goetz, Alexander	University of Colorado
Gordon, Daniel	Autometric
Green, Robert	JPL
Gross, Mike	University of Delaware
Henderson, Fred	The Geosat Committee
Henry, Paul K.	JPL
Heric, Matthew	Autometric
Herring, Mark	JPL
Heyada, Jan	JPL
Hom, John	San Diego State University
Hoshizaki, Tak	JPL
Hutsinpiller, Amy	University of Nevada - Reno
Inouye, Cindy	JPL
Kalman, Linda	The Aerospace Corp.
Karaska, Mark	Indiana State University
Klemas, Vic	University of Delaware

ATTENDEES (Cont'd)

Name	Affiliation
Koopmans, Bas	International Institute for Aerospace Surveys and Earth Sciences ITC.
Kowalik, William S.	Chevron Oil Field Research Co.
Kruse, Fred A.	University of Colorado
Kuzma, Thomas J.	Battelle Pacific NW Laboratory
LaPorte, Daniel	Santa Barbara Research Center
Lang, H.	JPL
Lansing, Jack	Santa Barbara Research Center
Lee, Jun-ji	JPL
Lehmann, Frank	DFVLR, Federal Republic of Germany
Link, Cristina	JPL
Liu, K. Y.	JPL
Lyon, R. J. P.	Stanford University
MacDonald, John	MacDonald Dettwiler
Mackin, Steve	University of Durham, England
Malila, William	ERIM
Meyer, Dave	EROS Data Center/USGS
Molinari, Lou	JPL
Mourad, A. George	Battelle Pacific NW Laboratory
Mustard, John	Brown University
Norris, David	JPL
Ocampo, Adriana C.	JPL
Olson, Jr., Charles E.	University of Michigan
Paley, Helen	JPL

ATTENDEES (Cont'd)

Name	Affiliation
Paylor, Earnest	JPL
Penny, John	UNOCAL Research
Peterson, Dave	NASA/Ames Research Center
Pieters, Carle M.	Brown University
Powers, Bill	Los Alamos National Lab
Prelat, Alfredo E.	UNOCAL
Press, Harry	JPL
Price, Curtis	NASA/Ames Research Center
Rand, Bob	U.S. Army Engineer, Topographic Lab
Rast, Michael	ESA-ESTEC
Reimer, John	JPL
Riggs, George	University of Montana
Rinker, Jack	U.S. Army Engineer, Topographic Lab
Roberts, Dar	University of Washington
Rock, Barry	University of New Hampshire
Rubin, David	JPL
Ruzek, Martin	NASA HQ
Satterwhite, Melvin	U.S. Army Engineer, Topographic Lab
Shipman, Hugh	University of Washington
Silverman, Steve	Santa Barbara Research Center
Smith, Milton	University of Washington
Soeller, Tony	UNOCAL
Staenz, Karl	University of Zurich - Irchel
Stanich, Charles	Daedalus Enterprises Inc.

ATTENDEES (Cont'd)

Name	Affiliation
Stewart, Meredith	U.S. Army Engineer, Topographic Lab
Swanberg, Nancy	NASA/Ames Research Center
Tucker, Deanne	JPL
Ustin, Susan	University of California, Davis
Vane, Deborah	JPL
Vane, Gregg	JPL
Walker, Richard	JPL
Warnaars, Fred	Hunter College
Westman, Walt	NASA Ames Research Center
Whitney, Wm. M.	JPL
Wickland, Diane E.	NASA HQ
Willis, Steve	University of Washington
Wong, Sam	JPL

Appendix C

Catalog of AIS Test Sites

CATALOG OF TEST SITES FLOWN WITH AIS
(FROM 12/82 THROUGH 3/87)

DATE	SITE NAME	INVESTIGATOR
12/2/82	Mammoth, CA	Gillespie
	Long Valley, CA	Gillespie
	Mud Lake, NV	Goetz
to	Goldfield, NV	Goetz
	Cuprite, NV	Goetz
	Pico Anticline, CA	Rock
12/3/82	Mt. Pass, CA	Kahle
4/25/83	Mud Lake, NV	Goetz
	Cuprite, NV	Goetz
	Death Valley, CA	Kahle
	Mt. Pass, CA	Kahle
to	Silver Bell, AZ	Goetz
	Imperial Valley, CA	Rock
	Los River, W VA	Rock
	Klamath Forest, CA	Strahler
5/24/83	Josephine County, OR	Rock
8/5/83	Cuprite, NV	Goetz
	Boreal Forest, MN	Pitts
	Sleeping Bear Dunes, MI	Olson
	Saginaw Forest, MI	Olson
to	Konza Prairie, KS	Blad
	Lost River, W VA	Rock
	Washington N.F., VA	Labovitz
	Mineral, W VA	Labovitz
8/15/83	Klamath N. F., CA	Strahler
10/18/83	Slate Belt, NC	Wickland
10/20/83	Vermont, NH	Vogelmann
10/21/83	New Hampshire	Vogelmann
10/27/83	Virginia	Bell
10/27/83	Wickland	Slate Belt, NC
10/28/83	Virginia	Labovitz
10/28/83	Lost River, W VA	Rock
10/28/83	Virginia	Masuoka
10/30/83	Wind River, WY	Lang
4/25/84	Cuprite, NV	Goetz
4/25/84	Goldfield, NV	Adams
4/27/84	Death Valley, CA	Kahle
4/27/84	Jasper Ridge, CA	Mouat, Peterson
4/27/84	Stanford, CA	Mouat
5/05/84	Virginia	Bell
5/05/84	Virginia	Masuoka

DATE	SITE NAME	INVESTIGATOR
5/09/84	Slate Belt, NC	Wickland
5/11/84	Slate Belt, NC	Wickland
7/10/84	Cuprite, NV	Goetz
7/10/84	Owens Valley, CA	Rock
7/10/84	Death Valley, CA	Kahle
7/10/84	Sequoia, CA	Peterson
7/18/84	Boreal Forest, MN	Pitts, Star
7/19/84	Sleeping Bear, MI	Olson
7/20/84	Monument Valley, UT	Pieters
7/25/84	Ubehebe & Owlshead, NV	Raines
7/25/84	Hot Creek, NV	Feldman
7/25/84	Yerington, NV	Lyon
7/26/84	Oregon Transect	Peterson
7/26/84	Josephine Cty, OR	Mouat
7/26/84	Josephine Cty, OR	Gillespie
7/31/84	Stockton, CA	Wrigley
8/07/84	Sand Hill, NE	Blad
8/10/84	Purdue, IL	Vanderbilt
8/16/84	Delaware Bay, DL	Klemas
8/17/84	Vermont, NH	Rock-Vogelmann
9/07/84	Blackhawk Island, WI	Peterson
9/08/84	Vermont	Rock-Vogelmann
9/09/84	PowderRiver, WY	Dykstra, Segal
9/09/84	Wind River, WY	Lang
10/30/84	Owens Valley, CA	Rock, Ustin
10/30/84	Cuprite, NV	Goetz, Vane
10/31/84	Mono Lake, CA	Conel
10/31/84	Bridgeport Basin, CA	Gillespie
10/31/84	Sierra Nevada, CA	Gillespie
4/2/85	Owens Valley, CA	Rock, Ustin
4/2/85	Cuprite, NV	Goetz, Vane
5/22/85	Owens Valley, CA	Rock, Ustin
5/22/85	Jasper Ridge, CA	Mouat
5/23/85	Owens Valley, CA	Rock, Ustin
5/23/85	Cuprite, NV	Goetz, Vane
5/23/85	Grapevine, NV	Kruse

DATE	SITE NAME	INVESTIGATOR
6/16/85	Cement, OK	Settle, McKeon
6/16/85	Sand Hills, NB	Blad
6/18/85	Sand Hills, NB	Blad
7/2/85	Virginia Range, NV	Feldman
7/24/85	Ivanhoe, NV	Krohn
7/24/85	Carlin, NV	Podwysocki
7/25/85	Ruby Range, MT	Rowan
7/25/85	Little Falls, ID	Gillespie
7/26/85	Wind River, WY	Lang
7/27/85	Monument Valley, UT	Pieters
7/30/85	Marysvale, UT	Podwysocki
7/31/85	Lake City, CO	Lee
8/2/85	Ozark Mtns., MO	Arvidson
8/2/85	Purdue, IN	Vanderbilt
8/6/85	Blackhawk Island, WI	Peterson, Aber
8/9/85	Oak Ridge, TN	Balick
8/11/85	Pilot Mtn, NC	Milton
8/11/85	Ringwood, NC	Bell
8/12/85	Vermont	Rock
8/12/85	New Hampshire	Rock
8/13/85	Virginia	Masuoka
8/13/85	Central Virginia	Bell
8/23/85	Bonanza, Alaska	Peterson
8/28/85	Bonanza, Alaska	Peterson
8/28/85	Poker Caribou, Alaska	Peterson
8/30/85	Oregon Transect, OR	Peterson
8/30/85	Squaw Butte, Oregon	Schrumpf
9/23/85	Gustine, CA	Peterson
9/23/85	Sequoia, CA	Peterson
9/23/85	Cuprite, CA	Vane
9/23/85	Mono Lake, CA	Conel
9/23/85	Yerington, NV	Lyon
9/23/85	Virginia Range, NV	Feldman

DATE	SITE NAME	INVESTIGATOR
	AUSTRALIA	
10/1/85	Temora	Laughton
10/1/85	Junction Creek	Logan
10/1/85	Dicks Creek	Gallaway
10/1/85	Yarralaw	Williams
10/1/85	Braidwood	Atkinson
10/1/85	Goulburn	Kalma
10/2/85	Wycanna	Jupp
10/2/85	Inverell	Atkinson
10/3/85	Puckapunyal	Morgan
10/3/85	Adelaide	Douglas
10/7/85	Loxton	Douglas
10/7/85	Broken Hill	O'Sullivan
10/7/85	Fowlers Gap	Milne
10/7/85	Wilkawillina	Huntington
10/7/85	Pine Creek	Hussey
10/8/85	Cascades	Houghton
10/8/85	Norseman	Burgess
10/8/85	St. Ives	Simpson
10/8/85	Yindarlgooda	Burgess
10/10/85	Murrin Murrin	Huntington
10/10/85	Agnew	Gregory
10/10/85	Skull Creek	Burgess
10/11/85	Dangin	Hick
10/11/85	York	Hick
10/11/85	Yalanbee	Hick
10/11/85	Dwellingup	Houghton
10/14/84	Jillawarra	Huntington
10/14/85	Port Hedland	Morgan
10/15/85	Sundown	Williams
10/15/85	Blina	Williams
10/15/85	Halls Creek	Otani
10/15/85	Ellendale B	O'Sullivan
10/15/85	Ellendale A	O'Sullivan
10/16/85	Munni Munni	Simpson
10/16/85	Coppins Gap	Huntington
10/16/85	Broadhurst	Swarbrick
10/19/85	Mount Isa	Simpson
10/19/85	Mary Kathleen	Huntington
10/19/85	Gorge Creek	Simpson
10/19/85	Phosphate Hill	Simpson
10/21/85	Palm Valley	Simpson
10/21/85	Stairway	Simpson
10/21/85	Allambi-Amadeus	Taylor
10/21/85	Riddock-Mordor	Horsfall
10/21/85	Hatches Creek	Horsfall

DATE	SITE NAME	INVESTIGATOR
10/22/85	Kidston	Logan
10/22/85	Bald Mountain	Gabell
10/22/85	Newcastle Range	Maffi
10/22/85	Chillagoe	Otani
10/22/85	Cairns	Kelly
10/24/85	Townsville	Morgan
10/24/85	Burdekin River	Pearce
10/26/85	Mt. Leyshon	Fraser
10/26/85	Burdekin River	Pearce
10/26/85	Bimurra	Maffi
10/26/85	Plateau	Munday/Swarbrick
10/26/85	Newcastle Range	Maffi
10/28/85	Mt. Leyshon	Fraser
10/28/85	Gregory	Gray
11/1/85	Hawaii	Kahle
11/2/85	Hawaii	Kahle
11/3/85	Hawaii	Kahle
11/7/85	Hawaii	Kahle
11/9/85	Kahoolawe, Hawaii	Elliot
5/7/86	Fresno, CA	Solomon
5/16/87	Cuprite, NV	Vane
5/16/87	Owens Valley, CA	Rock
5/16/86	Santa Monica Mtns, CA	Westman
7/14/86	Black Forest, Germany	DFVLR
7/15/86	Munich, Germany	Running
7/15/86	Hoglewald, Germany	DFVLR
7/16/86	Frankfurt, Germany	Running
7/16/86	Ranshofen, Austria	Banninger
7/16/86	Burghausen, Austria	Banninger
7/17/86	Frohnleiten, Austria	Banninger
7/17/86	Kuralpe, Austria	Banninger
7/17/86	Klagenfurt, Austria	Banninger
7/17/86	Hochobir, Austria	Banninger
7/17/86	Black Forest, Germany	DFVLR
7/18/86	Hochtor, Austria	Banninger
7/21/86	Hochobir, Austria	Banninger
7/21/86	Grossglochner, Austria	Banninger
7/22/86	Hochobir, Austria	Banninger
7/22/86	Hochtor, Austria	Banninger
7/22/86	Frankfurt, Germany	DFVLR

DATE	SITE NAME	INVESTIGATOR
7/23/86	Venice Lagoon, Italy	Kahle
7/23/86	Florence, Italy	Kahle
7/23/86	Mugelle, Italy	Kahle
7/25/86	Vesuvius, Italy	Kahle
7/29/86	Stromboli, Italy	Kahle
7/29/86	Vulcano, Italy	Kahle
7/29/86	Mt. Etna, Italy	Kahle
7/30/86	Tuscany, Italy	Kahle
8/4/86	Stockbridge, NY	Smith
8/5/86	Stockbridge, NY	Smith
8/6/86	Victoria Mine, NV	Atkinson
9/11/86	Tonopah Divide, NV	Abrams
9/11/86	Grapevine Mtns, NV/CA	Kruse
9/11/86	Cuprite, NV	Vane
9/11/86	San Francisco Bay, CA	Klemas
9/11/86	Jasper Ridge, CA	Peterson
9/15/86	Santa Monica Mtns., CA	Westman
9/18/86	Tucson Mtns., AZ	Adams
9/18/86	Cerro Pelon, NM	Peterson
9/19/86	29 Palms, CA	Star
9/19/86	Grover City, CA	Star
9/22/86	Owens Valley, CA	Rock
9/22/86	White Mtns., CA	Paylor
9/29/86	Meadow Valley, CA	Cogleton
9/29/86	Yerington, NV	Lyon
10/7/86	Sequoia National Park, CA	Peterson
10/14/86	Mojave, CA	Vane
10/14/86	Edwards AFB, CA	Vane
3/15/87	Hawaii, HI	Kahle
3/16/87	Tropical Hawaii, HI	Kahle
3/17/87	Tropical Hawaii, HI	Kahle
3/19/87	Maui Observatory, HI	Kahle
3/22/87	Tropical Hawaii, HI	Kahle
3/22/87	Hawaii, HI	Kahle

TECHNICAL REPORT STANDARD TITLE PAGE

1. Report No. JPL Pub. 87-30	2. Government Accession No.	3. Recipient's Catalog No.
4. Title and Subtitle Proceedings of the Third Airborne Imaging Spectrometer Data Analysis Workshop		5. Report Date August 15, 1987 6. Performing Organization Code
7. Author(s) Gregg Vane, ed.		8. Performing Organization Report No.
9. Performing Organization Name and Address JET PROPULSION LABORATORY California Institute of Technology 4800 Oak Grove Drive Pasadena, California 91109		10. Work Unit No. 11. Contract or Grant No. NAS7-918 13. Type of Report and Period Covered JPL Publication
12. Sponsoring Agency Name and Address NATIONAL AERONAUTICS AND SPACE ADMINISTRATION Washington, D.C. 20546		14. Sponsoring Agency Code RP-666-53-01-00-00

15. Supplementary Notes

16. Abstract

The third and final Airborne Imaging Spectrometer (AIS) Data Analysis Workshop was held at the Jet Propulsion Laboratory on June 2, 3, and 4, 1987. It was attended by 106 people from 9 countries. Papers were presented by 20 investigators: summaries of 17 of these papers are published in these Workshop Proceedings. After a morning devoted to a status overview of the JPL imaging spectrometer program the first day of the Workshop, the remaining time was spent discussing AIS calibration, performance, information extraction techniques, and the application of high spectral resolution imagery to problems in geology and botany. Partly as a result of improvements to the sensor and additional time spent in analyzing data since the last Workshop, this Workshop produced the most convincing evidence of the power of imaging spectroscopy presented to date. Nevertheless, much work yet remains to be done to pave the way for routine application of this new tool to the full suite of earth science problems addressable with high spectral resolution remote sensing. Considerable enthusiasm was expressed for the new sensors now becoming available to replace AIS, the Airborne Visible/Infrared Imaging Spectrometer (AVIRIS) and the Portable Instant Display and Analysis Spectrometer (PIDAS).

17. Key Words (Selected by Author(s))	18. Distribution Statement
Forestry Earth Resources Environment Pollution Geology and Mineralogy Information Theory	Unclassified -- Unlimited

19. Security Classif. (of this report)	20. Security Classif. (of this page)	21. No. of Pages	22. Price
Unclassified	Unclassified	vi + 183	

JPL 0184 R 9/83